Generation and manipulation of high-dimensional photonics states with AlGaAs chips

Giorgio Maltese

UNIVERSITÉ PARIS DIDEROT - PARIS 7
SORBONNE PARIS CITÉ

LABORATOIRE
MATÉRIAUX ET PHÉNOMÈNES QUANTIQUES

ÉCOLE DOCTORALE 564 :
PHYSIQUE EN ÎLE-DE-FRANCE

UFR DE PHYSIQUE

THÈSE

présentée par

Giorgio MALTESE

pour obtenir le grade de

Docteur en Sciences de l'Université Sorbonne Paris Cité

Generation and manipulation of high-dimensional photonics states with AlGaAs chips

directrice de thèse : professeur Sara Ducci

Soutenue publiquement le 20 mai 2019,
devant la commission d'examen composée de :

Maître de conf.	Virginia D'AURIA (Univ. Nice),	Rapporteure
Professeur	Marco LISCIDINI (Univ. Pavia),	Rapporteur
Professeur	Eleni DIAMANTI (Univ. Sorbonne),	Examinatrice
Professeur	Jean-Pierre HERMIER, (Univ. Versailles)	Président du jury
Maître de conf.	Maria AMANTI (Univ. Paris Diderot),	Co-encadrante de thèse
Professeur	Sara DUCCI (Univ. Paris Diderot),	Directrice de thèse

Contents

Acknowledgements

Before my PhD journey I was a master student with no real experience of academic research. Likewise, I did not have any clue about surfing. Today I feel that research and surfing have some similarities: they both require a considerable amount of energy and patience, the right techniques and the ability to identify the right waves to ride. Plus, in the daily research life as in the ocean, there are highs and lows to cope with. Luckily, in the last four years at MPQ laboratory I have met many kind researchers, who showed me how to enjoy academia by surfing with me.

I wish to express my first acknowledgment to Sara, my PhD advisor. Thank you for warmly welcoming me in your group and supporting every project, even when they were not giving the expected results. I am grateful that you gave me the freedom to explore the subject, while still guiding me from the right distance. I am also thankful for your meticulousness in reviewing several conference talks and this very manuscript.

The main work presented in this thesis was remarkably supported by Maria, my PhD co-supervisor. Apart from teaching me many laboratory and cleanroom tricks, you set an example with your endurance and passion for research. For example, I remember when you stayed with me in the lab at night, until very late hours, in order to complete some long-awaited measurements.

A special thank also goes to Florent Baboux, which has always given me useful insights and inspired me with his delightful way of giving talks and presenting research results. I am also thankful to Jean-Pierre Likforman and Luca Guidoni, who for several months shared with us their laser, lab tools and expertise.

I am grateful to the postdoc Yacine Halioua for the methods in numerical simulation he taught me at the beginning of my PhD, as I have made good use of them during all my thesis. I warmly thank Maria (again), the postdoc Qifeng Yao and Claire Aubert for teaching me clean room techniques by letting me work at their side. I also appreciated the formation and kind assistance provided by the clean room engineers Stéphan Suffit, Pascal Filloux and Chrisophe Manquest from Paris Diderot and Michael Rosticher from ENS. I learned the importance of presenting data in an effective and beautiful way from Guillaume Boucher, who introduced me to GnuPlot - I am sure you will be a great teacher!

Every day, my PhD work has been lightened by some great office mates: Saverio Francesconi, Nicolas Fabre, Louis Garbe, Jonathan Belhassen and Félicien Appas. A unique thank goes to Saverio, the ideal lab mate. It has always been a pleasure to share the lab with you, other than the daily lunch, tea times, conferences and

many other adventures I will never forget (especially skydiving as the first time was a bit scary). I had a good time with Jonathan, who shared his internship and PhD journey with me, and Louis, whose remarkable politeness and humor last until late office hours. Nicolas, I am thankful for you taking care of the avocado plant, when either me or Saverio could not. I thoroughly enjoyed the daily conversations and our short theoretical-experimental collaboration. In this regard, I would like to extend my thanks to all the theorists who worked with us: Simone Felicetti (good luck for your future research career!), Pérola Milman, Arne Keller and Thomas Coudreau. Félicien, I am confident that you will do a great PhD, including many successful clean room processing. I enjoyed the time we worked together during your internship. Likewise, I express my appreciation to the students Giulia Sinnl and Ulysse Najar for working with me during their master internship.

My teaching experience at IUT Diderot has been exceptional thanks to my supervisor, Christian Chauveau. I hope you still have some time to play music and theatre!

I am also grateful to Maria Luisa della Rocca and Vincent Repain for giving me the opportunity of experiencing public engagement with research at Palais de la découverte at the exposition 'Un chercheur une manip: explorer les matériaux quantiques'.

Among MPQ staff, I am indebted to Sandrine Di Concetto, Jocelyne Moreau and Anne Servouze, which made university bureaucracy easy to handle, and Monia Mestar who helped me organizing the PhD defense from abroad. I also acknowledge Patrick Lepert and Nicolas Martial from the mechanical workshop as they have always fabricated perfect pieces for the experimental setup.

During my stay at MPQ, I enjoyed the social atmosphere in which I had the pleasure to meet friendly PhD students, postdocs and professors. A not exhaustive but significant list includes: Valerio Gili, Giuseppe Marino, Samantha Sbarra, Carlo Gigli, Pierre Allain, Marco Ravaro, Giuseppe Leo, Angela Vasanelli, Zahra Asguari, Sébastien Cosme, Azzurra Bigioli, Allegra Calabrese, Alireza Mottaghizadeh, Mehdi Hamoumi, Williams Hease, Biswarup Guha, Alice Bernard, Cécile Ozanam, Fabrizio Minganti, Filippo Vicentini, Riccardo Rota, Cristiano Ciuti, Mathieu Jeannin, Jared Lolli and Peregrine Wade.

Out of the lab, I have been fortunate to become friends with a set of unique individuals. I have met most of them during my stay at the Crous residence Chevaleret. This has been possible thanks to the USPC international PhD students project, for which I am grateful to Thomas Coudreau, director of USPC Doctoral College. Among the friends which made me feel at home in rue du Chevaleret, I remember Manuel and Claudio, best fellows in an uncountable number of incredible adventures, in and out of Paris. Also thanks to Chiara, Isabella and Luca for the great dinners and barbecues, Martina for the music festivals, Valerio and Armand for coffee and amazing trips, Dima for the jam sessions, Margaux, Isa, Nikos and Nicola for the great soirées spent together. Lovely brunches at the Barge have been possible thanks to Nikola, Miki, Ana, Umberto and Swathi, while I thank my cousin Silvia, Zane and Thomas for the delicious home-cooked apéros and dinners,

tastier than any meal in a Michelin-starred restaurant.

After three years at the residence, I am grateful to Cariri and Alba for welcoming me in *El Pisi*, my second home in Paris (and thanks Vero for letting me your place). I appreciated the relaxed atmosphere, ideal for writing this manuscript, and the evenings spent watching movies or partying with Giulia, Martina and our other friends.

I also appreciate the support of my friends from Italy, for which the distance has never been an issue. In particular, my Politecnico di Milano mates, Andrea, Stefania, Luca and Rugge, and my lifelong friends from Bergamo, Alberto, Luca, Michele and Mauro. I am also grateful to Dr Valerio Castagna for his medical support and assistance, even from abroad.

Last but not least, I would like to express my deepest gratitude to my family for their everlasting support and to Ana for standing by my side during all this journey and beyond.

Introduction

The quantum essence of nature conveys concepts which are far from our every day experience. Among these, entanglement is one of the most surprising ones. In a bipartite entangled system, the states of two objects have to be described with reference to each other, regardless of their spatial separation. A specific measurement of one object, even if it gives a random outcome, determines the result of the same kind of measurement carried out on the other object. This nonlocal correlation cannot be explained by a theory of local hidden variables [1], as shown within the formalism of Bell inequalities [2] by many experiments in the past [3, 4, 5] and recently by "loophole-free" tests [6, 7, 8].

The comprehension of entanglement and other quantum phenomena has led to what we call nowadays the second quantum revolution [9], where the generation, manipulation and detection of entangled states are fundamental resources to develop new technologies. In this perspective, several countries have launched large research programmes. The Chinese programme has already demonstrated satellite-based Quantum Key Distribution (QKD) protocols [10, 11], while the European Quantum Flagship initiative has identified four strategic fields of quantum technologies: quantum communication, quantum simulation, quantum computation and quantum sensing and metrology. In the private sector, several start-ups have emerged and multinational companies have started to invest heavily, especially for applications in quantum communication (e.g. IDQ, Toshiba) and computing (e.g. Rigetti, IonQ, Google, Microsoft, IBM, Intel).

Nevertheless, the implementation of quantum information protocols for real world applications is challenging due to the competing tasks involved: quantum information carriers must be generated, manipulated and detected while being isolated from the uncontrolled environment. To address this problem, a wide range of technological platforms are under development, each one with its own assets and limitations. As instance, trapped ions [12] and superconducting circuits [13] are emerging as good candidates for quantum computing, while optical lattices [14] and photonics circuits [15] are promising for quantum simulation. In quantum metrology and sensing, neutral and Rydberg atoms, trapped ions and solid state spins (e.g. NV centers in diamonds) are the most attractive [16].

Photonics platforms are extremely adapted to quantum communication: photons travel at the speed of light and are immune to environmental perturbations, as they interact very weakly among themselves and with transparent media. Yet, for the same reason, the manipulation of photons is not straightforward and usually relies on probabilistic operations, hard to scale. Nonetheless, the possibility

of processing information using only linear-optical platforms [17], together with technological developments in integrated photonics, has led to the implementation of numerous quantum algorithms and simulation protocols [18, 19] on a photonic chip [20, 21, 22].

In this context, this thesis has contributed to enlarge the panel of possible applications in quantum information of integrated AlGaAs devices. The first achievement has been the generation of high-dimensional biphoton frequency-comb states, made possible by the numerical studies and the experimental characterization of AlGaAs sources of entangled photons in a monochromatic pump regime. In addition, the identification of two classes of spectrally different biphoton frequency-comb states, namely resonant and anti-resonant states, has led to the proposal and implementation of a manipulation protocol to control the symmetry of the emitted states. Furthermore, the development of new simulation routines and the optimization of clean-room techniques has brought to the realization of AlGaAs waveguides for the emission of light beams carrying spin angular momentum. The same techniques has led to the design of a similar device for the manipulation of light orbital angular momentum.

Integrated photon pair sources

In integrated quantum photonics two classes of devices are commonly used to generate photon pairs: quantum dots and parametric nonlinear sources [23, 24].

Quantum dots are nanometric structures which confine electrons and holes in the three dimensions of space (hence their name). Since their energy levels are discrete, they are also known as artificial atoms. The great advantage of quantum dots is that they emit single photons deterministically and on-demand. The ground state of a quantum dot can be excited in a biexcitonic state, formed by two electron-hole pairs. As it decays, two photons are produced on cascade: while one electron-hole pair recombines, a photon is emitted, leaving the quantum dot in a single excitonic state; this rapidly decays with the emission of another single photon. The total energy and momentum of the recombining electron-hole pair determines the energy and momentum of the emitted photons [25]. Therefore, quantum dots with different dimensions and electronic structures produce photons with different spectral properties. Quantum dots can be divided into two categories: colloidal quantum dots and epitaxial quantum dots.

Colloidal quantum dots are solution-processed nanoscale crystals of semiconducting materials [26], compatible with room temperature operations [27] and electrically-driven configurations [28]. Colloidal quantum dots can be synthetized in large batches and with a high monodispersity by using relatively inexpensive chemical synthesis, which can be followed by a wide range of chemical post-processes and thin-film assembly steps. The scalability and flexibility of their synthesis are a huge advantage for commercial applications, in both imaging and optoelectronic industries. In these last years, many efforts have been devoted to reduce photobleaching (permanent unability to fluoresce due to a photochemical alteration) [29] and

blinking effect (random fluctuations between bright and dark states) [30] affecting colloidal quantum dots, leading to important advances of their performances as single photons emitters.

Epitaxial quantum dots, also known as self-assembled quantum dot, are grown via an epitaxial growth from the vapour phase. Their growth has a random nature, in the sense that their positions and dimensions cannot be precisely predetermined. To address this problem, fabrication techniques for their deterministic placing [31] or methods based on in-situ lithography [32] have been developed. The efforts done by the community to keep under control the decoherence effects linked to the cristalline matrix (e.g. charge noise and spin noise [33]) has allowed to produce entangled photons under both optical [34] and electrical pumping [35]. In order to exploit excitonic states to produce single and entangled photons, the thermal energy of the system has to be smaller than the binding energy of these quasiparticles, which imply to work at cryogenic temperatures. Regarding the coupling with external optical fibers or devices, a high collection efficiency can be achieved using photonic crystal structures [36] or electrically controlled cavities [37].

Parametric nonlinear sources rely on the interaction of a pump beam with a nonlinear medium to produce photon pairs. In this case the devices work at room temperature but the generation process is probabilistic. Depending on the symmetry of the nonlinear material, Spontaneous Parametric Down Conversion (SPDC) or Spontaneous Four-Wave Mixing (SFWM) can take place. Nonlinear materials lacking of inversion symmetry, like lithium niobate (LN) or gallium arsenide (GaAs), can be used to implement SPDC. In SPDC, a high energy photon (pump photon) spontaneously decays into two low energy photons (signal and idler photons) sharing its energy. The process is efficient if the total momentum of the three interacting photons is conserved. This condition, called phase matching in a wave description, is not automatically satisfied due to the dispersion of the nonlinear media, but different solutions have been implemented. The first demonstrations of SPDC relied on crystals birefringence [38], with pump and emitted photons propagating along different directions with respect to the crystal axis. Nowadays, the implementation of a quasi-phase matching [39, 40] technique is widely adopted in dielectric waveguides. In this scheme the crystal structure is engineered to obtain a periodical inversion or inhibition of the nonlinearity, reversing or hindering the effect of the phase mismatch. Quasi-phase matching is particularly used in dielectric ferroelectric materials, such as periodically poled lithium niobate (PPLN) waveguides [41], and can also be implemented in the AlGaAs platform. However, orientation patterned AlGaAs waveguides suffer from high optical losses ($\sim$ 9dB/cm at 1.55μm) [42]. For this reason, in this thesis we resort to another strategy to satisfy phase matching, named modal phase matching. In modal phase matching, pump, signal and idler photons propagate in different guided modes. As instance, in our AlGaAs waveguide the guided pump photons are in a Bragg mode, while signal and idler photons in fundamental Gaussian modes. The waveguide's design allows to tailor the modes dispersions and to satisfy momentum conservation over a large bandwidth of the emitted photons

[43, 44].

SFWM can be implemented in centro-symmetric media, such as silicon. In this process, two pump photons annihilate to produce a photon pair. When the process is degenerate, pump photons have the same energy of signal and idler photons. In this case, and more generally when the SFWM spectra is narrow, the filtering of the pump beam may be challenging. Since SFWM is a third order nonlinear process, it is less efficient than SPDC occurring over the same propagation distance. Yet, SFWM structures with low propagation losses and high finesse allow to extend the effective nonlinear length and achieve a high generation rate of photon pairs. Some of the first demonstrations of SFWM in bulk optics relied on optical fiber loops [45] or silicon ridge waveguides within optical fiber loops [46]. Nowadays, fully integrated solutions are based on microring resonators [47, 48] having a high quality factor.

Integrated quantum photonics platforms

Integrated quantum photonics has many key advantages with respect to free space quantum optics, such as scalable and reconfigurable architectures, small system footprints and enhanced light-matter interaction. Thanks to significant developments in the field of classical photonics, several material platforms have emerged for the realization of a vast range of miniaturized components: pump sources, non-classical light sources, filters, waveguides, couplers, electro-optic modulators, quantum memories, detectors, etc.

One of the main challenges on the way towards a large diffusion of quantum technologies is the development of monolithic or hybrid platforms integrating the generation, the manipulation and the detection of quantum states of light. This motivating challenge is leading to continuous progress on a large variety of material platforms, such as silicon-based platforms, III-V materials, PPLN, silicate glasses, Hydex, diamond [49].

Silicon-based platforms are at the edge of integrated large-scale quantum information processing. **Silica on silicon** (**SoS**, SiO_2/Si) has been the first platform used to compile a quantum algorithm on a photonic chip [50, 20], while **Silicon on insulator** (**SOI**, Si/SiO_2/Si) is widely used in integrated quantum photonics thanks to the refractive step-index and electrical insulation offered by the oxide layer. One of the main advantages of silicon-based platforms is that they inherit the well-developed fabrication processes developed in the CMOS industry. Besides, silicon electrical and optical properties are favorable for quantum information processing. Silicon indirect bandgap at 1.12eV and low intrinsic concentration of carriers make it transparent in the telecom wavelength (1.55μm). Its strong $\chi^{(3)}$ nonlinearity enables SFWM, while its high refractive index allows waveguides with a small bend radius. Besides, SOI chips are compatible with the hybrid integration of nanowire superconducting single-photon detectors (SNSPDs), with almost 90% of quantum efficiency and low dark count rates ($\approx 10^4$Hz) [51]. On the other hand, some issues still need to be tackled. Two-photon absorption

limits the amount of intensity of the pump laser that can circulate in a silicon waveguide. Besides, due to silicon indirect bandgap, the on-chip integration of the pump source is challenging and probably requires the hybridization of SOI with another active material, such as GaAs or InP.

Silicon nitride (**SiN**, Si_3N_4/SiO_2) is an alternative silicon platform compatible with SOI and CMOS industry, presenting the advantage that it is exempt from nonlinear absorption. Therefore silicon nitride can sustain higher laser intensity, compensating the fact that its nonlinear coefficient $\chi^{(3)}$ and refractive indexes are lower than the ones of silicon. Silicon nitride ring resonators are used to efficiently generate biphoton frequency-combs states [52, 53], and fast optical switchers have been realized in silicon nitride waveguides [54, 55].

III-V platforms, such as **GaAs** and **InP**, offer additional features compared to silicon based platforms. Thanks to the direct gap of their electronic band structure, they are compliant with electrical injection. Moreover, GaAs and many other III-V alloys lack of inversion symmetry and possess a strong $\chi^{(2)}$ nonlinearity, enabling spontaneous parametric down conversion (SPDC). Finally, the use of III-V ternary (e.g. AlGaAs, InGaAs) or quaternary (e.g. AlInGaP) alloys permits the realization of integrated heterostructures. These unique features led to the demonstration of single-photon sources based on GaAs/InAs quantum dots [56, 37] and of sources of photon pairs based on AlGaAs, both optically pumped [44, 57] or electrically-driven [58, 59]. Furthermore, GaAs electro-optic effect enables a fast optical switching and fine control over modal birefringence [60]. Regarding the integration of the detection process, GaAs waveguides are compatible with superconducting nanowire detectors as well [61]. Nowadays, the main issue in III-V based devices is their linear losses, which are of the same order of magnitude than the ones of SOI-based devices but higher than the ones of SiN and SoS-based waveguides, limiting the scale of the possible chips to be used for quantum information processing.

Apart from silicon and III-V based materials, other platforms have distinguished in integrated quantum optics.

Periodically poled lithium niobate (PPLN) waveguides have been used to realize the first integrated efficient source of photon pairs [62]. Like lithium niobate (LN), PPLN waveguides have a high transparency and chemical stability, together with a strong $\chi^{(2)}$ nonlinearity and a large electro-optic effect. In addition, the periodical poling allows to satisfy and engineer the quasi-phase matching over distances in the centimeters scale, while the guided regime assures a tight confinement of the propagating light, enhancing the efficiency of SPDC [41]. Recently, the combination of a PPLN waveguide and standard telecom components has allowed the realization of a fully guided-wave squeezing experiment [63, 64]. The main limitations of PPLN waveguides are the difficulty of integrating on-chip the pump laser and the low refractive index which limits the miniaturization. To address the latter, LN-on-insulator has been recently developed, with the realization of microdisk [65], microring [66] and photonic crystal [67].

Silicate glasses can be engineered via **femtosecond laser direct writing** to obtain integrated waveguides. This fabrication technique is ideal for prototyping

or large-scale production since it is fast (writing speed in the order of cm/s), it does not need masks and it is single-step (the processing of the substrate is not required like in traditional lithographic techniques). The control of the focal point and the spatio-temporal shaping of the femtosecond laser beam [68] allows to write three-dimensional photonics circuits [69, 70, 71], planar circuits with a complex shape [72] and integrated optical waveplates [73, 21]. At present, the main challenge is to integrate active photonics components, such as pump sources, electro-optic modulators and single-photon detectors.

Hydex glass is a high index doped silica glass that is processed via standard clean room techniques. Developed in 2003 by Little Optics, its properties are a compromise between the low linear losses of silica and the high third order nonlinearity $\chi^{(3)}$ of semiconductors [74]. In addition, like silicon nitride, it has a two-photon absorption that is negligible (up to 25GW/cm^2 [75]). Thanks to these assets, Hydex microdisk are used to implement SFWM processes and efficiently generate biphoton frequency combs states of light [76, 77], as well as measuring ultrafast optical pulses [78].

To conclude, we note the recent developments in **diamond-on-insulator** platform [79, 80], which inherits from bulk diamond its electromechanical stability, high isotopic purity, wide band-gap and low concentration of free electrons. Besides, in combination with diamond waveguides and photonic crystals, nitrogen vacancy color centers in diamond are a candidate for the implementation of protocols coupling photonics and matter qubits [81, 82], leveraging on their bright fluorescence and the long coherence times ($\sim$ ms) of electrons spin [83].

Encoding quantum information in light degrees of freedom

In photon-based quantum technologies information is encoded and manipulated using one or more degrees of freedom of light [84]. Photons can carry information in the electric field oscillation direction (polarization qubits), spatial distribution (path qubits and orbital angular momentum qubits) and frequency (frequency-bin qubits), as well as in the source to detector propagation time (time-bin qubits or energy-time qubits).

Polarization qubits rely on the polarization state of single photons. A qubit is usually expressed in the horizontal and vertical polarization basis, in the rotated diagonal and antidiagonal basis or in the left and right circular polarization basis. Polarization qubits are widely adopted thanks to the relative ease of preparing and manipulating a polarization entangled biphoton state. As instance, this can be realized by using a type-II SPDC processes, polarizing beam splitters and wave plates, available in both free space and integrated devices [85]. Polarization qubits have been used to demonstrate, alone or in combination with other degrees of freedom, protocols for quantum simulation [21], computation [86, 87] and communication [88, 89], such as the famous BB84 scheme for QKD [90]. However, the feasibility of polarization encoding comes at the price of a two-dimensional Hilbert space, which limits the quantity of information per photon and thus the protocols performance (e.g. the achievable rate of secret key sharing in QKD).

Besides, birefringence and mechanical instabilities of optical fibers hinder the use of polarization in fibered quantum communication, making it more suitable for free-space optics.

Orbital angular momentum (OAM) qubits encoding relies on a set of beams with a helicoidal wavefront that carries an optical vortex along the propagation axis. The number of wavefront twists per wavelength (i.e. the vortex periodicity in the phase space) defines the OAM order. This is potentially unbounded, thus provinding an interesting alternative to polarization encoding for free-space quantum communication. For example, OAM qubits have been used to demonstrate QKD protocols with a high key generation rates per photon [91], superdense coding [92], teleportation based quantum repeaters [93] and quantum memories [94]. OAM states can be generated by using either free space optics tools (spiral wave plates, cylindrical lens pairs, spatial light modulators, q-plates, antennas metasurfaces, etc.), or integrated out-of-plane emitters (microlasers, microring resonators with angular gratings). In this context, the last part of this thesis is devoted to the design and realization of an integrated cylindrical mode converter, with potential applications in the generation and manipulation of OAM.

Spatial mode qubits (or path qubits) are represented by the spatial modes occupied by photons. In integrated optics, waveguide arrays are a natural implementation of large-scale path encoding, offering a total control over the number of paths (waveguides) and their coupling, obtained via directional or evanescent couplers and phase shifters. Recently, path qubits have been used to achieve the generation, control and characterization of a high-dimensional bipartite entanglement state [95], the simulation of the vibrational quantum dynamics of four-atom molecules [22] and to demonstrate the quantum interference of topological states of light [72].

Time-bin qubits are implemented by using an unbalanced Mach-Zehnder interferometer that introduces a short and a long path for the single photon, corresponding to a short and long arrival time. This protocol requires that the path difference is longer than the single photon coherence length and fluctuates less than the photon wavelength. Under these conditions, time-bin encoding can be used for quantum communication in both free-space and optical fibers, being robust to fibers depolarization and chromatic dispersion. At the end of last year, a three-state time-bin decoy QKD protocol has achieved the distribution of secret keys in optical fibers over more than 400 kilometers [96], while time-bin qubits quantum memories are currenlty under development [97].

Frequency-bin qubits are encoded in the photons frequency domain. In its original proposal [98], narrow-band filters were placed before the detectors to define the frequency-bins: photons which could not be distinguished by the filters belonged to the same frequency bin. Besides the discretization of the frequency space, frequency entanglement is the second ingredient of frequency-bin encoding. While in time-bin encoding entanglement results from the superposition of short and long paths, in frequency-bin encoding it emerges naturally from the conservation of energy governing nonlinear parametric processes. As instance, in SPDC the energies of signal and idler photons are uncertain, but their sum must

equal the energy of the pump photon. Therefore the use of a monochromatic pump laser generates a biphoton state with a strong frequency anti-correlation [98]. After its generation, a frequency-bin state can be manipulated straightforwardly by using electro-optic phase modulators in a single light spatial mode [99], with the advantage that frequency is immune to the birefringence of optical fibers and does not require stability. Still, for long-distance fiber-based QKD protocols, chromatic dispersion may pose a problem, even if its acitve control has been proved over distances up to 50km [100].

Generation and manipulation of frequency-comb states

In frequency-bin encoding, the frequency space of a biphoton state is divided into two bins. However, it is possible to use a cavity to filter the joint spectral amplitude of a biphoton state into many frequency bins and produce a high-dimensional frequency state. In the literature, this state is referred to as a two-photon mode-locked state [101], given the stable phase relationship existing among the various frequency modes, or biphoton frequency-comb state, from the comb-shaped signal and idler joint spectral amplitude. Frequency-comb state have been first investigated exploiting SPDC in dielectric crystals [101, 102, 103]; in these works, the comb is generated either by inserting the nonlinear crystal in a cavity or by putting the cavity after the generation of the state. More recently, a growing attention has been devoted to the generation of biphoton frequency-combs in integrated optical micro-resonators implementing SFWM. This approach overcomes the drawbacks of low scalability and high cost of bulk systems. Interesting results on the generation and coherent manipulation of high dimensional frequency states have been obtained in both Hydex [76] and silicon nitride [52, 53] micro-rings. In this work, we exploit the facets reflectivity of an AlGaAs ridge waveguide to realize a miniaturized nonlinear cavity and generate biphoton frequency-combs.

The dimensionality of the emitted frequency-comb depends on the resonator geometry and the optical properties of the nonlinear source. When the resonator free spectral range is much smaller than the biphoton bandwidth, a high-dimensional state can be achieved. Yet, the manipulation of a frequency-comb state imposes a constraint on the minimal and maximum extension of the resonator free spectral range. In order to address individual frequency modes, the free spectral range must be larger than the linewidth of programmable filters; at the same time, the mixing of adjacent frequency modes requires that the free spectral range is comparable with the bandwidth of the available electro-optic phase modulators. By using microring resonators with a free spectral range of 50GHz [104] and 200GHz [77], the groups of Morandotti and Weiner have demonstrated the coherent control over frequency-comb states by using off-the-shelf (although at the cutting edge of technology) telecom components. These demonstrations have potential applications in both quantum communication and quantum computing. As instance, a high-dimensional frequency state can lead to quantum communication protocols over longer distances. Indeed increasing the dimensionality of the state allows to reduce

the number of photons to encode and transmit information (with respect to qubits-based protocols). Therefore the effect of propagation losses, one of the main issues in fibered communication, is partially solved [105]. Alternatively, large-alphabet QKD protocols can be implemented, with an increase in the key transmission rate [106].

In quantum computing, the resilience of the frequency degree of freedom to the environment noise and the availability of telecom components has opened the way to quantum frequency processing [107]; in this approach a universal sets of gates is implemented by using a cascade of phase modulators and pulse shapers, in analogy to phase-shifters and beam splitter in spatial mode-based quantum processors [108, 109]. The most recent demonstration consists in a one-way quantum processing protocol based on a time-frequency d-level cluster state [110].

To conclude, we note that the discretization of the biphoton frequency space in more than two levels can be used to implement qubit states that can be processed by realistic noisy machines, such as Gottesman-Kitaev-Preskill (GKP) states [111]. In this case the redundant information of the d-level system is used to perform error correction codes on the quantum states.

Outline

The manuscript is divided into three parts, preceded by a chapter giving a brief background on integrated and nonlinear optics and on the optical properties of GaAs/AlGaAs semiconductor platform.

In the first part we present a theoretical study and the experimental characterization of an optically pumped AlGaAs source of photon pairs. We show how frequency and polarization entangled biphoton states are emitted via SPDC (chapter 1). Studying the phase matching function, we discuss the properties of the biphoton joint spectral amplitude, underlying its dependence on the source birefringence and chromatic dispersion (chapter 2). We present an experimental characterization of the source efficiency carried out as a function of the spatial shaping of the pump beam, its power, its wavelength and the source temperature (chapter 3). Additionally, we describe the development of a clean room processing technique to fabricate dry etched AlGaAs sources and show its application on active samples (chapter 4).

In the second part of the manuscript we take into account the cavity effect due to the AlGaAs waveguide facets reflectivity and we propose a scheme to generate and control the symmetry of broadband biphoton frequency states, acting on the interplay between cavity effects and relative temporal delay of the photons of the pair. In chapter 5 we show how resonant and anti-resonant biphoton frequency states can be generated by tuning the wavelength of the monochromatique pump beam, while in chapter 6 we demonstrate the proposed method by using Hong Ou Mandel interferometry.

In the last part, we report our work on the design, fabrication and characterization of collinear AlGaAs sources for the manipulation of the angular momentum of light. As a first step, we realize an integrated quarter-wave plate to transform an input beam, linearly polarized at 45°, into a circularly polarized beam that carries spin angular momentum (chapter 7). As a second step, we report our work on the design and the optimization of the clean room processing of an integrated cylindrical mode converter for both polarization directions. This device transforms a HG_{11} input beam into a LG_{01} output beam, which carries first order orbital angular momentum (chapter 8).

We conclude by summarizing the main results of this work, its potential applications and future developments.

Integrated nonlinear optics in AlGaAs waveguides

In this introductory chapter we briefly present some basic notions on the material platform and devices used in this work. We start by recalling the main aspects of the guided wave regime. We then introduce nonlinear optical processes, with a focus on second-order processes and a classical treatment of difference frequency generation. We conclude by presenting the optical properties of GaAs and AlGaAs, the semiconductor materials that we use to realize our integrated sources.

Integrated optics: waveguides

A waveguide is a structure where the energy of an electromagnetic radiation is confined along one or two dimensions along the residual dimensions while it propagates. In this thesis, we are interested in waveguides with a bidimensional confinement where light propagates along a specific direction, named propagation direction. The specific waveguide design determines the characteristics of its guided modes, in terms of frequency (central frequency, bandwidth and dispersion), polarization (transverse electric or transverse magnetic and birefringence) and spatial properties (mode profile and modal dispersion).

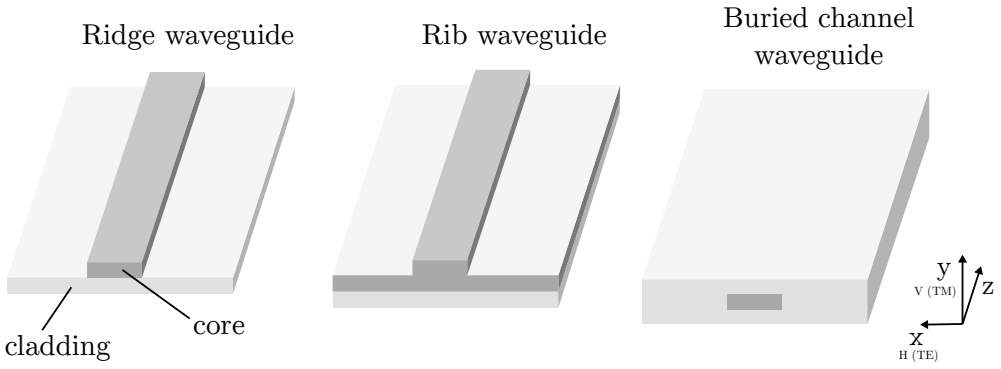

Figure 1 – Some examples of waveguides.

Figure (1) illustrates the most usual waveguide geometries: ridge, rib and buried channel waveguides. The waveguide core (in dark grey), has a refractive index that is higher than the surrounding cladding (light grey) and air regions: it thus bends and confines the propagating beam of light, in analogy to a focusing

lens. When the converging effect counter-balances the spreading of the propagating wave due to diffraction, a guided mode is supported in the waveguide [112]. In a dielectric waveguide, the dimensions of the guiding region are typically comparable with the wavelength of the propagating field.

We consider a waveguide that confines light along x and y axis and let it propagate along z axis. For a given frequency ω, the electromagnetic field can be written as:

$$\begin{aligned} \mathbf{E} &= E(x,y)\exp i(\omega t - kz)\ \hat{\mathbf{e}} \\ \mathbf{H} &= H(x,y)\exp i(\omega t - kz)\ \hat{\mathbf{h}} \end{aligned} \tag{1}$$

where k is the propagation constant along z and $\hat{\mathbf{e}}$ and $\hat{\mathbf{h}}$ the polarization directions. $E(x,y)$ and $H(x,y)$ are the spatial distributions of the electric and magnetic fields, determined by the wave equation:

$$\left[\boldsymbol{\nabla}^2 - \frac{\mathrm{d}^2}{\mathrm{d}z^2} + \left(\frac{\omega^2}{c^2}n^2(x,y) - k^2\right)\right]E(x,y) = 0 \tag{2}$$

where $n(x,y)$ is the refractive index profile, determined by the waveguide material composition and structure. If the waveguide is made of homogeneous dielectric layers, like the rib waveguide in figure (1), equation (2) holds in each region. At the borders among adjacent regions, the interface conditions of the electromagnetic field apply. In this manuscript, we will refer to the transverse electric TE (transverse magnetic TM) polarized modes as H (V) modes to keep the same notation used by the quantum optics community. The modes supported by the waveguide are those which are confined. This implies that they do not have a flow of energy in the transverse plane (zero electromagnetic energy at infinite distance in the xy plane) and the field distribution reaches a maximum value at some point in the xy plane (typically within the core). These two conditions are satisfied only for a limited and discretized number of values of the propagation constant k :

$$\frac{\omega^2}{c^2}n^2(\infty) < k^2 < \frac{\omega^2}{c^2}n^2_{core}(x,y) \tag{3}$$

If the waveguide is surrounded by air, $n^2(\infty) = 1$, while the refractive index of the core n_c has typically the highest value of the structure.

In the waveguide, where condition (3) is satisfied, the eigenstates of the transverse wave equation (2) present an oscillatory form in the transverse plane within the core region. Due to the confinement of the electric field, each guided mode has its own propagation constant.

On the other hand, externally to the waveguide, where condition (3) is not satisfied, the eigenstates have a decaying exponential form.

Whenever the external and internal eigenstates match, i.e.. by imposing that the tangential component of the electric (magnetic) field is continuous at each dielectric interface, a guided H (V) mode is supported by the waveguide.

Each guided mode propagates along the waveguide independently. Its propagation constant is usually expressed in terms of an effective refractive index n_{eff}:

$$k(\omega) = \frac{\omega}{c} n_{eff}(\omega) \tag{4}$$

which indicates the phase velocity of the mode as it propagates in the waveguide:

$$v_p(\omega) = \frac{c}{n_{eff}(\omega)} \tag{5}$$

The mode energy propagates at the group velocity v_g, which can be expressed as a function of the mode phase velocity and dispersion:

$$v_g^{-1}(\omega) = \frac{\mathrm{d}k}{\mathrm{d}\omega} = v_p^{-1} + \frac{\omega}{c} \frac{\mathrm{d}n_{eff}(\omega)}{\mathrm{d}\omega} \tag{6}$$

The mode spatial distribution $E(x, y)$ and propagation constant k can be found analytically in the case of a homogeneous one dimensional waveguide (see equations (11.2) in reference [112]), or numerically by solving the eigenvalue wave equation (2) for more complex 2D or 3D structures.

Nonlinear optics

Since the invention of laser in the 60s [113], the availability of intense and coherent beams of light has opened the way to explore novel interactions between light and matter, and in particular optical processes in nonlinear media.

The nonlinear interaction between light and matter can be in first approximation understood by adopting Lorentz model, which describes in a classic way the effect of an electromagnetic wave acting on a medium. When an electromagnetic wave interacts with the medium, a dipolar-type interaction occurs between the wave and the electrons bound to the atoms of the medium. During this interaction, the wave drives the oscillation of the electrons within the crystal potential.

If the amplitude of the electric field carried by the wave is much lower than the amplitude of the electric field existing between the electrons their nuclea, independently on the material nonlinearity, the wave-electron system can be modeled as a driven harmonic oscillator. This approach provides the medium linear susceptibility and thus the complex refractive index, as a function of the wave frequency [114]. On the other hand, when the amplitudes of the two electric fields are comparable, the oscillator response includes a nonlinear component. The classical equation of motion of the oscillating electron is [115]:

$$\frac{d^2x}{dt^2} + 2\gamma \frac{dx}{dt} + \omega_0^2 x + \sum_{i=2}^{n} a_i x^i = \frac{F(t)}{m} = -\frac{e}{m} E(t) \tag{7}$$

The first three contributions describe a damped harmonic oscillator. More specifically, the first term (d^2x/dt^2) describes the electron acceleration, the second term ($2\gamma\, dx/dt$) the damping of its motion (e.g. due to non-radiative interactions) and the third one ($\omega_0^2 x$) the elastic restoring force of the nucleus on the electron.

The last term ($\sum_{i=2}^{n} a_i x^i$) is the sum over the nonlinear components of the restoring force arising from the anharmonic potential.

Depending on laser intensity and on the crystal geometry, various nonlinear phenomena have been observed and studied. Non-centrosymmetric crystals like potassium titanyl phosphate (KTP), lithium niobate ($LiNbO_3$) and gallium arsenide (GaAs) allow for both even and odd order nonlinear phenomena, while, for symmetry reasons, only odd order nonlinear phenomena can take place in centrosymmetric crystals, like silicon (Si), silicon nitride (Si_3N_4), amorphous glass (Hydex, etc.), etc.

Our work is based on second-order nonlinear processes in the AlGaAs platform. In these types of processes, when two waves at ω_s and ω_i interact with the nonlinear medium, the anharmonic terms yield to the generation of additional waves at the frequencies $\omega_s + \omega_i$ (Sum Frequency Generation, SFG), $\omega_s - \omega_i$ (Difference Frequency Generation, DFG), $2\omega_s$ and $2\omega_i$ (Second Harmonic Generation, SHG) and of a DC signal (optical rectification).

A non-classical frequency mixing process, called Spontaneous Parametric Down Conversion (SPDC), may also occur when only one of the two waves enters in the nonlinear medium. In this case, the input wave, called pump, interacts with vacuum fluctuations, which play the role of the second wave in DFG. Vacuum fluctuations permeate every quantum state, included the vacuum state, since they arise from the fundamental quantum-mechanical uncertainty of the electric field. During this interaction, a pump photon decays (is *down converted*) into two photons sharing their energy, called signal and idler. The interaction is known as *parametric* since it does not change the properties of the medium. Given the underlying conservation of total energy and momentum, SPDC generates pairs of entangled photons with correlation functions depending on the optical properties (such as birefringence and dispersion) of the nonlinear medium.

We will discuss more extensively SPDC in section (1.2), where we study the SPDC process occurring in our source. In the following section, we briefly recall Difference Frequency Generation (DFG). This nonlinear process can be seen as the classical counterpart of SPDC as it can be described in a purely classical picture [116, 117].

Difference Frequency Generation

From equation (7) we derive the electron motion and the induced dipole moment $\mathbf{p} = e\mathbf{x}$. The vector sum over the induced dipoles leads to the polarization vector $\mathbf{P} = \epsilon_0 \chi \mathbf{E}$, the macroscopic response of the medium to the incoming optical wave $\mathbf{E}$. Due to the anharmonicity, the polarization includes a nonlinear component in addition to the linear one: $\mathbf{P} = \mathbf{P_L} + \mathbf{P_{NL}}$.

The evolution of the optical wave $\mathbf{E}$ is described by a driven wave equation, derived from the Maxwell equations in the electric dipole approximation [118]:

$$\nabla^2 \mathbf{E} - \frac{1}{c^2}\frac{\partial^2 \mathbf{E}}{\partial t^2} - \frac{4\pi}{c^2}\frac{\partial^2 \mathbf{P_L}}{\partial t^2} = \frac{4\pi}{c^2}\frac{\partial^2 \mathbf{P_{NL}}}{\partial t^2} \tag{8}$$

with c the speed of light in vacuum and ϵ_0 the vacuum permittivity.

The nonlinear polarization $\mathbf{P_{NL}}(\mathbf{r}, t)$ acts as a driving source which induces an electromagnetic wave. The relative phase velocity between the driving wave and the induced wave, given by the medium dispersion (and birefringence if the two have different polarization), determines if the amplitude of the induced wave grows or not while it propagates.

If we suppose that two optical waves, named pump ($\mathbf{E_p}$) and signal ($\mathbf{E_s}$), enter in the nonlinear medium, the input field is given by:

$$\mathbf{E}(\mathbf{r}, t) = \mathbf{E_p}(\mathbf{r}, t) + \mathbf{E_s}(\mathbf{r}, t) \tag{9}$$

For simplicity, we consider pump and signal to be quasi-monochromatic beam propagating along the z-axis with a specific modal profile:

$$\begin{aligned} \mathbf{E_p}(\mathbf{r}, t) &= \mathrm{Re}[A_p(\mathbf{r}, t) \exp(ik_p z - \omega_p t)]\, \mathbf{e_p} \\ \mathbf{E_s}(\mathbf{r}, t) &= \mathrm{Re}[A_s(\mathbf{r}, t) \exp(ik_1 z - \omega_1 t)]\, \mathbf{e_s} \end{aligned} \tag{10}$$

with $k_{p,s}$ the wavevectors, $\mathbf{e}_{p,s}$ the directions of oscillation of the electric fields and $A_{p,s}$ their envelopes, including the modes transverse spatial profiles (supposed constant in time) and amplitudes along the propagation direction: $A_{p,s}(\mathbf{r}, t) = A_{p,s}(x, y)A_{p,s}(z, t)$.

Due to $\mathbf{P_{NL}}$, several nonlinear process may take place. For simplicity, we only consider second-order nonlinear phenomena. In order to keep a light notation, we suppose the second-order nonlinear optical susceptibility $\chi^{(2)}$ to be constant. The nonlinear polarization response reads:

$$\begin{aligned} \mathbf{P}_{NL} = \epsilon_0 \chi^{(2)} \mathbf{E}^2 = \frac{1}{2} \epsilon_0 \chi^{(2)} \mathrm{Re}\Big[& A_p^2(\mathbf{r}, t) e^{i2(k_p z - \omega_p t)} + \\ & A_s^2(\mathbf{r}, t) e^{i2(k_s z - \omega_s t)} + \\ & 2A_p(\mathbf{r}, t) A_s(\mathbf{r}, t) e^{i[(k_p + k_s)z - (\omega_p + \omega_s)t]} + \\ & 2A_p(\mathbf{r}, t) A_s^*(\mathbf{r}, t) e^{i[(k_p - k_s)z - (\omega_p - \omega_s)t]} + \\ & A_p(\mathbf{r}, t) A_p^*(\mathbf{r}, t) + A_s(\mathbf{r}, t) A_s^*(\mathbf{r}, t) \Big] \mathbf{e}_{NL} \end{aligned} \tag{11}$$

where $\mathbf{e}_{NL}$ is the nonlinear polarization oscillation direction. The various terms indicate SHG for the pump ($A_p^2(z, t)$), SHG for the signal ($A_s^2(z, t)$), SFG ($A_p(z, t)A_s(z, t)$), DFG ($A_p(z, t)A_s^*(z, t)$) and optical rectification ($A_p(z, t)A_p^*(z, t) + A_s(z, t)A_s^*(z, t)$).

In the following, we focus on DFG and neglect the other nonlinear phenomena, so that the nonlinear polarization expression simplifies into:

$$\mathbf{P}_{NL} = \epsilon_0 \chi^{(2)} \mathrm{Re}\Big[A_p(\mathbf{r}, t) A_s^*(\mathbf{r}, t) e^{i[(k_p - k_s)z - (\omega_p - \omega_s)t]} \Big]\, \mathbf{e}_{NL} \tag{12}$$

Figure (2) illustrates the three interacting waves in DFG. As the pump at ω_p and the signal at ω_s drive the charge displacement in the nonlinear medium, they generate a third wave, called idler, at $\omega_i = \omega_p - \omega_s$.

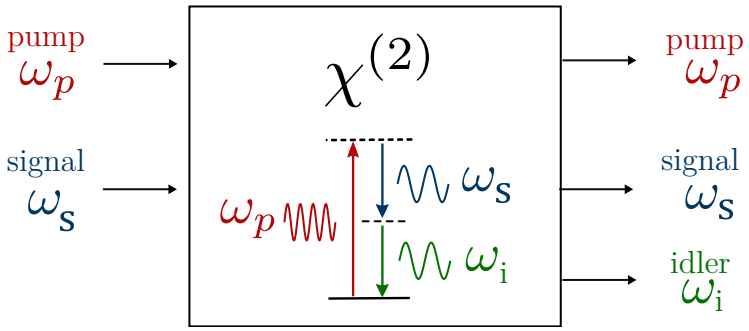

Figure 2 – Sketch of the process of Difference Frequency Generation (DFG).

Here we will consider a nonlinear process having a low efficiency, so we suppose the pump beam to be undepleted: $A_p(x, y, z, t) = A_p(x, y, 0, t)$. For the same reason, the envelopes of signal and idler increase slowly. Under the Slowly Varying Envelope Approximation (SVEA), $|\partial^2 A/\partial z^2| << |k\partial A/\partial z|$, the wave equations (8) for signal and idler fields simplify into two coupled equations for their envelopes. After integrating over the transverse plane (x, y), they read:

$$\begin{cases} dA_s/dz = \frac{i}{2}\kappa_s A_i^* \exp(i\Delta k z) \\ dA_i/dz = \frac{i}{2}\kappa_i A_s^* \exp(-i\Delta k z) \end{cases} \tag{13}$$

where $\Delta k = k(\omega_p) - k(\omega_s) - k(\omega_i)$ is the phase-mismatch between the three interacting waves, and the coefficients $\kappa_{s,i}$ are proportional to the strength of the nonlinear interaction:

$$\begin{aligned} \kappa_s &= \frac{8\pi^2}{n_s \lambda_s} \chi^{(2)} \rho A_p \\ \kappa_i &= \frac{8\pi^2}{n_i \lambda_i} \chi^{(2)} \rho A_p \end{aligned} \tag{14}$$

with ρ the spatial overlap between the spatial distributions of pump and signal/idler modes; $0 \leq \rho \leq 1$, with $\rho = 1$ for a perfect overlap and $\rho = 0$ if there is no overlap.

We observe in equation (13) that, for a fixed pump envelope A_p, at each position z and instant of time t, the growth of the signal envelope A_s depends on the value of the idler envelope A_i and viceversa.

Since $A_i(x, y, 0, t) = 0$, $A_s(x, y, 0, t) \neq 0$, stationary solutions of (13) can be found using the Manley-Rowe relations [119]:

$$\begin{aligned} A_s(z) &= A_s(0)[\cosh(\gamma z) + i\Delta k(2\gamma)^{-1} \sinh(\gamma z)] \\ A_i(z) &= iA_s(0) \sinh(\gamma z) \end{aligned} \tag{15}$$

with $\gamma^2 = (\kappa_s \kappa_i^*)^2 - \Delta k^2$.

Figure (3) illustrates the evolution of the idler envelope as a function of the propagation distance, normalized to the coherence length $L_{coh} = \pi/\Delta k$. Different scenarios occur depending on the phase mismatch Δk and the nonlinear coefficient $\chi^{(2)}$. The cases of no phase matching (NPM, blue), modal phase matching for

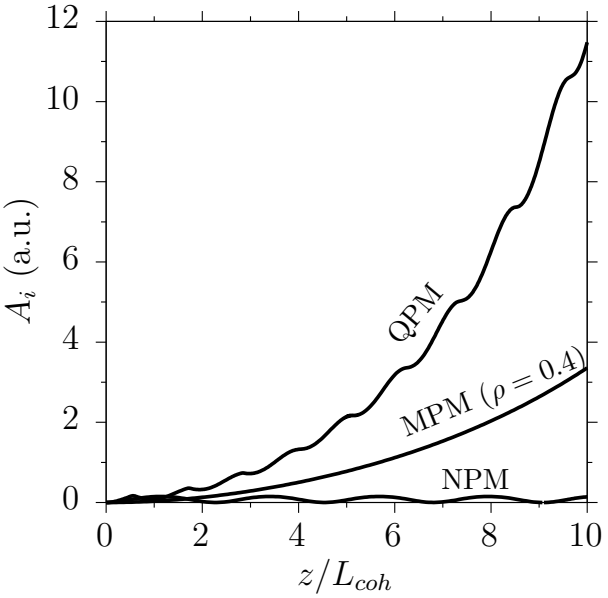

Figure 3 – Evolution of the idler envelope in DFG process in the case of no phase matching (NPM), modal phase matching with a mode overlap of $\rho = 0.4$ (MPM) and quasi phase matching with a perfect mode overlap (QPM). The idler envelope has a sinusoidal modulation in NPM, grows exponentially for MPM and exponentially with a sinusoidal modulation in QPM.

$\rho = 0.4$ (MPM, red line) and quasi-phase matching for $\rho = 1$ (QPM, green line) are presented.

In NPM there is a phase mismatch ($\Delta k \neq 0$) and the nonlinear coefficient is constant ($\chi^{(2)}(z) = \text{cost}$). Along the propagation direction, an exchange of energy between pump and signal/idler alternates. Photons are continuously generated and annihilated, as described by the oscillation of the complex exponential term in equation (15). As a result, $A_s(z)$ oscillates with a periodicity of $2L_{coh}$.

QPM takes places if the nonlinear material is engineered to have a nonlinear coefficient $\chi^{(2)}(z)$ reversed or inhibited every odd multiples of $\Delta z = L_{coh}$. The medium becomes invariant with respect to periodical (instead of continuous) translation along the propagation direction and the momentum conservation transforms into a quasi-phase matching condition. Since the product $\chi^{(2)} \exp(i\Delta k z)$ in equation (13) is positive for every z, $A_s(z)$ does not decrease during its propagation. There is an effective positive flow of energy from pump to signal and idler waves. The modulation of $\chi^{(2)}$ is realized by periodical poling in various crystals [62], or via orientation-patterning in semiconductors like GaAs [120].

In MPM signal and idler envelopes growth exponentially with z because there is a perfect phase matching. In bulk optics sources, like nonlinear crystals (BBO, KTP, $LiNbO_3$), the intrinsic birefringence is used to satisfy phase matching. This often results in non collinear signal and idler beams.

One of the main advantage of integrated photonics is to have signal and idler propagating in the same spatial mode. When non birefringent materials are used, a phase matching scheme exploiting modal dispersion, called modal phase matching,

is a versatile solution to achieve efficient nonlinear conversion.

The device studied in this thesis is an AlGaAs Bragg reflector waveguide, where the pump mode is a so-called Bragg mode, based on a photonic bandgap confinement created with Bragg reflectors, while signal and idler are two fundamental Gaussian modes. The modal dispersion of the pump Bragg mode compensates the GaAs normal dispersion, allowing for a perfect phase matching over a large frequency bandwidth [121, 122]. The only limiting factor of this choice is the overlap integral between the interacting modes, which is typically of the order of 0.4 [123]. The details of our source are presented in the next chapter, in paragraph (1.1).

Optical properties of GaAs and AlGaAs

GaAs is a III-V semiconductor compound formed by Gallium (Ga) and Arsenide (As) atoms. GaAs clean room processing is a well established technique. This material, thanks to its physical properties, enables:

I second-order nonlinear processes (SFG, DFG, SPDC, etc.)

II Electro-optics modulation.

III Laser emission (direct bandgap of $E_g = 1.42$eV, $\lambda_g = 870$nm).

In this section we briefly review GaAs structure and properties, in the perspective of its utilization in integrated quantum optic devices.

The GaAs crystals has a non-centrosymmetric zincblende (cubic) lattice belonging to the $\bar{4}$3m symmetry group. Figure (4) presents a sketch of its unit cell.

GaAs crystal is usually grown on its [001] plane, along (001) direction (grey surface and vector in figure (4)). Once the target growth thickness is achieved, the crystal is cleaved in a sample of desired dimension. For our devices, GaAs samples on 2 inches wafer are grown via MBE at C2N by A. Lemaitre. The cleaving is conventionally performed on the [110] plane (blue surface in figure (4)) for two main reasons. The first one is that [110] is the weakest surface according to GaAs electron density distribution and surface polarity [124]. [110] surfaces present the same electron density distribution, so there is no electrostatic attraction between them. This is not the case for [111] planes, which alternate to two kinds of surfaces polarities, $(111)A$ and $(111)B$, attracting each other [125]. The second reason is that the cleaving along (110) is compatible with the use of GaAs electro-optics properties to control waveguide birefringence. When the waveguide longitudinal direction is oriented along $(1\bar{1}0)$ (blue vector in figure (4)), the electric fields of the two orthogonally polarized modes oscillate along (001) and $(\bar{1}\bar{1}0)$. By applying a DC electric field in the vertical direction (001), it is possible to induce a difference among the refractive index of the two modes and thus birefringence. This effect is not achievable when the waveguide is oriented along

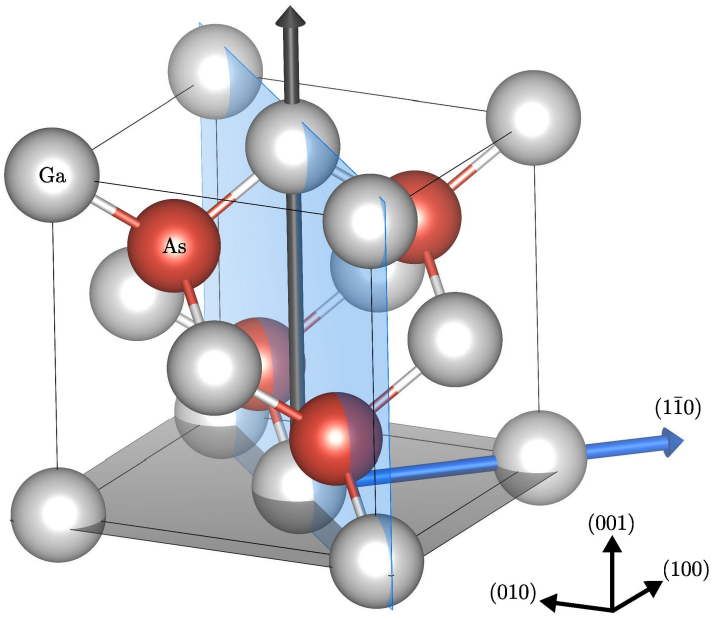

Figure 4 – GaAs crystal structure. The dark arrow along the (001) direction indicates the MBE growth direction. The blue arrow along the (1$\bar{1}$0) direction represents the orientation of our waveguide propagation axis with respect to the crystal lattice.

(100) and the two guided modes are polarized along (001) and (010) directions [126].

As anticipated, since the lattice symmetry lacks of an inversion center, GaAs is suitable for linear electro-optic effect, piezoelectricity and presents a second-order nonlinear response. Belonging to the cubic $\bar{4}$3m class, the form of its second-order nonlinear optical tensor can be reduced to [126]:

$$M = \begin{bmatrix} 0 & 0 & 0 & d_{14}(\omega_p, \omega_s, \omega_i) & 0 & 0 \\ 0 & 0 & 0 & 0 & d_{14}(\omega_p, \omega_s, \omega_i) & 0 \\ 0 & 0 & 0 & 0 & 0 & d_{14}(\omega_p, \omega_s, \omega_i) \end{bmatrix}$$

In general, d_{14} depends on the frequencies of the three interactings photons in nonlinear experiments. However, at frequencies far from the material energy gap, the nonlinear coefficient varies slowly with the frequency. In the numerical calculation presented in this manuscript, we use the value of d_{14} measured in a SHG experiment performed in reference [127] for the fundamental beam at $\lambda_s = \lambda_i = 1533$nm, which is very close to the central degeneracy frequency of the photon pairs emitted by our source. It has been found $d_{14} = 119$pm/V.

Figure (5) reports the GaAs band diagram [128] (panel a) and the real part of GaAs refractive index as a function of the wavelength (panel b) that we calculate at 20°C using Afromowitz model [129]. We see that the electronic band structure associated to GaAs lattice is characterized by a direct band-gap at room temperature of $E_g = 1.424$eV (870nm). For this reason, GaAs is widely used as an

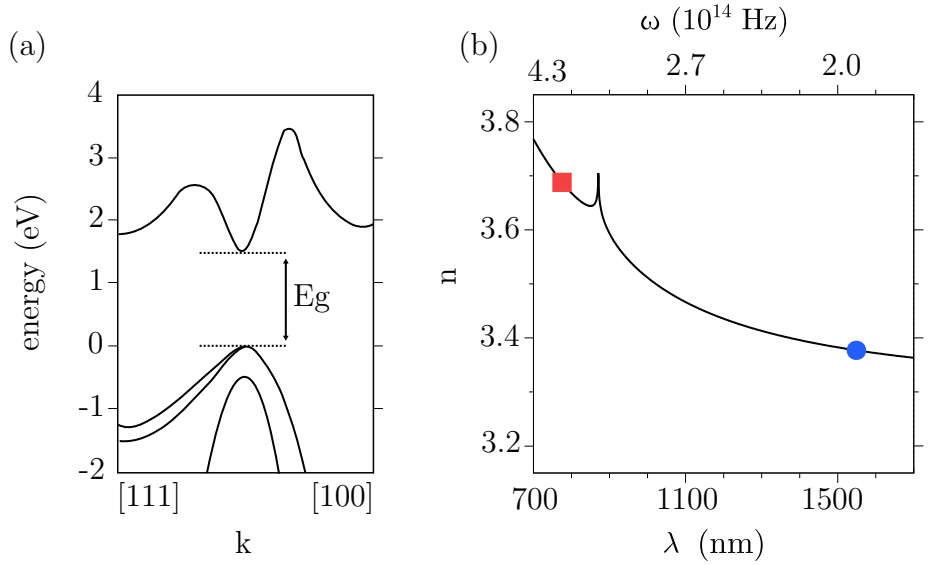

Figure 5 –
(a) GaAs energy band diagram (data from [128])
(b) GaAs chromatic dispersion (calculated using Afromowitz model [129]).

active medium in solid-state infrared laser diodes.

GaAs chromatic dispersion, calculated via Afromowitz model [129], is normal in the visible to Mid-Infrared region, with an exception for the frequency range surrounding its energy gap. In order to take advantage of the already developed network of optical fibers and off-the-shelf telecom components, we are interested in a source that emits biphoton states at the telecom wavelength (e.g. within S,C and L-bands). As instance, we consider a source emitting photon pairs at 1550nm by using pump photons at 775nm via SPDC. This source cannot be based on bulk GaAs for two reasons. First, since this wavelength corresponds to GaAs energy gap, pump photons would be absorbed. Second, due to normal dispersion, the refractive index of the pump photon (red square, $n = 3.69$) would be much higher than the refractive index of the degenerate signal and idler photons (blue dot, $n = 3.38$), preventing the fulfillment of the the phase matching condition. The normal dispersion cannot be compensated by birefringence, since GaAs is not birefringent. On the other hand, it can be compensated by a modal dispersion, made possible by developing a specific integrated design based on AlGaAs, as we present in the next chapter.

The lattice similarity between GaAs and AlAs allows to realize heterostructures to implement a large variety of opto-electronics devices. During the growth of AlGaAs, part of Ga species are replaced by Aluminum (Al) atoms. The resulting alloy is $Al_xGa_{1-x}As$, where x within 0 and 1 determines the alloy between AlAs and GaAs.

$Al_xGa_{1-x}As$ inherits from GaAs a zincblende crystal structure, with nearly the same lattice constant. As a consequence, GaAs and $Al_xGa_{1-x}As$ optical properties are similar, with the advantage that the refractive index as well as the gap of the latter can be slightly engineered by tuning the relative concentration of Al over

Ga species.

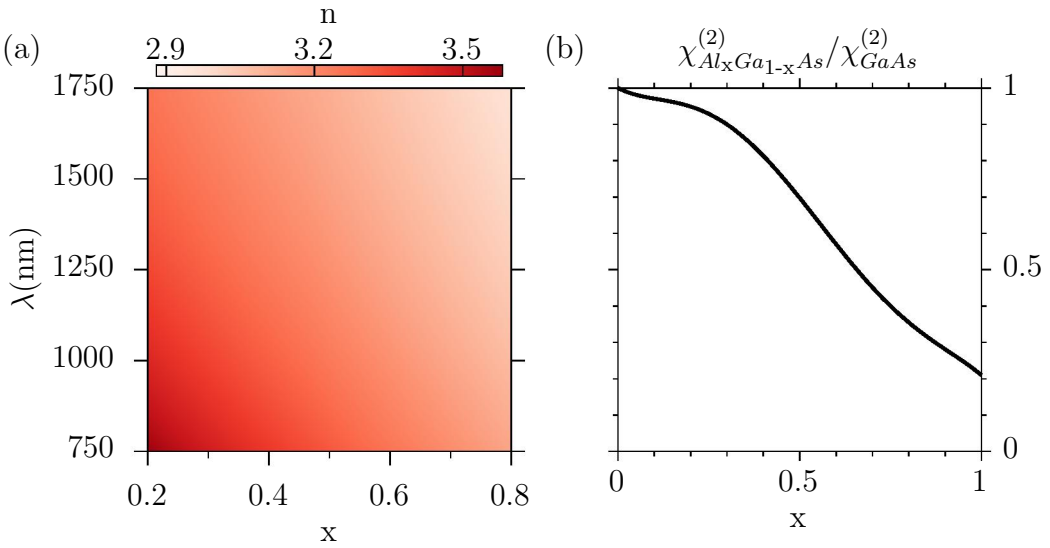

Figure 6 – $Al_xGa_{1-x}As$ optical properties versus Al concentration.
(a) Refractive index.
(b) second-order nonlinearity.

Figure (6, a) shows the refractive index of AlGaAs as a function of Al composition and frequency, based on Gehrsitz model [130].

We notice that, for a given frequency, an increase in the percentage of Al atoms corresponds to a decrease of the refractive index. The reason is that AlAs has a wider energy gap than GaAs [131].

As a result, during an $Al_xGa_{1-x}As$ growth, it is possible to tune the refractive index layer by layer by varying the relative percentage of Al with respect to Ga. In the telecom range ($\lambda = 1550$nm), the material refractive index varies in the range $n = [2.9, 3.3]$, corresponding to a percentage of Al of $Al = [0.8, 0]$. In our device, we do not use higher value of Al because the material would undergo a fast oxidation process, leading to a degradation of its optical properties.

According to Miller's rule, the second-order susceptibility response is proportional to the first order susceptibility [132]. Indeed, AlAs has a lower nonlinear coefficient than GaAs, as confirmed by Ohashi experimental model [133]. In figure (6, b) we report the second-order nonlinear coefficient (χ^2) of $Al_xGa_{1-x}As$ calculated via Ohashi model.

The variation of the nonlinear coefficient with the Al percentage can be used to optimize a nonlinear process in some particular geometries: as instance, this has been exploited by implementing a quasi-phase matching geometry in an AlGaAs source proposed by our team based on a transverse pump configuration and a counterpropagative phase matching scheme [134, 135].

Part I

Bragg reflector waveguides: from design to experimental characterization

Chapter 1

Working principle and emitted biphoton state

In this chapter we present the working principle of our source, a Bragg reflector waveguide based on the AlGaAs platform allowing for a type-II SPDC process. The three interacting modes are a horizontally polarized Bragg mode (pump) and the two orthogonally polarized fundamental Gaussian modes (signal and idler).

By evaluating the nonlinear overlap integral of the three interacting modes with the nonlinear medium, we estimate a conversion efficiency of around 10^{-8} photon pairs per pump photon.

The quantum state describing each photon pair, named biphoton state, is derived by following a quantum theory of SPDC. The properties of the biphoton state depend on the frequency correlations between signal and idler photons, described by their Joint Spectral Amplitude (JSA).

1.1 Working principle of Bragg reflector waveguides

The first works using modal phase matching in AlGaAs waveguide with the goal to achieve electrically injected photon pair sources have been done using total internal reflection modes [136, 137]. That approach presented the disadvantage of requiring layers of high Al content, leading to a rapid oxidation of the devices.

In 2006, following an idea of Yeh [43, 138], Bragg reflectors started to be investigated [44, 139]. In these last years, this approach has led to many important results for the development of quantum sources working at room temperature and telecom wavelength. In particularly, our group has demonstrated an electrical driven source of photon pairs [58], as well as indistinguishably and energy-time entanglement in passive devices [140].

As illustrated in figure (1.1, a), a Bragg reflector waveguide is a ridge waveguide along the propagation direction (z axis) and a unidimensional photonic crystal made by two distributed Bragg reflectors along the vertical direction (y axis). This structure allows to confine and guide, apart from fundamental Gaussian modes, photons whose electric field has a specific distribution in the transverse (xy) plane, known as Bragg mode. The confinement of the Bragg mode is done through the

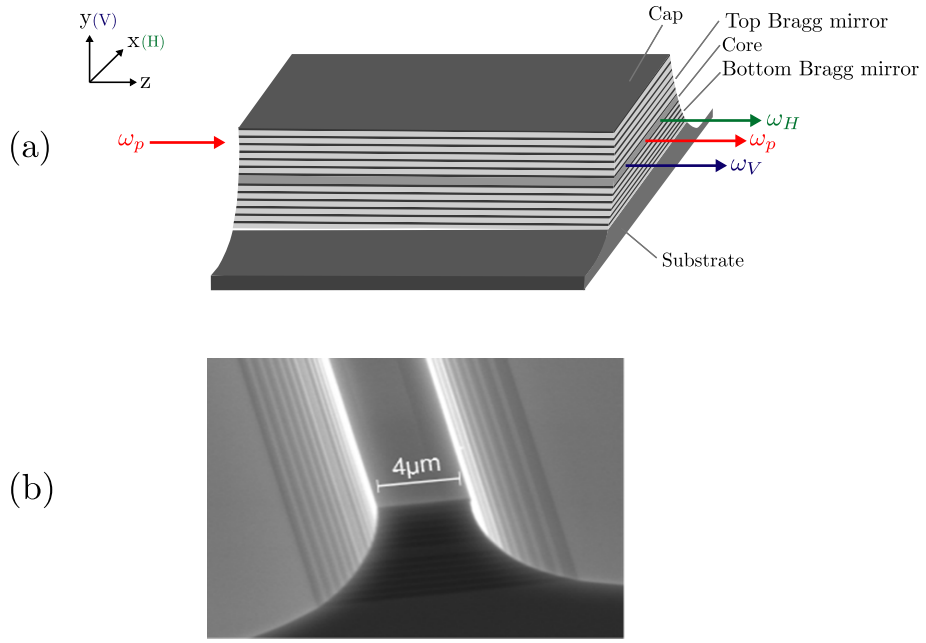

Figure 1.1 – GaAs device studied in this manuscript.
(a) Sketch of the waveguide indicating the core and cladding regions.
(b) SEM image of the waveguide input facet and flanks.

top and bottom Bragg mirrors. As shown in figure (1.1, a), each mirror consists of six stacks of alternating high and low refractive index bilayers, corresponding respectively to a low and high Al concentration. When the composition and thickness of these layers are properly chosen ($t_H = \lambda/(4n_H)$, $t_L = \lambda/(4n_L)$, with λ the pump mode wavelength and n_H and n_V the high and low refractive index of Bragg mirror layers), a constructive interference takes places so that a Bragg mode is supported by the waveguide [141, 142].

Table (1.1) reports the nominal epitaxial structure of our source. The dimensions and composition of the waveguide layers along the y axis, and thus the corresponding value of refractive index at the pump, signal and idler degeneracy wavelengths, are determined in the design phase. This design was conceived by A. Orieux, a previous PhD student in our group. The vertical profile is designed to support a (TE) H-polarized Bragg mode at 770.5nm. The two Bragg mirrors surround a core layer, which confines and guide by total internal reflection two fundamental Gaussian H and V-polarized modes at telecom wavelength, centered at 1541.5nm. For more details regarding the choice of Al contents and thicknesses, we refer to the second chapter of her thesis manuscript [143].

In figure (1.1, b) we present a SEM image of a fabricated ridge waveguide. Top and bottom ridges widths are approximately 4µm and 10µm. The sidewalls present an exponential profile due to the isotropy of the wet etching technique used to fabricate the device.

Given the refractive index mismatch between semiconductors and surrounding air, AlGaAs waveguides act as Fabry-Perot cavities. In the first part of this thesis

Layer	Cycles	Δy (nm)	x (%)	$n_{770.5nm}$	n_{1541nm}
Cap	1	250	0	3.692	3.378
Top Bragg	6	276	80	3.122	2.978
		114	25	3.487	3.239
Core	1	298	45	3.336	3.142
Bottom Bragg	6	114	25	3.487	3.239
		276	80	3.122	2.978
Substrate	1	-	0	3.692	3.378

Table 1.1 – Nominal epitaxial structure of our source.
Δy: layer thickness
x: layer Al composition, as percentage of Al in $Al_xGa_{1-x}As$
n_λ: layer refractive index at the wavelength λ.

(chapters (1-3)) we neglect the cavity effect, which will be studied in chapter (5).

1.1.1 Modal dispersion

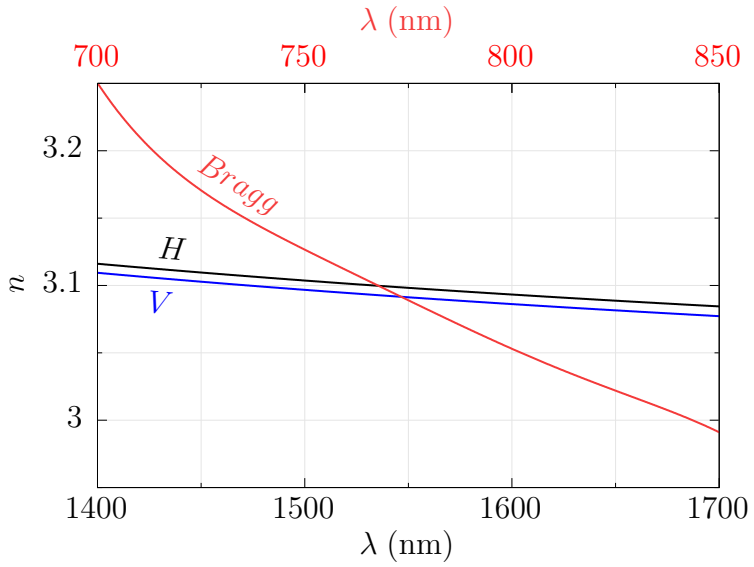

Figure 1.2 – Numerically calculated dispersion of the modal effective index of pump (H-polarized Bragg mode, in red), signal (H-polarized fundamental Gaussian mode, in black) and idler (V-polarized fundamental Gaussian mode, in blue).

Figure (1.2) presents the numerical calculation of the pump, signal and idler modal effective index for photon pairs emitted in the telecom range $\lambda = (1400 - 1600)\,\text{nm}$. In this calculation, to save computational energy and time, we simulate the source in one dimension via a commercial eigenmode solver (Lumerical MODE) by considering only its profile along y at the center of the waveguide, i.e. its vertical cut along $x = 0\,\mu\text{m}$. This choice is justified by the fact that the waveguide is large enough to neglect the effect of the confinement along x on the modal effective index. In this case, the modes are far from a cut-off condition

induced by the waveguide width and we have verified that the modal effective index of the 3D structure converge to the ones calculated in the 2D simulation. To minimize the number of simulations to perform, we calculate the modal effective index sampling the wavelength with steps of $\lambda = 10\,\text{nm}$. From these sampling points, we obtain $n(\lambda)$ by fitting the data with a high order polynomial function. The fitting operation does not lead to inaccurate results as $n(\lambda)$ does not present discontinuities due to the absence of material resonances in this spectral range.

We notice in figure (1.2) that the Bragg mode has an effective index lower than the H-polarized Gaussian mode and higher than the V-polarized Gaussian modes in the wavelength range $\lambda_p \in [767.5, 773.5]\text{nm}$. At degeneracy, the pump wavelength that satisfies the phase matching condition for the nominal structure of table (1.1) is 770.5nm, corresponding to a wavelength of 1541nm for signal and idler photons.

1.1.2 Guided modes involved in the spontaneous parametric down conversion process and conversion efficiency

In this paragraph we first present the 2D spatial distribution of pump, signal and idler modes calculated numerically via Lumerical MODE. From the modes spatial distribution we calculate the SPDC nonlinear overlap integral and we give an estimation of the SPDC efficiency.

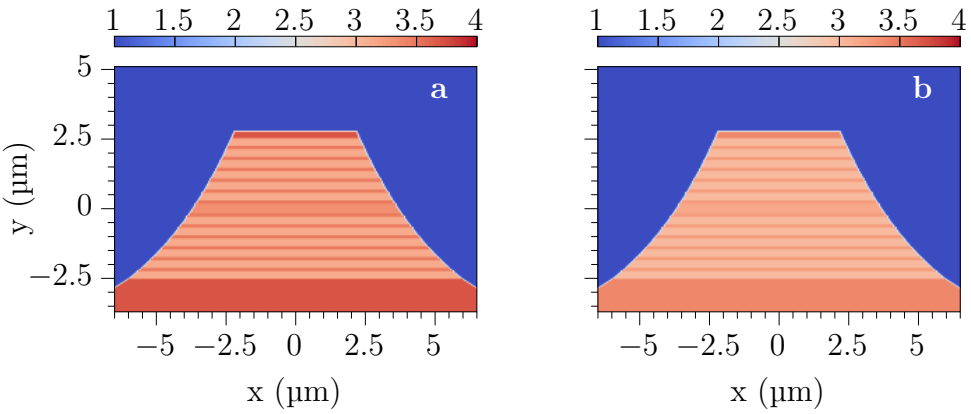

Figure 1.3 – Numerical simulation of the refractive index of the waveguide layers calculated at:
(a) $\lambda = 770.5\text{nm}$ (pump wavelength).
(b) $\lambda = 1541\text{nm}$ (signal and idler degeneracy wavelength).

Figure (1.3) presents the refractive index profile at 770.5nm (a) and 1541nm (b) used in simulations. They have been calculated using the Gehrsitz model [130]. We notice that, as expected by GaAs normal dispersion, the refractive index of each layer decreases with the wavelength.

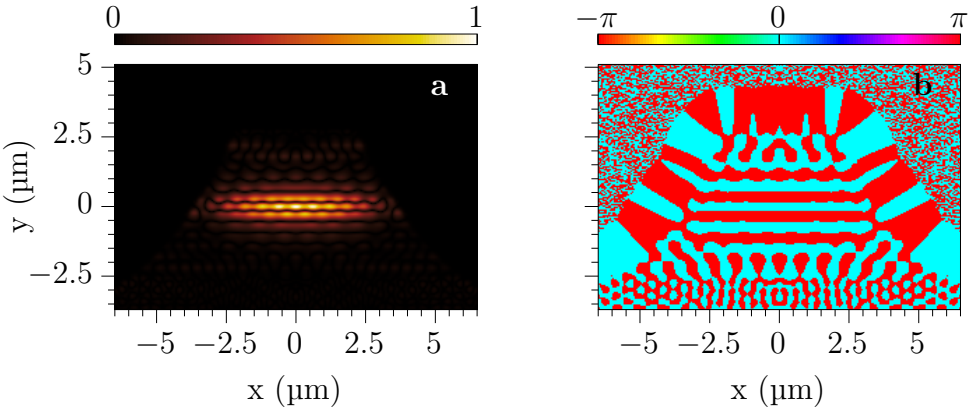

Figure 1.4 – Numerical simulation of the intensity (a) and phase (b) profile of the H-polarized Bragg mode at $\lambda = 770.5$nm.

The intensity (a) and phase (b) profile of the pump mode at $\lambda = 770.5$nm are shown in figure (1.4). Along the y direction, we can distinguish alternating out-of-phase lobes, typical of a Bragg mode profile [144]. Along the x direction, there are additional oscillations which arise from the waveguide exponential sidewalls. The Bragg mode has a horizontal (H) polarization and its calculated effective refractive index at 770.5nm is $n_p = 3.0895$.

Figures (1.5) and (1.6) illustrate the spatial distribution of the H-polarized (TE) and V-polarized (TM) fundamental Gaussian mode, calculated at 1541nm.

The H-polarized mode has an electric field that is continuous at the interfaces between high and low refractive index layers, contrary to the electrical field of V-polarized mode that is not continuous across each step index. Their modal refractive index are $n_H = 3.098$, $n_V = 3.081$.

We define the normalized nonlinear overlap integral $\bar{\Gamma}$ as the product of the normalized spatial distributions of pump (A_p), signal (A_H) and idler (A_V) modes, weighted by material second order nonlinear coefficient ($\chi^{(2)}$):

$$\bar{\Gamma} = \iint \mathrm{d}x\,\mathrm{d}y \chi^{(2)}(x,y)\, A_p(x,y) A_H(x,y) A_V(x,y) \tag{1.1}$$

with

$$1 = \iint \mathrm{d}x\,\mathrm{d}y |A_i(x,y)|^2 \tag{1.2}$$

for $i = \{p, H, V\}$.

By using the calculated pump (1.4), signal (1.5) and idler (1.6) modes, and the value of the nonlinear coefficient of each layer of the waveguide, calculated according to [133] at room temperature ($T = 20°$C), we find that $\bar{\Gamma} = 1.7 \cdot 10^{-6}\, V^{-1}$.

An estimation of the SPDC efficiency can thus be retrieved from a semi-classical approach [145, 143]. The average number of signal-idler pairs generated per each

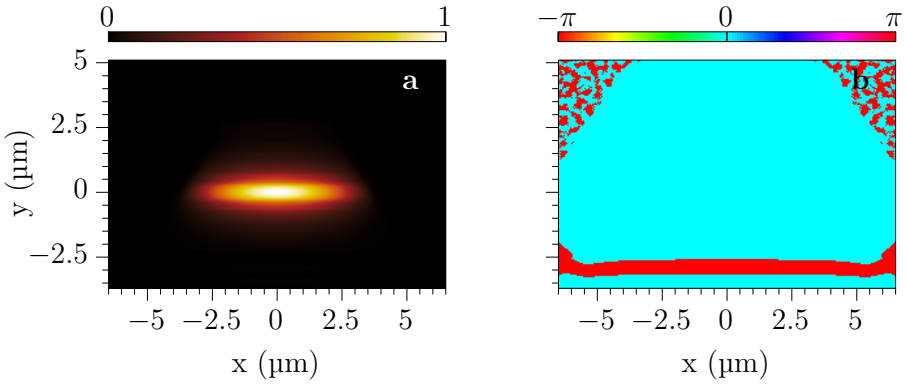

Figure 1.5 – Numerical simulation of the intensity (a) and phase (b) profile of the H-polarized fundamental Gaussian mode at $\lambda = 1541$nm.

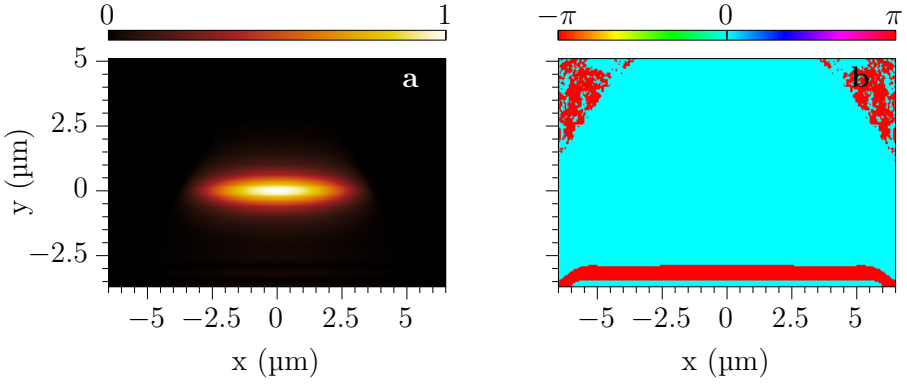

Figure 1.6 – Numerical simulation of the intensity (a) and phase (b) profile of the V-polarized fundamental Gaussian mode at $\lambda = 1541$nm.

pump photon is given by:

$$\eta = \frac{N_{pair}}{N_p} = \frac{2\hbar\,\omega_p\,\omega_H\,\omega_V}{\epsilon_0\,c^3\,n_p\,n_H\,n_V}\frac{\Delta\omega^{FWHM}}{2\pi}|\bar{\Gamma}|^2 L^2 \tag{1.3}$$

where ω_p, ω_H, ω_V are the frequency of pump, signal and idler photons, n_p, n_H, n_V their effective refractive index, $\Delta\omega^{FWHM}$ the average linewidth of signal and idler spectra and L the length of the nonlinear medium.

In the case of our device, $L = 2$mm; if we choose frequency degenerate SPDC, then $n_p = 3.0895$, $n_H = 3.098$ and $n_V = 3.081$.

The linewidth of signal and idler spectra is found numerically to be $\Delta\omega^{FWHM} =$ 69THz.

By plugging all these parameters in equation (1.3), we find that:

$$\eta = 1.37 \cdot 10^{-8} \text{ photon pairs/pump photon} \tag{1.4}$$

i.e. we need in average $1/\eta = 7.3 \cdot 10^7$ pump photons to generate one signal-idler pair.

1.2 Quantum theory of collinear spontaneous parametric down conversion

The goal of this section is to present a quantum theory of light describing the generation of photon pairs as well as the correlation properties between the photons of the pair.

Different approaches can be employed for a quantum theory of SPDC.

A versatile approach tailored for photonic integrated devices, such as ridge waveguides or microresonators, has been recently proposed by Yang, Liscidini and Sipe [146]. Their work is based on the quantum scattering theory of light and it keeps into account the modes spatial distribution and dispersion of the waveguide. By recurring to a Schrödinger description of the quantum state (i.e. the state wavefunction evolves in time, while the operators are time-independent [147]), a full quantum state of the emitted pairs is retrieved, including the possibility of generation of multiple photon pairs per pump photon. The advantage of this versatile description is that it can be applied also to SHG, the classical reversed process of SPDC, or DFG, the classical counterpart of SPDC. Their performances are directly comparable, as instance the number of generated pairs as a function of the pump power or of the length of the nonlinear medium [116].

In our work, we are mostly interested in continous-wave and low power pumping regime, in which the probability of generating multiple pairs per pump photon is negligible. Therefore we resort to a simpler approach, limited to a low pump power regime, based on the perturbation theory. We rely on the Heisenberg picture (i.e. the state wavefunction is constant in time, while the operators acting on it

evolve [148]), similarly to the first theorical studies on the quantum properties of the biphoton states carried out by Mandel, Ou and coworkers [149, 150]. More particularly, we follow the analysis proposed by Guillaume Boucher, a previous PhD student of our group, in his manuscript [151]. His study describes a counter-propagating SPDC scheme in an AlGaAs ridge waveguide and comprehends the spatial distribution and dispersion of the supported modes. In the following, we adapt this approach for the case of a collinear SPDC scheme in an AlGaAs ridge waveguide.
We start with the identification of the modes involved in the SPDC process, expressed in their quantized forms. We proceed by defining the perturbation term of the linear Hamiltonian, given by the SPDC nonlinear interaction Hamiltonian. Finally, we determine the biphoton state emitted by the source by solving the Schrödinger equation including the nonlinear perturbation term.

1.2.1 Interacting modes

SPDC is a nonlinear process with a very low efficiency. In our source, for waveguides having a typical length of $L \approx 2$mm, approximately one pair of photons is generated every 10^8 pump photons. Therefore we assume that the pump beam is undepleted during the process and treat it classically.

Since we are in a guided regime, we assume that the pump beam propagates along the waveguide propagation direction z in the positive direction, so that its wavevector is $\mathbf{k_p} = k_p(\omega)\hat{\mathbf{u}}_\mathbf{z}$, with $k > 0$.

We also suppose that the pump mode is horizontally (TE) polarized, along $\hat{\mathbf{u}}_\mathbf{x}$ with respect to the axis reference in figure (1.1), and has a Bragg spatial distribution, whose amplitude and phase profiles are shown in figure (1.4).

The expression of the pump mode is:

$$\mathbf{E}_p(\mathbf{r}, t) = \frac{1}{\sqrt{2\pi}} \int_0^{+\infty} \mathrm{d}k \, \hat{\mathbf{u}}_\mathbf{x} \, E_p(\mathbf{r}, k) e^{i(k_p z - \omega_k t)} + \text{c.c.} \tag{1.5}$$

where c.c. indicates the complex conjugate.

As we are interested in the frequency correlations between the two photons of the pair, we reformulate the field in its spectral components. In a guided regime, the mode propagation constant or wavevector k and frequency ω are related via the modal effective index (4). The integral becomes:

$$\mathbf{E}_p(\mathbf{r}, t) = \frac{1}{\sqrt{2\pi}} \int_0^{+\infty} \mathrm{d}\omega \, \hat{\mathbf{u}}_\mathbf{x} \, E_p(\mathbf{r}, \omega) e^{i(k_p(\omega) z - \omega_k t)} + \text{c.c.} \tag{1.6}$$

We neglect the probability of generating multiple pairs per pump photon due to the low SPDC efficiency. Therefore, only single signal-idler pairs will be generated. We consider that they are orthogonally polarized fundamental Gaussian modes, as we will show a posteriori once the phase matching condition is derived.

Following the quantization procedure (for more details see (4.3.5) in [152]), we express the signal and idler modes as a function of creation ($\hat{a}^\dagger$) and annihilation

($\hat{a}$) operators:

$$\hat{\mathbf{E}}(\mathbf{r},t) = \sqrt{\frac{L}{2\pi}} \sum_{\sigma} \int_0^{+\infty} \mathrm{d}k \, \hat{\mathbf{u}}_\sigma \, E_\sigma(\mathbf{r},k) e^{i(k_\sigma z - \omega_k t)} \hat{a}(k) + \mathrm{h.c.} \tag{1.7}$$

where L is the nonlinear medium length, $\sigma = \{H, V\}$ indicates the modes polarization and h.c. the Hermitian conjugate. The term $\sqrt{L}$ arises from the modes normalization given the continuity condition of k along the propagation direction (for the moment we neglect the cavity effect induced by the waveguide's facets reflectivity). $\hat{a}^\dagger$ and $\hat{a}$ satisfy the usual commutations relations under a proper normalization of the modes [146]. Again, we express the field in its frequency components:

$$\hat{\mathbf{E}}(\mathbf{r},t) = \sqrt{\frac{L}{2\pi}} \sum_{\sigma} \int_0^{+\infty} \mathrm{d}\omega \, \hat{\mathbf{u}}_\sigma \, \frac{1}{\sqrt{v_g^\sigma(\omega)}} E_\sigma(\mathbf{r},\omega) e^{i(k_\sigma(\omega) z - \omega_k t)} \hat{a}(\omega) + \mathrm{h.c.} \tag{1.8}$$

where the term depending on the group velocity, v_g^σ is added to ensure a canonical form for the creation and annihilation operators in the frequency basis (see paragraph (V) of reference [146] for more details).

1.2.2 Nonlinear interaction

The nonlinear interaction between the three interacting fields in the medium is expressed by the following Hamiltonian:

$$\hat{\mathrm{H}}_{\mathrm{NL}}(t) = \epsilon_0 \int \mathrm{d}\mathbf{r} \chi^{(2)}(\mathbf{r}) \hat{\mathbf{E}}_p(\mathbf{r},t) \hat{\mathbf{E}}_H(\mathbf{r},t) \hat{\mathbf{E}}_V(\mathbf{r},t) \tag{1.9}$$

where $\chi^{(2)}(\mathbf{r})$ is the second-order nonlinear optical susceptibility of the medium. In our waveguide based on AlGaAs, $\chi^{(2)}(\mathbf{r})$ varies with the relative concentration of Al and Ga species, as illustrated in figure (6).

The electric fields of pump, signal and idler waves are expressed as a combination of a frequency positive term E^+ and a conjugate frequency negative term E^- (the former included in the c.c. or h.c. terms). E^+ contains the creation operator, while E^- the annihilation operator. Thus the product $\hat{\mathbf{E}}_p \hat{\mathbf{E}}_H \hat{\mathbf{E}}_V$ leads to eight possible combinations for such operators. Hereafter we consider only the combination $\hat{\mathbf{E}}_p^+ \hat{\mathbf{E}}_H^- \hat{\mathbf{E}}_V^-$, in which one pump photon is annihilated and the two orthogonally polarized signal and idler photons are created. This choice is justified a posteriori by the conservation of momentum. The nonlinear Hamiltonian simplifies into:

$$\hat{\mathrm{H}}_{\mathrm{NL}}(t) = \epsilon_0 \int \mathrm{d}\mathbf{r} \chi^{(2)}(\mathbf{r}) \hat{\mathbf{E}}_p^+(\mathbf{r},t) \hat{\mathbf{E}}_H^-(\mathbf{r},t) \hat{\mathbf{E}}_V^-(\mathbf{r},t) \tag{1.10}$$

1.2.3 Biphoton state: the Joint Spectral Amplitude (JSA)

The Schrödinger equation of the generated biphoton state depends on the nonlinear Hamiltonian $\hat{H}_{NL}(t)$ according to:

$$i\hbar\frac{\mathrm{d}}{\mathrm{d}t}\left|\Phi(t)\right\rangle = \hat{\mathrm{H}}_{\mathrm{NL}}(t)\left|\Phi(t)\right\rangle \tag{1.11}$$

In low pump regime the output state reads:

$$\left|\Phi(t)\right\rangle = \left|0\right\rangle + \frac{1}{i\hbar}\int_{-\infty}^{t}\mathrm{d}t\hat{\mathrm{H}}_{\mathrm{NL}}(t)\left|0\right\rangle \tag{1.12}$$

where the initial state is the vacuum state, $\left|\Phi(t\to-\infty)\right\rangle = \left|0\right\rangle$. The output state is the superposition of the vacuum state and the biphoton state, so we rewrite it as:

$$\left|\Phi(t)\right\rangle = \left|0\right\rangle + \beta\left|\Psi\right\rangle \tag{1.13}$$

with β the probability amplitude of generating the biphoton state $\left|\Psi\right\rangle$. Since at the output of our source there are no other nonlinear processes, we can extend the integration time to infinity. According to the Hamiltonian (1.10), the state reads:

$$\left|\Psi\right\rangle = \frac{\epsilon_0}{i\beta\hbar}\int\mathrm{d}t\int\mathrm{d}\mathbf{r}\chi^{(2)}(\mathbf{r})\hat{\mathbf{E}}_p^+(\mathbf{r},t)\hat{\mathbf{E}}_H^-(\mathbf{r},t)\hat{\mathbf{E}}_V^-(\mathbf{r},t)\left|0\right\rangle \tag{1.14}$$

We plug in the expression of the fields (1.6,1.8), to find:

$$\left|\Psi\right\rangle = \frac{1}{\beta}\frac{\epsilon_0 L}{i\hbar(2\pi)^{3/2}}\iiint\mathrm{d}\omega_p\,\mathrm{d}\omega_1\,\mathrm{d}\omega_2\int\mathrm{d}\mathbf{r}\chi^{(2)}(\mathbf{r})E_p(\mathbf{r},\omega_p)E_H(\mathbf{r},\omega_1)E_V(\mathbf{r},\omega_2)$$
$$\frac{1}{\sqrt{v_g^H(\omega_1)v_g^V(\omega_2)}}e^{i\Delta kz}\Big(\int\mathrm{d}te^{-i\Delta\omega t}\Big)\hat{a}_H^\dagger(\omega_1)\hat{a}_V^\dagger(\omega_2)\left|0\right\rangle \tag{1.15}$$

where $\Delta\omega = \omega_p - \omega_1 - \omega_2$ is the difference in frequency between the three interacting photons, $\Delta k = k_p(\omega_p) - k_H(\omega_1) - k_V(\omega_2)$ their difference in linear momentum, known as phase mismatch. The subscripts p (pump), 1 (signal) and 2 (idler) have been added to indicate the frequency of the three interacting photons. The integral over time leads to the conservation of energy condition:

$$\int\mathrm{d}te^{-i\Delta\omega t} = 2\pi\delta(\Delta\omega) = 2\pi\delta(\omega_p - \omega_1 - \omega_2) \tag{1.16}$$

Equation (1.15) simplifies into:

$$\left|\Psi\right\rangle = \iint\mathrm{d}\omega_1\,\mathrm{d}\omega_2 C(\omega_1,\omega_2)\hat{a}_H^\dagger(\omega_1)\hat{a}_V^\dagger(\omega_2)\left|0\right\rangle \tag{1.17}$$

where $C(\omega_1,\omega_2)$ is the biphoton Joint Spectral Amplitude (JSA). The JSA is a complex-valued function which gives the probability amplitude that the biphoton

state is given by a signal photon (H-polarized) at frequency ω_1 and an idler photon (V-polarized) at frequency ω_2. Its expression is:

$$\begin{aligned} C(\omega_1,\omega_2) =& \frac{1}{\beta}\frac{\epsilon_0 L}{i\hbar(2\pi)^{1/2}}\frac{1}{\sqrt{v_g^H(\omega_1)v_g^V(\omega_2)}} \\ & \int \mathrm{d}\mathbf{r}\chi^{(2)}(\mathbf{r})E_p(\mathbf{r},\omega_1+\omega_2)E_H(\mathbf{r},\omega_1)E_V(\mathbf{r},\omega_2)e^{i\Delta kz} \end{aligned} \tag{1.18}$$

The squared norm of the JSA is the Joint Spectral Intensity (JSI), a real function which represents the probability density in the frequency space for the biphoton state, normalized as:

$$1 = \iint \mathrm{d}\omega_1\,\mathrm{d}\omega_2|C(\omega_1,\omega_2)|^2 = \iint \mathrm{d}\omega_1\,\mathrm{d}\omega_2 C(\omega_1,\omega_2)C^*(\omega_1,\omega_2) \tag{1.19}$$

As long as pump, signal and idler modes are supported by the waveguide, their spatial distribution is approximately constant with their frequency. So we can write:

$$\begin{aligned} &E_p(\mathbf{r},\omega_1+\omega_2) \approx \phi_p(\omega_1+\omega_2)E_p(x,y) \\ &E_H(\mathbf{r},\omega_1) \approx E_H(x,y) \\ &E_V(\mathbf{r},\omega_2) \approx E_V(x,y) \end{aligned} \tag{1.20}$$

where $\Phi_p(\omega_1+\omega_2)$ is the pump laser frequency distribution, modeled as a Lorentzian function.

The JSA (1.18) simplifies into:

$$C(\omega_1,\omega_2) = \frac{1}{\beta}\frac{\epsilon_0}{i\hbar(2\pi)^{1/2}}\frac{L}{\sqrt{v_g^H v_g^V}}\Gamma\,\phi_p(\omega_1+\omega_2)\,\phi_{PM}(\omega_1,\omega_2) \tag{1.21}$$

where Γ is the nonlinear overlap defined as:

$$\Gamma = \iint \mathrm{d}x\,\mathrm{d}y\chi^{(2)}(x,y)\,E_p(x,y)E_H(x,y)E_V(x,y) \tag{1.22}$$

Since E_p, E_H and E_V are field *amplitudes* ($[\mathrm{V}\cdot\mathrm{m}^{-1}]$), the nonlinear overlap Γ is expressed in unit of $[\mathrm{V}^2\cdot\mathrm{m}]$. We note that this differs from the normalized nonlinear overlap $\bar{\Gamma}$ ($[\mathrm{V}^{-1}]$) defined in (1.1) using the normalized fields spatial distributions ($[\mathrm{m}^{-1}]$).

The JSA, being the spectral density of a wavefunction, has the unit of time ($[\mathrm{s}] = [\mathrm{Hz}^{-1}]$), in agreement with the normalization (1.19) and expression (1.21); the pump spectral amplitude ϕ_p has the unit of time ($[\mathrm{s}]$), while the products of Γ ($[\mathrm{V}^2\cdot\mathrm{m}]$), $L/\sqrt{v_g^H v_g^V}$ ($[s]$) and $\epsilon_0/\hbar$ ($[\mathrm{m}^{-1}\cdot\mathrm{V}^{-2}\cdot\mathrm{s}^{-1}]$) is dimensionless, like the normalization factor β.

ϕ_{PM} is the phase matching term representing the conservation of momentum for the three interacting photons. From equation (2.2.18) of reference [114], we approximate it as a real-valued function:

$$\phi_{PM}(\omega_1, \omega_2) = \mathrm{sinc}(\Delta k L) \tag{1.23}$$

In the wave picture, the phase matching condition indicates that the three interacting waves have to travel at the same speed to assure an efficient (i.e. irreversible) flow of energy from the pump to the signal and idler waves. When this mismatch is equal to zero, $\Delta k = k_p(\omega_1 + \omega_2) - k_H(w_1) - k_V(\omega_2) = 0$, $\phi_{PM} = 1$ and the SPDC process is maximally efficient.

In our collinear device, the condition $\Delta k = 0$ can be achieved only if the three guided waves are co-propagating, as previously supposed. Besides, according to the modes dispersion profile illustrated in (1.2), only the use of a Bragg mode as pump beam and two fundamental Gaussian modes as signal and idler allow to satisfy the condition $\Delta k = 0$, which justify a posteriori our choice of their spatial mode profiles.

1.3 Characterization of biphoton states via Hong-Ou-Mandel interference

The frequency correlations between the two photons of a pair can be revealed via Hong-Ou-Mandel (HOM) interferometry [153]. In HOM interference, two single photons enter a beam splitter via different inputs and interfere. According to their frequency correlations, they may exit from the same output (bunching or coalescence) or different outputs (anti-bunching or anti-coalescence).

In the case of an entangled biphoton pair, the HOM interference is not simply the interference of two single photons. More fascinatingly, it is the interference of the whole biphoton quantum state with itself, i.e. the superposition of the probability amplitudes corresponding to all the paths available to the biphoton state [154, 155]. The shape of the interference pattern is determined by the JSA mirror-symmetry along the $\omega_- = \omega_1 - \omega_2$ direction with respect to frequency degeneracy ($\omega_- = 0$). In this section we introduce the beam splitter transformation and present two typical HOM interferograms, for a Gaussian and a sinc-shaped JSA.

Beam Splitter

The beam splitter is the core of Hong-Ou-Mandel quantum interference.

As figure (1.7) illustrates, a beam splitter is a port with two inputs and two outputs. When a photon enters in the beam splitter, it has a certain probability of being transmitted (i.e. to exit from the same channel) and a complementary probability of being reflected (i.e. to exit from the other channel).

We consider the situation in which two identical photons enter in a beam splitter from two different inputs (figure (1.8)). From the classical probability theory we would expect four equally probable outcomes:

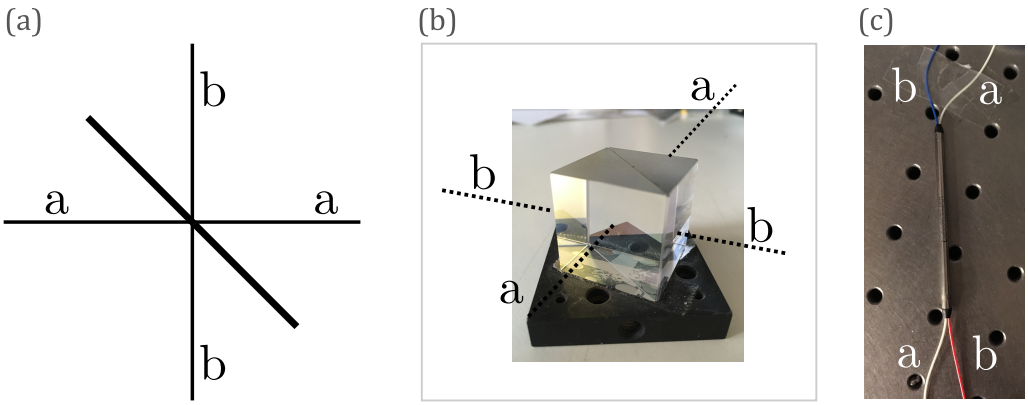

Figure 1.7 – Beam splitter: a port with two inputs and two outputs.
(a) Schematic. A photon in path a can be transmitted on the same path or reflected into path b. Analogously, a photon in path b can be transmitted or reflected into path a.
(b,c) Examples of two beam splitters from our lab: (b) a cube beam splitter and (c) a fibered beam splitter.

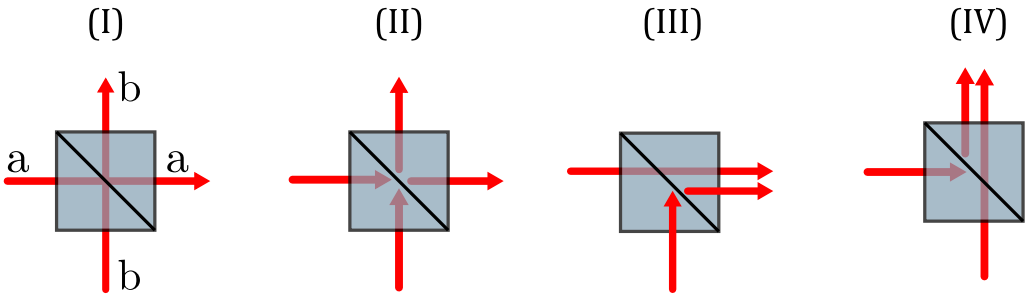

Figure 1.8 – Beam splitter outcomes when two photon enter in two different inputs.

(i) Both photons are transmitted (figure (1.8, I)).

(ii) Both photons are reflected (figure (1.8, II)).

(iii) Photon in a is transmitted, photon in b is reflected (figure (1.8, IV)).

(iv) Photon in a is reflected, photon in b is transmitted (figure (1.8, III)).

However, in the case of single photons originating from a SPDC process, nature follows the rules of quantum physics. Instead of probabilities, we need to consider the probability *amplitudes* associated to each of the four paths, since the beam splitter does not record which one of the four possibility occurs. These amplitudes are complex terms that interfere with each others, giving results that may be contrary to common sense expectation.

To understand how the beam splitter acts on the photons probability amplitudes, we deduce its transformation matrix following references [156, 157]. Given the two states $|a\rangle$ and $|b\rangle$, representing one photon at input a and one photon at input

b (see figure (1.8)) and the transmission and reflection coefficients t and r, the transformation associated to the beam splitter is:

$$\begin{pmatrix} a \\ b \end{pmatrix} \rightarrow \begin{pmatrix} t & r \\ r & t \end{pmatrix} \begin{pmatrix} a \\ b \end{pmatrix}$$

where we define M the beam splitter transformation matrix. We now suppose that the beam splitter is lossless, which is a good approximation in most experimental applications. A lossless device has an unitary transformation matrix, which means that $M^{-1}M = M^{\dagger}M = 1$, where the matrix elements of $M^{\dagger}$ are as $M^{\dagger}_{a,b} = M^{*}_{b,a}$. By imposing:

$$\begin{pmatrix} t & r \\ r & t \end{pmatrix} \begin{pmatrix} r^{*} & t^{*} \\ t^{*} & r^{*} \end{pmatrix} = \begin{pmatrix} 1 & 0 \\ 0 & 1 \end{pmatrix}$$

we find that the following two conditions on the transmission and reflection coefficients:

$$\begin{cases} |t|^2 + |r|^2 = 1 \\ r^{*}t + rt^{*} = 0 \end{cases} \tag{1.24}$$

These conditions imply that the transmission and reflection coefficients are complex numbers. Their square value gives the probability of reflection and transmission, respectively. So we write:

$$\begin{cases} t = |t|e^{i\theta} = |t| \\ r = |r|e^{i\phi} \end{cases} \tag{1.25}$$

where we have set $\theta = 0$ for simplicity, without loosing in generality. By substituting in the second equation in (1.24), we find:

$$2rt\cos\phi = 0 \tag{1.26}$$

that is satisfied for $\phi = \pi/2$.

From now on we consider the case of a 50/50 beam splitter, in which the probability of transmission and reflection are the same: $|t|^2 = |r|^2 = 1/2$.

The reflection and transmission coefficients of equation (1.25) become:

$$\begin{cases} t = 1/\sqrt{2} \\ r = i/\sqrt{2} \end{cases} \tag{1.27}$$

Therefore, the beam splitter transformation matrix is:

$$M = \frac{1}{\sqrt{2}} \begin{pmatrix} 1 & i \\ i & 1 \end{pmatrix} \tag{1.28}$$

We now apply the beam splitter transformation matrix M in the case of one single photon in channel a and another single photon in channel b. The initial quantum state is the path encoded state $|a\rangle\,|b\rangle$ and is transformed according to:

$$\begin{pmatrix} a \\ b \end{pmatrix} \rightarrow \begin{pmatrix} 1 & i \\ i & 1 \end{pmatrix} \begin{pmatrix} a \\ b \end{pmatrix} = \begin{pmatrix} a+ib \\ ia+b \end{pmatrix}$$

So the state evolution is:

$$\begin{aligned} |a\rangle\,|b\rangle &\rightarrow \big(\,|a\rangle + i\,|b\rangle\,\big)\big(i\,|a\rangle + |b\rangle\,\big) \\ &= \big(\underbrace{|a\rangle\,|b\rangle}_{\text{(I)}} - \underbrace{|a\rangle\,|b\rangle}_{\text{(II)}}\big) + i\big(\underbrace{|a\rangle\,|a\rangle}_{\text{(III)}} + \underbrace{|b\rangle\,|b\rangle}_{\text{(IV)}}\big) \\ &= i\big(\underbrace{|a\rangle\,|a\rangle}_{\text{(III)}} + \underbrace{|b\rangle\,|b\rangle}_{\text{(IV)}}\big) \end{aligned} \tag{1.29}$$

In equation (1.29) the two probability amplitudes related to the cases (I) and (II) of figure (1.8). cancel out. This is the bunching phenomena: two identical photons come out from the same beam splitter output channel.

Link between the Joint Spectral Amplitude and the Hong-Ou-Mandel interferogram

The analysis of different scenarios of the behaviour of separable photons and entangled biphoton states in a HOM interferometer is given by two reviews by Weihs and Zeilinger [158] and Wang [159]. A detailed study of the outcome of a HOM experiment using the state produced by our device (taking into account also the effect of the facets reflectivity) will be done in section (6.5).

We will show that in the case of two entangled photons the HOM coincidence probability ($p_{ab}(\tau)$) as a function of the biphoton JSA ($C(\omega_1, \omega_2)$) is:

$$p_{ab}(\tau) = \frac{1}{2}\Big[1 - Re\Big[\iint d\omega_1 d\omega_2 C^*(\omega_1,\omega_2)C(\omega_2,\omega_1)e^{-i(\omega_1-\omega_2)\tau}\Big]\Big] \tag{1.30}$$

Figure (1.9) illustrates the JSI ($C(\omega_1, \omega_2)C^*(\omega_1, \omega_2)$) and the corresponding HOM outcome in the case of biphoton states having Gaussian and sinc shaped JSA along ω_-, which are two representative cases commonly presented in quantum optics textbooks. A sinc shaped JSA originates from a nonlinear source having a phase matching function in the form $\mathrm{sinc}(\alpha\omega_-)$, while the Gaussian JSA comes for instance from the shaping of a biphoton state done by a filter having a Gaussian spectral profile.

When the JSA is mirror-symmetric, i.e. $C(\omega_1, \omega_2) = C(\omega_2, \omega_1)$, the HOM coincidences probability of equation (1.30) is the Fourier Transform of the JSI along $\omega_1 - \omega_2$. Therefore, a Gaussian JSA (black continuous line in figure (1.9)) corresponds to a Gaussian HOM dip, while a sinc shaped JSA (red dashed line in figure (1.9)) to a triangle dip. In the paragraphs (2.1.4, 2.1.5) of the next chapter we will see how the HOM interference pattern transforms when the JSA is not perfectly mirror-symmetric or has different shapes.

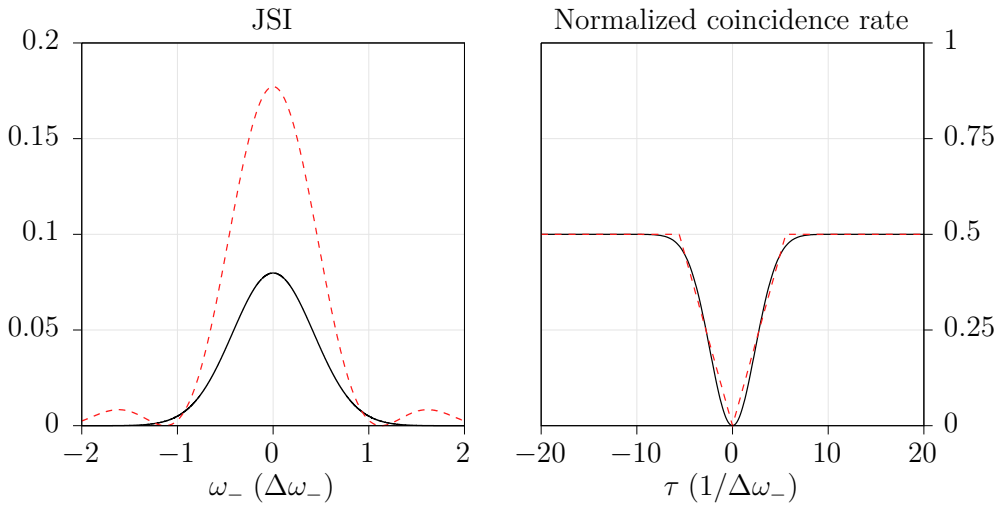

Figure 1.9 – JSI and corresponding HOM interference pattern of a Gaussian (black continuous line) and a sinc shaped (red dashed line) biphoton JSA.

Chapter 2

Impact of the source optical properties on the Joint Spectral Amplitude

In this chapter we describe the frequency correlation between the two photons of the pair by analyzing the different terms appearing in the JSA expression (1.21).

We show that the phase matching term is shaped by three main optical properties of the device. The first one is the modal birefringence, which is the difference in refractive index between the pump mode and the degenerate signal-idler modes. The other two are the birefringence and the chromatic dispersion of the signal and idler modes in the telecom range.

In our study we focus on the CW optical pumping regime. We show that by tuning the pump frequency we are able to generate an anti-correlated biphoton state that either possesses a large bandwidth or exists in a coherent superposition of two distinct frequency channels. The former is a resource for some quantum communication protocols, like a multi-user Quantum Key Distribution demonstrated by our group [160]. The latter may be used in a multiple photon pair SPDC regime to implement Schrödinger cat-like states, a qubit candidate for quantum information processing [161].

2.1 Joint Spectral Amplitude in (ω_+, ω_-) basis

In order to investigate the frequency correlations of the quantum state, we neglect the normalization factor of expression (1.21), so that the JSA expression is:

$$C(\omega_1, \omega_2) = \phi_p(\omega_1 + \omega_2)\phi_{PM}(\omega_1, \omega_2) \tag{2.1}$$

†

One important property of the biphoton state is its mirror symmetry with respect to the degeneracy frequency. The mirror symmetry determines the state

†A complete expression of the JSA should include the cavity effect for signal and idler photons, resulting from their reflections at the waveguide input and output facets. If we define f_H and f_V

symmetry under particle exchange and thus the result of the interference that is obtained when the state is sent through a HOM interferometer. In order to reveal the state mirror symmetry, it is handy to rewrite the JSA in the (ω_+,ω_-) basis, rotated by 45° respect to (ω_1,ω_2), according to the transformation:

$$\begin{cases} \omega_+ = \omega_1 + \omega_2 \\ \omega_- = \omega_1 - \omega_2 \end{cases} \tag{2.3}$$

The JSA in the new basis reads:

$$C(\omega_+, \omega_-) = \phi_p(\omega_+)\phi_{PM}(\omega_+, \omega_-) \tag{2.4}$$

In order to compare this treatment with the experimental data, we also introduce $\lambda_- = \lambda_1 - \lambda_2$, the wavelength difference between the signal and idler photons. We remind that the frequency and wavelength basis are related by:

$$\lambda_- = \frac{2\pi c(\omega_1 - \omega_2)}{\omega_1\omega_2} = \frac{8\pi c\,\omega_-}{(\omega_+ - \omega_-)(\omega_+ + \omega_-)} \overset{C.W.pump}{\approx} \frac{8\pi c\,\omega_-}{(\omega_p - \omega_-)(\omega_p + \omega_-)}$$

2.1.1 Pump spectral profile

The pump spectral profile ϕ_p describes the energy distribution of the pump photons propagating in the device and contributing to the SPDC process. Following the conservation of energy ($\omega_1 + \omega_2 = \omega_p$), the pump spectral amplitude depends only on the variable ω_+.

In the CW pumping regime, ϕ_p can be modeled along ω_+ as a Lorentzian function, described by a central frequency ω_p and a linewidth $\Delta\omega_L$ (FWHM). For our experiments, we use a CW pumping laser (TOPTICA$^{\text{TM}}$ Photonics DL pro 780), at $\omega_p = 2465 \cdot 10^{15}$THz ($\lambda_p = 764$nm) and $\Delta\omega_L < 500$kHz. To simplify the calculations, since $\Delta\omega_L$ is much narrower than the spectral width of the other features characterizing the JSA (i.e. the cavity free spectral range which we will discuss in the next chapters), we can approximate the Lorentzian function to a Dirac delta function:

$$\phi_p(\omega_+) = \frac{1}{\pi}\frac{\Delta\omega_L/2}{(\omega_+ - \omega_p)^2 + (\Delta\omega_L/2)^2} \overset{\Delta\omega_L \to 0}{\approx} \delta(\omega_+ - \omega_p) \tag{2.5}$$

2.1.2 Phase matching function

In this paragraph we illustrate the dependence of the phase matching term ϕ_{PM} on the optical properties of the device, such as its birefringence, chromatic dispersion

the Fabry-Perot functions of signal and idler photons, the JSA would read:

$$C(\omega_1, \omega_2) = \phi_p(\omega_1 + \omega_2)\phi_{PM}(\omega_1, \omega_2) f_H(\omega_1) f_V(\omega_2) = \phi_p(\omega_1 + \omega_2)\phi_{PM}(\omega_1, \omega_2) f_{cav}(\omega_1, \omega_2) \tag{2.2}$$

In this first part of this manuscript we neglect the cavity effect on the JSA, studied in chapter (5).

and modal dispersion. In section (1.2.3) we have shown that the expression of the phase matching function is:

$$\phi_{PM} = \mathrm{sinc}(\Delta k L) \tag{2.6}$$

where L is the device length and Δk the difference in wavevector among pump, signal and idler wavevectors. In our collinear source, pump, signal and idler photons propagate along the same direction. Therefore Δk is given by:

$$\begin{aligned} \Delta k &= k_p - k_{signal} - k_{idler} \\ &= k(\omega_p) - k(\omega_1) - k(\omega_2) \end{aligned} \tag{2.7}$$

Our source is designed to satisfy a type-II phase matching process, where the pump is H-polarized, the signal is H-polarized and the idler V-polarized. According to the dispersion relation of the waveguides modes (equation (4)), we can rewrite the phase-mismatch as:

$$\Delta k = \frac{1}{c}[\omega_p n_{H,p}(\omega_p) - \omega_1 n_H(\omega_1) - \omega_2 n_V(\omega_2)] \tag{2.8}$$

which in (ω_+,ω_-) basis is:

$$\Delta k = \frac{1}{c}\Big[\omega_+ n_{H,p}(\omega_+) - \Big(\frac{\omega_+ + \omega_-}{2}\Big) n_H\Big(\frac{\omega_+ + \omega_-}{2}\Big) - \Big(\frac{\omega_+ - \omega_-}{2}\Big) n_V\Big(\frac{\omega_+ - \omega_-}{2}\Big)\Big] \tag{2.9}$$

We now simplify the expression of the phase-mismatch by considering the dispersion and birefringence properties of the interacting modes. In our source, figure (1.2) shows that the dispersion can be approximated as a linear function of the frequency over the bandwidth of interest, i.e. the bandwidth of the emitted biphoton state.

$$n(\omega + \Delta\omega) = n(\omega) + \Delta\omega \frac{dn}{d\omega}\Big|_\omega \tag{2.10}$$

By plugging (2.10) into (2.9), we obtain:

$$\begin{aligned} \Delta k = \frac{1}{c}\Big\{ & \omega_+ n_{H,p}(\omega_+) - \Big(\frac{\omega_+ + \omega_-}{2}\Big)\Big[n_H\Big|_{\frac{\omega_+}{2}} + \frac{dn_H}{d\omega}\Big|_{\frac{\omega_+}{2}}\Big(\frac{\omega_-}{2}\Big)\Big] + \\ & - \Big(\frac{\omega_+ - \omega_-}{2}\Big)\Big[n_V\Big|_{\frac{\omega_+}{2}} - \frac{dn_V}{d\omega}\Big|_{\frac{\omega_+}{2}}\Big(\frac{\omega_-}{2}\Big)\Big]\Big\} \end{aligned} \tag{2.11}$$

Looking at the dispersion relations (1.2), we also observe that the chromatic dispersion of each mode is constant and does not depend on polarization within the considered bandwidth. On the other hand, the pump mode at 775nm has a frequency close to GaAs band gap, so, following Kramers–Kronig relations, its chromatic dispersion is higher than the one of the signal and idler modes in the telecom range. So we write for every $\omega_+/2$ within the bandwidth of interest:

$$\frac{dn_H}{d\omega}\Big|_{\frac{\omega_+}{2}} = \frac{dn_V}{d\omega}\Big|_{\frac{\omega_+}{2}} = \frac{dn}{d\omega}\Big|_{\frac{\omega_+}{2}} \tag{2.12}$$

$$\frac{dn_{H,p}}{d\omega} > \frac{dn}{d\omega} \tag{2.13}$$

By plugging equation (2.12) into (2.11), we obtain that the wavevector mismatch is given by the sum of three main contributions:

$$\Delta k = \Delta k_{modal}(\omega_+) + \Delta k_{birefringence}(\omega_-) + \Delta k_{dispersion}(\omega_-) \tag{2.14}$$

where Δk_{modal} is the modal birefringence mismatch, proportional to the pump frequency and the modal birefringence Δn_{modal} (the difference between the effective index of the pump photons at $\omega_p = \omega_+$ and the average effective index of the two orthogonally polarized signal and idler modes at $\omega_+/2$):

$$\Delta k_{modal}(\omega_+) = \frac{\omega_+}{c}\left[n_{H,p}(\omega_+) - \frac{n_H(\omega_+/2) + n_V(\omega_+/2)}{2}\right] = \frac{\omega_+}{c}\Delta n_{modal}(\omega_+) \tag{2.15}$$

$\Delta k_{birefringence}$ is the birefringence mismatch, proportional to ω_- and Δn, the birefringence between signal and idler modes (Δn is a constant since the refractive index varies linearly with the frequency (2.10) and the dispersion is polarization independent (2.12)):

$$\Delta k_{birefringence}(\omega_-) = -\left(\frac{\omega_-}{2c}\right)\left[n_H\left(\frac{\omega_+}{2}\right) - n_V\left(\frac{\omega_+}{2}\right)\right] = -\left(\frac{\omega_-}{2c}\right)\Delta n \tag{2.16}$$

$\Delta k_{dispersion}$ is the dispersion mismatch, proportional to signal and idler chromatic dispersion $dn/d\omega$ and to the square of ω_-:

$$\Delta k_{dispersion}(\omega_-) = -\left(\frac{\omega_-^2}{2c}\right)\frac{dn}{d\omega}\Big|_{\frac{\omega_+}{2}} \tag{2.17}$$

By plugging the three phase mismatch terms (2.15, 2.16, 2.17) into equation (2.6), we find that the expression of the phase matching term is:

$$\phi_{PM}(\omega_+, \omega_-) = \mathrm{sinc}\left\{\frac{L}{c}\left[\omega_+\Delta n_{modal}(\omega_+) - \omega_-\left(\frac{\Delta n}{2} + \frac{\omega_-}{2}\frac{dn}{d\omega}\right)\right]\right\} \tag{2.18}$$

Figure (2.1) illustrates the different terms contributing to the expression of phase matching (2.18) in the modes dispersion profiles. In the following, we study in detail the impact of the three terms appearing in equation (2.18) and figure (2.1) on the shape of the phase matching function.

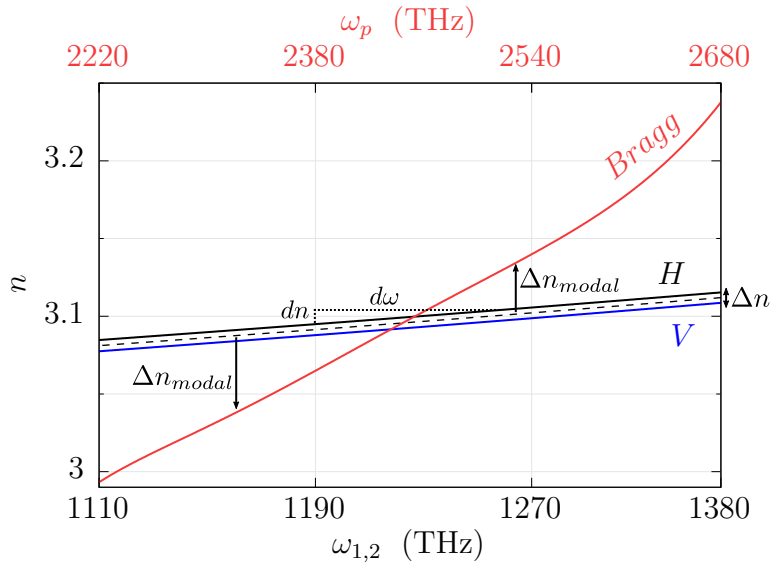

Figure 2.1 – Numerically calculated dispersion for the three interacting modes: pump (Bragg, red), signal (H, black) and idler (V, blue) fundamental modes.

2.1.3 Impact of modal birefringence

Among the three contributions to the phase-mismatch, $\Delta k_{modal}(\omega_+)$ is the only one depending on the optical properties of the pump Bragg mode. Since it is not dependent on ω_-, it determines the phase matching condition when signal and idler photons are frequency degenerate ($\omega_- = 0$). In the CW pumping monochromatic regime ($\omega_+ \to \omega_p$), at a specific pump frequency, the modal birefringence is a constant given by:

$$\Delta n_{modal}(\omega_+) \to \Delta n_{modal}(\omega_p) = n_{H,p}(\omega_p) - \frac{n_H(\omega_p/2) + n_V(\omega_p/2)}{2} \tag{2.19}$$

As shown in figure (2.1), due to the fact that the pump mode has a higher chromatic dispersion than that of the generated modes, a small variation of the pump wavelength makes that $\Delta n_{modal}(\omega_p)$ passes from negative to zero to positive. We define $\omega_p = \overline{\omega}_p$ as the pumping frequency for which Δn_{modal} is zero:

$$\Delta n_{modal}(\omega_p) = n_{H,p}(\overline{\omega}_p) - \frac{n_H(\overline{\omega}_p/2) + n_V(\overline{\omega}_p/2)}{2} = 0 \Rightarrow \Delta k_{modal}(\overline{\omega}_p) = 0 \tag{2.20}$$

Experimentally, we find $\overline{\omega}_p/2$ (and thus $\overline{\omega}_p$) by performing a SHG measurement by injecting a monochromatic telecom laser, polarized along the diagonal direction, into the waveguide and searching for the optimal resonance wavelength.

2.1.4 Impact of polarization birefringence and chromatic dispersion

In this section, we consider a waveguide pumped at the frequency $\overline{\omega}_p$. The wavevector mismatch is determined only by signal and idler birefringence Δn and the chromatic dispersion $dn/d\omega$. The phase matching function is thus:

$$\begin{aligned}\phi_{PM}(\overline{\omega}_p, \omega_-) &= \mathrm{sinc}[(\Delta k_{birefringence} + \Delta k_{dispersion})L] \\ &= \mathrm{sinc}\left[\frac{L\omega_-}{2c}\left(\Delta n + \omega_- \frac{dn}{d\omega}\right)\right]\end{aligned} \tag{2.21}$$

The term $\Delta k_{birefringence}(\omega_-)$ (equation (2.16)) is proportional to ω_- and to Δn. If $\Delta k_{birefringence}$ is different from zero and $\Delta k_{dispersion} = \Delta k_{modal} = 0$, the emitted biphoton state is centered at $\omega_- = 0$ and has a bandwidth inversely proportional to Δn.

$\Delta k_{dispersion}(\omega_-)$ (equation (2.17)) is proportional to the square of ω_- and to $dn/d\omega$. When $\Delta k_{dispersion}$ is different from zero while $\Delta k_{birefringence} = \Delta k_{modal} = 0$, the biphoton state is centered at $\omega_- = 0$ with a bandwidth inversely proportional to the square root of $dn/d\omega$.

In bulk GaAs, the birefringence is zero due to its isotropic crystal lattice. However, our waveguide has a birefringence induced by its anisotropic geometry. As shown in figure (1.3), the core is not squared but rectangular, with a thickness of 0.36µm and an average width of 6-7µm.

The chromatic dispersion derives from the material dispersion, which is normal in the telecom range where signal and idler are generated. If we define $\Delta\omega_-^{FWHM}$ as the biphoton state frequency FWHM, in a narrow band biphoton state, $\Delta\omega_-^{FWHM} dn/d\omega$ is much lower than Δn and the impact of the chromatic dispersion on the phase matching function is negligible. Conversely, for a large band biphoton state, $\Delta\omega_-^{FWHM} dn/d\omega \sim \Delta n$, thus the chromatic dispersion changes the shape of the phase matching function. This is usually the case for a biphoton state emitted by a Bragg reflection waveguide.

From the numerical calculation presented in figure (2.1), we extract the following birefringence and dispersion values for our source:

$$\begin{aligned}\Delta n &= 7 \cdot 10^{-3} \\ dn/d\omega &= 1.33 \cdot 10^{-16}\ \mathrm{Hz}^{-1}\end{aligned} \tag{2.22}$$

At $\overline{\omega}_p/2 + \Delta\omega_-^{FWHM}$, we find that the two contributions in equation (2.14) are comparable and they both need to be taken into account:

$$\begin{aligned}|\Delta k_{birefringence}(\omega_-^{FWHM})| &= 4.17 \cdot 10^3\ \mathrm{m}^{-1} \\ |\Delta k_{dispersion}(\omega_-^{FWHM})| &= 4.00 \cdot 10^3\ \mathrm{m}^{-1}\end{aligned} \tag{2.23}$$

We now analyze the impact of birefringence on the biphoton frequency correlations.

Figure (2.2) reports the phase matching function versus the birefringence. As the birefringence increases, a branch centered in $\omega_- = -\Delta n(dn/d\omega)^{-1}$ emerges

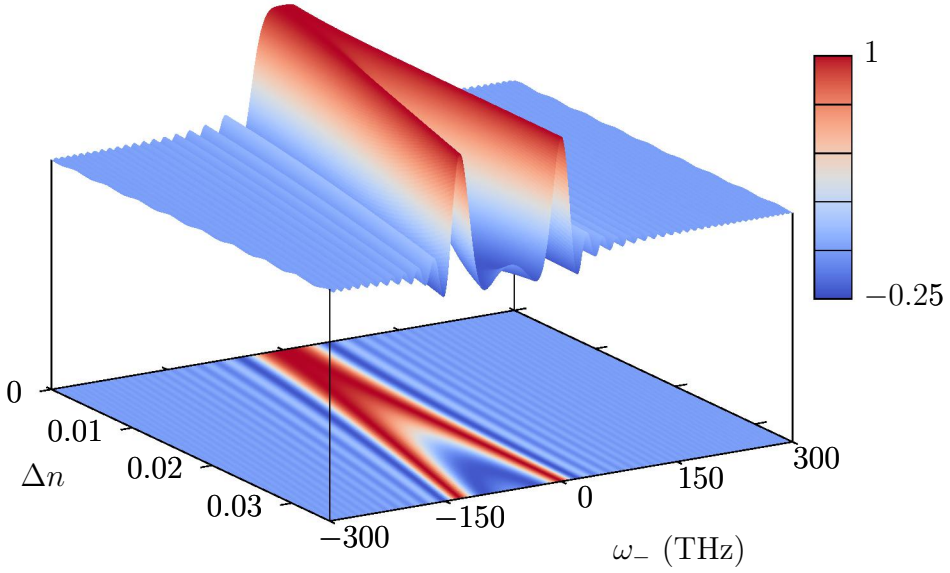

Figure 2.2 – Phase matching function ϕ_{PM} (2.21) versus ω_- and the waveguide birefringence Δn, calculated using the dispersion (2.22) and optimal pumping condition (2.20).

and moves away from the lobe centered in $\omega_- = 0$. Therefore, the mirror symmetry of the phase matching function with respect to ω_- reduces.

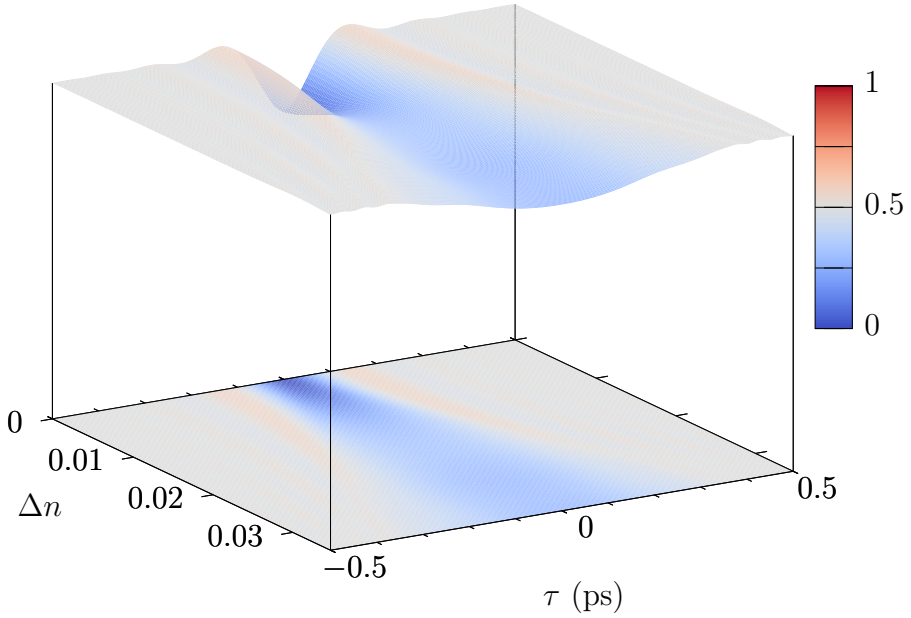

Figure 2.3 – HOM interference pattern versus waveguide birefringence Δn for the biphoton state having the phase matching function reported in figure (2.2).

The corresponding figure (2.3) shows the HOM interference of the biphoton emitted as a function of the source birefringence. As the symmetry decreases with the birefringence, the visibility of the HOM interference reduces. Figure (2.4) shows the biphoton JSI and HOM interference pattern for different values of Δn. In (a, b) the birefringence is zero, the JSI is perfectly symmetric and the HOM interference has unitary visibility. Regarding the shape of the HOM pattern (b), we note that it is not a triangular function as we would expect from a sinc-shaped phase matching term linear in ω_- (see figure (1.9)). There are some oscillations on the side of the central dip, decaying to the baseline value of 0.5 as the delay increases.

The presence of rebounds arises from dispersion, responsible for a phase matching function whose argument is proportional to ω_-^2 instead of ω_-: $\phi_{PM}(\omega_-) \approx \mathrm{sinc}(\alpha\omega_-^2)^2$.

As birefringence increases, the visibility of the HOM dip decreases. In (c, d) the birefringence value is the same as the one estimated in our source (2.22) and the visibility decreases to 0.67.

At higher values of birefringence, the visibility value tends asymptotically to 0.5 (f, h). The reason is that, as the birefringence increases, the phase matching function has a central lobe that is perfectly mirror symmetric, and a second side lobe that has no symmetry at all (a, c, e, g). In a HOM interference, only the

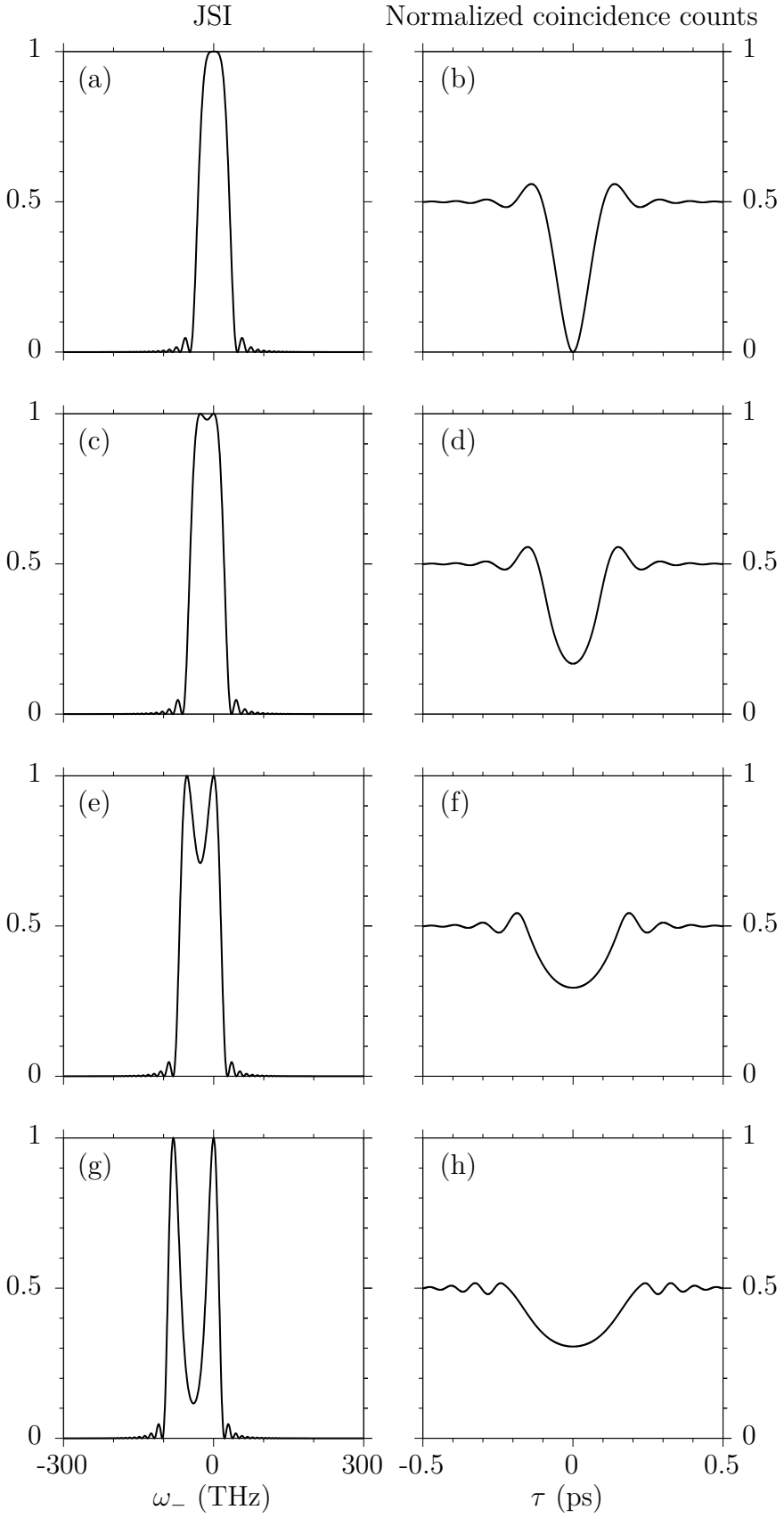

Figure 2.4 – Biphoton JSI and corresponding HOM interference pattern for a monochromatic pump. The different cases correspond to the phase matching function reported in figure (2.2), for different values of birefringence:
(a, b) $\Delta n = 0$, (c, d) $\Delta n = 0.007$, (e, f) $\Delta n = 0.014$, (g, h) $\Delta n = 0.021$.

former half of the biphoton state leads to indistinguishable paths, with the result that the visibility is halved.

2.1.5 Impact of modal birefringence and chromatic dispersion

In this section we consider the case in which the waveguide birefringence is zero. At the same time, we relax the hypothesis $\omega_p = \overline{\omega}_p$ (equation (2.20)), so that the modal phase matching term is generally not null. We also take into account the linear chromatic dispersion, by considering the case of our source (2.22). In this case, the phase matching functions reads:

$$\phi_{PM}(\omega_p, \omega_-) = \text{sinc}\left[\frac{L}{c}\left(\omega_p \Delta n_{modal}(\omega_p) - \omega_-^2 \frac{1}{2}\frac{dn}{d\omega}\right)\right] \tag{2.24}$$

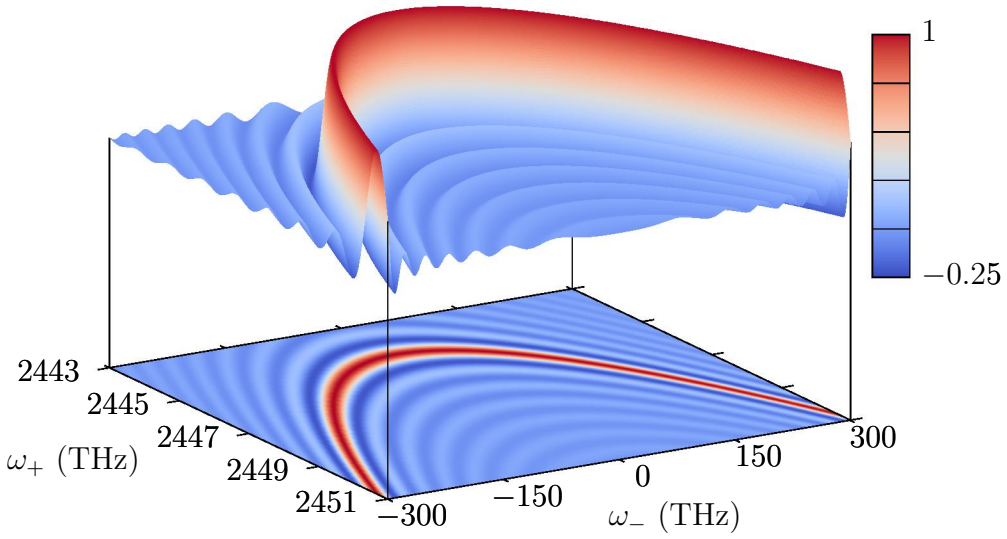

Figure 2.5 – Phase matching term ϕ_{PM} (2.21) as a function of pump frequency, in ideal zero birefringence condition.

Figure (2.5) illustrates this phase matching function as a function of the pump frequency. The figure branching feature is easily understood by considering that the phase matching is maximum equal to one when its argument is zero. Due to the presence of the dispersion term, which is quadratic in ω_-, this is satisfied for two opposite values of ω_-:

$$\omega_{-,max} = \pm\sqrt{2\omega_p \Delta n_{modal}(\omega_p)\left(\frac{dn}{d\omega}\right)^{-1}} \tag{2.25}$$

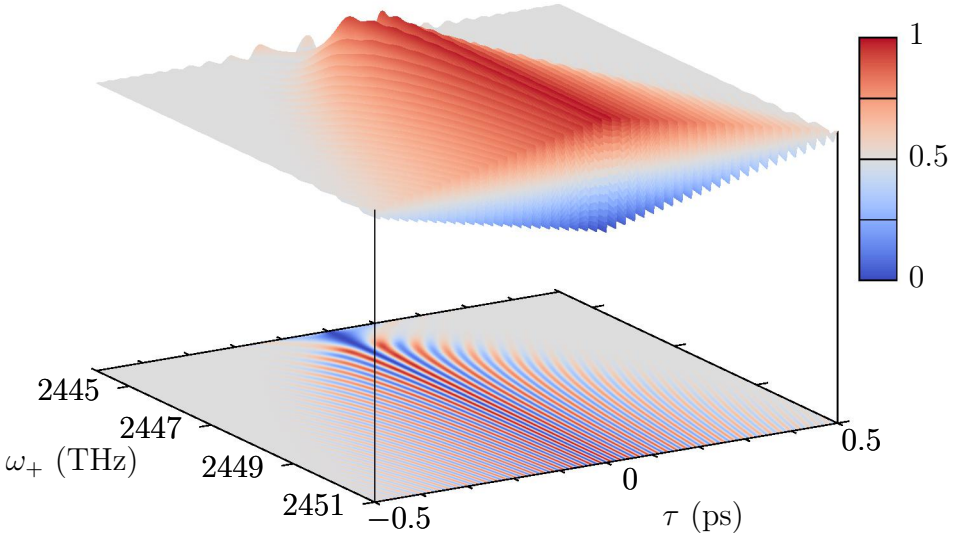

Figure 2.6 – HOM interference pattern versus the pump detuning ω_+, corresponding to the phase matching function reported in figure (2.5).

When $n_{modal}(\omega_p) > 0$, which is verified for pump frequency above the degeneracy condition ($\omega_p > \overline{\omega}_p$), two types of photon pairs can be emitted. In the first pair, the signal photon has frequencies $\omega_1 = \omega_- + \omega_p$ and the idler photon $\omega_2 = \omega_- - \omega_p$. Viceversa, the second pair consists of a signal photon at ω_2 and an idler photon at ω_1. The absolute frequency difference between the signal and idler photons increases with ω_p. Since $\Delta n_{modal}(\omega_p)$ is approximately linear with respect to ω_p (for $\omega_p < 2620$THz, as illustrated in the dispersion relation of figure (2.1)), the distance between the biphoton pairs grows linearly with the pump frequency:

$$\Delta\omega_{-,max} \propto 2\sqrt{\omega_p \Delta n_{modal}(\omega_p)} \approx \omega_p \tag{2.26}$$

As reported in figure (2.6), while the pump frequency increases and the two branches move away, the corresponding HOM pattern displays a spatial beating feature [162]. The frequency of the beating oscillation increases with the pump frequency and distance between the two branches.

The effect is highlighted in figure (2.7), where we compare the JSI and HOM at some representative pump frequencies. In panels (a,b) $\omega_p = \overline{\omega}_p$, so the argument of the phase matching function (2.24) is proportional to ω_-^2. The HOM pattern shown in (b) is the same as the one in figure (2.4, b).

In panels (c, e, g), while the CW pump frequency increases, the central peak of the JSI separates into two peaks which move away. The generated two-photon state is a coherent superposition of two dinstict frequency states with opposite phase.

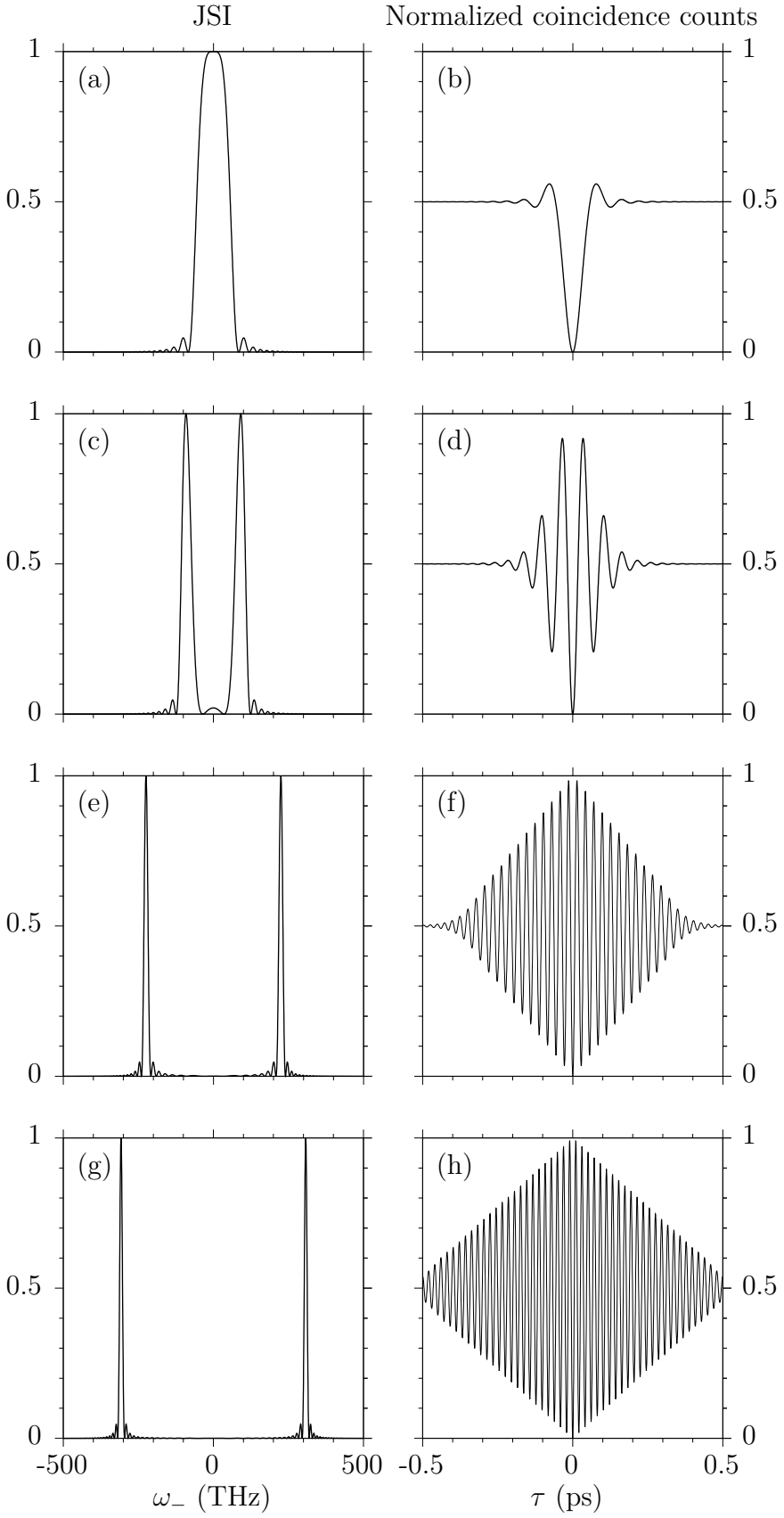

Figure 2.7 – biphoton JSI and corresponding HOM interference pattern for the phase matching function reported in figure (2.5), for different CW pumping frequencies:
(a, b) $\omega_p = 2444.6$THz, (c, d) $\omega_p = 2445.2$THz, (e, f) $\omega_p = 2448.1$THz, (c, d) $\omega_p = 2451.0$THz.

These kind of states were originally proposed and demonstrated [163, 164, 165] as the superposition of two Fock states (or number states) where the number of photons is unknown, with potential applications in quantum metrology and quantum information processing [166].

In this case, the two-photon state is the superposition of two single-photon states. Still, these states may be useful in metrology application thanks to their unique HOM interference pattern. As we observe in panels (d, f, h), the interference pattern is composed by many peaks within a beating envelope. The number of peaks increases with the distance in frequency between the two components of the states.

We observe that the same HOM interference spatial beating phenomena can be observed by performing a symmetric frequency filtering on the state in panel (a). This operation can be achieved by placing two frequency filters at each output of the HOM beam splitter, with the two filters centered at different frequencies [162]. The combination of HOM interference and filtering of the biphoton state has been reinterpreted in terms of engineering of Schrödinger cat-like state by a PhD student of our group, N. Fabre.

On the other hand, by using a dispersive collinear source, we are able to emit such a state by simply tuning the CW pump frequency, without the need of any external filters. The only requirement is that the birefringence of the source is zero. The experimental confirmation of this proposal is currently being carried out by our group.

2.2 Complete simulation of the phase matching function

Now that we have analyzed the phase matching function and seen the effect of its different terms on the corresponding HOM interference pattern in the case of a monochromatic pump, we study the specific case of our AlGaAs source. We calculate numerically the general expression of the phase matching function (equation (2.6)). We use the calculated dispersion relation in figure (2.1), and the typical length of our source of $L = 2$mm. In doing so, we are considering all the contributions to the phase-mismatch: modal birefringence, birefringence and chromatic dispersion.
In order to compare these numerical simulations to the results in the previous paragraphs, we consider photon pairs emitted in the frequency range of $\omega_{1,2} = 1222.4 \pm 300.0$THz ($\nu_{1,2} = 194.6 \pm 47.7$THz), corresponding to $\lambda_{1,2} = 1540.9 \pm 377.1$nm.

However, from an experimental point of view we are mostly interested in signal and idler photons emitted within a narrower frequency range, corresponding to the telecom S, C and L-band: $\omega_{1,2} = 1224.4 \pm 65$THz, or $\lambda_{1,2} = 1540.9 \pm 83$ nm. Within this frequency range, the photon pairs can be transmitted by the standard optical fibers and detected by the single-photon APD detectors we use (ID230).

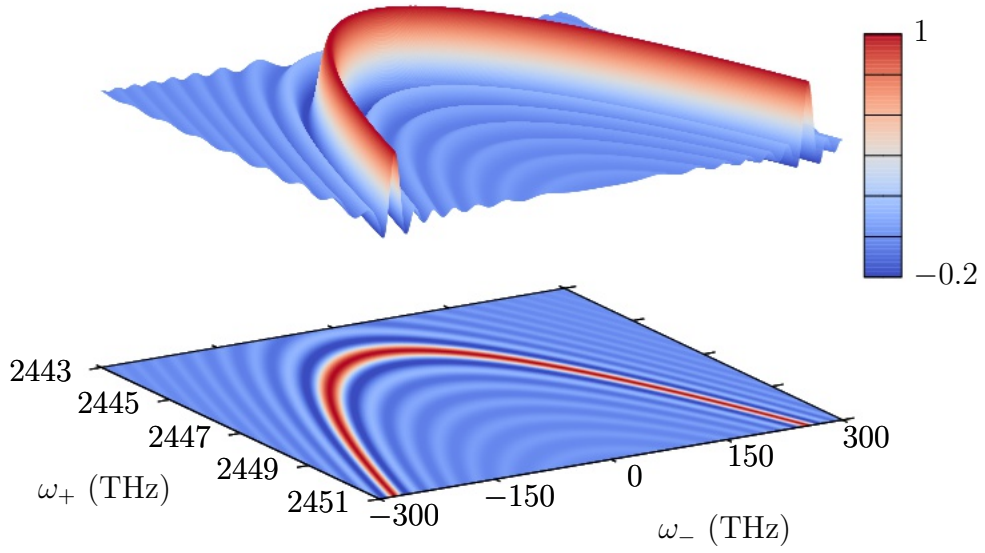

Figure 2.8 – Numerically simulated phase matching function ϕ_{PM} in the case of our source, calculated from the dispersion relation shown in figure (2.1).

Figure (2.8) shows the phase matching profile. When signal and idler are frequency degenerate (i.e. $\omega_- = 0$) the maximum of the phase matching function is found at $\omega_+^{max} = 2444.7\text{THz}$ (770.5 nm). For a generic value of ω_-, the phase matching maxima are disposed along a parabolic curve with respect to ω_-. As previously illustrated (equation (2.25)), the parabolic shape stems from the presence of chromatic dispersion, proportional to the square of ω_-.

In addition, the phase matching function is asymmetric due to birefringence. We can quantify this asymmetry by fitting the region of phase matching maxima by a second order polynomial. The asymmetry is proportional to the first order term in the following expression:

$$\omega_+^{max}(\omega_-) = 2444.7\,\text{THz} + 2.1 \cdot 10^{-3}\,\omega_- + 8.9 \cdot 10^{-17}\,\omega_-^2 \tag{2.27}$$

which in wavelength is:

$$\lambda_+^{max}(\lambda_-) = 770.5\,\text{nm} - 6.6 \cdot 10^{-4}\,\lambda_- - 2.8 \cdot 10^{-5}\,\lambda_-^2 \tag{2.28}$$

As figures (2.9) and (2.10) illustrate, the effect of this asymmetry is to reduce the visibility of the HOM measurement of the emitted biphoton state. In panel (b), we see that at the pumping frequency $\omega_p = \overline{\omega}_p$, the HOM visibility is 0.88. The effect of the birefringence is even more visible for higher pumping frequencies. In (c) we see that the state is only partly mirror symmetric and the visibility in (d) is only 0.48. In (e, g) the states are almost no longer mirror symmetric

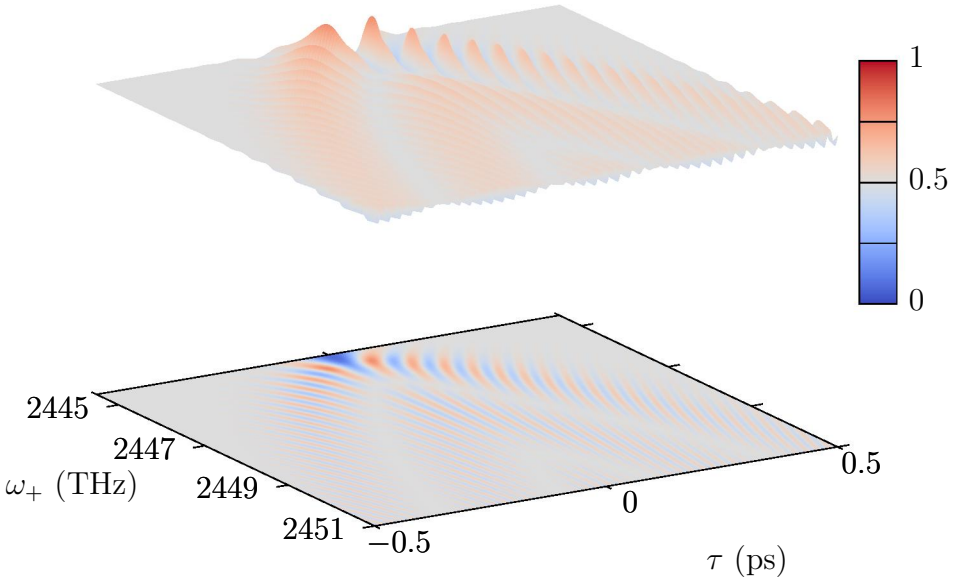

Figure 2.9 – Numerically simulated HOM interference pattern versus the pump detuning ω_+ in the case of our source, corresponding to the phase matching function reported in figure (2.8).

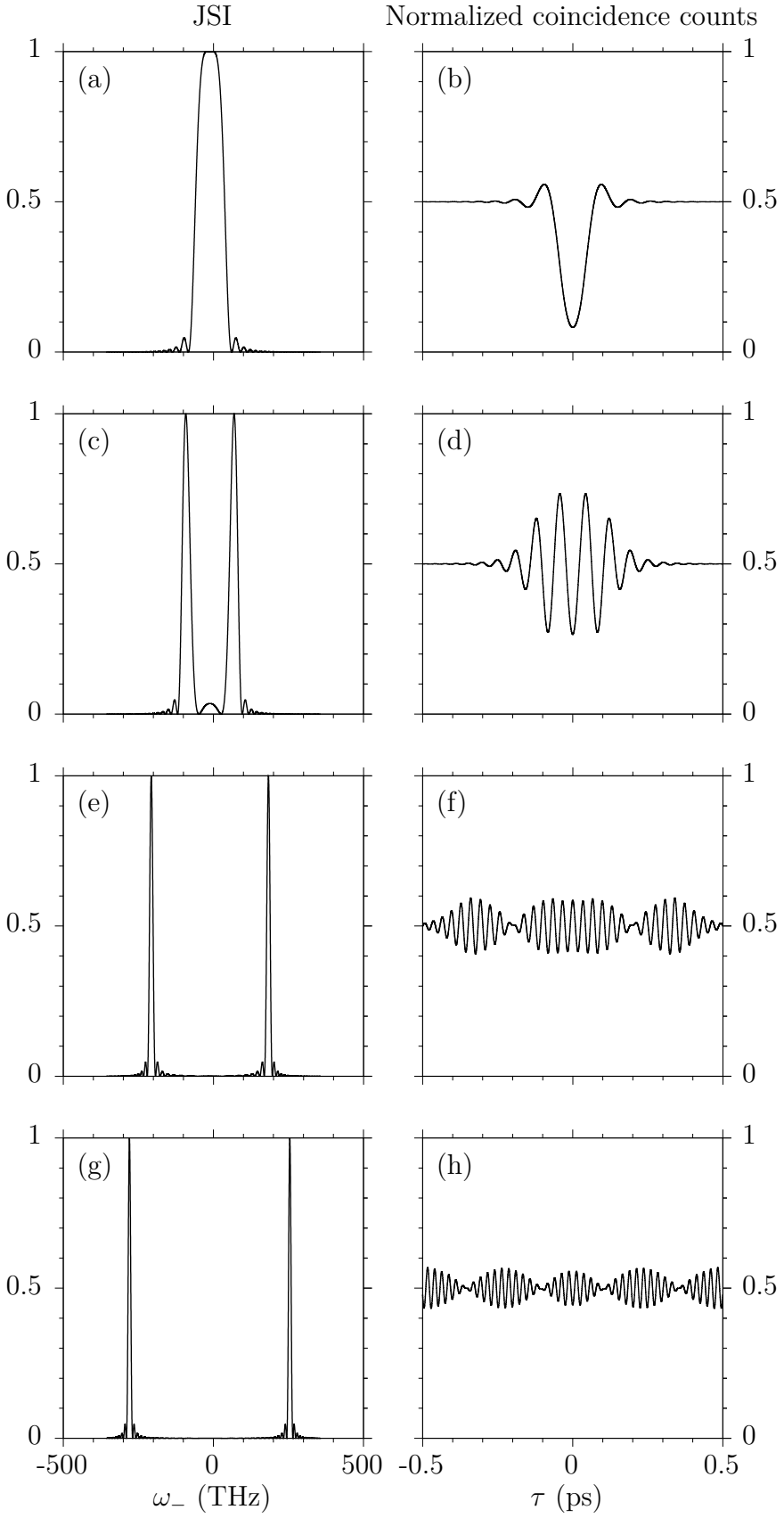

Figure 2.10 – Numerically calculated JSI and corresponding HOM interference pattern in the case of our source, for different CW pumping frequencies: (a, b) $\omega_p = 2444.6$THz , (c, d) $\omega_p = 2445.2$THz , (e, f) $\omega_p = 2448.1$THz, (c, d) $\omega_p = 2451.0$THz.

and the visibility in (f, h) is lower than 0.2. As a consequence, this value of birefringence precludes the emission of experimentally detectable cat-like states whose components are, at the same time, well-separated in frequency and mirror symmetric.

A reduction of birefringence is necessary to emit mirror-symmetric states which can be detected with high visibility in a HOM interference experiment. A possible way to achieve a low birefringence in a Bragg reflector waveguide has been recently proposed by the group of Weihs [167]. Their proposal is to add two layers with an increasing refractive index (decreasing Al content) around the core, reducing the waveguide asymmetry and thus minimizing birefringence.

An alternative is to actively control the birefringence by electro-optic effect in the source. This solution has already being demonstrated on the GaAs platform for the manipulation of single and biphoton states [60]. The design and fabrication process of an integrated biphoton source and electro-optics modulator are currently under development in our group.

Chapter 3

Experimental characterization of the device in the CW optical pumping regime

In this chapter we investigate the source efficiency in the CW pumping regime, both theoretically and experimentally. As figures of merit, we consider the measured coincidence rate (R_c), proportional to the source Pair Production Rate (PPR), and the Coincidences-to-accidental ratio (CAR), the ratio between the true coincidences due to the photon pairs and the accidental coincidences due to the background noise.

We measure R_c and CAR in CW monochromatic regime as a function of the source temperature and the pump beam power, frequency and spatial mode distribution.

We find that the source performance depends on the phase matching function and the Fabry-Perot interference of signal, idler and pump photons within the waveguide.

3.1 Conversion efficiency and Joint Spectral Amplitude

In the following, we consider SPDC in AlGaAs waveguide under CW monochromatic pump operation. If we neglect the source cavity effect, the efficiency of the SPDC is determined by the phase matching function for a given pump frequency:

$$\begin{aligned} \eta_{PM}(\omega_p) &= \iint \omega_+\omega_-\delta(\omega_+ - \omega_p)|\phi_{PM}(\omega_p,\omega_-)|^2 \\ &= \int \omega_-|\phi_{PM}(\omega_p,\omega_-)|^2 \end{aligned} \tag{3.1}$$

We normalize η_{PM} to its maximum value, corresponding to an optimal pumping frequency, i.e. $\eta_{PM}(\omega_p^{opt}) = \max\{\eta_{PM}(\omega_p)\} := 1$.

Figure (3.1) reports $\eta_{PM}(\omega_p)$ calculated using the phase matching function shown in figure (2.8). The SPDC reaches its highest efficiency when the pump frequency is $\omega_p = \overline{\omega}_p = 2444.71\text{THz} = 2\omega_d$ ($\lambda_p = 770.5\,\text{nm}$). This corresponds to

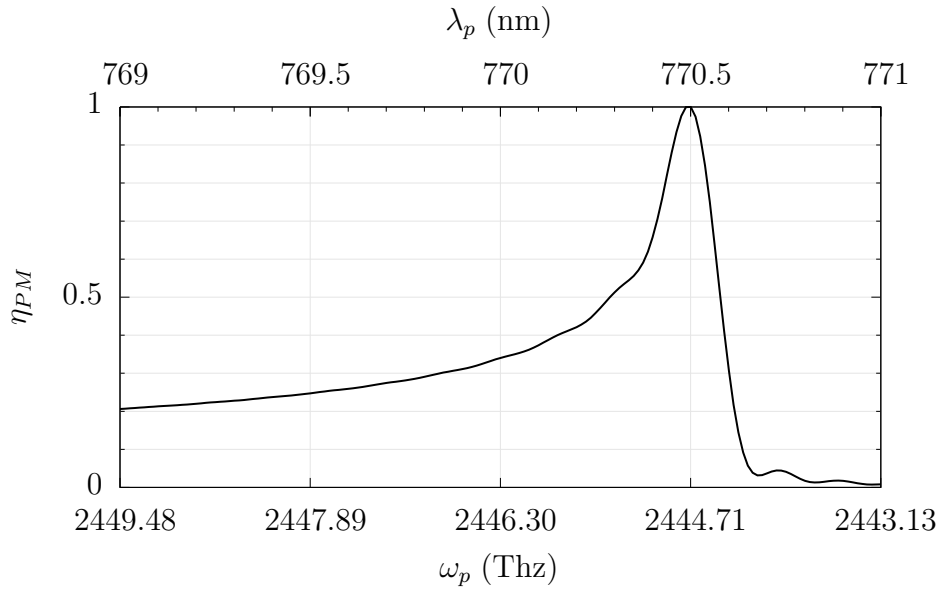

Figure 3.1 – SPDC efficiency according to the source phase matching function, under a CW monochromatic pump regime and neglecting the source cavity effect.

value of the pump frequency presented in equation (2.20), for which the modal birefringence mismatch is equal to zero.

When we use pump frequencies higher than the optimal frequency $\overline{\omega}_p$ ($\omega_p >$ 2444.71THz, left part in figure (3.1)), the efficiency decreases slowly, reducing to one half for $\Delta\omega_p = 0.79$THz ($\Delta\lambda_p = -0.25$nm) and to one fourth for $\Delta\omega_p = 1.91$THz ($\Delta\lambda_p = -0.6$nm). In this frequency region, the mismatch induced by modal birefringence is counter-balanced by the mismatch related to the normal chromatic dispersion.

On the contrary, at pump frequencies shorter than $\overline{\omega}_p$ ($\omega_p <$ 2444.71THz, right part in figure (3.1)), modal birefringence and chromatic dispersion contributions to the mismatch are negative, so the efficiency decreases very rapidly to zero and there are no frequency states available to the photons pairs.

3.2 Setup

Figure (3.2) illustrates the experimental setup used to generate, collect and detect photon pairs.

A CW diode laser (TOPTICA$^{\text{TM}}$ Photonics DL pro 780) provides a tunable monochromatic pump beam within the frequency range of $\omega_p = [2462, 2340]$THz ($\lambda_p = [765, 805]$nm), with a linewidth $\Delta\nu_p \sim 100$kHz. A small fraction of the pump beam is sent to an Optical Spectrum Analyzer (OSA, Yokogawa$^{\text{TM}}$ AQ6370C) to monitor its wavelength with a precision of $\pm$10pm. The main fraction of the beam is sent on a in-house made holographic mask (HM). The mask grating is designed to convert an incoming Gaussian beam into a Bragg mode matching the spatial distribution shown in figure (1.4). The mask acts on the first order diffraction, so higher order modes are filtered out.

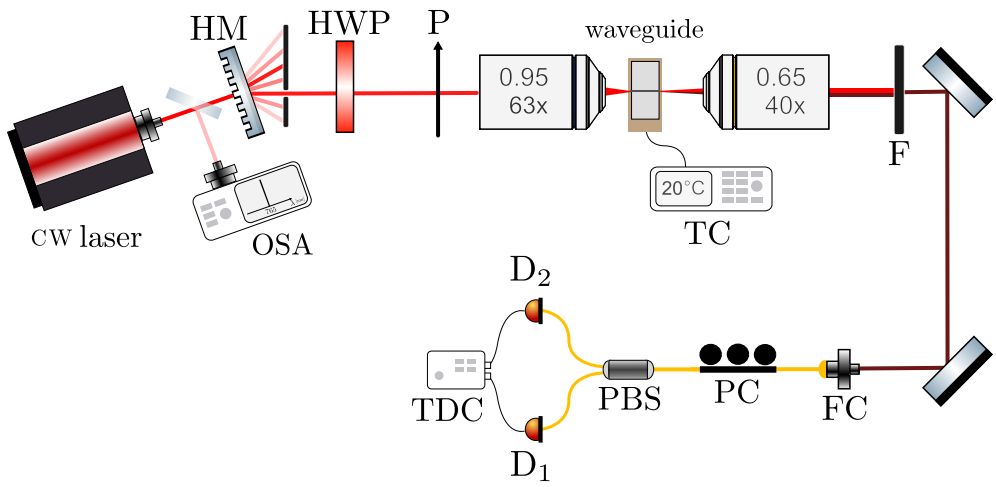

Figure 3.2 – Sketch of the experimental setup for the HOM interference. OSA: optical spectrum analyzer, HM: holographic mask, HWP: half-wave plate, P: polarizer, TC: temperature controller, F: low-pass filter, FC: fiber coupler, PC: polarization controller, PBS: polarising beam splitter, D_1,D_2: single-photon detectors, TDC: time-to-digital converter.

A polarizer (P) sets the polarization of the pump beam to the horizontal direction (H-polarized or TE). A half-wave plate (HWP) is placed before the polarizer to finely control the pump power. The coupling of the pump beam into the waveguide is achieved through a microscope objective having a high numerical aperture (NA), compatible with the high-diffracting Bragg beam (NA=0.95, 63X) [144]. A thermocouple and a Peltier cooler, connected to a PID controller, monitor and keep the waveguide temperature constant at 20°C. If not otherwise stated, we perform all the experiments presented in this thesis at this temperature.

The output coupling is achieved via a second microscope objective (NA=0.65, 40X). A frequency low-pass filter blocks the emitted pump beam, while the photon pairs are coupled in the fibered part of the setup through a fiber coupler (FC). Photons are separated by a polarizing beam splitter (PBS) and sent to single-photon detectors (D). A polarization controller (PC) is used to align photons polarization axis with the ones of the PBS. Our two single-photon detectors are free-running InGaAs/InP avalanche photodiodes (idQuantique^{TM} ID230). Each detector efficiency is set to 25% and dead time to 25µs. A time-to-digital converter (TDC, QuTau^{TM} QuTools) measures the time differences between the detection events of each detector in a start and stop configuration.

3.3 Characterization of the two-photon emission

To evaluate the performance of AlGaAs sources of photon pairs we consider two parameters:

- The detected net coincidence rate ($R_{c,net}$), the product of the Pair Production

Rate (PPR, the number of photon pairs emitted by the source per unit of time) and the setup transmission and detection efficiency for signal and idler photons (T_s, T_i):

$$R_{c,true} = \text{PPR}\ T_s\ T_i \approx \text{PPR}\ (T_s)^2 \tag{3.2}$$

The optics elements of our setup (figure (3.2)) have the following transmission and detection efficiency:

- The free space to fiber collection system, including the output microscope lens and the fiber coupler (FC), has a collection efficiency of approximately $T_s^{coupler} \approx 0.5$.
- The fibered setup consists in commercially available fibers (ThorLabs$^{\text{TM}}$ 780HP) of approximately 5m length. Their nominal attenuation at the telecom wavelength (4.0 dB/km, $9.2 \cdot 10^{-4}$/m) is negligible with respect to other optical elements in the setup. Yet, additional transmission losses arise at the interconnection among adjacent patch fiber cables. Typically, there are two interconnections along each signal and idler path, resulting in $T_s^{fibers} \approx 0.7$.
- Each detector registers only 25% of the incoming single photons (i.e. in a coincidence measurement one pair out of 16 are detected), so that $\eta_s^{detector} = 0.25$.

The resulting setup transmission and detection efficiency of a single photon is estimated to:

$$T_s = T_s^{collection}\ T_s^{fibers}\ \eta_s^{detector} = 8.7 \cdot 10^{-2} \tag{3.3}$$

and the net coincidence rate is given by:

$$R_{c,net} = \text{PPR}\ (T_s^{collection}\ T_s^{fibers}\ \eta_s^{detector})^2 = \text{PPR} \cdot 7.7 \cdot 10^{-3} \tag{3.4}$$

- The Coincidence-to-Accidental Ratio (CAR), a signal-to-noise figure of merit defined as the ratio of true coincidences (i.e. coincidences due to photon pairs) versus undesired accidental coincidences (i.e. coincidences due to uncorrelated events). In terms of coincidences rates, the CAR reads:

$$\text{CAR} = \frac{R_{c,net}}{R_{acc}} = \frac{R_c - R_{acc}}{R_{acc}} \tag{3.5}$$

We explore a pump power regime where the generation of multiple pairs, originating from the superpoissonian statistic of SPDC, can be neglected. Thus accidental coincidences are detected when:

1. Each detector registers a dark count.

2. Each detector registers a photon not originating from SPDC. As instance, the two photons may originate from the background luminescence of AlGaAs sources [143].

3. One detector registers a photon originating from SPDC, while the other detector registers a dark-count or a photon originating from the background luminescence. This occurs when the complementary photon of the pair was lost, as it is absorbed during its propagation in the waveguide, not collected in the fibered setup, scattered at the fibers interconnections or not detected.

Since each detector (idQuantique^{TM} ID230) has a rate of dark counts of $d = 20$–25Hz, the probability that every second both detectors register a dark count is negligible compared to the typical coincidence rate signal ($R_{c,net} > 100$Hz, as shown in figure (3.3)). For this reason, we consider the accidental coincidences as given by the contributions (2) and (3).

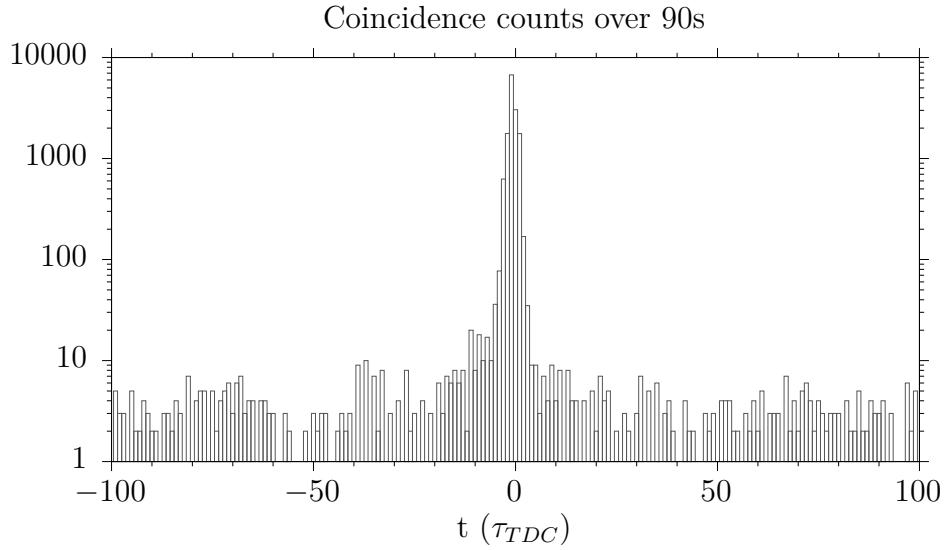

Figure 3.3 – Example of a coincidence measurement.
Sample: `ABQ71_C1_3_G2G12`.

In a coincidence measurement the main peak is given mostly by $R_{c,net}$ while signal in the remaining time bin correspond to R_{acc}.

Figure (3.3) is an example of a coincidence measurement, carried out on the sample `ABQ71_C1_3_G2G12`, for an input pump power of 15mW, a pump wavelength of $\lambda_p = 764.55$nm and an integration time of 90s. The electronic delay between the two detectors is set to zero at the coincidences peak and expressed in unit of the TDC sampling resolution ($\tau_{TDC} = 81$ps).

Within the peak, we count 14271 raw coincidences. Out of the peak, we count 366 accidental coincidences over a range of $\Delta\tau_{noise} = 94\tau_{TDC}$, corresponding to approximately 35 accidental coincidences within the peak. Therefore net and

accidental coincidence rates are given by:

$$\begin{aligned} R_{c,net} &= (14271 - 35)/90\text{s} = 158\text{Hz} \\ R_{acc} &= 35/90\text{s} = 0.4\text{Hz} \end{aligned} \tag{3.6}$$

and the corresponding CAR:

$$\text{CAR} = R_{c,net}/R_{acc} = 395 \tag{3.7}$$

Effect of pump beam shaping

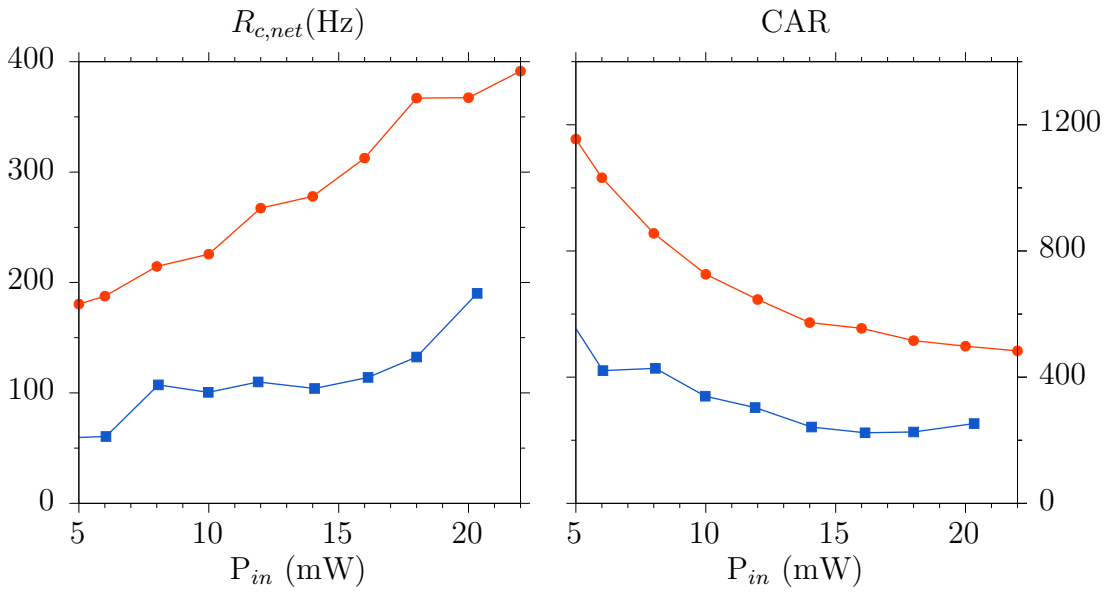

Figure 3.4 – Source performances as a function of the pump power when a holographic mask shapes the pump beam into a Bragg mode (red dots) and in the absence of mask (blue squares).
Sample: `ABQ71_C1_3_G2G12`.

Our source works using a modal phase matching scheme based on a pump Bragg mode (see figure (1.4)). The coupling of the free space pump beam into the Bragg mode supported by the waveguide is fundamental for an efficient SPDC process (otherwise the SPDC overlap integral defined in equation (1.1) would be zero). The excitation of the waveguide Bragg mode can be enhanced by shaping the free space Gaussian pump beam into a Bragg mode. For this scope, a previous post-doc of our group designed a holographic mask which converts an input Gaussian beam into a Bragg mode.

In order to estimate the efficiency of the holographic mask to shape the pump beam into a Bragg mode, we perform a comparative study. In figure (3.4) we present experimental results of $R_{c,net}$ and CAR measurements as a function of the injected pump power (P_{in}), in the presence (red) and absence (blue) of the holographic mask.

P_{in} is measured by means of a powermeter placed just before the waveguide input facet (after the polarizer P in the scheme of figure (3.2)). In this measurement, performed by the master student Félicien Appas, the pump wavelength is set to 764.66nm, the source temperature to 20° and the acquisition time to 30s.

We observe that both R_c and CAR increase by approximately a factor of two when the mask is used. We conclude that by using the mask the power of the pump beam that couples into the waveguide Bragg mode doubles and so it does the efficiency of the SPDC process. The following measurements are carried out in the presence of the holographic mask.

Pump power dependence

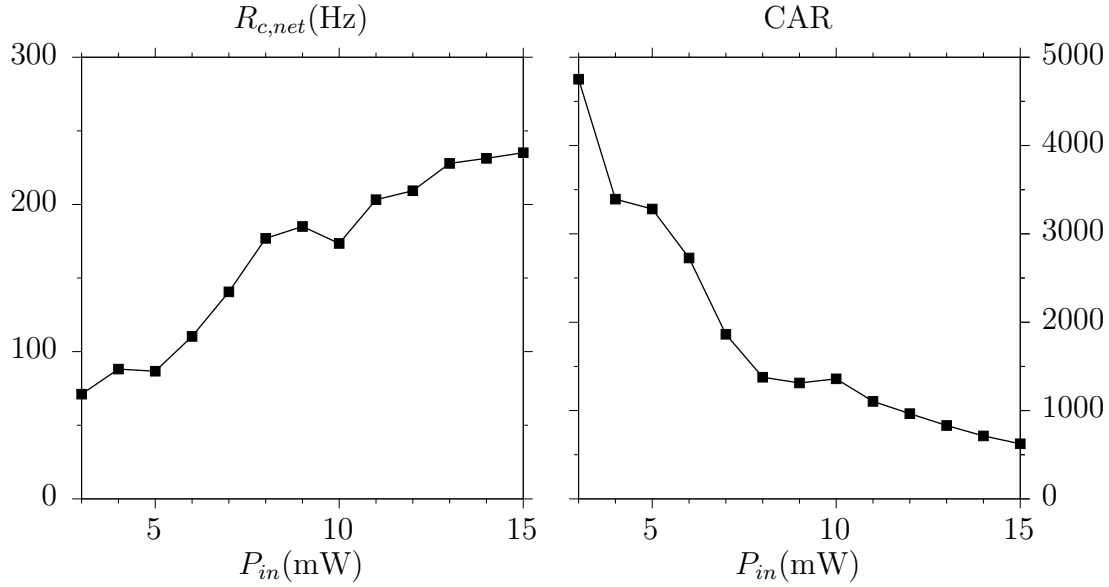

Figure 3.5 – Source performances as a function of the pump power.
Sample: `ABQ71_C1_2_G2G12`.

Figure (3.5) reports the measured $R_{c,net}$ and CAR as a function of P_{in} using the sample `ABQ71_C1_2_G2G12`. The pump wavelength is set to 764.575nm, the waveguide temperature to 20°C and the integration time to 30s per acquisition point. We see that $R_{c,net}$ is proportional to P_{in}, in agreement with SPDC equations (i.e. the rate of produced photon pair is linear up to a saturation to the integral over signal and idler frequencies of the squared norm of the JSA, reported in equation (1.18)). Conversely, the CAR is inveresly proportional to P_{in}. This behavior is understood since R_{acc} is proportional to P_{in}^2 [168] .

Pump frequency dependence

We proceed by measuring $R_{c,net}$ and CAR as a function of the pump wavelength (λ_p). We use an integration time of 30s per acquisition and a constant input pump power at 15mW. This measurement was carried out with the master student Giulia Sinnl and is shown in figure (3.6) .

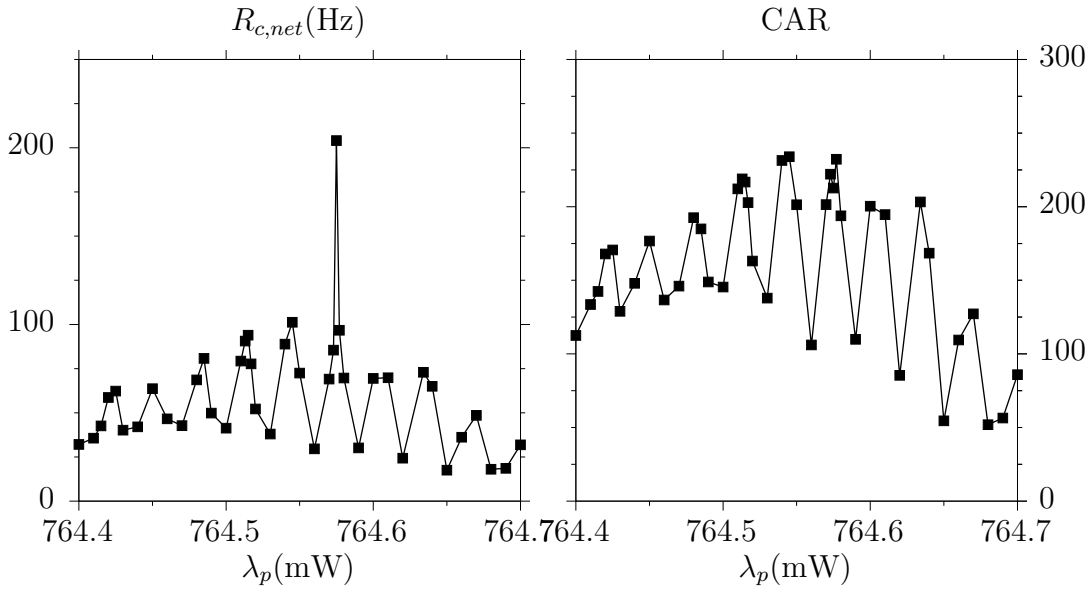

Figure 3.6 – Source performances as a function of the pump power.
Sample: `ABQ71_C1_2_G2G12`.

As λ_p increases, $R_{c,net}$ and CAR follow a fast oscillatory trend within a slow asymmetric envelope. The fast oscillatory trend is a sign of a Fabry-Perot interference. We measure an average oscillation period of $\Delta\lambda_p = 39$pm, which corresponds to the free spectral range of the pump photons ($\Delta\omega_p = 20$GHz at 764.5nm). We deduce that the fast oscillations are due to the waveguide cavity effect on the pump photons: as the wavelength of the monochromatic pump beam changes, the amount of the pump power that couples in the waveguide (cavity) varies due to the Fabry-Perot effect. The optimal pump wavelength which gives the maximum point of $R_{c,net}$ may be due to a favorable interplay between pump, signal and idler Fabry-Perot resonances.

Temperature dependence

In figure (3.7) we present the measurement of $R_{c,net}$ and CAR as a function of the source temperature (T), for a constant pump power of 15mW. The pump wavelength is set to 764.503nm and the integration time to 20s per acquisition.

Both $R_{c,net}$ and CAR present an oscillatory behavior with respect to T, further confirming the waveguide cavity effect observed in the previous measurements: as the temperature changes, the waveguide (cavity) optical length varies with the Fabry-Perot resonances of signal, idler and pump photons.

Besides, $R_{c,net}$ and CAR are two envelopes centered around approximately 19.5°. The reason is that for lower and higher values of the source temperature the modes effective index change and the phase matching condition is no longer satisfied.

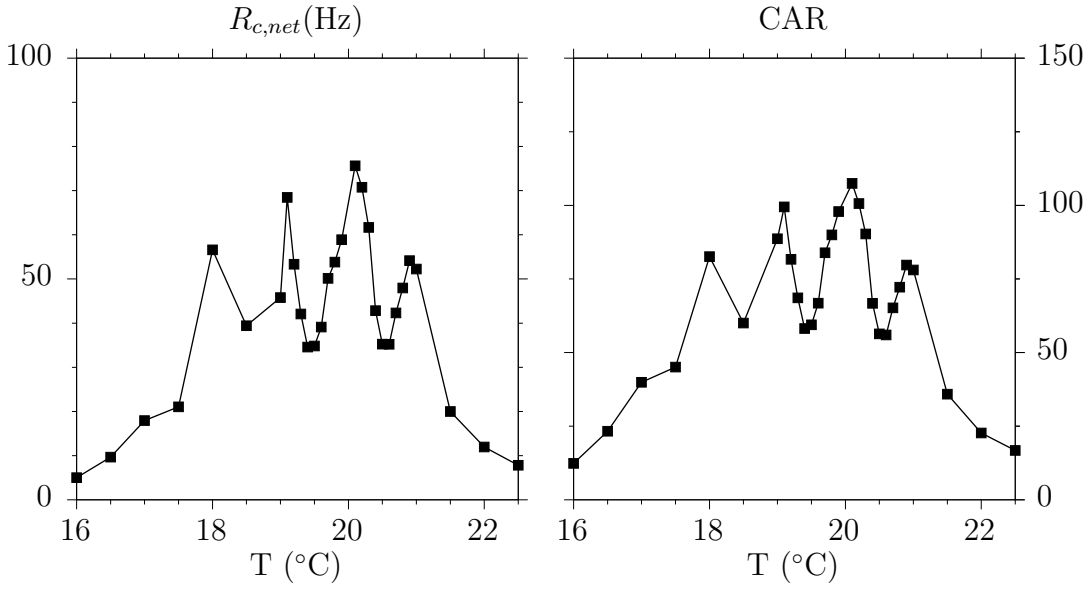

Figure 3.7 – Source performances as a function of its temperature.
Sample: `ABQ71_C1_3_G2G12`.

Chapter 4

Development of a dry etching process and application to an electrically driven source

In this chapter we present the development and optimization of a clean room process based on electron beam lithography and inductive coupling plasma etching for the fabrication of AlGaAs waveguides. Contrary to previous fabrication processes based on photolithography and wet etching, this process is more robust and it leads to a higher spatial resolution. Thanks to the optimization work presented in this chapter, we can fabricate vertically etched waveguides with a roughness in the order of 10nm for an etching depth of 2μm. The robustness and control offered by this processing protocol has been exploited to fabricate AlGaAs devices for SAM/OAM manipulation, presented in chapters (7) and (8), and start the development of dry etched electrical driven sources, presented at the end of this chapter.

4.1 Motivation

The realization of passive and active integrated optical devices with well-controlled functionalities, characterized by a high aspect-ratio and many parallel sub-components (e.g. waveguide arrays), requires a robust clean room process able to precisely control the shapes of the waveguides.

In the previous works of our group [58, 169, 160], a clean room process based on photolithography (PL) employing ma-N 2405 resist and chemical wet etching was used to fabricate AlGaAs sources of entangled photons. The combination of PL and wet etching provides a fast fabrication process, thanks to the parallel illumination of the chip offered by the PL technique.

Yet, due to the use of wet etching, this process is not robust.

Firstly, the isotropic nature of wet etching leads to waveguides having decaying exponential edges. Due to this shape, it may not be straightforward to use wet etching in the fabrication of more complex photonic circuits (e.g. evanescent couplers, multi-layered circuits, etc.).

Moreover, wet etching process depends strongly on the solvent viscosity and on the soaking speed and orientation. Therefore during the soaking of one sample (having a typical size of 1cm × 1cm), depending on the different zones of its surfaces, the etching efficiency and the shape of the fabricated waveguides can vary.

For the same reason, the same design is hard to be reproduced among wet etching processes performed in different times or by different clean room users. Furthermore, the lack of control on the waveguide design leads to an incertitude about the geometrically induced birefringence. This parameters needs to be controlled and minimized to generate a biphoton state with well controlled frequency correlations, as we have presented in the JSA chapter.

To overtake such limitations, we have optimized a new fabrication process based on electron beam lithography (EBL) and inductively coupled plasma etching (ICP). EBL permits to draw on the resist waveguides with a high lateral resolution, according to the low electrons diffraction-limit. ICP anisotropic etching allows to obtain vertically shaped ridge waveguides over the typical size of our chip (1cm × 1cm).

4.2 Fabrication: background

4.2.1 Electron beam lithography

Electron beam lithography (EBL) is a high-resolution and direct-write exposure method.

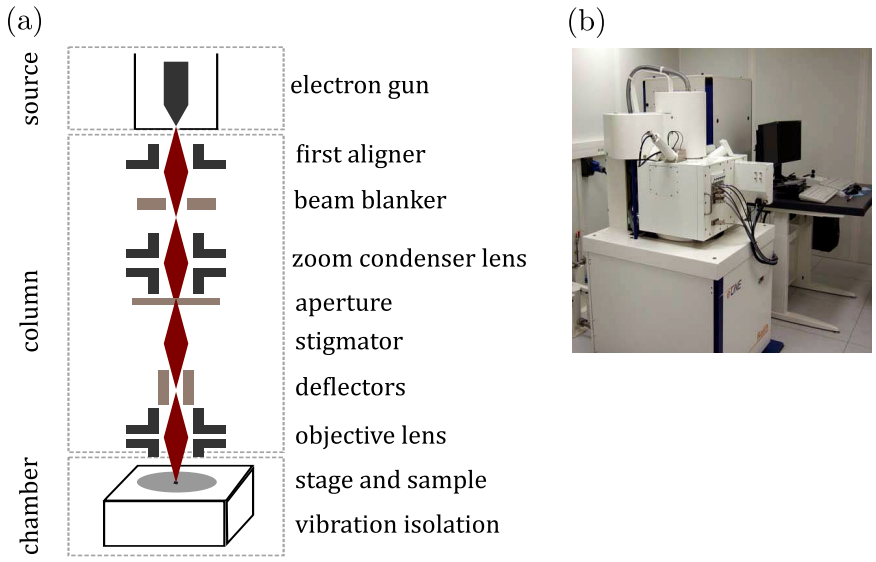

Figure 4.1 – EBL system.
(a) Scheme of a typical one.
(b) EBL system used for the fabrication of the devices presented in this thesis.

Figure (4.1, a) illustrates the fundamental parts of an EBL machine. Electrons are generated by a source kept under vacuum ($p \approx 2 \cdot 10^{-9}$mbar), named electron

gun. They are guided towards the sample through an electron optical system: a beam aligner, condenser lenses, a stigmator, a pair of deflectors and an objective lens direct, shape and focus the electron beam on the sample. In addition, there is a beam blanker to quickly deflect the beam, in order to avoid undesired exposure of the sample. Inside another chamber under vacuum ($p \approx 2 \cdot 10^{-5}$mbar), a mechanical stage holds the sample and positions it with respect to the electron beam. A vibration isolation system is necessary to maintain the alignment between the beam and stage constant during the exposure, while the whole EBL equipment is controlled through a computer. More details about the EBL single components are given in [170, 171]

In this work, we use the Raith eLine lithography system of the Ecole Normale Superiore clean room in Paris, shown in figure (4.1, b).

EBL high-resolution feature derives form the small wavelength associated to electrons. According to de Broglie expression ($\lambda = h/\sqrt{2mK}$, with $K = eV$ the kinetic energy proportional to the applied electrical potential V), in an electrical potential difference of $V = 10$kV, an electron's wavelength is only 0.12Å, several order of magnitude smaller than a photon's wavelength in UV lithography (typically 100 to 400nm). Yet, in EBL there are other phenomena that reduce the resolution. Firstly, the electron beam column has a limited minimum spot size due to the repulsion forces among electrons. Moreover, during the exposure, both inelastic (forward) and elastic (backward) scattering events occur while electrons penetrate the resist and the underlying material.

In inelastic scattering, an electron interacts with the external shield of an atom. In the resist, inelastic scattering ionizes the atom, inducing chain scission (in the case of positive resit) or cross-linking (in the case of negative resist). Besides, it generates additional electrons, which, in turn, have enough energy to contribute to the resist exposure (chain scission or cross-linking) process. These electrons, named secondary electrons, overwhelm in number the beam primary electrons, and thus are the major cause of the resist exposure.

On the other hand, in a backscattering event, an electron reflects from the heavy nucleus of an atom, conserving its kinetic energy. When backscattering events occur in the substrate, electrons return back to the resist. Due to the combination of elastic and inelastic events, electrons propagate in the resist for some micrometers before loosing their energy. As instance, for an exposure of ma-N resist that makes use of a 10kV acceleration potential, an electron has a free path of at least 10µm.

As a result of backscattering, secondary electrons expose resist area far from the position of the incident beam. This undesired side effect, called proximity effect, is the main limitation for EBL resolution. Since the free path of elastically reflected electrons decreases with their energy and increase with resist thickness, the proximity effect is reduced for thin resist and high-energy exposures.

Concerning the exposure method, EBL uses a sequential pixel-by-pixel writing. In analogy to a pencil that draws on a paper, a tightly focused electron beam scans the surface of the sample covered by the resit. Therefore, the exposure

pattern can be changed at every lithography without the need of a different mask, as in PL. Yet, the offered versatility is counter-balanced by a slow speed (0.0001-1.0 cm^2/s, depending on the desired resolution [172]). For this reason, EBL is not used for industry high volume lithographic processes and it is mainly adopted for prototyping in academic or industrial research.

4.2.2 Inductively coupled plasma etching

Inductively Coupled Plasma (ICP) is a dry etching technique based on Reactive Ion Etching (RIE), which uses reactive ions to etch material from a piece of wafer. The etching is mostly physical: as ions bombards the wafer, they destroy its crystalline lattice by transferring their high kinetic energy. At the second order, the etching is also chemical as chemical reactions occur when the different kinds of ions touch the wafer surface, changing its electrical properties and mechanical resistance.

The advantage of ICP with respect to RIE is that the generation of plasma and its acceleration are two decoupled processes. The plasma is created by a source of magnetic field controlled via a RF signal at 2MHz. Thus it is accelerated by a DC field towards the sample to be etched. ICP plasma is more dissociated into ions free atoms and radicals than RIE plasma. A faster etching is possible at lower plasma pressure and a lower ion bombarding energy is required.

We carry out ICP etching by using a Sentech SI500 machine and $SiCl_4$ chemistry. The ICP procedure consists in three steps: cleaning of the chamber, conditioning and etching. A cleaning by nitrogen purging assures that the chamber is free from contaminants or etching species deriving from previous etching processing. The conditioning lasts for about 15 minutes to stabilize the plasma source and the RF signal and fill the chamber with the desired etching species. The etching is constantly monitored by means of an interferometer laser, which points onto the sample surface, nearby a waveguide ridge. A visible red laser light is sent onto the sample surface; part of the light is reflected at the sample GaAs surface, while part travels within the sample until is reflected at the first GaAs-AlGaAs interface. As these two signals superimpose, they give raise to either positive or destructive interference, depending on thickness of the inner layer. A sudden drop in the interferometer signal occurs when an entire layer of GaAs is completely etched. By counting the number of drops in the interference signal, we are able to know the etching depth and we manually stop the etching when desired. We measure the etched depth via a profilometer (Dektak 150) and analyze the quality of the etching by observing the sample at the scanning electron microscope.

4.3 Fabrication: optimization

4.3.1 Steps

Figure (4.2) shows the fabrication steps of EBL and ICP etching. After cleaving a piece of wafer of about $1cm^2$, we follow the following steps:

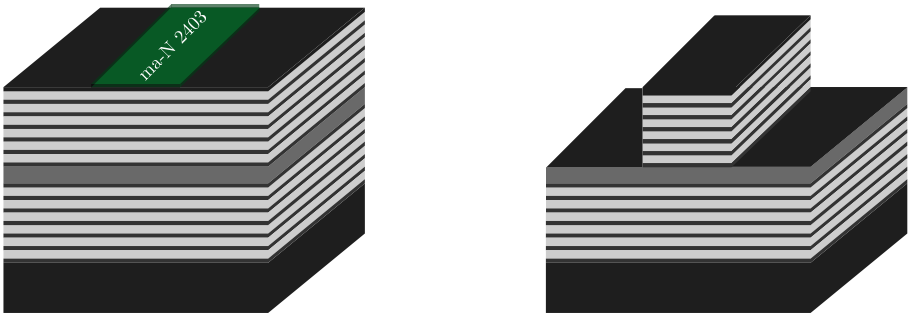

(1) Resist spinning, lithography and developing

(2) ICP etching

Figure 4.2 – Sketch of the fabrication process.

1. Spin coating of the negative resist ma-N 2403. The deposition parameters are given in table (4.1). By performing an optical or electrical lithography, followed by the development of the exposed area, we draw an ensemble of resist-made waveguides (the green stripe).

ma-N 2403 resist deposition	
hard baking	T= 120°C for t= 4 min
waiting time	t= 30s
TI-prime adhesion promoter	v_{spin} = 6000rpm, t_{spin} = 30s, t_{ramp} = 3s
ma-N 2403	v_{spin} = 3000rpm, t_{spin} = 30s, t_{ramp} = 3s
soft baking	T= 90°C for t= 1 min

Table 4.1 – ma-N 2403 resist deposition parameters.

2. ICP etching to obtain ridge waveguides. We only etch the top Bragg mirror and do not etch the waveguide core in order to avoid additional roughness and defects at the surface of the active region, which would lead to unwanted electron-hole recombination in active devices.

4.3.2 Resist

In this process, we choose to use the negative resist ma-N 2403 [173]. The last two digits indicate, in micrometers, the expected thickness of the resist after its spinning on the sample, according to the spin-coating parameters given in table (4.1). The thickness to be deposited depends on the processed material (e.g. AlGaAs, Si, etc.) and desired etching depth.

Table (4.2) reports thicknesses and pattern resolutions offered by ma-N series resists. We notice that, as the resist thickness increases, its patterning resolution decreases. The resist ma-N 2403 gives the best compromise between resolution (50nm) and thickness (0.3µm). As instance, for the fabrication of dry AlGaAs electrical injected sources, we need to etch slightly less than 2.5µm of AlGaAs. If we use the ICP etching processes developed in our clean room, ma-N resists etch

Resist label (ma-N)	2401	2403	2405	2410
Film thickness (μm)	0.1	0.3	0.5	1.0
EBL pattern resolution (nm)	<50	50	100	150

Table 4.2 – Thickness and resolution of ma-N resists. In red color ma-N 2403 resist, used in the developed process.

approximately 10 times slower than AlGaAs (the precise value depending on the Al content and the ICP etching parameters), we cannot use ma-N 2401, which would be completely etched before the end of the etching process.

We note that previous works in our group used ma-N 2405 [169], whose resolution is two times worse than the one given by ma-N 2403. The reason is that these processes were developed for AlGaAs optical pumped sources, which require an etching depth slightly below 5μm and thus the resist ma-N 2405, 0.5μm thick.

4.3.3 Photolithography versus electron beam lithography

We start by comparing the two lithography processes, photo lithography (PL) and electron beam lithography (EBL), followed by the same ICP etching process. Both lithographies are carried out using the negative resist ma-N 2403, spin coated using the standard parameters presented in table (4.1). For PL, we use a hard contact configuration and ma-N 2403 under UV exposure. In EBL, we write the negative resist with a dose of 120μC/cm^2. Both developments are done using AZ® 726 MIF, a metal ion free developer. The ICP etching is based on a low-powerful slow recipe and $SiCL_4$ and Ar chemistry.

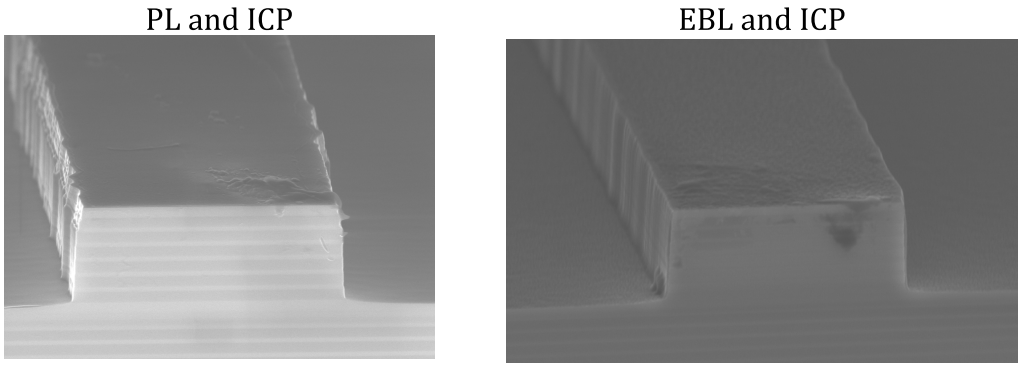

Figure 4.3 – SEM image of two waveguides fabricated using PL followed by ICP (left) and EBL followed by ICP (right).
PL sample: `D9T167_D6`.
EBL sample: `D9T167_G1`.

Figure (4.3) presents a SEM image of the two waveguides fabricated with the two processes, after removal of resist and cleaving. We are mostly interested in comparing the sidewalls roughness. From a SEM imaging we find that the waveguide fabricated via PL presents a peak-to-dip sidewalls roughness of approximately 150nm, while the one fabricated via EBL a peak-to-dip roughness smaller than

40nm. Given these preliminary results, we do not consider anymore the PL and ICP process and we proceed with the optimization of the EBL and ICP processes.

4.3.4 Electron beam lithography

To retrieve the optimal EBL parameters, we perform a dose test. We design a mask of 10 waveguides, 4µm wide, with increasing dose from 100µC/cm^2 to 190µC/cm^2. We set the electron beam aperture to 10µm, an acceleration voltage of 20kV and a writing field of 1mm. We measure at the Faraday cup an average current of 13.5pA, so we set up a night exposure which takes slightly less than 6 hours.

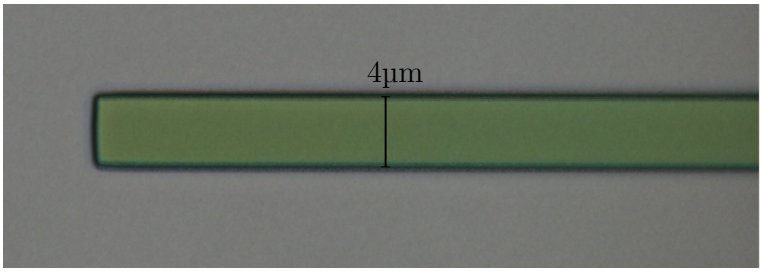

Figure 4.4 – Optical microscope image of the resist when the development is complete, for the lowest exposure dose of 100µC/cm^2.

As developer we use AZ® 726 MIF. After dipping the sample in the developer, we rinse it with water and dry it with nitrogen. By checking at the optical microscope the waveguides endings, we determine the required development time. In our case, we focus on the waveguide written at the lowest dose, since it takes the longest time to develop. As soon as the waveguide ending appears squared and sharp, the development is complete, as illustrated in figure (4.4). The waveguide width, measured by optical microscopy, is approximately 4µm, close to the expected value (within the optical microscopy diffraction-limited resolution). We find that the development consists in repeating twice the following steps: 10s in AZ® 726 MIF, 5s in H_20, 60s in another H_20 baker and N_2 drying.

Once the developer is removed, we cleave the sample into two pieces to test two different ICP recipes previously developed in our laboratory.

The first ICP recipe is based on low RF acceleration voltage and power ($V = 115V$, $P = 15W$), low plasma power ($20W$) and the etching species $SiCl_4$ and Ar. The second ICP recipe is uses higher RF voltage and power ($V = 180V$, $P = 60W$), twice as much plasma power ($40W$) and H_2 in addition to the previous etching species.

We measure an etching rate (time) of 1µm/18.2 min (57 min) for the first recipe and 1µm/7.5 min (23 min) for the second one. Thus in the following we refer to the first recipe as slow recipe and to the second one as fast recipe.

The comparison between the two ICP processes as a function of the employed dose is shown in figure (4.5). In the case of fast ICP processing (4.5, a), we observe an important and unacceptable roughness.

The reason is that, in this case, the resist is completely removed before the end of the fast ICP etching process. The uncovered waveguide edges are hit along

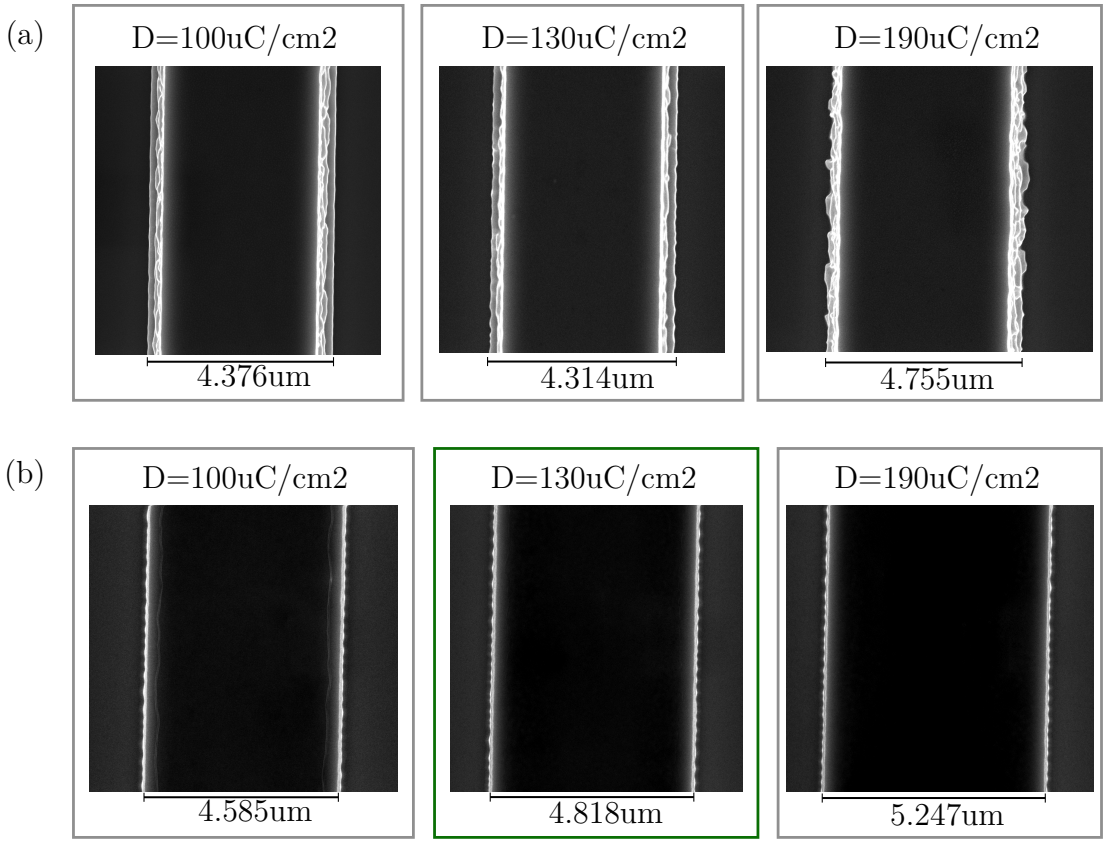

Figure 4.5 – SEM images of waveguides fabricated using the fast (a) and slow (b) ICP recipe for different values of dose D.
(a) Sample: `D9T167_C1_2`.
(b) Sample: `D9T167_C1_1`.

the vertical direction by the accelerated plasma ions and the waveguide sidewalls become very rough.

The slow ICP process (4.5, b) assures a better result. As figure (4.11) shows, less energetic ions do not completely remove the resist at the waveguide borders, even if a "roof effect" is still visible. To quantify the roughness level and identify the optimal dose, we analyze the top-view SEM images of figure (4.5, b) via ImageJ using Analyze Stripes plugin [174, 175]. We extract the waveguide left and right edges profiles (the oscillatory white borders in figure (4.5, b)) as curved lines. Then we calculate the roughness as the lines standard deviation versus straight and correctly oriented lines. We find that the waveguide fabricated with a dose of $130\mu C/cm^2$ has the lowest roughness of $\sigma = 7.2$nm. The other two waveguides shown in figure (4.5, b) have a standard deviation of $\sigma = 8.0$nm for $D = 100\mu C/cm^2$ and of $\sigma = 18.7$nm for $D = 190\mu C/cm^2$. We conclude that the optimal recipe is EBL with a dose of $130\mu C/cm^2$ combined with the slow ICP recipe.

4.4 Application to an electrically driven source of entangled photons

4.4.1 Wet etched source

An electrically driven AlGaAs source of entangled photon pairs has been previously designed, fabricated and demonstrated by our group [58, 59].

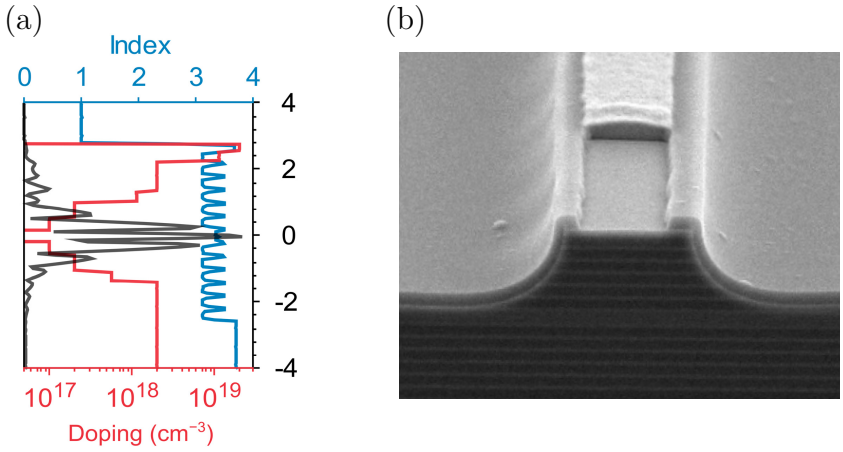

Figure 4.6 – Electrically driven source of entangled photons (from ref. [59]).
(a) Material refractive index, doping profile and Bragg mode distribution along the waveguide central vertical axis.
(b) MEB image of the waveguide facet.

The design of the structure (figure (4.6, a)) is similar to that of conventional quantum well laser diodes, except for the lasing mode which is a Bragg mode. The fabrication process used to fabricate the devices presented in [58, 59] is based on PL, using ma-N 2405 negative resist, and wet etching, as we can deduce from the exponential sidewalls edges visible of figure (4.6, b).

Figure (4.7) presents some numerical simulations done on the wet etched source, before the deposition of upper and lower electrical contacts, showing (a) the input facet refractive index profile at 775nm and (b) the calculated Bragg mode intensity. We notice that, due to the exponential sidewalls induced by wet etching, the Bragg mode has an horizontal extension of about 10µm.

From these numerical simulations, we calculate the overlap integral between the Bragg mode and the quantum well, situated in the middle of the core region and having a thickness of 8.5nm. We find $\Gamma = 2.45\%$. By propagating the Bragg mode in proximity of a waveguide facet using a 3D FDTD commercial solver, we also calculate that it has a modal reflectivity of $R = 0.86$.

Starting from these results, we numerically calculate the carrier transport and recombination in the hetero-junction by using a home-made software based on a self-consistent model of the drift-diffusion and Poisson equations. The chosen parameters are a quantum well radiative recombination coefficient of

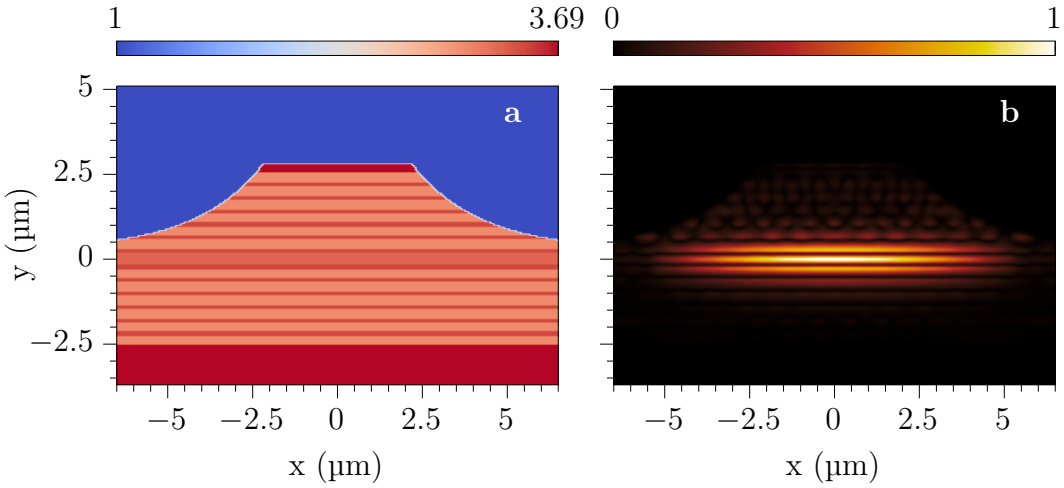

Figure 4.7 – Numerical simulations on a wet etched active waveguide.
(a) Geometry and refractive index profile.
(b) Bragg mode intensity profile at 775nm.

$R^{rad} = 5 \times 10^{-17} m^3 s^{-1}$ and a Shockley-Read-Hall non-radiative time of $\tau^{SRH} = 5$ns [176].

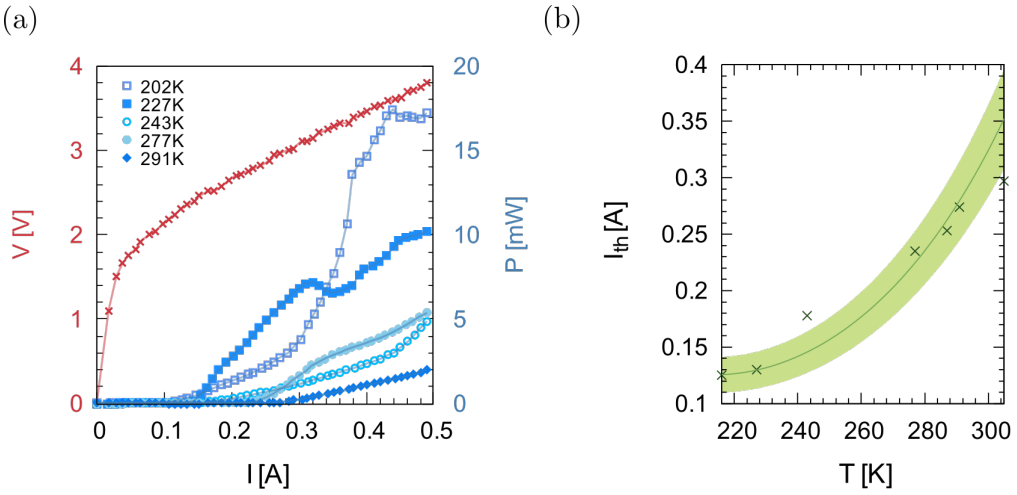

Figure 4.8 – Characterization and simulation of the electricall driven wet etched waveguide lasing operation (from ref. [59]).
(a) Voltage bias (crosses) and emitted power versus injected current.
(b) Measured (crossed) and calculated (continuous line) threshold current as a function of the temperature.

The characterization of the lasing emission under electrical pumping of a representative wet etched waveguide is shown in figure (4.8). Panel (a) reports the power-current-voltage (PIV) curves, measured under pulsed electrical injection for a pulse duration of 60ns and a repetition rate of 40kHz.

Panel (b) reports the lasing threshold current (I_{th}) as a function of the temperature. The measured values (green crosses) are in agreement with our

numerical calculations (continuous dark green line), carried out at different values of temperature. The uncertainty on the simulated I_{th} (light green stripe) comes from the uncertainty on the device contact geometrical surface (the product of the top contact width and the length of the waveguide), estimated to be $S = 1.9(\pm 0.2) \times 10^{-4}\text{cm}^2$.

4.4.2 Dry etched source

In this section we present our results on the application of the new processing technique applied to active samples having the same nominal epitaxial structure of the one used in [58, 59].

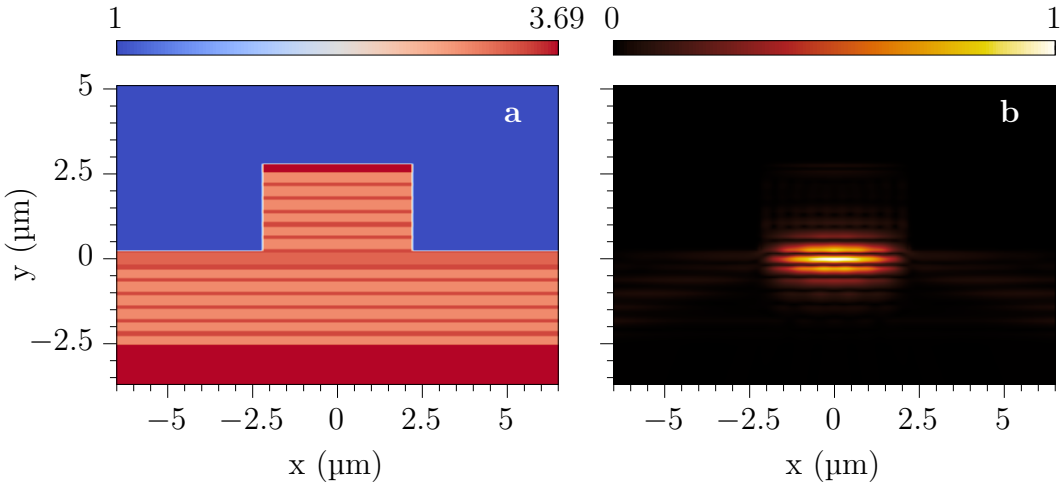

Figure 4.9 – Numerical simulation for a dry etched electrically driven source.
(a) Geometry and refractive index profile.
(b) Bragg mode intensity profile at 775nm.

The goal is to obtain an electrically driven waveguide having a vertically etched ridge. Figure (4.9, a) represents the refractive index profile and the desired shape, before the deposition of the electrical contacts. The etching must be performed down to the last layer of the top Bragg mirror and the ridge width set to approximately 5µm, in order to compare the dry etching processing with the previously developed wet etching process, whose corresponding waveguides are shown in figure (4.7, a).

We notice in inset (b) that, in comparison with the wet etched waveguide (4.7, b), the Bragg mode profile is more confined under the ridge.

Fabrication

The necessary fabrication steps are sketched in figure (4.10). After EBL (1) and ICP etching (2), we observe the waveguide at the SEM to check that there are no fabrication issues, that the etching depth is correct and the roughness acceptable.

Figure (4.11) shows a zoom of an ending of one etched waveguide (we note that the waveguide ending is rounded due to EBL proximity effect; after cleaving, the waveguide ridge is rectangular).

We can distinguish the individual layers of the top Bragg mirror: low refractive index layers (dark grey) and high refractive index layers (light grey). We confirm that we have etched almost completely the top Bragg mirror. We stopped the etching in the last low refractive index (the number 6 from the top, see figure (4.9)), placed just above the thin high index layer and the core. The waveguide roughness

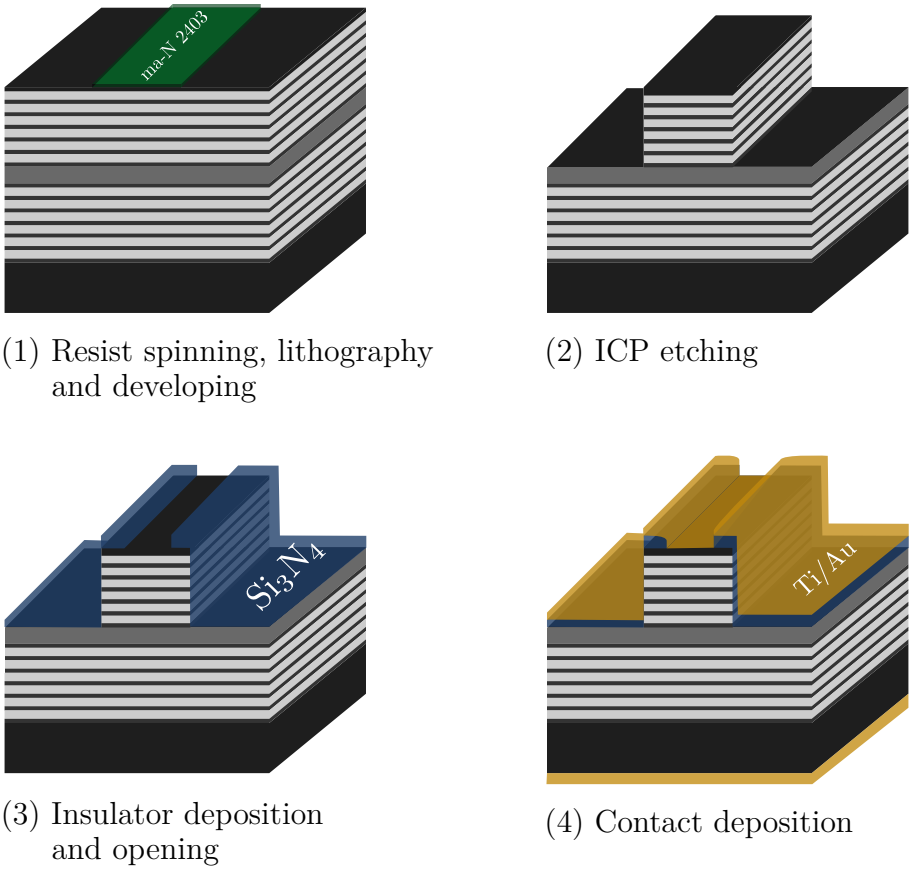

(1) Resist spinning, lithography and developing

(2) ICP etching

(3) Insulator deposition and opening

(4) Contact deposition

Figure 4.10 – Sketch of the fabrication process of a dry electrically driven active sample.

is in the tolerance and the resist, still present at the top of the waveguide, has covered the underlying sample during the whole etching process.

We continue the fabrication process with the deposition of the upper and lower electrical contacts. The necessary steps are:

3. Deposition of an insulator layer of Si_3N_4, followed by an optical lithography and reactive-ion etching (RIE) to leave an opening for the upper contact around the waveguide central axis.

4. Evaporation of a Ti/Au (10nm/400nm) upper contact and a Ge/Au/Ni/Au (15nm/50nm/10nm/200nm) bottom contact. To achieve homogeneous contacts and deposit on the waveguide sidewalls, during the evaporation the sample is continuously turned and titled at 40°.

Figure (4.12) shows one of the fabricated waveguide, after the steps (3), (4) presented in figure (4.10) and the cleaving of the input and output waveguide facets. We can distinguish the top and bottom Bragg mirrors and the top electrode on the waveguide ridge. The top Bragg mirror is completely etched and the ridge width is approximately 5µm.

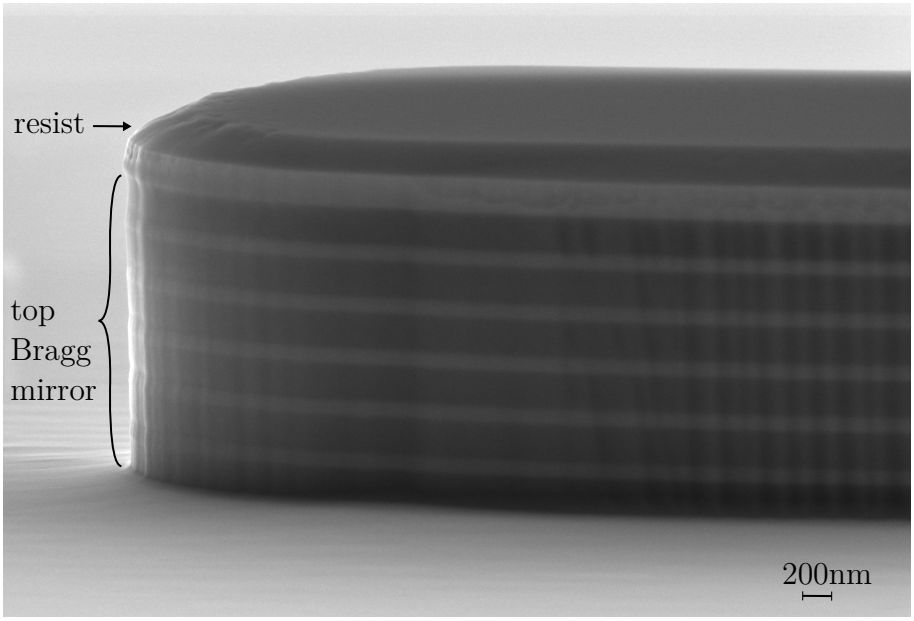

Figure 4.11 – Ending of a waveguide after step (2) of figure (4.10), processed using the developed fabrication process (D=130μC/cm^2, slow ICP recipe). Sample: `H1Y021_D2_2`.

4.4.3 Characterization

Voltage and optical power versus intensity

To evaluate the performance of the fabricated source (sample `H1Y021_D1`), we measure the voltage and emitted optical power as a function of the injected current. We set the holder heat-sink temperature to 20°C and apply a pulse duration of 200ns with a a repetition rate of 50kHz. The voltage-current curve (red squares, figure (4.13), left) presents a turn-on voltage of $V = 1.94V$. This value is close to the quantum well band-gap ($\approx$ 1.59eV). In accordance with standard diodes, the voltage-current curve is logarithmic at small forward bias. Yet, for higher bias we do not observe any knee voltage, sign that the lasing threshold is not reached.

From the size of the top electrode ($A \approx 2\text{mm} \cdot 3\mu\text{m}$), we calculate the injected density current. Even at values of density current much higher than for typical laser diodes, we do not observe the lasing threshold.

Since the lasing process does not occur, the emitted optical power (black dot in figure (4.13), left) is not linear versus the injected current, but grows exponentially, as in the case of an electroluminescent luminescent device.

To confirm this, we have plotted the emitted optical power versus injected electrical power (figure (4.13), right). The optical power results to be linearly proportional to the injected electrical power, as in the case for luminescent emitters.

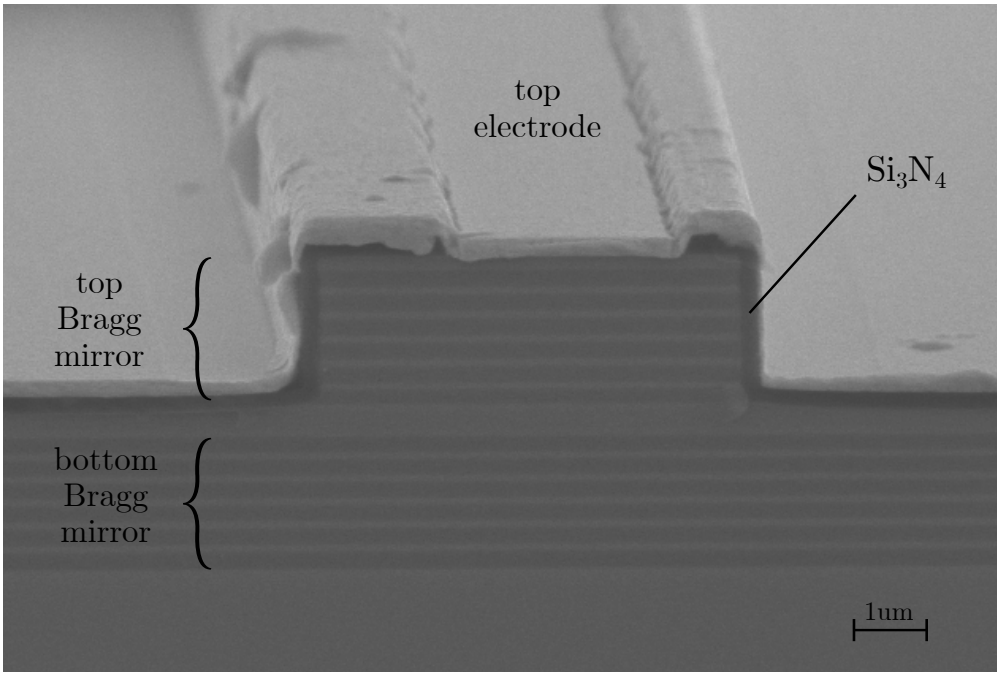

Figure 4.12 – SEM image of the facet of the fabricated dry etched source after all fabrication steps presented in figure (4.10) and cleaving. Sample: `H1Y021_D2_2`.

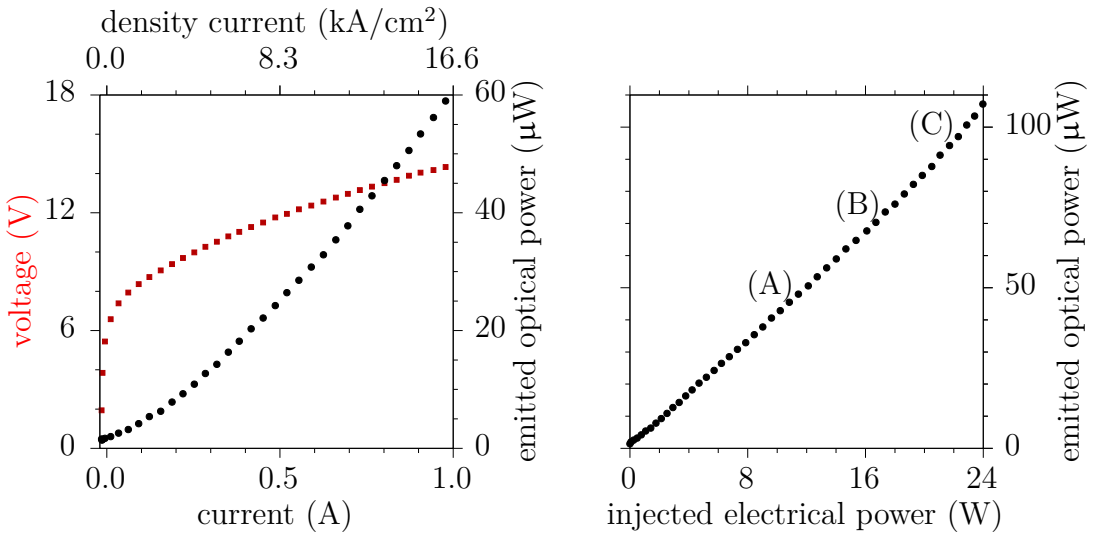

Figure 4.13 – Characterization of the voltage and optical power under electrical injection.
Left: voltage (red squares) and optical power (black dots) versus injected current.
Right: optical versus electrical power.
Sample: `H1Y021_D1`.

Voltage and optical power versus injected current as a function of temperature

The characterization of the the source at different temperature, carried out by the master student Ulysse Najar, is shown in figure (4.14).

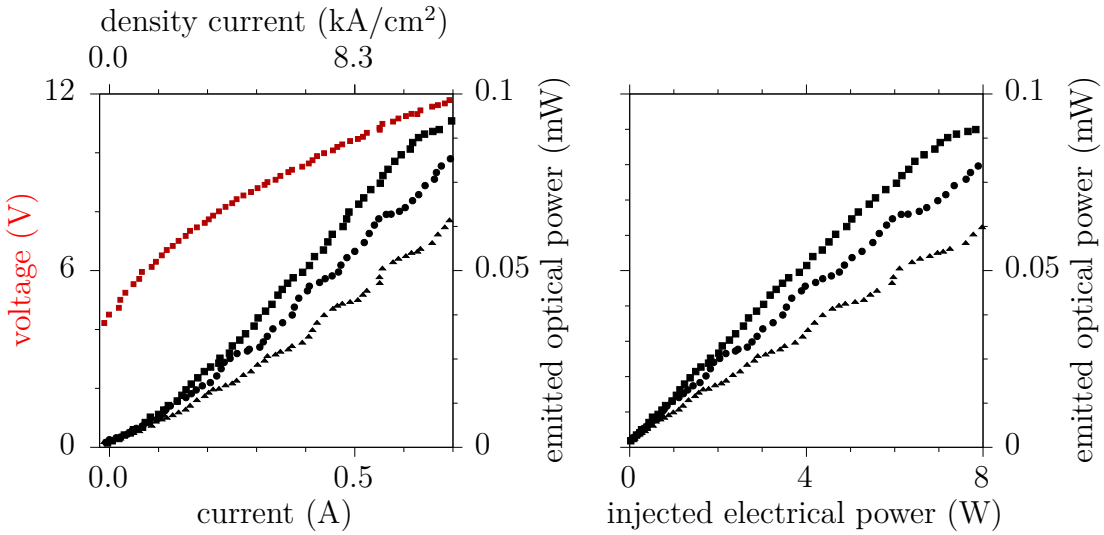

Figure 4.14 – Optical power versus injected current (left) and electrical power (right) at different temperatures: 19°C (squares), 22°C (dots) and 24°C (triangles).

The V-I curves (red squares in figure (4.14), left) obtained at various temperature overlap, so for clarity we only report the one at 24°C. At lower temperature the source is more efficient and the emission becomes closer to the one of a diode. The reason is that a lower temperatures reduces the efficiency of non-radiative recombination processes.

Since we only explore a small temperature range (19 to 24°C), it could be useful to test the device at lower temperatures by means of a cryostat, as done in [59]. This characterization is planned for the next months.

Discussion: lasing threshold and losses

To understand the reason for which our active sample does not lase, we analyze the dependence of the gain threshold on different parameters. Following [177], we find that in QW semiconductor laser, embedded in a cavity long L, the variation of the optical intensity I after one round-trip is given by:

$$\Delta I = 2I[\sigma_{QW}(N_2 - N_1)L - \gamma] \tag{4.1}$$

where σ_{QW} is the QW transition cross section, proportional to the QW electron-hole radiative recombination, $N_2 - N_1$ the population inversion between the QW levels in the conduction and valence band, and γ the total losses experienced by the light in a half round-trip. These losses divide into absorption (α_{abs}), radiative (α_{rad}), scattering (α_{scat}) losses and emission losses at the two cavity mirrors, which have a reflectivity R_1 and R_2:

$$\gamma = (\alpha_{abs} + \alpha_{rad} + \alpha_{scat})L - \frac{1}{2}\ln R_1 \ln R_2 \tag{4.2}$$

The gain threshold in equation (4.1) is established at the critic population

inversion N_c for which the net gain equals the losses:

$$g_{th} = \sigma_{QW} N_c L = \gamma \tag{4.3}$$

In order to minimize the lasing threshold and thus the injected current, the device must have low level of losses, with ideally zero radiative and scattering losses and absorption outside the QW. The origin of these losses in our waveguides is the following:

1. Radiation losses (α_{rad}) are related to the design of the waveguide as they depend on the mode confinement. In our source the lasing mode is a Bragg mode, so its radiative losses are determined by the design of the top and bottom Bragg mirrors. The confinement of the Bragg mode is assured by chosen design (see the numerical simulation in figure (4.9)).

2. Absorption losses (α_{abs}) are due to photons absorbed by the defects of the wafer material, outside the quantum well. They depends on the quality of the growth process.

3. Scattering losses (α_{scat}) are due to surface roughness. Surface imperfections are created during the etching process. This is highly dependent on the etching technique (dry or wet). The scattering losses can be modeled according to Tien's scattering losses theory [178] resulting proportional to the squared value of the Bragg wavevector (k_{Bragg}) and the sidewalls roughness variance (σ), and inversely proportional to the waveguide average width (w):

   $$\alpha_{scattering} \propto (k_{Bragg}\sigma)^2 w^{-1} \tag{4.4}$$

   The dependence of the scattering losses on the modes wavevector and waveguide width is easy to be understood: modes traveling slower along narrower waveguides reflect more often during their propagation, thus they are more sensitive to the surface roughness.

   Since the scattering loss depends on the square value of the surface roughness, it is fundamental to reduce it as much as possible. Notable results have been obtained in passive GaAs/AlGaAs single-mode rib waveguides fabricated via reactive ion etching, with $\alpha \approx 0.05\text{cm}^{-1}$ [179]. However, in our structure we expect higher propagation losses. The first reason is that the Bragg mode is less confined than a fundamental Gaussian mode and thus it is more sensitive to the waveguide sidewalls imperfections. Besides, the rib waveguide studied in [179] is superficially etched, having an aspect ratio smaller than 10%. In our Bragg reflector structure, we need to etch almost entirely the top Bragg mirror to assure that the Bragg mode is properly guided and does not leak into the substrate. Therefore the amount of imperfections resulting from the etching process is higher.

According to these three origins of losses, we make two possible hypothesis for which our sample does not reach the lasing threshold.

The first hypothesis is that $\alpha_{scattering}$ are too high, although the standard deviation of the sidewalls roughness is lower than 10nm (see the commentary to figures (4.5)). In this case, a quick solution is to fabricate waveguides having a ridge larger than 5µm. According to equation (4.4), this would lead to lower scattering losses. Besides, to quantify $\alpha_{scattering}$ induced by the dry etched process, we may compare the results of this process to the ones based wet etching, immune from roughness.

The second hypothesis is that the doping profile introduced during the MBE growth does not correspond to the designed structure. To check this hypothesis, we may carry out capacitance–voltage profiling (C-V profiling) measurements. With this technique we could estimate the doping profile layer by layer.

Part II

Biphoton frequency-comb states: generation and manipulation

Chapter 5

Cavity effect on the Joint Spectral Amplitude

In chapter 2 we described the features of the emitted biphoton and their relation with the source birefringence and chromatic dispersion without considering the facets reflectivity. In this chapter we go further and consider the waveguide as an optical cavity. We show how the cavity effect shapes the JSA into a chessboard-like pattern, resulting from signal and idler Fabry-Perot frequency-comb resonances distributions.

We focus on the monochromatic pump regime as a tool to manipulate the state at the generation stage by tuning the pump beam wavelength. We present two classes of states, resonant and anti-resonant, which are the basis of the manipulation protocol presented in chapter 6.

To conclude, we present the experimental reconstruction of the biphoton JSI via stimulated emission tomography, for both resonant and anti-resonant states, and discuss how such states can be used as frequency encoded qudits.

5.1 AlGaAs waveguide as a Fabry-Perot cavity

Figure (5.1, a) shows a SEM image of the waveguide from a lateral view. Given that the effective index of the supported signal (H-polarized) and idler (V-polarized) modes is approximately $n \sim 3.1$ (figure (2.1)), at the waveguide-air interface there is a step-index of $\Delta n \sim 2.1$. The Fresnel reflectivity at the waveguide facets induces a Fabry-Perot effect for the guided modes.

To experimentally verify the presence of the waveguide cavity effect, we measure the transmission function of the waveguide. We use a CW laser in the telecom range (Tunics), linearly polarized along either H (signal) or V (idler) directions, and measure its transmitted power through the device as a function of the wavelength.

Figure (5.2) reports an extract of this measurement at 1519 ± 1nm, for H-polarized (blue squares) and V-polarized (green dots) photons. The transmitted power is normalized to half of its average value. The contrast of the Fabry-Perot fringes ($\kappa = (T_{max} - T_{min})/(T_{max} + T_{min})$) depends on the cavity reflectivity and propagation losses of the two orthogonally polarized photons [180, 181], which we

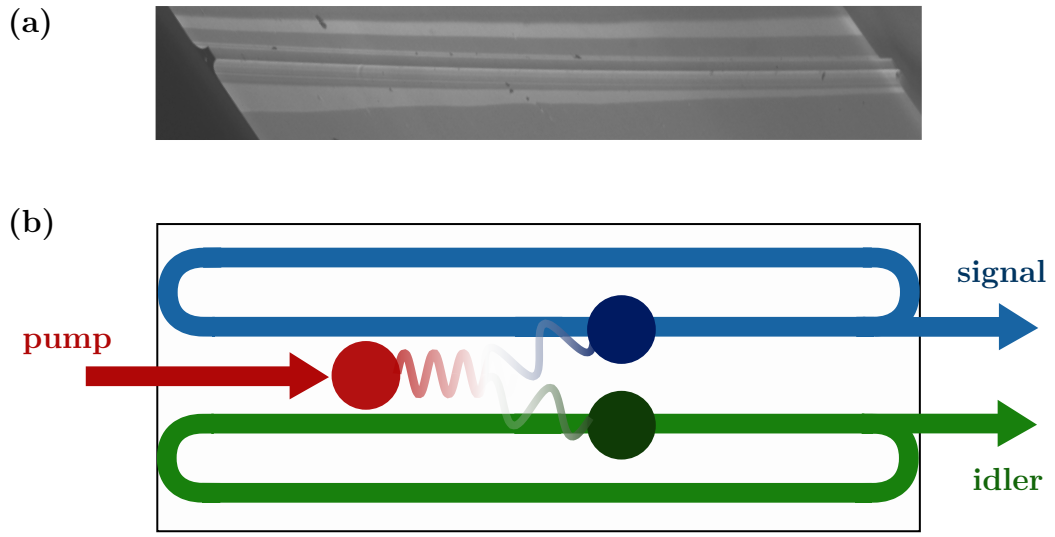

Figure 5.1 –
(a) Waveguide lateral view at the SEM.
(b) Sketch of the waveguide cavity effect for signal and idler photons.

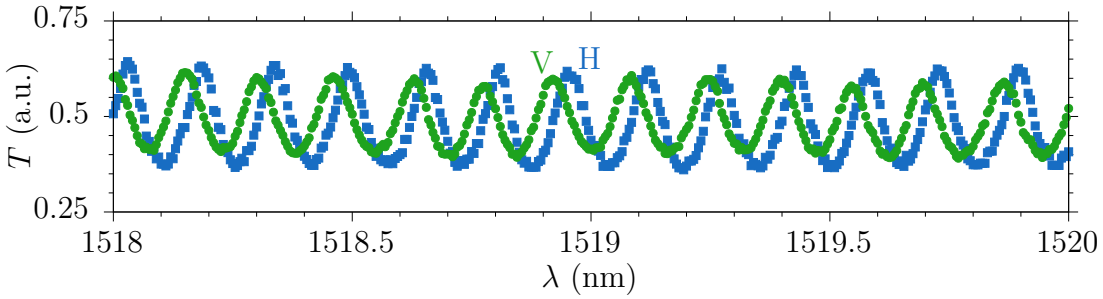

Figure 5.2 – Normalized power for H-polarized (blue squares) and V-polarized (green dots) photons transmitted through the waveguide.

respectively indicate as R_H, R_V and α_H, α_V. In the framework of Fabry-Perot cavity description, their dependence on the wavelength is given by:

$$\begin{aligned} R_H e^{-\alpha_H L n_H(\lambda)} &= \frac{1-\sqrt{1-\kappa_H^2}}{\kappa_H} \\ R_V e^{-\alpha_V L n_V(\lambda)} &= \frac{1-\sqrt{1-\kappa_V^2}}{\kappa_V} \end{aligned} \tag{5.1}$$

From the measurement in figure (5.2) we see that $\kappa_H > \kappa_V$. If we suppose that H and V-polarized photons experience the same propagation losses ($\alpha_H \sim \alpha_V$), this implies that $R_H > R_V$. To confirm the difference in reflectivity between the two orthogonal polarizations, we perform a 3D finite-difference time-domain (FDTD) simulation with a commercial solver (Lumerical) in order to calculate the modal reflectivity at $\lambda = 1519$nm. We suppose that input and output facets are identical

and their shape corresponds to the one illustrated in figure (1.3). The numerical simulation confirms that signal (H) reflectivity is higher than idler (V) reflectivity:

$$\begin{aligned} R_H^{in} &= R_H^{out} = R_H = 0.297 \\ R_V^{in} &= R_V^{out} = R_V = 0.243 \end{aligned} \tag{5.2}$$

From the Fabry-Perot interference we also infer the cavity free spectral range. From the data of figure (5.2) we calculate, for both polarization directions, an average free spectral range ($\Delta\lambda_{fsr}$, $\Delta\nu_{fsr}$) and corresponding cavity round-trip (τ_{RT}) of:

$$\begin{aligned} &\Delta\lambda_{fsr}^{1.55\mu m} = 154\text{pm}; \quad \Delta\nu_{fsr} = 20.00\text{GHz}; \quad \Delta\omega_{fsr} = 125.72\text{GHz} \\ &\tau_{RT} = 50.00\text{ps} \end{aligned} \tag{5.3}$$

Since the waveguide is approximately $L = 2$mm long, we deduce that signal and idler average group index are approximately $n_g = c/(2L\nu_{fsr}) = 3.75$, higher than the corresponding GaAs material refractive group index of 3.52 [182]. Besides, we observe the presence of some birefringence, as H-polarized and V-polarized transmission curves do not overlap.

5.2 Single mode cavity function

In order to illustrate the cavity effect on the biphoton JSA, we start by considering the effect of the cavity on the spectral profile of signal and idler modes. By treating them as classical coherent states, we retrieve the cavity filtering function presented in optics textbooks.

The cavity round-trips corresponding to monochromatic signal and idler modes having a specific frequency ω are:

$$\begin{aligned} \tau_H(\omega) &= 2Ln_H(\omega)/c \\ \tau_V(\omega) &= 2Ln_V(\omega)/c \end{aligned} \tag{5.4}$$

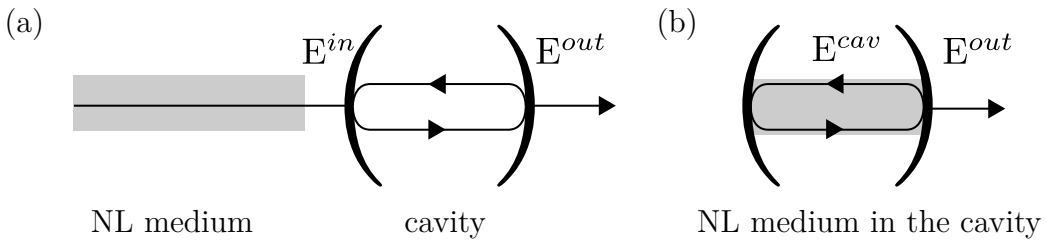

Figure 5.3 – Configurations of NL and cavity:
(a) NL medium followed by cavity.
(b) NL embedded within the cavity.

We distinguish two situations. In the first one, illustrated in figure (5.3, a), the cavity is placed after the nonlinear medium. In this case we are interested in

signal and idler modes which are *transmitted* through the cavity. The transmission of their electric fields is given by the complex-valued Airy distributions [183]:

$$\begin{aligned} f_H^{trans}(\omega) &= \frac{\mathrm{E}_H^{in}}{\mathrm{E}_H^{out}} = \frac{(1-R_H)e^{i\omega\tau_H/2}}{1-R_H e^{i\omega\tau_H}} \\ f_V^{trans}(\omega) &= \frac{\mathrm{E}_V^{in}}{\mathrm{E}_V^{out}} = \frac{(1-R_V)e^{i\omega\tau_V/2}}{1-R_V e^{i\omega\tau_V}} \end{aligned} \tag{5.5}$$

In the second situation, shown in figure (5.3, b) the nonlinear medium is embedded within the cavity. This is the case of our AlGaAs source, since the waveguide constitutes both the nonlinear medium and the cavity. In this case we are interested in signal and idler modes which are *emitted* by the cavity output facet. The emission of their electric fields is given by [184]:

$$\begin{aligned} f_H^{emis}(\omega) &= \frac{\mathrm{E}_H^{cav}}{\mathrm{E}_H^{out}} = \frac{\sqrt{1-R_H}e^{i\omega\tau_H/2}}{1-R_H e^{i\omega\tau_H}} \\ f_V^{emis}(\omega) &= \frac{\mathrm{E}_V^{cav}}{\mathrm{E}_V^{out}} == \frac{\sqrt{1-R_V}e^{i\omega\tau_V/2}}{1-R_V e^{i\omega\tau_V}} \end{aligned} \tag{5.6}$$

where the factors $\sqrt{1-R_{H,V}} = \sqrt{T_{H,V}}$ originate from the fact that signal and idler modes do not undergo a transmission at the cavity input facet.

Figure (5.4) compares transmission (left) and emission function (right), for a given polarization mode, in case of low (R=0.3, (a) row) and high (R=0.9, (b) row) reflection coefficients.

Transmission and emission functions are two Fabry-Perot functions sharing the same periodicity. Photons are transmitted (emitted) by the cavity with unitary (maximal) efficiency at the resonance condition. If we indicate with L the one-pass physical length of the cavity, $n_\mu(\omega)$ the group refractive index of the polarized modes ($\mu = H, V$) and ω the photon pulsation, the resonance condition reads:

$$2m\pi := \Delta\phi = k2L = \frac{\omega_{m,\mu} n_\mu(\omega)}{c} 2L \tag{5.7}$$

with the resonant modes $\omega_{m,\mu}$ given by:

$$\omega_{m,\mu} = m\left(2\pi \frac{c}{n_\mu(\omega)2L}\right) = m\,\omega_{fsr,\mu} = m2\pi/\tau_\mu \tag{5.8}$$

The resonance condition (5.7) implies that the electric field of the resonant modes acquires a phase of π during *one pass* through the cavity. Therefore, the electric field of the transmitted modes accumulates a phase-shift of either 0 or π *, with respect to its phase at the cavity entrance. For this reason, in both transmission and emission scenarios, adjacent resonant modes are in counter-phase, as shown in figure (5.4).

We deduce that the cavity modifies the spectral profile of the transmitted or emitted modes in two ways. First, it redistributes their spectral components by

* we use the convention of periodical phase space defined in $[0, 2\pi)$.

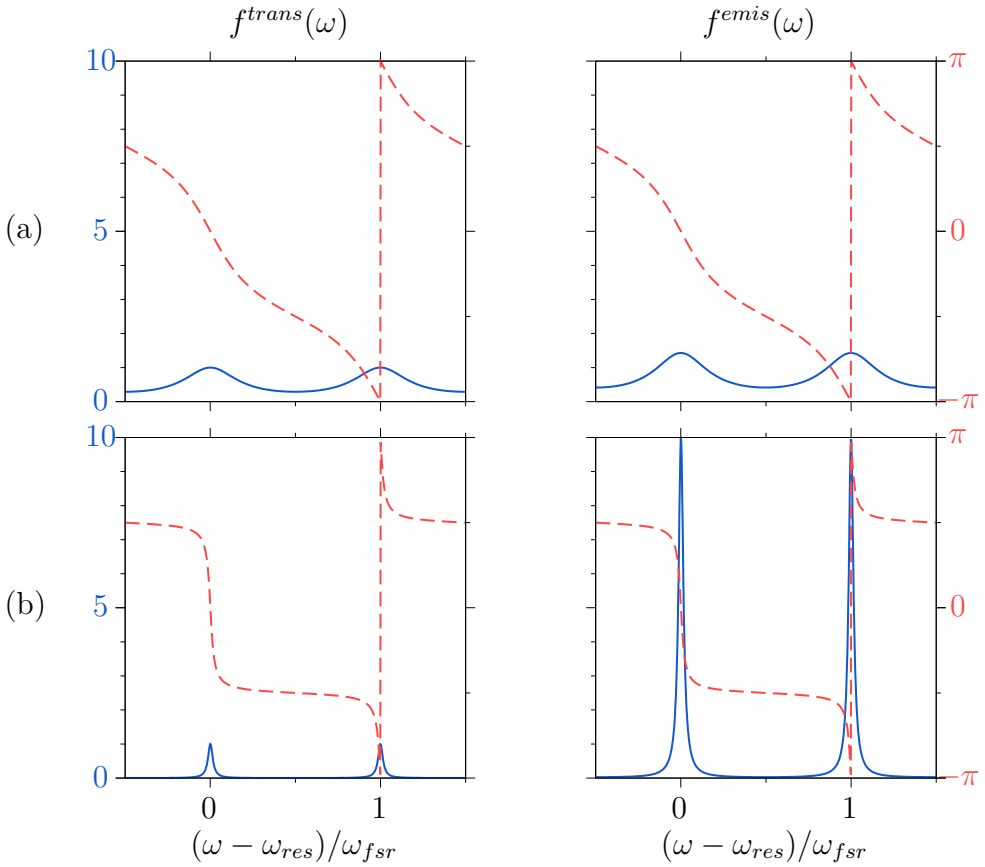

Figure 5.4 – Comparison of transmission (left) and emission (right) functions: modulus squared (continuous blue line) and phase (dashed red line), for a reflectivity of R=0.3 (a) and R=0.9 (b).

enhancing the ones which are multiple of its free spectral range. Second, it modifies the relative phase among them, with adjacent peaks in counter-phase.

At resonance, transmission and emission cavity functions reach their maximum values of:

$$\begin{aligned} f_{max}^{trans} &= 1 \\ f_{max}^{emis} &= \frac{1}{\sqrt{1-R}}; \end{aligned} \tag{5.9}$$

Since $0 < R < 1$, $f_{max}^{emis} > f_{max}^{trans}$. The reason for this difference is straightforward: when the cavity is placed after the source, there is a probability $T = 1 - R$ that a photon is reflected from the input cavity facet and lost. At cavity resonances, the photon emission is amplified, i.e. it is higher than one. As instance, for $R = 0.9$ (figure (5.4, b)) the squared emission function reaches the value of 10.

In between two resonant frequencies, transmission and emission functions take

their lowest value of:

$$\begin{aligned} f_{min}^{trans} &= \frac{1-R}{1+R} \\ f_{min}^{emis} &= \frac{\sqrt{1-R}}{1+R}; \end{aligned} \tag{5.10}$$

Again, since $0 < R < 1$, $f_{min}^{emis} > f_{min}^{trans}$. If $R \to 1$ both amplitudes tend to zero (the photons do not exit from the cavity), while for $R \to 0$ both tend to one (there is no cavity).

We also observe in figure (5.4) that both transmission and emission functions contrasts increase with the reflectivity. Starting from (5.9) and (5.10), we find:

$$\begin{aligned} c^{trans} &= |f^{trans}|_{max}^2 - |f^{trans}|_{min}^2 = \left(\frac{2R}{1+R}\right)^2 \\ c^{emis} &= |f^{emis}|_{max}^2 - |f^{emis}|_{min}^2 = \left(\frac{2R}{\sqrt{1-R}(1+R)}\right)^2 \end{aligned} \tag{5.11}$$

so that the transmission contrast is related to the emission contrast by:

$$c^{trans} = (1-R)c^{emis} = Tc^{emis} \tag{5.12}$$

where the factor $(1-R) = T$ accounts for the additional transmission at the input cavity facet which the photons need to undergo in the transmission case.

To conclude the analysis, we give an expression of the cavity finesse.

According to the expression of Ismail and colleagues [185], based on the Taylor criterion and exempt from any approximations on the form of the Airy function, the free spectral range reads:

$$\Delta\omega_{FWHM} = \Delta\omega_{fsr}\frac{2}{\pi}\arcsin\left(\frac{1-R}{2\sqrt{R}}\right) \tag{5.13}$$

and the cavity finesse:

$$F = \frac{\Delta\omega_{fsr}}{\Delta\omega_{FWHM}} = \frac{\pi}{2}\left[\arcsin\left(\frac{1-R}{2\sqrt{R}}\right)\right]^{-1} \tag{5.14}$$

5.3 Two modes cavity function

After introducing the cavity functions for single photons, we extend the analysis to biphoton states. In order to describe the case of AlGaAs waveguides (5.1b), (5.3b)), in the following we only present the *biphoton emission cavity function*. Anyway, given that emission and transmission functions are proportional, it is straightforward to extend this analysis to the biphoton transmission cavity function.

For sake of brevity, from now on we refer to the biphoton cavity emission function simply as *cavity function*. The biphoton cavity function is given by the product of signal and idler emission functions:

$$f_{cav}(\omega_1, \omega_2) = f_H(\omega_1) f_V(\omega_2) = \frac{\sqrt{1-R_H}\sqrt{1-R_V}\, e^{i(\omega_1 \tau_H(\omega_1) + \omega_2 \tau_V(\omega_2))/2}}{(1 - R_H e^{i\tau_H(\omega_1)\omega_1})(1 - R_V e^{i\tau_V(\omega_2)\omega_2})} \tag{5.15}$$

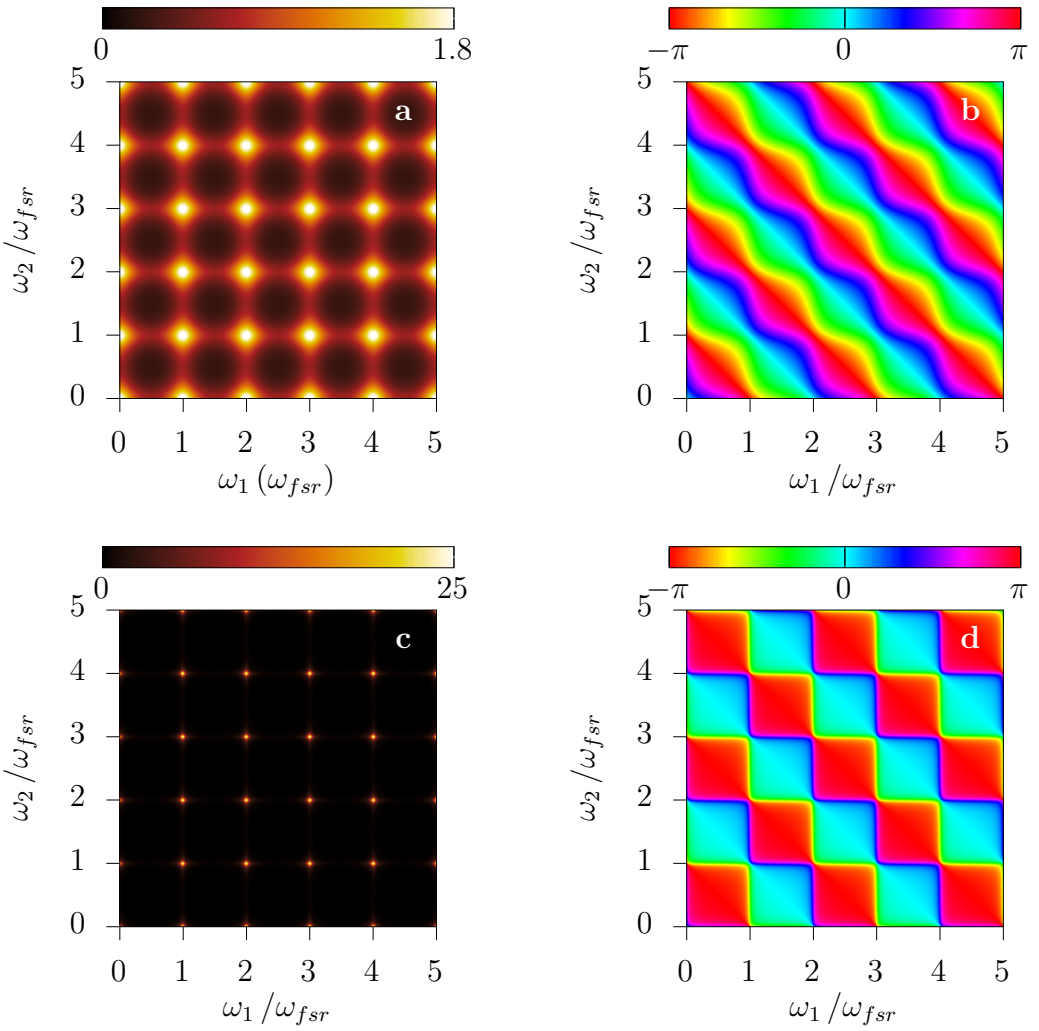

Figure 5.5 – Biphoton cavity emission function for $R = 0.27$ (a, b) and $R = 0.8$ (c, d).
(a, c) Modulus squared value.
(b, d) Phase.

Figure (5.5, a, b) represents the cavity function in the case of a non dispersive and non birefringent low-reflective cavity, with $R = R_H = R_V = 0.27$, the average value of reflectivity of input and output facets in our AlGaAs waveguide. Figure (5.5, c, d) illustrates the cavity function for an analogous high-reflective cavity, with $R = 0.8$.

In analogy to the classical case (figure (5.4), right), the presence of a cavity enhances the emission of resonant biphoton modes.

The squared modulus of the cavity function (a,c) is characterized by a chessboard pattern, resulting from the repetition of the Fabry-Perot pattern (figure (5.4)) along signal (horizontal direction) and idler (vertical direction) orthogonal frequency spaces. The biphoton resonances are given by the product of signal and idler single photon ones. Therefore, for a fixed signal (idler) mode, consecutive biphoton modes are in counter-phase, as illustrated in figure (5.5, d): if we choose a cut of the function at a signal resonant mode (e.g. $w_1 = 1(\omega_{fsr})$), the biphoton peaks have a phase that alternates among 0 (light blue color) and π (red color). This property will be important for the generation of two different kind of frequency-comb states under a CW monochromatic pump regime, which we will present in paragraph (5.4).

In figure (5.5) we distinguish cavity resonances ($\omega_{1,2} = 0, 1, 2, 3, 4, 5$) and intermediate frequencies ($\omega_{1,2} = 0.5, 1.5, 2.5, 3.5, 4.5$), for which the cavity function is real and takes respectively the maximum and minimum value of:

$$\begin{aligned} f_{cav,max} &= \frac{1}{\sqrt{1-R_H}\sqrt{1-R_V}} \\ f_{cav,min} &= \frac{\sqrt{1-R_H}\sqrt{1-R_V}}{(1+R_H)(1+R_V)} \end{aligned} \tag{5.16}$$

If we consider for simplicity an average reflection coefficient, $R_H = R_V = R$, the maximum (minimum) value of the biphoton cavity function (5.15) is simply the squared value of the maximum (minimum) single mode emission function (5.9):

$$\begin{aligned} f_{cav,max} &= (f_{max})^2 = \frac{1}{(1-R)} \\ f_{cav,min} &= (f_{min})^2 = \frac{1-R}{(1+R)^2} \end{aligned} \tag{5.17}$$

The contrast, following its definition, is slightly higher than the squared modulus of the single mode emission contrast (c^{emis}) introduced in (5.11):

$$c_{cav} = |f_{cav,max}|^2 - |f_{cav,min}|^2 = \frac{8R(1+R^2)}{(1-R)^2(1+R)^4} = \frac{(1+R^2)}{2R^3}(c^{emis})^2 \tag{5.18}$$

Along signal (horizontal direction ω_1) and idler (vertical direction ω_2) frequency spaces, the linewidth and finesse of the biphoton intensity peaks are given by the single photon Fabry-Perot linewidths, expressed in (5.13) and (5.14). For this reason, in figure (5.5) the shape of the intensity chessboard peaks transforms from a large rhombus to a narrow cross star as the cavity reflectivity increases. This property may be useful to engineer the biphoton. As instance, Jeronimo-Moreno and colleagues [184] propose to control the cavity reflection coefficients and free spectral range to couple the biphoton state with specific atomic system transitions.

In our work, we are mostly interested in the biphoton frequency correlation properties, arising from the symmetry of the JSA with respect to the degeneracy frequency (see chapter (2). For this reason, we express the cavity function (5.15) in the (ω_+, ω_-) basis according to transformation (2.3), to obtain:

$$\begin{aligned} f_{cav}(\omega_+, \omega_-) &= f_H\Big(\frac{\omega_+ + \omega_-}{2}\Big) f_V\Big(\frac{\omega_+ - \omega_-}{2}\Big) \\ &= \frac{\sqrt{1-R_H}\sqrt{1-R_V}\exp\{\frac{i}{2}[\tau_H(\frac{\omega_+ + \omega_-}{2}) + \tau_V(\frac{\omega_+ - \omega_-}{2})]\}}{\Big(1 - R_H \exp\left[i\tau_H(\frac{\omega_+ + \omega_-}{2})\right]\Big)\Big(1 - R_V \exp\left[i\tau_V(\frac{\omega_+ - \omega_-}{2})\right]\Big)} \end{aligned} \tag{5.19}$$

We can simplify this expression in the case of our AlGaAs source, where the effective index is linear with the frequency (2.10) and the chromatic dispersion is independent on the polarization direction (2.12). Under these assumptions, we expand the expression of the two round-trip times:

$$\begin{aligned} \tau_H = \tau_H\Big(\frac{\omega_+ + \omega_-}{2}\Big) = \frac{2L}{c}\Big[n_H\Big|_{\frac{\omega_+}{2}} + \frac{\omega_-}{2}\frac{dn}{dw}\Big] = \tau_H\Big|_{\frac{\omega_+}{2}} + \omega_-\frac{L}{c}\frac{dn}{dw} \\ \tau_V = \tau_V\Big(\frac{\omega_+ - \omega_-}{2}\Big) = \frac{2L}{c}\Big[n_V\Big|_{\frac{\omega_+}{2}} - \frac{\omega_-}{2}\frac{dn}{dw}\Big] = \tau_V\Big|_{\frac{\omega_+}{2}} - \omega_-\frac{L}{c}\frac{dn}{dw} \end{aligned} \tag{5.20}$$

The expression of the cavity function becomes:

$$\begin{aligned} &f_{cav}(\omega_+, \omega_-) = \sqrt{1-R_H}\sqrt{1-R_V} \\ &\exp\left[i\frac{\omega_+}{4}\left(\tau_H\Big|_{\frac{\omega_+}{2}} + \tau_V\Big|_{\frac{\omega_+}{2}}\right)\right]\exp\left[i\frac{\omega_-}{2}\left(\tau_H\Big|_{\frac{\omega_+}{2}} - \tau_V\Big|_{\frac{\omega_+}{2}} + \omega_-\frac{dn}{dw}\right)\right] \\ &\left\{\left[1 - R_H\exp\left(i\tau_H\frac{\omega_+ + \omega_-}{2}\right)\right]\left[1 - R_V\exp\left(i\tau_V\frac{\omega_+ - \omega_-}{2}\right)\right]\right\}^{-1} \end{aligned} \tag{5.21}$$

5.3.1 Cavity function in the absence of dispersion and birefringence

In the case of absence of birefringence and dispersion ($\tau_H = \tau_V = \tau$), and for cavity mirrors reflectivities $R_H = R_V = R$, the expression (5.21) simplifies into:

$$f_{cav}(\omega_+, \omega_-) = \frac{(1-R)\exp\Big(i\omega_+\tau/2\Big)}{\Big(1 - R\exp\{i\tau(\frac{\omega_+ + \omega_-}{2})\}\Big)\Big(1 - R\exp\{i\tau(\frac{\omega_+ - \omega_-}{2})\}\Big)} \tag{5.22}$$

The numerator term includes a global phase term, proportional to ω_+. The denominator is the product of two sinusoidal functions in $\omega_+/2$, translated of $\pm\omega_-/2$.

Figure (5.6) illustrates the cavity function in the (ω_+, ω_-) basis, for $R = 0.27$ and $R = 0.8$.

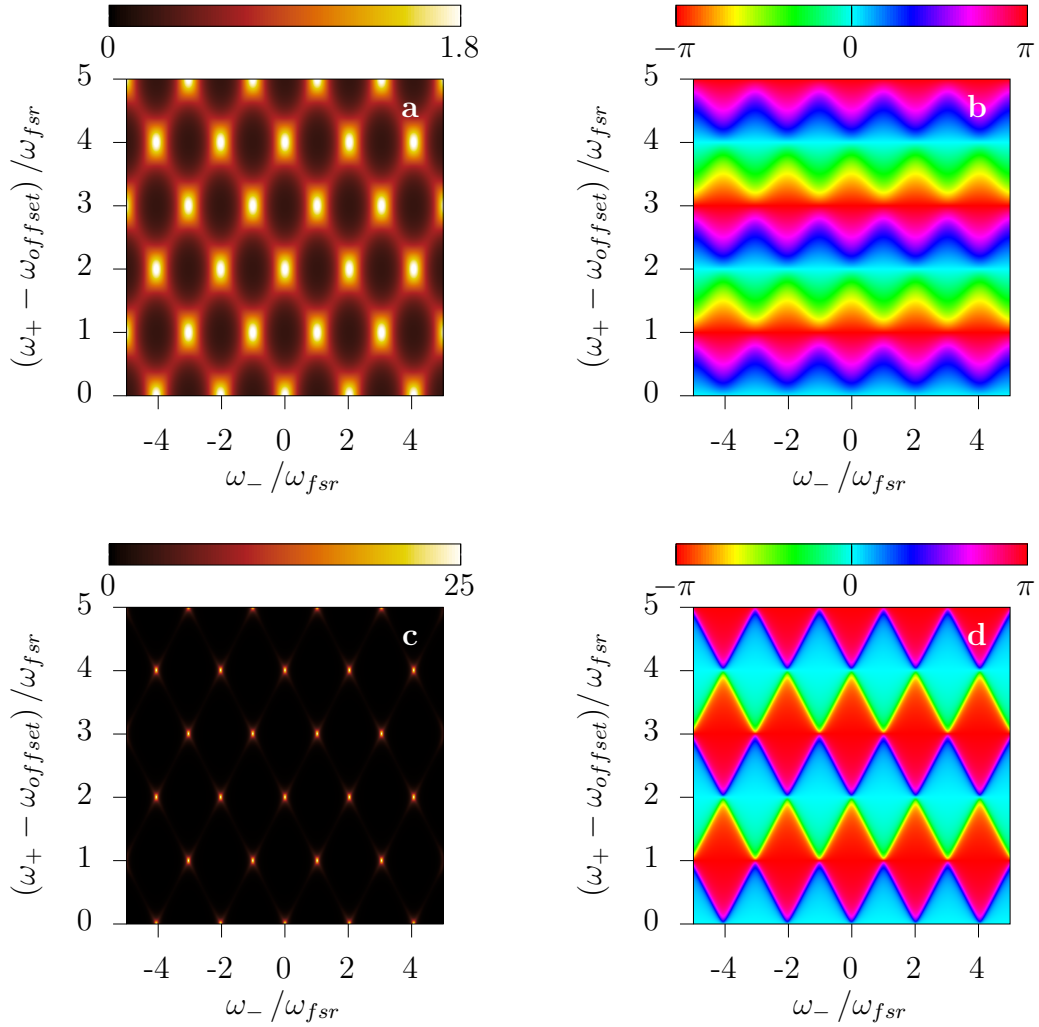

Figure 5.6 – Two photon cavity emission function in (ω_+, ω_-) for $R = 0.27$ (a, b) and $R = 0.8$ (c, d).
(a, c) Squared absolute value.
(b, d) Phase.

Due to the arguments $\omega_+/2 \pm \omega_-/2$ of the sinusoidal function in (5.22), the periodicity of the cavity function along ω_+ and ω_- is two times the value of signal and idler free spectral range. This comes from the definition of this rotated basis (2.3), which implies that $\Delta\omega_+ = \Delta\omega_- = \Delta\omega_1 + \Delta\omega_2$, and thus:

$$\omega_{+,fsr} = \omega_{-,fsr} = \omega_{1,fsr} + \omega_{2,fsr} \tag{5.23}$$

In the absence of birefringence and chromatic dispersion, signal and idler free spectral range coincide ($\omega_{1,fsr} = \omega_{2,fsr} = \omega_{fsr}$) and the expression (5.23) simplifies into:

$$\omega_{+,fsr} = \omega_{-,fsr} = 2\omega_{fsr} \tag{5.24}$$

For a constant ω_+, we distinguish along ω_- two different Fabry-Perot patterns,

depending on weather ω_+ is an even or odd multiple of the cavity free spectral range.

As reference for the phase profiles shown in figure (5.6 b, d), we choose that the cavity function at $(\omega_-, (\omega_+ - \omega_{offset})/\omega_{fsr}) = (0, 0)$ has a phase of zero.

If $\omega_+ = m\omega_{fsr}$, m even, the Fabry-Perot along ω_- has a peak centered in $\omega_- = 0$ and all the peaks share a phase of 0 (e.g. $m = 0, 2, 4$ in figure). We define this pattern as resonant state.

If $\omega_+ = n\omega_{fsr}$, n odd, the Fabry-Perot along ω_- has two maxima in $\omega_- = \pm\omega_{fsr}$, with a minimum at $\omega_- = 0$. Its peaks share a phase of π (e.g. $m = 1, 3, 5$ in figure). We define this pattern as anti-resonant state.

Both states have a multi-peak spectrum as a classical frequency comb and can be defined as biphoton combs. Resonant and anti-resonant combs are perfectly symmetric around the degeneracy frequency $\omega_- = 0$, but the arrangement of the resonances with respect to $\omega_- = 0$, is different.

In the resonant comb, the resonances are disposed at even multiples of the cavity free spectral range ($\omega_{fsr} = 0, \pm 2, \pm 4$ in figure (5.6)). Conversely, in the anti-resonant frequency comb, the resonances correspond to odd multiples of the cavity free spectral range ($\omega_{fsr} = \pm 1, \pm 3, \pm 5$ in figure (5.6)).

This difference is essential for the manipulation of the two combs, which we will present in chapter (6).

5.3.2 Birefringence effect

The effect of birefringence on the cavity function is to translate the chessboard pattern along the anti-diagonal direction in the (ω_+,ω_-) space. We consider a cavity without chromatic dispersion and with birefringence Δn, defined as:

$$\Delta n = n_H - n_V \tag{5.25}$$

Signal (H) and idler (V) resonances, introduced in (5.8), are given by:

$$\begin{aligned} \omega_{H,m} &= m\left(2\pi\frac{c}{n_H 2L}\right) \\ \omega_{V,m} &= m\left(2\pi\frac{c}{n_V 2L}\right) = m\left(2\pi\frac{c}{(n_H + \Delta n)2L}\right) \end{aligned} \tag{5.26}$$

The idler resonances decrease with the birefringence, so that the peaks of the cavity function $f_{cav}(\omega_1, \omega_2)$ translate vertically downwards.

In the (ω_+, ω_-) space, while birefringence defined as (5.25) increases, $f_{cav}(\omega_+, \omega_-)$ translates along the anti-diagonal, top-left to bottom-right verse.

We illustrate this effect in [186], an animated plot of the cavity function norm and phase versus the dephasing accumulated between signal and idler modes after one round-trip, due to birefringence. We see that, while birefringence increases, idler resonances $\omega_{V,m}$ may superpose to lower-order signal resonances, such as

$\omega_{H,m-1}$ or more $\omega_{H,m-k}$. In these fortuitous cases, the pattern of the birefringent cavity function is the same as in the case of no birefringence.

However, in general birefringence reduces the mirror-symmetry of $f_{cav}(\omega_1, \omega_2)$ around the degeneracy frequency, i.e. the mirror-symmetry of $f_{cav}(\omega_+, \omega_-)$ with respect to $\omega_- = 0$. As signal and idler become more distinguishable, the amplitude of the interference of the biphoton with itself reduces, and thus the possibility of manipulate the state. We will illustrate the impact of birefringence to the biphoton auto-correlation properties in the next chapter, in section (6.6).

5.3.3 Dispersion effect

In the case of a dispersive cavity, signal and idler resonances are given by:

$$\begin{aligned} \omega_{H,m} &= m\left(2\pi\frac{c}{n_H(\omega)2L}\right) \\ \omega_{V,m} &= m\left(2\pi\frac{c}{n_V(\omega)2L}\right) \end{aligned} \tag{5.27}$$

In the case of a cavity with normal (anomalous) dispersion, the distance among consecutive resonances, i.e. the free spectral range, decreases (increases) with the frequency. Being proportional to ω_-^2, the dispersion effect becomes important for large values of ω_-, accessible to large-band biphoton states.

5.4 Simulated cavity function for the AlGaAs source

In this section we calculate the cavity function of our integrated AlGaAs source. As we proceed numerically, we do not need to make any approximation on the waveguide dispersion and we use directly equation (5.15). We use the modes dispersion calculated numerically by using Lumerical MODE (2.1) and their reflection coefficients at the input and output facets calculated via a 3D-FDTD simulation (5.2). We suppose the typical length of our sources, 2mm, set during the cleaving operation.

We present a zoom of the calculated cavity function in figure (5.7). From equation (5.13), we find that the linewidth of the peaks of the *absolute value* of the cavity function ($\Delta\omega_{FWHM}$) is half of the free spectral range. From the data of figure (5.7), we find that the cavity function linewidth is $\Delta\omega_{FWHM}^{intensity} = 0.36\Delta\omega_{fsr}$ and finesse $F = 2.78$. This value is compatible with the resolution of two adjacent peaks for a 2mm long waveguide.

We also notice that, in comparison with the ideal cavity case in figure (5.6 a, b), the chessboard patterns is slightly translated to the left with respect to the $\omega_- = 0$ central axis, as a consequence of birefringence. The effects of the cavity chromatic dispersion are not visible over this narrow ω_- frequency range.

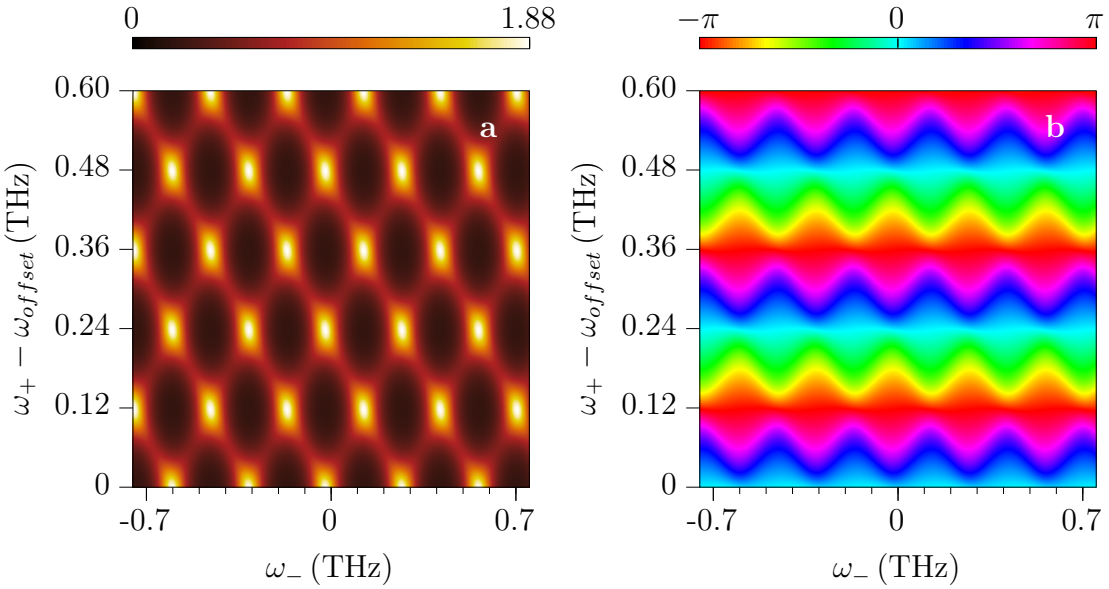

Figure 5.7 – Two photon cavity emission function of our AlGaAs source (ω_{offset} = 2444.85THz).
(a) Modulus squared.
(b) Phase.

We retrieve the expression of the JSA of the biphoton state emitted by our source by multiplying the JSA previously found in (2.3) by the cavity term (5.21):

$$C(\omega_+, \omega_-) = \phi_{pump}(\omega_+)\phi_{PM}(\omega_+, \omega_-)f_{cav}(\omega_+, \omega_-) \tag{5.28}$$

with the biphoton state normalization:

$$\begin{aligned} 1 = \eta &= \iint d\omega_- d\omega_+ C(\omega_+, \omega_-)C^*(\omega_+, \omega_-) \\ &= \iint d\omega_- d\omega_+ \phi_{pump}\phi^*_{pump}\phi_{PM}\phi^*_{PM}f_{cav}f^*_{cav} \end{aligned} \tag{5.29}$$

In the JSA expression (5.28), we can think of the pump spectral profile ($\phi_{pump}(\omega_+)$) as a filter that selects specific regions of the phase matching ($\phi_{PM}(\omega_+, \omega_-)$) and cavity ($\phi_{PM}(\omega_+, \omega_-)$) functions.

In this section we study the JSA in the CW monochromatic pump regime. In the commentary of paragraph (5.3.1) emerges the interest of using a monochromatic pump beam (or, more generally, a pump with a spectral profile narrower than the linewidth along ω_+ of the Fabry-Perot peaks), capable of generating quantum states that include only 0 phase peaks or π phase peaks. As we will present in the next chapter, these quantum states can be used for the manipulation of the state symmetry. We underline that this property is unique of CW monochromatic pumping and frequency-entanglement. If we consider a large bandwidth optical beam going through the cavity, its spectral profile would have alternating 0 phase peaks and π phase peaks (as in figure (5.4)), incompatible with the manipulation protocol proposed in this work, presented in chapter (6).

A monochromatic pump spectral profile can be modeled with a Lorentzian function (2.5). By using the general expression of the phase matching term (2.18), the JSA reads:

$$\begin{aligned} C(\omega_+,\omega_-) &= \phi_{pump}(\omega_+)\phi_{PM}(\omega_+,\omega_-)f_{cav}(\omega_+,\omega_-) \\ &= \frac{1}{\pi}\frac{\Delta\omega_L/2}{(\omega_+-\omega_p)^2+(\Delta\omega_L/2)^2} \\ &\quad \operatorname{sinc}\left\{\frac{L}{c}\left[\omega_+\Delta n_{modal}(\omega_+)-\omega_-\left(\frac{\Delta n}{2}+\frac{\omega_-}{2}\frac{dn}{d\omega}\right)\right]\right\} \\ &\quad \sqrt{1-R_H}\sqrt{1-R_V}\frac{\exp\left\{i\frac{\omega_+}{4}\left[\tau_H\left(\frac{\omega_+}{2}\right)+\tau_V\left(\frac{\omega_+}{2}\right)\right]\right\}}{\left(1-R_H\exp\left\{i\tau_H(\frac{\omega_++\omega_-}{2})(\frac{\omega_++\omega_-}{2})\right\}\right)} \\ &\quad \frac{\exp\left\{i\frac{\omega_-}{2}\left[\tau_H\left(\frac{\omega_+}{2}\right)-\tau_V\left(\frac{\omega_+}{2}\right)+\omega_-\frac{dn}{dw}\right]\right\}}{\left(1-R_V\exp\left\{i\tau_V(\frac{\omega_+-\omega_-}{2})(\frac{\omega_+-\omega_-}{2})\right\}\right)} \end{aligned} \tag{5.30}$$

and the corresponding biphoton state:

$$|\Psi\rangle = \iint d\omega_+ d\omega_- C(\omega_+,\omega_-)\hat{a}_H^\dagger\left(\frac{\omega_++\omega_-}{2}\right)\hat{a}_V^\dagger\left(\frac{\omega_+-\omega_-}{2}\right)|0\rangle \tag{5.31}$$

Joint Spectral Amplitude in the CW monochromatic pumping regime

If the pump spectral linewidth is much smaller than the linewidth of the Fabry-Perot peaks along ω_+, we can approximate the pump Lorentzian profile to a Dirac delta distribution centered in $\omega_+ = \omega_p$. This approximation holds for the monochromatic pump laser (TOPTICA$^{\text{TM}}$ Photonics DL pro 780) and AlGaAs waveguide ($L \sim 2$mm) used in this work, for which $\Delta\nu_p \sim 100\text{kHz} << \Delta\nu_{fsr} \sim 20\text{GHz}$.

By rewriting the pump term as done in (2.5), the biphoton state simplifies into:

$$|\Psi\rangle = \int d\omega_- \phi_{PM}(\omega_p,\omega_-)f_{cav}(\omega_p,\omega_-)\hat{a}_H^\dagger\left(\frac{\omega_p+\omega_-}{2}\right)\hat{a}_V^\dagger\left(\frac{\omega_p-\omega_-}{2}\right)|0\rangle \tag{5.32}$$

so that we can introduce a reduced JSA, that for a given ω_p depends only on ω_-:

$$C(\omega_p,\omega_-) = \phi_{PM}(\omega_p,\omega_-)f_{cav}(\omega_p,\omega_-) \tag{5.33}$$

with for a general cavity:

$$\begin{aligned} f_{cav}(\omega_p,\omega_-) = \sqrt{1-R_H}\sqrt{1-R_V}&\frac{\exp\left\{i\frac{\omega_p}{4}\left[\tau_H\left(\frac{\omega_p}{2}\right)+\tau_V\left(\frac{\omega_p}{2}\right)\right]\right\}}{\left(1-R_H\exp\left\{i\tau_H(\frac{\omega_p+\omega_-}{2})(\frac{\omega_p+\omega_-}{2})\right\}\right)} \\ &\frac{\exp\left\{i\frac{\omega_-}{2}\left[\tau_H\left(\frac{\omega_p}{2}\right)-\tau_V\left(\frac{\omega_p}{2}\right)+\omega_-\frac{dn}{dw}\right]\right\}}{\left(1-R_V\exp\left\{i\tau_V(\frac{\omega_p-\omega_-}{2})(\frac{\omega_p-\omega_-}{2})\right\}\right)} \end{aligned} \tag{5.34}$$

If the cavity has no birefringence and dispersion, given $R_H = R_V = R$:

$$f_{cav}(\omega_p, \omega_-) = \frac{(1-R)\exp\left(i\omega_p\tau/2\right)}{\left(1 - R\exp\left\{i\tau(\frac{\omega_p+\omega_-}{2})\right\}\right)\left(1 - R\exp\left\{i\tau(\frac{\omega_p-\omega_-}{2})\right\}\right)} \tag{5.35}$$

We see in equation (5.35) that, for a given reflectivity and round-trip time, the cavity function along ω_- depends only on the pump frequency ω_p. Following the commentary to figure (5.6), we focus on two periodical values of pump frequency, for which the cavity function (5.35) takes real values and its degeneracy frequency ($\omega_- = 0$) is either resonant or anti-resonant with respect to the cavity:

$$\begin{aligned} \omega_p &= 2n\,\Delta\omega_{fsr}, && \text{resonant state} \\ \omega_p &= (2n+1)\,\Delta\omega_{fsr}, && \text{anti-resonant state} \end{aligned} \tag{5.36}$$

with n an integer number.

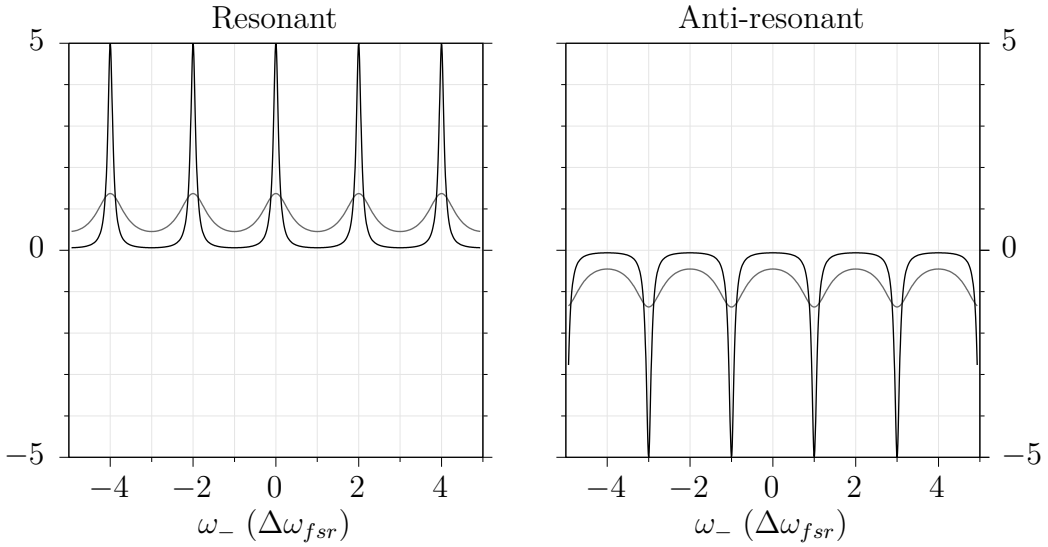

Figure 5.8 – Resonant and anti-resonant cavity functions, as defined in (5.35, 5.36), for R=0.8 (black) and R=0.27 (grey).

We represent the resonant and anti-resonant cavity functions, for two values of cavity modal reflectivities, in figure (5.8). The resonant function has a maximum in $\omega_- = 0$ and is positive (phase of 0), while the anti-resonant function has a minimum in $\omega_- = 0$ and is negative (phase of π).

The resonant function has been introduced for the first time by Ou and coworkers [101], defined as a biphoton mode-locked state. The anti-resonant state has been introduced by Olindo and colleagues in [187], generated using a slightly different optics setup, with two individual cavities for signal and idler, both placed after the nonlinear source. However, to our best knowledge, the anti-resonant function has never been investigated in the frequency space or proposed as a tool for the manipulation of the biphoton state symmetry, as we will demonstrate in the next chapter.

5.5 Characterization of the biphoton Joint Spectral Intensity via Stimulated Emission Tomography

To demonstrate that we can generate either resonant or anti-resonant frequency-comb states, we experimentally reconstruct their Joint Spectral Intensity (JSI). The JSI is the squared norm of the JSA and gives the probability density that signal and idler photons are detected at a specific combination of frequencies (ω_1, ω_2).

The JSI can be measured in a signal-idler coincidence setup that makes use of dispersive fibers, which associate signal and idler frequencies to specific arrival times. However, single-photon detectors have a limited time resolution, in the order of 100ps for APDs (Avalanche PhotoDiodes) and 10ps for SNSPDs (Superconducting Nanowire Single-Photon Detectors). It follows that this direct method cannot detect the spectral feature of the JSI with a high resolution.

An alternative approach to reconstruct the JSI is offered by Stimulated Emission Tomography (SET). SET has been proposed by Liscidini and Sipe in [117], experimentally demonstrated in our group [188, 151] and nowadays is a widely used technique in the quantum optics community. The principle of SET is to use Difference Frequency Generation (DFG) to emulate SPDC. A pump beam and a monochromatic beam at ω_s (named seed), are sent in a nonlinear crystal. An idler beam is generated via DFG and its intensity spectral profile is acquired by an Optical Spectrum Analyzer (OSA). Liscidini and Sipe demonstrate that the spectral power of the idler beam at ω_2 is proportional to value of the JSI of a biphoton in (ω_s, ω_2) that would be generated via an SPDC process carried out by using the same pump beam. By sweeping the seed frequency ω_s and acquiring the idler spectra, it is possible to reconstruct the JSI in the whole signal and idler frequency space. SET offers high spectral resolution and short measurement time. The spectral resolution limit, instead of being related to the single photon response time, is set by the OSA. In our case, we use a Yokogawa AQ6370C, which has a spectral resolution of 20pm. The integration time is reduced because, given a seed frequency ω_s, a single scan of the OSA allows to reconstruct a cut of the JSI along (ω_s, ω_2).

Given such advantages, we use the SET technique to reconstruct the JSI of the biphoton frequency-comb emitted by our source.

5.5.1 Measurement of the Joint Spectral Intensity

Figure (5.9) illustrates the optical setup used to perform the SET. A CW diode laser (TOPTICA^{TM} Photonics DL pro 780) provides a monochromatic pump beam at 764.335nm ($\omega_p = 2464.43$THz) and 38mW. A telecom CW diode laser (Tunics-PR) is used as seed beam. We scan the seed in the (1528.5nm,1600nm) range, with steps of 40pm. Pump and seed beams are horizontally polarized by means of two polarizers (P). After the waveguide, the emitted idler beam and the transmitted pump and seed beams are collected by means of a microscope lens. The pump beam is filtered by a chromatic filter (F), while a fibered polarizing

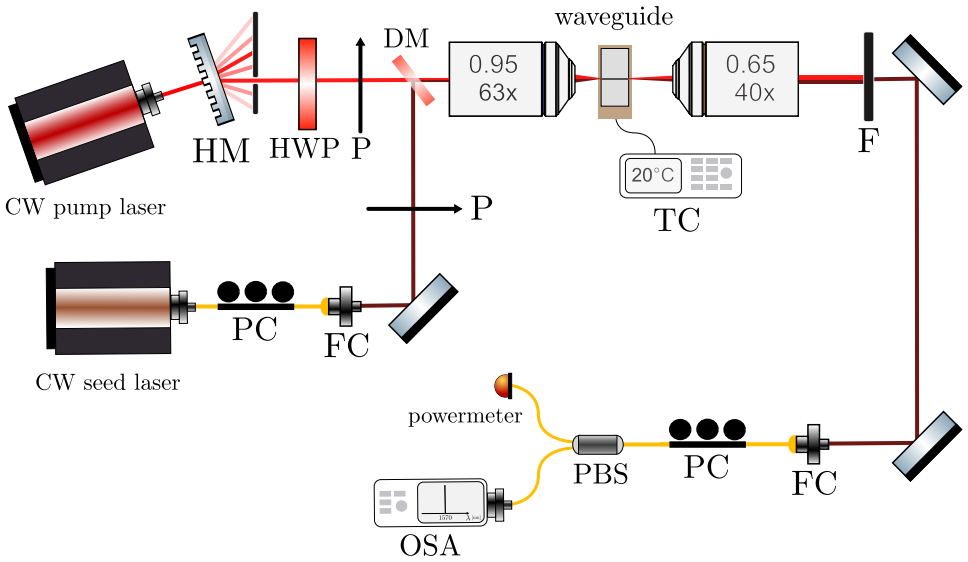

Figure 5.9 – Sketch of the experimental setup for the JSI experiment. HM: holographic mask, HWP: half-wave plate, P: polarizer, PC: polarization controller, FC: fiber coupler, DM: dichroic mirror, TC: temperature controller, F: low-pass filter, PBS: polarising beam splitter, OSA: optical spectrum analyzer.

beam splitter (PBS) is used to send the idler beam in the OSA and the seed beam in the powermeter, to monitor that its power is constant during the whole experiment. We set the OSA spectral resolution to 20pm and intensity sensitivity to 1pW (HIGH3 option for Yokogawa AQ6370C).

At each frequency of the seed, we set the OSA to acquire an idler spectra on a 200pm range. To automatize the measurement, before each acquisition our program centers the OSA scan to the maximum of the idler spectrum. The idler spectra maxima are inferred from the acquisition of two idler spectra, corresponding to the seed minimum and maximum wavelengths.

Figure (5.10) shows a zoom of the performed measurement, in the seed range of $(1554\text{nm}, 1556\text{nm})$. We find seed and idler free spectral ranges of $\Delta\omega_{fsr} = 120.6\text{GHz}$ ($\nu_{fsr} = 19.2\text{GHz}$, $\lambda_{fsr} \approx 150\text{pm}$ at 1555nm), compatible with the previous measurement (5.3) and simulation (5.7).

We note that SET does not allow to measure the JSI at degenerate seed and idler wavelengths. The splitting ratio of the PBS in figure (5.9) is not perfect and a small part of the H-polarized seed power enters in the OSA input, together with the power of the V-polarized idler beam. When seed and idler wavelengths superpose, since seed power is much higher than idler one, the seed power hides the idler power. Experimentally, we find that the measurement can be performed for idler photons which are at least 1nm apart from the degeneracy point.

To generate a more intense idler beam, we amplify the seed CW laser (figure (5.9)) by using a telecom C-band amplifier, working in the wavelength range $(1530\text{nm}, 1565\text{nm})$. Since the degeneracy wavelength of our devices (`ABQ71_C1` samples) is approximately 1530nm, we inject seeds photons at $\lambda_{seed} > 1531\text{nm}$, and detect idler photons at $\lambda_{idler} < 1529\text{nm}$.

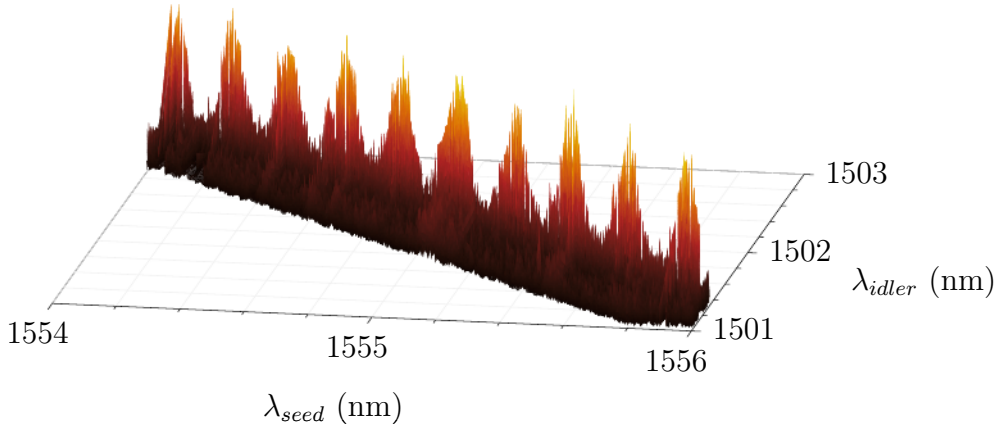

Figure 5.10 – Example of a JSI measured via the SET technique, with seed steps of 10pm (idler resolution of 20pm), and a pump wavelength of 764.335nm.

5.5.2 Resonant and anti-resonant frequency-comb states

By using SET, we experimentally validate the possibility of generating resonant and anti-resonant states, shown in figure (5.8) and defined in equation (5.35).

In order to find the set of ω_p corresponding to resonant and anti-resonant states (5.36), we first perform a measurement of coincidences while finely tuning the pump frequency. For a constant pump power within the cavity (assured by monitoring the pump power after the waveguide), resonant and anti-resonant ω_p correspond to a local maxima in the coincidence rate (see the direct coincidence measurement of figure (6.25), presented in the manipulation chapter).

Once we identify ω_p of resonant and anti-resonant states, we perform SET. Figure (5.11) shows the two JSI measurements corresponding to the resonant (lower JSI) and anti-resonant (upper JSI) states. The resonant state is measured for a pump wavelength of $\omega_p = 2464.431 \pm 0.033$THz ($\lambda_p = 764.335 \pm 0.010$nm), while the anti-resonant for a pump wavelength of $\omega_p = 2464.373 \pm 32$THz ($\lambda_p = 764.353 \pm 0.010$nm).

Figure (5.12) is a zoom of this measurement, within the range of $\lambda_{seed} \in (1539.4, 1540.5)$nm, transposed in (ω_+, ω_-) basis and expressed in unit of signal and idler free spectral range. We clearly see that the two patterns are out of phase, corresponding to the resonant (R, top) and anti-resonant (AR, bottom) states.

5.5.3 Qudit state

The quantum state having the JSI reported in figure (5.10) can be seen as the implementation of a frequency-encoded d-dimensional quantum state (qudit) [77]

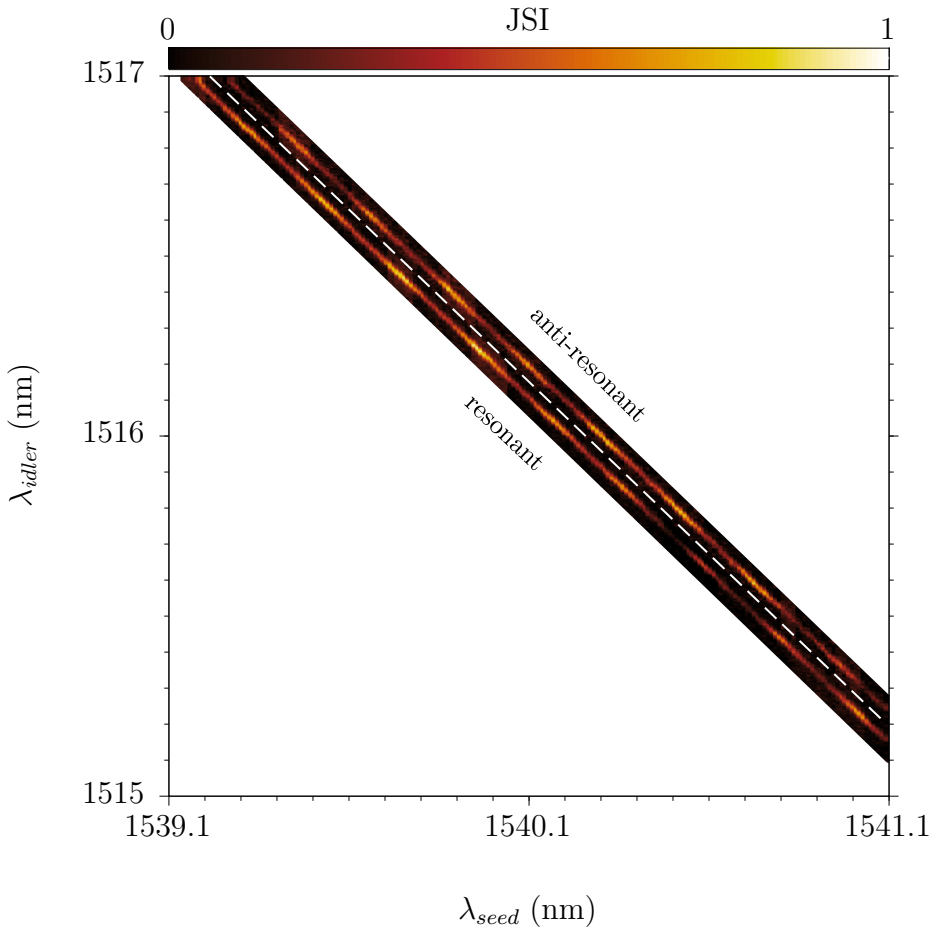

Figure 5.11 – Measured JSI of resonant ($\lambda_p = 764.335\text{nm} \pm 10\text{pm}$) and anti-resonant ($\lambda_p = 764.353\text{nm} \pm 10\text{pm}$) states, measured via SET technique, with seed steps of 10pm.

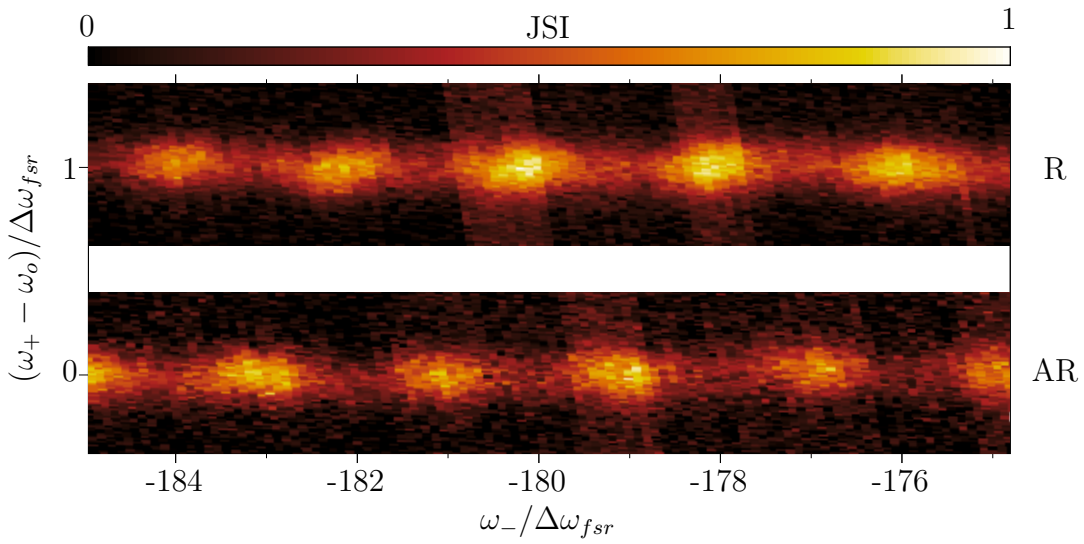

Figure 5.12 – Measured JSI of resonant (R) and anti-resonant (AR) states, corresponding to $\lambda_{seed} \in (1539.4, 1540.5)$nm in figure (5.11), replotted in (ω_+, ω_-) basis.

of the form:

$$|\Psi\rangle = \sum_{i}^{d} a_i \, |\omega_i, \omega_{d-i}\rangle \tag{5.37}$$

with (ω_i, ω_{d-i}) the peaks positions in signal and idler space, a_i the peaks values and d an integer that defines the biphoton bandwidth (imposed by the phase matching function, according to the properties of the nonlinear source).

The qudit state can be an useful resource for quantum communication. One of the main challenges in quantum communication is to deal with the losses experienced by the photons while they travel in fibers across long distances (e.g. hundreds of kilometers). A d-level encoding, rather than the qubits two-level encoding, allows to transfer the same amount of information using a small amount of carriers, thus reducing the impact of photon losses [105]. As instance, it has been shown theorically that a Quantum Key Distribution (QKD) protocol based on d-dimensional carriers offer a secret key rate and robustness to noise that increase with d [189, 190]. Furthermore, a feasible QuDit QKD protocol has been proposed in [191], where photon-counting spectrometers and phase modulators are used to implement frequency and arrival-time measurements on the frequency entangled modes shared between Alice and Bob.

The second feature of the state (5.37) is that it encodes information in the frequency degree of freedom. Contrary to polarization encoding, frequency is not vulnerable to polarization fluctuations occurring in standard (non polarization maintaining) optical fibers. As a counterpart, the implementation of frequency

QKD requires non trivial setup, like the photon-counting spectrometers proposed in [191], more expensive than the typical setup used in polarization encoding QKD.

Chapter 6

Manipulation of the biphoton state path symmetry

In this chapter we propose and demonstrate a scheme to generate frequency-comb biphoton states whose frequency and path components have a specific symmetry under particle exchange. This scheme is based on a type-II SPDC nonlinear process pumped by a monochromatic beam, a cavity and a delay line.

We analyze this scheme using three complementary descriptions:

1. Path-frequency, in which we explicitly calculate the wavefunction of the biphoton state as it propagates through the optical setup.
2. JSA symmetry, where we focus on the symmetry of the biphoton JSA.
3. Time-path, where we use Feynman space-time paths, by extending an analysis made by Ou in reference [101].

In the last part of the chapter, we implement this scheme by using an AlGaAs waveguide, which integrates the nonlinear source and the cavity. We demonstrate symmetry control by performing a HOM interference experiment.

6.1 Background and principle

Biphoton states entangled in more than one degree of freedom (DOF) have already demonstrated to be useful resources for quantum information [192]. As instance, for biphoton states containing two degrees of freedom (DOFs), the symmetry of the first DOF can be manipulated by accessing to the second one of the biphoton state.

So far, schemes based on either spatial distribution of the pump electric-field [193] or Orbital Angular Momentum (OAM) [194] have been realized. However, such schemes are not easily integratable, since spatial filtering and manipulation are hard to achieve in fully integrated devices such as waveguides and optical fibers.

In the prospective of future on-chip miniaturization, frequency is a good candidate as a manipulating DOF, since it is robust against decoherence and can be manipulated using on-chip electro-optic modulators and filters. In analogy to the symmetry manipulation based on the electric field spatial distribution or OAM, the frequency space has to be discretized to be used as a resource for the state symmetry manipulation. The discretization of the biphoton frequency space can be achieved by placing a cavity after or around a nonlinear source (see chapter (5)). In this work we use a more compact solution exploiting an AlGaAs waveguide that acts at the same time as the nonlinear material and the cavity.

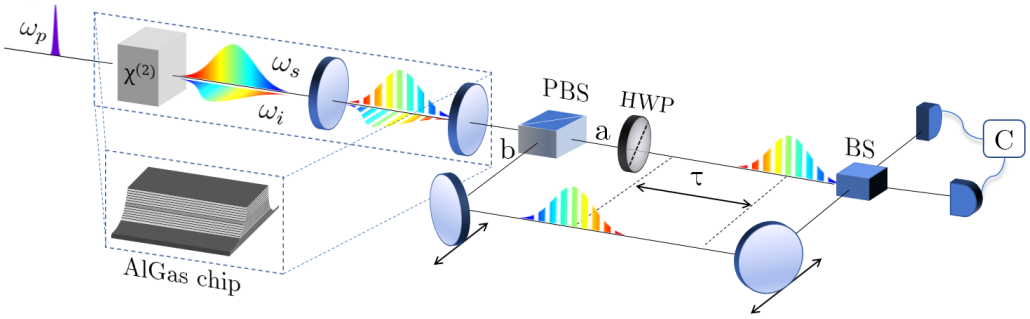

Figure 6.1 – Scheme for the manipulation of a biphoton frequency-comb state. An AlGaAs waveguide, implementing a type-II SPDC crystal and a Fabry-Perot cavity, is used to generate a biphoton frequency-comb state. A polarizing beam splitter (PBS) separates the two orthogonally polarized photons into two arms (a, b). A half-wave plate (HWP) makes the two photons indistinguishable in polarization and a delay line, represented by two movable mirrors in b, introduces a delay (τ) between the two photons. To read the result of the state manipulation, a beam splitter (BS) makes the biphoton state interferes with itself. The result of the interference is measured in a temporal correlation measurement (C) performed using two single-photon detectors.

The manipulation scheme is shown in the sketch of figure (6.1). We pump an AlGaAs chip with a monochromatic pump beam at the frequency ω_p to generate a frequency-comb biphoton state, entangled in both frequency and polarization. Given that signal and idler are orthogonally polarized, the polarization DOF can be easily transformed by a polarization beam splitter (PBS) into a path DOF. In our optical setup, the two paths correspond to the interferometers arms, indicated by a and b. By introducing a length difference among a and b, we introduce a delay between signal and idler photons. For specific values of this delay, the wavefunction symmetry in frequency and path can be manipulated.

At time delays τ odd multiple of half the cavity round-trips, the path part of the resonant (anti-resonant) frequency-comb state is a $|\Psi^+\rangle$ ($|\Psi^-\rangle$) Bell state. Since $|\Psi^+\rangle$ ($|\Psi^-\rangle$) is symmetric (anti-symmetric), we refer to this state as bosonic (fermionic).

To read the outcome of the manipulation scheme, we rely on Hong-Ou-Mandel interference. The symmetry of the path part of the state determines the behavior of the biphoton state when it interferes with itself in a beam splitter (BS) in a

coincidence measurement. A bosonic biphoton condenses on a single path mode: the two photons exit from the same arm of the beam splitter (bunching). On the contrary, in the case of a fermionic state, the beam splitter is transparent for the biphoton state: the two photons exit from different output paths (anti-bunching).

6.2 Path-frequency description

In this section we explicitly calculate the wavefunction of the emitted biphoton frequency-comb state while it propagates through the HOM setup shown in figure (6.1). The goal is to illustrate the manipulation of the symmetry and path components of the state.

Our source emits a biphoton state $|\Psi\rangle$ entangled in both polarization $|\psi_{polarization}\rangle$ [160] and frequency $|\psi_{frequency}\rangle$ via a type-II SPDC process in a CW monochromatic pump regime. The frequency distribution of the two entangled photons is described by the JSA function, which in the following we indicate as $C_{H,V}(\omega_1, \omega_2)$.

The source implements collinear SPDC and the photon pairs are emitted along the direction and sense of propagation of the pump beam, which propagates back and forth in the waveguide as it is reflected at its input and output facets. We only collect the photon pairs coming from the waveguide output facet, discarding the photons emitted from the waveguide input facets. So we post-select only signal and idler photons that are in the same path mode, namely the waveguide input to output direction.
By taking into account both polarization and frequency DOFs, following the type-II phase matching process, the wavefunction of the emitted state reads:

$$\begin{aligned} |\Psi\rangle =& \frac{1}{\sqrt{2}} \iint d\omega_1 d\omega_2 C_{H,V}(\omega_1, \omega_2) \hat{a}_H^\dagger(\omega_1) \hat{a}_V^\dagger(\omega_2) |00\rangle \\ =& \frac{1}{\sqrt{2}} \iint d\omega_1 d\omega_2 C_{H,V}(\omega_1, \omega_2) |H, \omega_1\rangle |V, \omega_2\rangle \end{aligned} \tag{6.1}$$

where $\hat{a}_H^\dagger(\omega_1)$ and $\hat{a}_V^\dagger(\omega_2)$ are the creation operators for signal and idler photons, respectively.

We observe that when the JSA function $C_{H,V}(\omega_1, \omega_2)$ is perfectly mirror symmetric with respect to the degeneracy frequency (i.e. $C_{H,V}(\omega_1, \omega_2) = C_{H,V}(\omega_2, \omega_1)$), the state (6.1) can be written as a the sum of Bell states $|\Psi^+\rangle$:

$$\begin{aligned} |\Psi\rangle &= \iint_D d\omega_1 d\omega_2 C_{H,V}(\omega_1, \omega_2) \Big(|H, \omega_1\rangle |V, \omega_2\rangle + |V, \omega_1\rangle |H, \omega_2\rangle \Big) \\ &= \iint_D d\omega_1 d\omega_2 C_{H,V}(\omega_1, \omega_2) \Big| \Psi^+, \omega_1, \omega_2 \Big\rangle \end{aligned} \tag{6.2}$$

with:

$$D = \{ (\omega_1, \omega_2) |\ \omega_1 > 0,\ \omega_2 > \omega_1 \} \tag{6.3}$$

Analogously, when $C_{H,V}(\omega_1, \omega_2)$ is perfectly mirror anti-symmetric with respect to the degeneracy frequency, the state can be decomposed into Bell states $|\Psi^-\rangle$:

$$\begin{aligned} |\Psi\rangle &= \iint_D d\omega_1 d\omega_2 C_{H,V}(\omega_1, \omega_2)\Big(|H, \omega_1\rangle |V, \omega_2\rangle - |V, \omega_1\rangle |H, \omega_2\rangle \Big) \\ &= \iint_D d\omega_1 d\omega_2 C_{H,V}(\omega_1, \omega_2) \left|\Psi^-, \omega_1, \omega_2\right\rangle \Big) \end{aligned} \tag{6.4}$$

On the contrary, when $C_{H,V}(\omega_1, \omega_2)$ does not possess any mirror symmetry with respect to degeneracy point (i.e. $C_{H,V}(\omega_1, \omega_2)C_{H,V}(\omega_2, \omega_1) = 0 \ \forall \ (\omega_1, \omega_2)$), the state cannot be decomposed in a Bell states basis since it lacks of polarization entanglement (even if, as long as it satisfies $C_{H,V}(\omega_1, \omega_2) \neq C_H(\omega_1)C_V(\omega_2)$, it has frequency entanglement).

The analysis of these three examples shows us that, in a biphoton state emitted by a type-II SPDC process, the degree of entanglement and the symmetry of the polarization state depend on the JSA symmetry on the $\omega_- = \omega_1 - \omega_2$ direction.

More generally, we can rewrite the state in equation (6.1) using the Bell states $|\Psi^+\rangle$,$|\Psi^-\rangle$ as a basis:

$$\begin{aligned} |\Psi\rangle =& \frac{1}{\sqrt{2}} \iint d\omega_1 d\omega_2 \frac{C_{H,V}(\omega_1, \omega_2)}{2}\Big(2 |H, \omega_1\rangle |V, \omega_2\rangle + \\ &+ |V, \omega_1\rangle |H, \omega_2\rangle - |V, \omega_1\rangle |H, \omega_2\rangle \Big) \\ =& \frac{1}{\sqrt{2}} \iint d\omega_1 d\omega_2 \frac{C_{H,V}(\omega_1, \omega_2)}{2}\Big(\left|\Psi^+, \omega_1, \omega_2\right\rangle + \left|\Psi^-, \omega_1, \omega_2\right\rangle \Big) \end{aligned} \tag{6.5}$$

when the JSA is anti-symmetric, the integral in $|\Psi^+, \omega_1, \omega_2\rangle$ is zero and the state is given by a sum of $|\Psi^-, \omega_1, \omega_2\rangle$ states (equation (6.2)). Viceversa, when the JSA is symmetric, the integral in $|\Psi^-, \omega_1, \omega_2\rangle$ is zero and the state is given by a sum of $|\Psi^+, \omega_1, \omega_2\rangle$ states (equation (6.4)).

While taking into consideration this decomposition of the state, we describe its propagation in the optical setup shown in figure (6.1).

A polarising beam splitter (PBS) separates the two orthogonally polarized photons into two paths. As instance, let us suppose that the horizontally polarized photon is transmitted in the path a, while the vertically polarized photon is reflected in the path b. The associated transformation is:

$$\begin{cases} |H\rangle \rightarrow |a_H\rangle \\ |V\rangle \rightarrow i\,|b_V\rangle \end{cases} \tag{6.6}$$

We suppose that the state (6.1) is entangled in polarization (i.e. $C_{H,V}(\omega_1, \omega_2)$ is symmetric with respect to the degeneracy frequency). In this case, the PBS transforms the polarization entanglement into path entanglement. The biphoton

state is now path entangled among the two interferometer arms, the upper arm a and lower arm b, as labeled in the scheme of figure (6.1). The state is:

$$|\Psi\rangle = |\psi_{path}\rangle \otimes |\psi_{frequency}\rangle = \frac{i}{\sqrt{2}} \iint d\omega_1 d\omega_2 C_{H,V}(\omega_1, \omega_2) \, |a_H, \omega_1\rangle \, |b_V, \omega_2\rangle \tag{6.7}$$

To make the two photons indistinguishable, we place a half-wave plate (HWP) in the path a to rotate the polarization of the incoming photon by $\pi/2$, according to the transformation:

$$\begin{cases} |a_H, \omega_1\rangle \rightarrow |a_V, \omega_1\rangle \\ |b_V, \omega_2\rangle \rightarrow |b_V, \omega_2\rangle \end{cases} \tag{6.8}$$

To keep a light notation, we omit the global phase term resulting from this polarization rotation since it does not affect the symmetry of the biphoton state. As the two photons are now in the same polarization state, we can omit the polarization labels and only use the path ones:

$$|\Psi\rangle = \frac{i}{\sqrt{2}} \iint d\omega_1 d\omega_2 C_{H,V}(\omega_1, \omega_2) \, |a, \omega_1\rangle \, |b, \omega_2\rangle \tag{6.9}$$

We introduce an optical delay in arm b, so the two photons are delayed by $\tau = t_2 - t_1$:

$$\begin{aligned} |a, \omega_1\rangle &\rightarrow e^{-i\omega_1 t_1} \, |a, \omega_1\rangle \\ |b, \omega_2\rangle &\rightarrow e^{-i\omega_2 t_2} \, |b, \omega_2\rangle = e^{-i\omega_2 (t_1 + \tau)} \, |b, \omega_2\rangle \end{aligned} \tag{6.10}$$

The biphoton state after the temporal delay line is:

$$|\Psi\rangle = \frac{i}{\sqrt{2}} \iint d\omega_1 d\omega_2 e^{-i(\omega_1 + \omega_2) t_1} e^{-i\omega_2 \tau} C_{H,V}(\omega_1, \omega_2) \, |a, \omega_1\rangle \, |b, \omega_2\rangle \tag{6.11}$$

We now suppose to pump the device in CW regime. In this case the condition $\omega_1 + \omega_2 = \omega_p$ determines a strong anti-correlation along the anti-diagonal direction $\omega_- = \omega_1 - \omega_2$. At a fixed pump frequency, the frequency state depends only on the variable ω_-, as we can approximate $\omega_+ \rightarrow \omega_p$. Thus we express the JSA in the 45° rotated frequency basis (ω_+,ω_-), according to transformation (2.3).

To highlight the role of the cavity, for the moment we ignore the phase matching contribution by supposing a negligible phase-mismatch $\Delta k = 0$ (i.e. the phase matching term is unitary over an infinite bandwidth). In the case of our source, the JSA expressed in (5.30) simplifies into:

$$C_{H,V}(\omega_+, \omega_-) = \delta(\omega_+ - \omega_p) f_{cav}(\omega_p, \omega_-) \tag{6.12}$$

where we $f_{cav}(\omega_p, \omega_-)$ is the cavity emission function defined in (5.35).

The double integral in equation (6.11) simplifies into a single integral which depends only on the frequency difference ω_-:

$$|\Psi\rangle = \frac{i}{\sqrt{2}} e^{-i\omega_p(t_1+\tau/2)} \int d\omega_- f_{cav}(\omega_p, \omega_-) e^{i\omega_-\tau/2} \left|a, \frac{\omega_p+\omega_-}{2}\right\rangle \left|b, \frac{\omega_p-\omega_-}{2}\right\rangle \tag{6.13}$$

To keep a light notation, we rewrite the state vectors neglecting the biphoton central frequency:

$$\left|a, \frac{\omega_p+\omega_-}{2}\right\rangle \left|b, \frac{\omega_p-\omega_-}{2}\right\rangle = \left|a, \omega_d+\frac{\omega_-}{2}\right\rangle \left|b, \omega_d-\frac{\omega_-}{2}\right\rangle \rightarrow \left|a, \frac{\omega_-}{2}\right\rangle \left|b, -\frac{\omega_-}{2}\right\rangle \tag{6.14}$$

Since the manipulation scheme relies on the discretization of the frequency space, we start by considering the ideal case, given by a nonlinear cavity with high-reflecting facets, with $R \rightarrow 1$.

In this case, we can approximate $f_{cav}(\omega_p, \omega_-)$ as a train of Dirac deltas functions along ω_-.

The position of the Fabry-Perot peaks depends on the biphoton state resonance condition with respect to the cavity. We express ω_- in unit of the cavity free spectral range $\Delta\omega_{fsr}$, given by:

$$\Delta\omega_{fsr} = \frac{2\pi}{\tau_{RT}} \tag{6.15}$$

with τ_{RT} previously defined in expression (5.4).

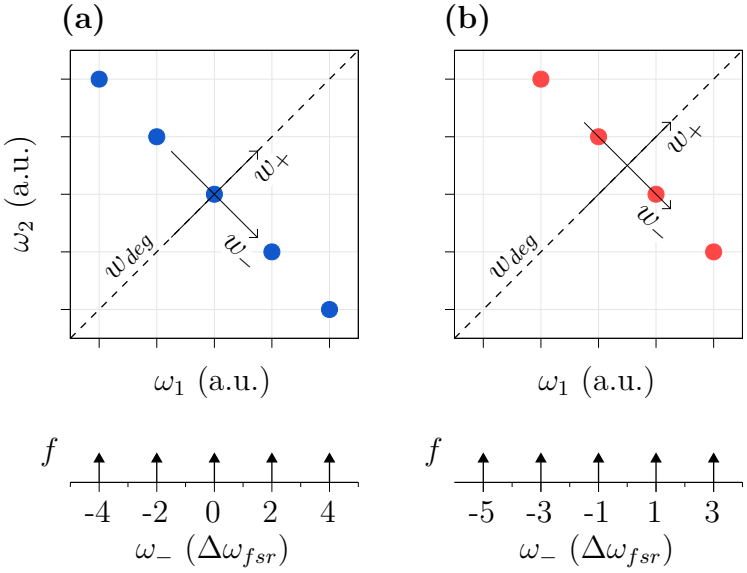

Figure 6.2 – Sketch of the JSA in CW pumping regime for two different pump frequencies. Blue (red) color indicates a positive (negative) amplitude.
(a) Resonant state.
(b) Anti-resonant state.

Following the definition of ω_- (2.3), the distance between consecutive Fabry-Perot peaks in $f_{cav}(\omega_p, \omega_-)$ is $2\Delta\omega_{fsr}$.

When the biphoton state is resonant (figure (6.2, a)), peaks are distributed at odd multiple of $\Delta\omega_{fsr}$:

$$f_R(\omega_-) = \frac{1}{2d} \sum_{m=-d}^{d} \delta\Big(\omega_- - 2m\Delta\omega_{fsr}\Big) \tag{6.16}$$

On the contrary, if the biphoton state is anti-resonant (figure (6.2, b)), the central frequency $\omega_- = 0$, namely the degeneracy frequency $\omega_1 = \omega_2 = \omega_d$, does not belong to the cavity resonances, which occupy the even multiple of $\Delta\omega_{fsr}$ along ω_-:

$$f_{AR}(\omega_-) = \frac{1}{(2d-1)} \sum_{m=-d}^{d-1} \delta\Big(\omega_- - (2m+1)\Delta\omega_{fsr}\Big) \tag{6.17}$$

We remind that we can experimentally generate a resonant state or an anti-resonant state by tuning the monochromatic pump frequency, as demonstrated in section (5.5.2).

By substituting the expression of the cavity function (6.16) in (6.13), the state reads:

$$|\Psi_R\rangle = \frac{ie^{-i\omega_p(t_1+\tau/2)}}{2\sqrt{2}d} \sum_{m=-d}^{d} e^{i\Delta\omega_{fsr}\tau m} \, |a, m\Delta\omega_{fsr}\rangle \, |b, -m\Delta\omega_{fsr}\rangle \tag{6.18}$$

On the other hand, by substituting the anti-resonant JSA (6.17), we find:

$$|\Psi_{AR}\rangle = \frac{ie^{-i\omega_p(t_1+\tau/2)}}{\sqrt{2}(2d-1)} \sum_{m=-d}^{d-1} e^{i\Delta\omega_{fsr}\tau(m+1/2)} \left|a, \left(m+\frac{1}{2}\right)\Delta\omega_{fsr}\right\rangle \left|b, -\left(m+\frac{1}{2}\right)\Delta\omega_{fsr}\right\rangle \tag{6.19}$$

We see that the state path symmetry depends on the phases of the complex exponential in the sum over the frequency modes.

Therefore, for a given cavity free spectral range $\Delta\omega_{fsr}$, we can manipulate such symmetry by playing on two ingredients:

1. The biphoton resonance with respect to the cavity. The resonant condition gives the state (6.18) and the anti-resonant condition the state (6.19)

2. τ, the time delay in the HOM interferometer.

Under the hypothesis that that the chromatic dispersion is negligible, the time delay does not depend on the photon frequency $\tau(\omega) = \tau$.

For the moment, we consider a time delay τ which is multiple of half of the cavity round-trip. In these conditions, we expect the biphoton state to interfere with itself, as Ou's group explained and demonstrated in [101] in the resonant case.

We further explore Feynman diagrams in section (6.4) and present a complementary analysis in section (6.3), where we study the delayed biphoton JSA.

At $\tau = n\tau_{RT}/2$, the phases of the resonant states (equation (6.18)) become:

$$\alpha_R = \Delta\omega_{fsr}\tau m = \frac{2\pi}{\tau_{RT}} n \frac{\tau_{RT}}{2} m = nm\pi = (-1)^m \pi = \pi \tag{6.20}$$

where the latter passage follows from the fact that n and m are integer numbers and we consider a phase cycle of $(-\pi, \pi)$ (i.e. $-\pi = \pi$). The state vectors have the same coefficients, thus the path part of the state (6.18) is symmetric and the state is bosonic.

On the other hand, the phases of the anti-resonant states (equation (6.19)) are:

$$\alpha_{AR} = \Delta\omega_{fsr}\tau\left(m + \frac{1}{2}\right) = \frac{2\pi}{\tau_{RT}} n \frac{\tau_{RT}}{2}\left(m + \frac{1}{2}\right) = n\left(m + \frac{1}{2}\right)\pi \tag{6.21}$$

For even values of n, this phase is a constant:

$$\alpha_{AR} = (-1)^m \pi = \pi \tag{6.22}$$

While, for odd values of n, it takes alternating opposite values:

$$\alpha_{AR} = (-1)^m \frac{\pi}{2} \tag{6.23}$$

so that the path part of the anti-resonant state (6.19) presents a fermionic symmetry.

To summarize, at time delays that are multiples of the cavity round-trip τ_{RT} ($\tau = \tau_{RT}, 2\tau_{RT}, ..$), the path path of the state is bosonic independently on the state resonance condition.

On the other hand, the most fascinating scenario occurs if:

1. The state is anti-resonant (figure (6.2 (b))
2. The time delay is an odd multiple of half of the cavity round-trip $\tau_{RT}/2$ ($\tau = 1/2\tau_{RT}, 3/2\tau_{RT}, ..$)

In this case, the path state acquires a fermionic symmetry.

We remind that, in both resonant and anti-resonant cases, the biphoton state emitted by our source (equation (6.2)) has a symmetric JSA, corresponding to a polarization (path after the PBS) part with a bosonic symmetry. If the time-delay is an odd multiple of half of the cavity round-trip and the state is anti-resonant, the path part of the state transforms from bosonic to fermionic. Since the biphoton wavefunction must be bosonic, the JSA transforms from even to odd, as we show in section (6.3).

We underline that the use of a monochromatic pump and the resulting frequency entanglement are necessary ingredients for the symmetry manipulation.

While the cavity patterns the biphoton frequency space into a chess-like board, the CW pumping - through the energy conservation underlying the SPDC process - is responsible for a frequency entangled state, with a strong anti-correlation feature as shown in figure (6.3, a). In this case, the emitted state is *either* resonant (blue color in figure) *or* anti-resonant (red color in figure), and the manipulation can take place.

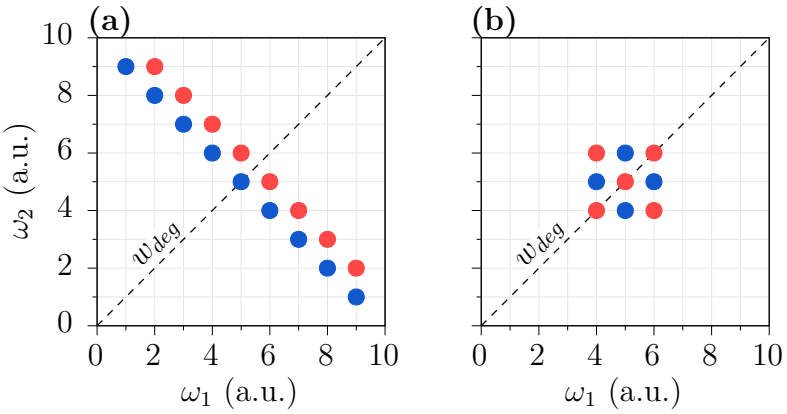

Figure 6.3 – Sketches of the JSA of frequency entangled and unentangled states. Blue (red) color indicates a positive (negative) amplitude.
(a) JSA of one entangled resonant state (blue) and JSA of one entangled anti-resonant state (red). Both can be generated by a monochromatic pump beam.
(b) JSA of an uncorrelated state, generated by a large bandwidth pump.

Conversely, a short-pulse (large bandwidth) pumping regime would generate a biphoton state with a lower or even zero degree of frequency entanglement (which can be evaluated in a Schmidt modes decomposition). As instance, we show in figure (6.3, b) a state that has no frequency entanglement. In this case, the JSA function is a superposition of *both* resonant *and* anti-resonant states. The biphoton quantum interference at the beam splitter would give both bunching and anti-bunching, which compensate each other. As instance, this has been demonstrated in [193], in a manipulation scheme of the polarization DOF based on the engineering of the pump spatial distribution.

We progress now on the study of the evolution of the state. In the setup sketched in figure (6.1), we see that after the interferometer delay line, the biphoton state arrives at the 50/50 beam splitter, where it interferes with itself. This interference depends on the symmetry under particle exchange of the path component of the state [158, 157], so that we can consider the beam splitter as a reader of the

biphoton path symmetry. Indeed, the beam splitter transforms a path symmetric state (symmetric JSA) into a N00N (N=2) Fock state ($|2\rangle|0\rangle + |0\rangle|2\rangle$), and a path anti-symmetric state (anti-symmetric JSA) into a $|1\rangle|1\rangle + |1\rangle|1\rangle$ Fock state. Following transformation (1.28), the path wavevectors transform according to:

$$\begin{cases} |a\rangle \rightarrow \frac{1}{\sqrt{2}}(|a\rangle + i\,|b\rangle) \\ |b\rangle \rightarrow \frac{1}{\sqrt{2}}(i\,|a\rangle + |b\rangle) \end{cases} \tag{6.24}$$

Applying the beam splitter transformation to equation (6.11), we find the expression of the state after the beam splitter:

$$\begin{aligned} |\Psi\rangle = \frac{i}{\sqrt{2}} \iint & d\omega_1 d\omega_2 e^{-i(\omega_1+\omega_2)t_1} e^{-i\omega_2\tau} C_{H,V}(\omega_1,\omega_2) \\ & \Big[i\Big(|a,\omega_1\rangle\,|a,\omega_2\rangle + |b,\omega_1\rangle\,|b,\omega_2\rangle \Big) + \Big(|a,\omega_1\rangle\,|b,\omega_2\rangle - |b,\omega_1\rangle\,|a,\omega_2\rangle \Big) \Big] \\ = \frac{i}{\sqrt{2}} \iint & d\omega_1 d\omega_2 e^{-i(\omega_1+\omega_2)t_1} e^{-i\omega_2\tau} C_{H,V}(\omega_1,\omega_2) \Big[i\,|\psi_b\rangle + |\psi_f\rangle \Big] \end{aligned} \tag{6.25}$$

The two possible outcomes are highlighted. The first is the N00N state with N=2, which we label as $|\psi_b\rangle$ to indicate its bosonic nature. The second is the anti-symmetric state, which we call as $|\psi_f\rangle$ to indicate its fermionic nature.

Equation (6.25) shows that the JSA symmetry determines the outcome of the biphoton interference at the beam splitter. To evaluate the correlation between the two paths a and b, we post-select the state $|\Psi\rangle$ choosing the fermionic state $|\psi_f\rangle$. The relationships among the eigenvalues of $|\psi_f\rangle$ gives the correlation between the two output ports of the beam splitter. When the JSA is symmetric, the coefficients which multiply $|a,\omega_1\rangle\,|b,\omega_2\rangle$ and $|b,\omega_1\rangle\,|a,\omega_2\rangle$ are exactly the opposite, so we expect a zero correlation. The two photons never exit from the same output port: bunching occurs. On the other hand, when the JSA is anti-symmetric, these coefficients are identical, so the paths correlation is the highest. If we consider a normalized JSA, this correlation takes the value of one. We define this scenario where the two photons always take different paths as anti-bunching.

To experimentally study the correlation between the two path modes, we place one single-photon detector on the output port a and another single-photon detector on the output port b (figure 6.1). This measurement scheme cannot detect the bosonic state $|\psi_b\rangle$ so that it post-selects the state $|\Psi\rangle$, which becomes:

$$\begin{aligned} |\Psi\rangle &= \frac{i}{\sqrt{2}} \iint d\omega_1 d\omega_2 e^{-i(\omega_1+\omega_2)t_1} e^{-i\omega_2\tau} C_{H,V}(\omega_1,\omega_2)\,|\psi_f\rangle \\ &= \frac{i}{\sqrt{2}} \iint d\omega_1 d\omega_2 A(\omega_1,\omega_2,\tau)\,|\psi_f\rangle \end{aligned} \tag{6.26}$$

where the term $A(\omega_1,\omega_2,\tau)$ groups the state dependence on the biphoton JSA and HOM delay. For simplicity, we suppose that each detector has a flat frequency

response within the biphoton frequency bandwidth. The operator associated to the correlation measurement is [195]:

$$\hat{M} = \int d\omega_a \hat{a}^\dagger(\omega_a) \left|0\right\rangle_a \left\langle 0\right|_a \hat{a}(\omega_a) \int d\omega_b \hat{b}^\dagger(\omega_b) \left|0\right\rangle_b \left\langle 0\right|_b \hat{b}(\omega_b) \tag{6.27}$$

The correlation measurement leads to:

$$\begin{aligned} p_{ab}(\tau) = \left\langle \Psi \right| \hat{M} \left| \Psi \right\rangle =& \frac{1}{8}\Big[\int d\omega_1' \int d\omega_2' A^*(\omega_1', \omega_2', \tau) \left\langle \psi_f \right| \Big] \hat{M} \Big[\int d\omega_1 \int d\omega_2 A(\omega_1, \omega_2, \tau) \left| \psi_f \right\rangle \Big] \\ =& \frac{1}{8} \int d\omega_1 \int d\omega_2 \int d\omega_1' \int d\omega_2' \int d\omega_a \int d\omega_b A^*(\omega_1', \omega_2', \tau) A(\omega_1, \omega_2, \tau) \\ & \Big[\delta(\omega_1' - \omega_a)\delta(\omega_2' - \omega_b) - \delta(\omega_1' - \omega_b)\delta(\omega_2' - \omega_a) \Big] \\ & \Big[\delta(\omega_1 - \omega_a)\delta(\omega_2 - \omega_b) - \delta(\omega_2 - \omega_a)\delta(\omega_1 - \omega_b) \Big] \end{aligned} \tag{6.28}$$

After substituting $A(\omega_1, \omega_2, \tau)$, integrating along $\omega_a, \omega_b, \omega_1', \omega_2'$ and using the normalization of the JSA ($|C_{H,V}(\omega_1, \omega_2)|^2 = |C_{H,V}(\omega_2, \omega_1)|^2 = 1$), we can simplify the former expression and obtain the well-known HOM correlation probability:

$$p_{ab}(\tau) = \frac{1}{2}\Big[1 - Re\Big[\iint d\omega_1 d\omega_2 C_{H,V}^*(\omega_1, \omega_2) C_{H,V}(\omega_2, \omega_1) e^{-i(\omega_1 - \omega_2)\tau} \Big] \Big] \tag{6.29}$$

Under the hypothesis of JSA with a mirror symmetry, equation (6.29) further simplifies into:

$$p_{ab}(\tau) = \frac{1}{2}\Big[1 - Re\Big[\iint d\omega_1 d\omega_2 |C_{H,V}(\omega_1, \omega_2)|^2 e^{-i(\omega_1 - \omega_2)\tau} \Big] \Big] \tag{6.30}$$

We see in equation (6.30) that the correlation probability depends on the difference in frequency between signal and idler photons. We rewrite the JSA in the (ω_+, ω_-) basis, following the transformation (2.3). Furthermore, we suppose to be under CW pumping regime. Substituting the expression of the JSA (6.12), the correlation probability simplifies into:

$$\begin{aligned} p_{ab}(\tau) &= \frac{1}{2}\Big[1 - Re\Big[\iint d\omega_+ d\omega_- C^*(\omega_+, \omega_-) C(\omega_+, -\omega_-) e^{-i\omega_- \tau} \Big] \Big] \\ &= \frac{1}{2}\Big[1 - Re\Big[\int d\omega_- |f_{cav}(\omega_p, \omega_-)|^2 e^{-i\omega_- \tau} \Big] \Big] \end{aligned} \tag{6.31}$$

where f_{cav} is the cavity transmission function along ω_-, at the pumping frequency ω_p. We note that equation (6.31) is a particular case of the HOM coincidences probability expressed in (1.30) in the case of our source, i.e. a waveguide-cavity under CW pumping regime.

High reflectivity and infinite bandwidth

In this paragraph we study the influence of the biphoton resonance condition on the HOM interferometry measurement.

As done previously, we consider an ideal cavity for which $R \to 1$, so that $|f_{cav}|^2$ can be written as a train of Dirac delta functions. When the state is resonant, the analytical solution of the HOM correlation probability reads:

$$\begin{aligned} p_{R,ab}(\tau) &\approx \frac{1}{2}\Big[1 - \frac{1}{2d}\sum_{m=-d}^{d} Re\Big[\int d\omega_- \delta(\omega_- - 2m\bar{\omega}) e^{-i\omega_-\tau}\Big]\Big] \\ &= \frac{1}{2}\Big[1 - \frac{1}{2d}\sum_{m=-d}^{d} \cos(2m\bar{\omega}\tau)\Big] \\ &= \frac{1}{2}\Big[1 - \frac{1}{2d}\sum_{m=-d}^{d} \cos\Big(4\pi m\frac{\tau}{\tau_{RT}}\Big)\Big] \end{aligned} \tag{6.32}$$

and in the anti-resonant case:

$$\begin{aligned} p_{AR,ab}(\tau) &\approx \frac{1}{2}\Big[1 - \frac{1}{2d+1}\sum_{m=-d}^{d+1} Re\Big[\int d\omega_- \delta[\omega_- - (2m+1)\bar{\omega}] e^{-i\omega_-\tau}\Big]\Big] \\ &= \frac{1}{2}\Big[1 - \frac{1}{2d+1}\sum_{m=-d}^{d+1} \cos[(2m+1)\bar{\omega}\tau]\Big] \\ &= \frac{1}{2}\Big[1 - \frac{1}{2d+1}\sum_{m=-d}^{d+1} \cos\Big[2(2m+1)\pi\frac{\tau}{\tau_{RT}}\Big]\Big] \end{aligned} \tag{6.33}$$

If the JSA is resonant ($m = 2n$, figure (6.2, b)), the cosine in equation (6.32) is equal to 1 for every m, so $p_{ab}(\tau) = 0$ and there is photon coalescence. Indeed, the path part of the biphoton wavefunction at the beam splitter is symmetric. so bunching occurs.

As before, we consider time delays which are multiple of half of the cavity round-trip. By plugging $\tau = \tau_{RT}(2n+1)/2$ ($n \in N$), for every m, the cosine in equation (6.32) is equals to one, while the cosine in equation (6.33) is equals to minus one.

The resulting correlation probability is:

$$p_{ab}\Big(\frac{\tau_{RT}(2n+1)}{2}\Big) = \begin{cases} 0 \text{ at resonance (figure (6.2, a))} \\ 1 \text{ at anti-resonance (figure (6.2, b))} \end{cases} \tag{6.34}$$

In the case of a delayed resonant (anti-resonant) state we observe a HOM coalescence (anti-coalescence) pattern, which confirms that bunching (anti-bunching) occurs.

biphoton resonance	**Path Symmetry at BS**	**Interference Outcome**
Resonant	Symmetric	Bunching
Anti-resonant	Anti-symmetric	Anti-bunching

Table 6.1 – biphoton state features and corresponding outcome of the HOM interference for odd half-cavity round-trip time delays.

Table (6.1) summarizes the experimental HOM outcome as a function of the biphoton state resonance condition and related symmetry of the path state at the beam splitter for a delay of $\tau = \tau_{RT}(2n+1)/2$.

To conclude our path-frequency analysis, we comment briefly on the dimensionality of the frequency-comb required for the manipulation of the state symmetry. We can observe that the expressions of the correlation probability (6.32),(6.33) do not depend on d, the number of comb teeth in the biphoton frequency state, given that $d \geq 2$.

In the bosonic scenario, the presence of a single comb tooth is enough. Indeed, when the state is resonant (figure (6.2, a)), $m = 2n$. The trivial case $m = 0$, corresponding to the presence of one resonance, is sufficient for the biphoton state to exist and interference to take place.

In the fermionic scenario, the presence of at least two comb teeth is necessary. When the state is anti-resonant (figure (6.2, b)), $m = 2n + 1$, so $m \geq 1$, with $m = 1$ corresponding to the presence of two resonances. As long as the bandwidth of the biphoton state is larger than two times the cavity free spectral range, the discretization of its JSA can take place.

It follows that the manipulation of the state symmetry does not require a high-dimensional qudit. On the other hand, it is compatible with high-dimensional frequency-comb states. The only requirements is that the birefringence is negligible within the biphoton JSA bandwidth. Indeed, birefringence would degrade the state symmetry and thus the interference visibility, as we will see in section (6.6).

6.3 Joint Spectral Amplitude symmetry description

Previously, we demonstrated how to manipulate the symmetry of the path part of the state by following the evolution of the total biphoton frequency-comb wavefunction. In this paragraph we propose a more compact demonstration based only on the analysis of the wavefunction symmetry. The underlying principle is that the biphoton wavefunction $|\Psi\rangle$ must posses a bosonic symmetry under particle exchange, since photons, due to their integer spin, are bosonic particles [158]. After the polarizing beam splitter (PBS in the scheme of figure (6.1)), as indicated in equation (6.7), the biphoton state includes a frequency and a path component: $|\Psi\rangle = |\psi_{path}\rangle \otimes |\psi_{frequency}\rangle$. Therefore, if $|\psi_{frequency}\rangle$ is symmetric, $|\psi_{path}\rangle$ must be symmetric as well. Viceversa, when $|\psi_{frequency}\rangle$ is anti-symmetric, $|\psi_{path}\rangle$ must be anti-symmetric so that the total wavefunction $|\Psi\rangle$ is symmetric. By controlling the symmetry of $|\psi_{frequency}\rangle$, we can tune the symmetry of $|\psi_{path}\rangle$, which is responsible for the behavior of the biphoton state at the beam splitter: a symmetric $|\psi_{path}\rangle$ gives bunching, while an anti-symmetric $|\psi_{path}\rangle$ anti-bunching. In the following we show how to control the symmetry of $|\psi_{frequency}\rangle$ in a frequency-comb biphoton state, by delaying one photon with respect to the other and finely tuning the pumping wavelength with respect to the cavity resonances.

So let consider $|\psi_{frequency}\rangle$ emitted by a nonlinear cavity source. As we can

see in equation (6.37), $|\psi_{frequency}\rangle$ is completely described by the biphoton JSA, $C_{H,V}(\omega_1, \omega_2)$. Following the scheme in figure (6.1), we study how the JSA evolves in the HOM experiment.

To simplify our demonstration, for the moment we also ignore the source birefringence. In this condition, the JSA is mirror-symmetric along the degeneracy direction ($\omega_1 = \omega_2 = \omega_d$), so we rewrite it as: $C_{H,V}(\omega_1, \omega_2) = C_{V,H}(\omega_1, \omega_2) = C(\omega_1, \omega_2)$. We separate the two photons by means of a PBS and make the two polarization identical by means of a HWP. Then, we delay the first photon (identified by the frequency ω_1) with respect to the second one (identified by the frequency ω_2), by a time delay τ. While the biphoton Joint Temporal Amplitude (JTA, the joint probability amplitude which gives the joint probability of detecting signal and idler photons at time t_s and t_i) is translated in time, the JSA acquires a phase proportional to ω_1 and the accumulated delay τ:

$$C(\omega_1, \omega_2) \rightarrow C_\tau(\omega_1, \omega_2) = C(\omega_1, \omega_2) e^{i\tau\omega_1} \tag{6.35}$$

We suppose that we are operating under CW pumping regime. We rewrite the JSA in the (ω_+, ω_-) basis, according to the transformation (2.3). In the new basis, the JSA reads:

$$C_\tau(\omega_+, \omega_-) = C(\omega_+, \omega_-) e^{i\tau\omega_+/2} e^{i\tau\omega_-/2} \tag{6.36}$$

$C(\omega_+, \omega_-)$ is the JSA of the state emitted by the cavity source. Its expression in the (ω_+, ω_-) basis is given by equation (5.30). In CW pumping regime , we can approximate $\phi_{pump}(\omega_+) \approx \delta(\omega_+ - \omega_p)$ and the biphoton state becomes:

$$\begin{aligned} |\Psi\rangle =& \iint d\omega_+ d\omega_- \delta(\omega_+ - \omega_p) \phi_{PM}(\omega_+, \omega_-) f_{cav}(\omega_+, \omega_-) e^{i\tau\omega_+/2} e^{i\tau\omega_-/2} \\ & \left| a, \frac{\omega_+ + \omega_-}{2} \right\rangle \left| b, \frac{\omega_+ - \omega_-}{2} \right\rangle \\ =& e^{i\tau\omega_p/2} \int d\omega_- \phi_{PM}(\omega_p, \omega_-) f_{cav}(\omega_p, \omega_-) e^{i\tau\omega_-/2} \left| a, \frac{\omega_p + \omega_-}{2} \right\rangle \left| b, \frac{\omega_p - \omega_-}{2} \right\rangle \end{aligned} \tag{6.37}$$

We see that the frequency part of the state is described by a reduced JSA, which, for a given pump frequency, is a function of only ω_-:

$$C_\tau(\omega_p, \omega_-) = \phi_{PM}(\omega_p, \omega_-) f_{cav}(\omega_p, \omega_-) e^{i\tau\omega_-/2} \tag{6.38}$$

Since the symmetry of $C_\tau(\omega_p, \omega_-)$ determines the photons statistics, let us analyze it by looking at the symmetry of each contributing term.

The phase matching term $\phi_{PM}(\omega_p, \omega_-)$ is a real function (see chapter (2)). When the chromatic dispersion is negligible and the modal birefringence is zero, it is symmetric with respect to ω_- (equation (2.24)).

The cavity transmission function $f_{cav}(\omega_p, \omega_-)$, defined in (5.34), is a complex-valued function*. Under the hypothesis that the source has no birefringence, it is a symmetric function, independently on the pumping frequency ω_p. For simplicity,

*when we define the parity of a complex-valued function f, we consider both real and imaginary

in the following we consider the case in which H and V-polarized photons have the same reflectivity. We also suppose that there is no chromatic dispersion, so the expression of $f_{cav}(\omega_p, \omega_-)$ is given by equation (5.35).

The delay term $e^{i\tau\omega_-/2}$ is a complex-valued function as well. Its real part, $\cos(\tau\omega_-/2)$, is symmetric, while its imaginary part, $\sin(\tau\omega_-/2)$, is anti-symmetric. The interplay between the symmetric real part and the anti-symmetric imaginary part allows the manipulation of the JSA symmetry.

The reason is that both $f_{cav}(\omega_p, \omega_-)$ and $e^{i\tau\omega_-/2}$ are periodic functions. f_{cav} has a periodicity given by the cavity optical length:

$$\Omega_{RT} = 2\pi/(\tau_{RT}/2) \tag{6.39}$$

While the period of $e^{i\tau\omega_-/2}$ depends on the accumulated delay τ:

$$\Omega_{\tau} = 2\pi/(\tau/2) \tag{6.40}$$

As a consequence, when the state is anti-resonant respect to the cavity (see equation (5.36) and figure (5.8)), by properly choosing the time delay τ, we reveal the JSA imaginary part, which is anti-symmetric, while filtering out the even real part, which is symmetric.

The evolution of the JSA with respect to the temporal delay is illustrated in figure (6.4). The JSA $C_\tau(\omega_p, \omega_-)$ of a resonant and an anti-resonant state (equation (6.38)) are illustrated for time delays of $\tau = 0$ (a, b), $\tau = \tau_{RT}/2$ (c, d), $\tau = \tau_{RT}$ (e, f) and $\tau = 3\tau_{RT}/2$ (g, h). In the numerical calculation, we choose a cavity with a high cavity reflectivity value by setting $R = 0.95$. For clarity, we only plot a zoom of the JSA around $\omega_- = 0$. Thus the influence of the phase matching term, which acts as an envelope that is slowly varying with ω_-, is not visible.

Following the symmetry of the exponential term $e^{i\tau\omega_-/2}$, the real part of the JSA (in blue) is a symmetric function, while its imaginary part (in red) is an anti-symmetric function. Depending on the biphoton state resonance and delay time τ, either the real or imaginary part of the JSA is filtered out.

Even if the cavity is placed before the delay line, we can think that, as $R \to 1$, the cavity transmission function samples the exponential delay term. At lower values of the cavity reflectivity the sampling effect still occurs, but its effect is smeared along larger peaks in ω_-.

On the left (insets (a),(c),(e),(g)), we show the resonant JSA. Its peaks are disposed along ω_- at multiple periods of Ω_{RT}. There, independently on τ, the exponential function is always real, so the JSA is symmetric.

Conversely, the anti-resonant state has a JSA which is either real (symmetric) or imaginary (anti-symmetric) depending on τ, as we illustrate on the right (insets (b),(d),(f),(h)). The reason is that the peaks of the anti-resonant state are placed along ω_- at half-periods of Ω_{RT}. For $\tau = (2n+1)\tau_{RT}/2$ (insets (d), (h)), the

---

parts:
$f(x)$ symmetric (even) $\Leftrightarrow \mathrm{Re}[f(x)] = \mathrm{Re}[f(-x)]$, $\mathrm{Im}[f(x)] = \mathrm{Im}[f(-x)]$
$f(x)$ anti-symmetric (odd) $\Leftrightarrow \mathrm{Re}[f(x)] = -\mathrm{Re}[f(-x)]$, $\mathrm{Im}[f(x)] = -\mathrm{Im}[f(-x)]$

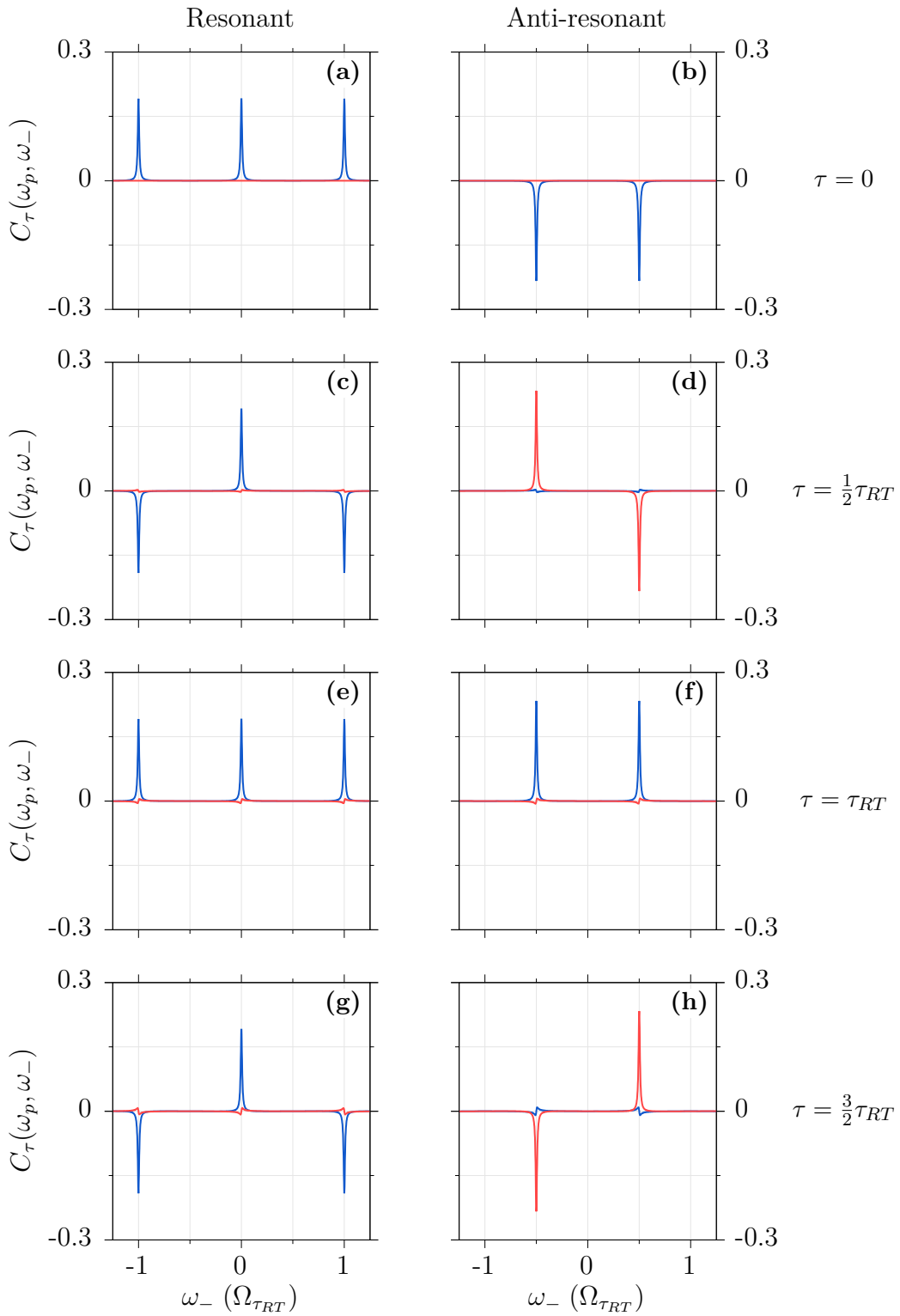

Figure 6.4 – Evolution of resonant (a, c, e, g) and anti-resonant (b, d, f, h) JSA with respect to the delay time τ, calculated for a cavity reflectivity of $R = 0.95$. In blue we indicate the JSA real part, in red the JSA imaginary part.
(a, b) $\tau = 0$, (c, d) $\tau = \tau_{RT}/2$, (e, f) $\tau = \tau_{RT}$, (g, h) $\tau = 3\tau_{RT}/2$.

cavity samples the imaginary pat of the delay function , so the resulting JSA is anti-symmetric. Viceversa, for $\tau = (2n)\tau_{RT}/2$ (insets (b), (f)), the cavity samples the real part of the exponential function, so the resulting JSA is symmetric.

The same behavior occurs periodically at longer time delays which are either even or odd multiples of the cavity half round-trip. We retrieve the same results as in equation (6.34), which we summarize in the following scheme:

$$\text{at } \tau = \frac{\tau_{RT}(2n)}{2} \begin{cases} \nearrow \text{resonant state} \rightarrow \text{symmetric JSA} \rightarrow \text{bunching} \\ \searrow \text{anti-resonant state} \rightarrow \text{symmetric JSA} \rightarrow \text{bunching} \end{cases}$$

$$\text{at } \tau = \frac{\tau_{RT}(2n+1)}{2} \begin{cases} \nearrow \text{resonant state} \rightarrow \text{symmetric JSA} \rightarrow \text{bunching} \\ \searrow \text{anti-resonant state} \rightarrow \text{anti-symmetric JSA} \rightarrow \text{anti-bunching} \end{cases} \tag{6.41}$$

By following the evolution of the state spectral symmetry, we find the same result as in the description of the complete wavefunction in the frequency and path DOFs (6.34).

We study here the case of a cavity having lower reflectivity. In figure (6.5) we plot the evolution of the JSA versus the time delay, emitted by a cavity with $R = 0.27$. The previous considerations hold, but we expect that the effect of symmetry manipulation is smeared out. The real and imaginary part of the JSA have the same order of magnitude and opposite symmetry, so their contributes to the state symmetry partially cancel out. Bunching and anti-bunching occur with a probability that is no longer close to one, so the visibility of the HOM dip or peak decreases.

We illustrate the continuous evolution of the JSA versus the accumulated time delay in figure (6.6), for a reflectivity of $R = 0.95$.

In the resonant case (top insets), the JSA is real and symmetric at multiples of half-cavity round-trip ($\tau = 0$, $0.5\tau_{RT}$, τ_{RT}, $1.5\tau_{RT}$, $2\tau_{RT}$) and imaginary and anti-symmetric for values of time delay which are in between ($\tau = 0.25\tau_{RT}$, $0.75\tau_{RT}$, $1.25\tau_{RT}$, $1.75\tau_{RT}$).

The JSA of the anti-resonant state (bottom insets) has a periodicity along τ that is double. In the anti-resonant case, the JSA is real and symmetric at even multiple of half-cavity round-trip ($\tau = 0$, τ_{RT}, $2\tau_{RT}$), and imaginary and anti-symmetric at odd multiples of half-cavity round-trip times ($\tau = 0.5\tau_{RT}$, $1.5\tau_{RT}$). The evolution of JSA with a lower reflectivity of $R = 0.27$ is illustrated in figure (6.7). As we previously commented, we see that, at a specific time delay, the JSA does not possess anymore a well-defined symmetry. Real (symmetric) and imaginary (anti-symmetric) parts have the same order of magnitude, so the visibility of the HOM replicas lowers.

To conclude our study, we can quantify the JSA symmetry with respect to the $\omega_- = 0$ axis by introducing a parameter s. Since the JSA is a complex-valued

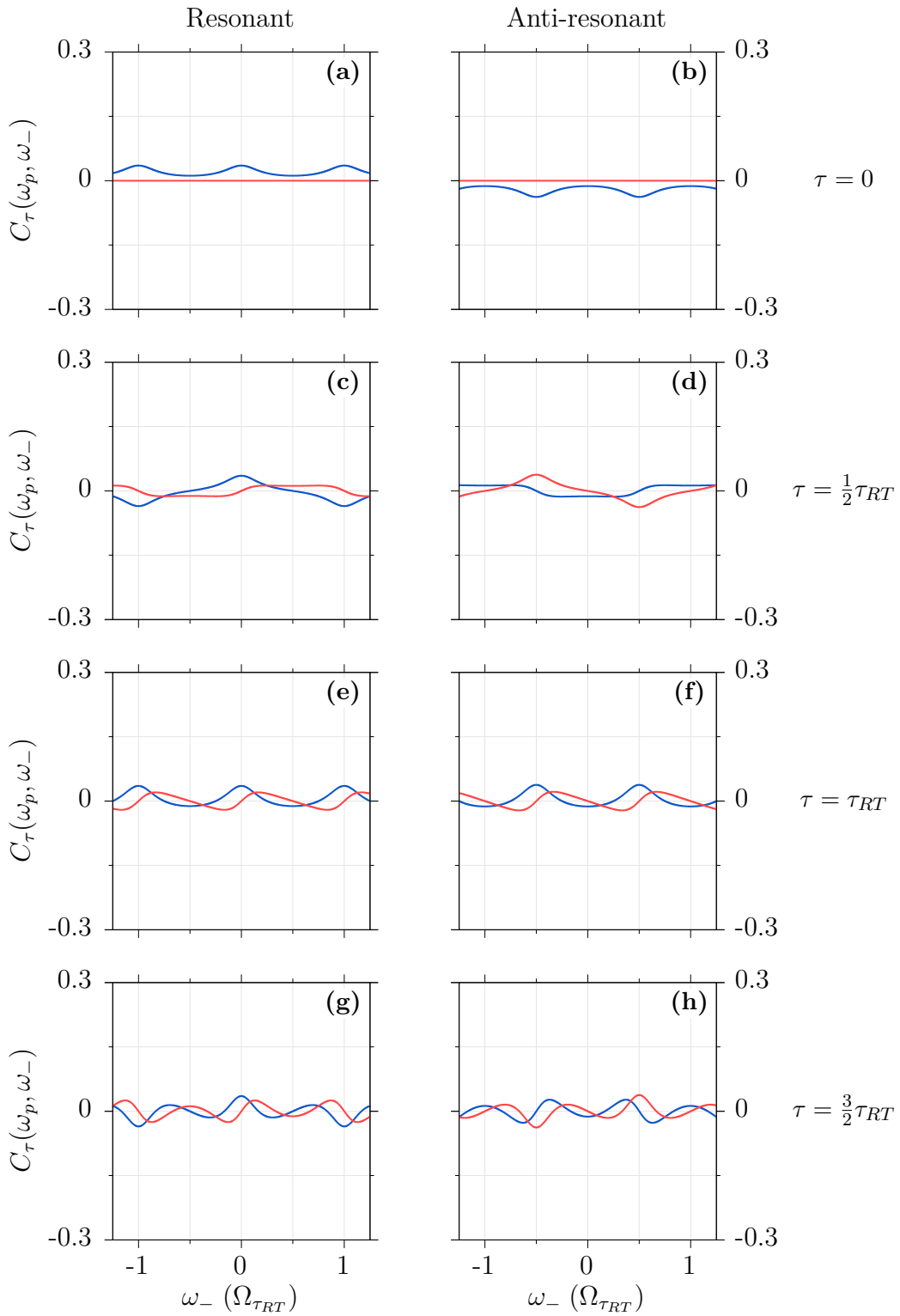

Figure 6.5 – Evolution of resonant (a, c, e, g) and anti-resonant (b, d, f, h) JSA with respect to the delay time τ, calculated for a cavity reflectivity of $R = 0.27$. In blue we indicate the JSA real part, in red the JSA imaginary part.
(a, b) $\tau = 0$, (c, d) $\tau = \tau_{RT}/2$, (e, f) $\tau = \tau_{RT}$, (g, h) $\tau = 3\tau_{RT}/2$.

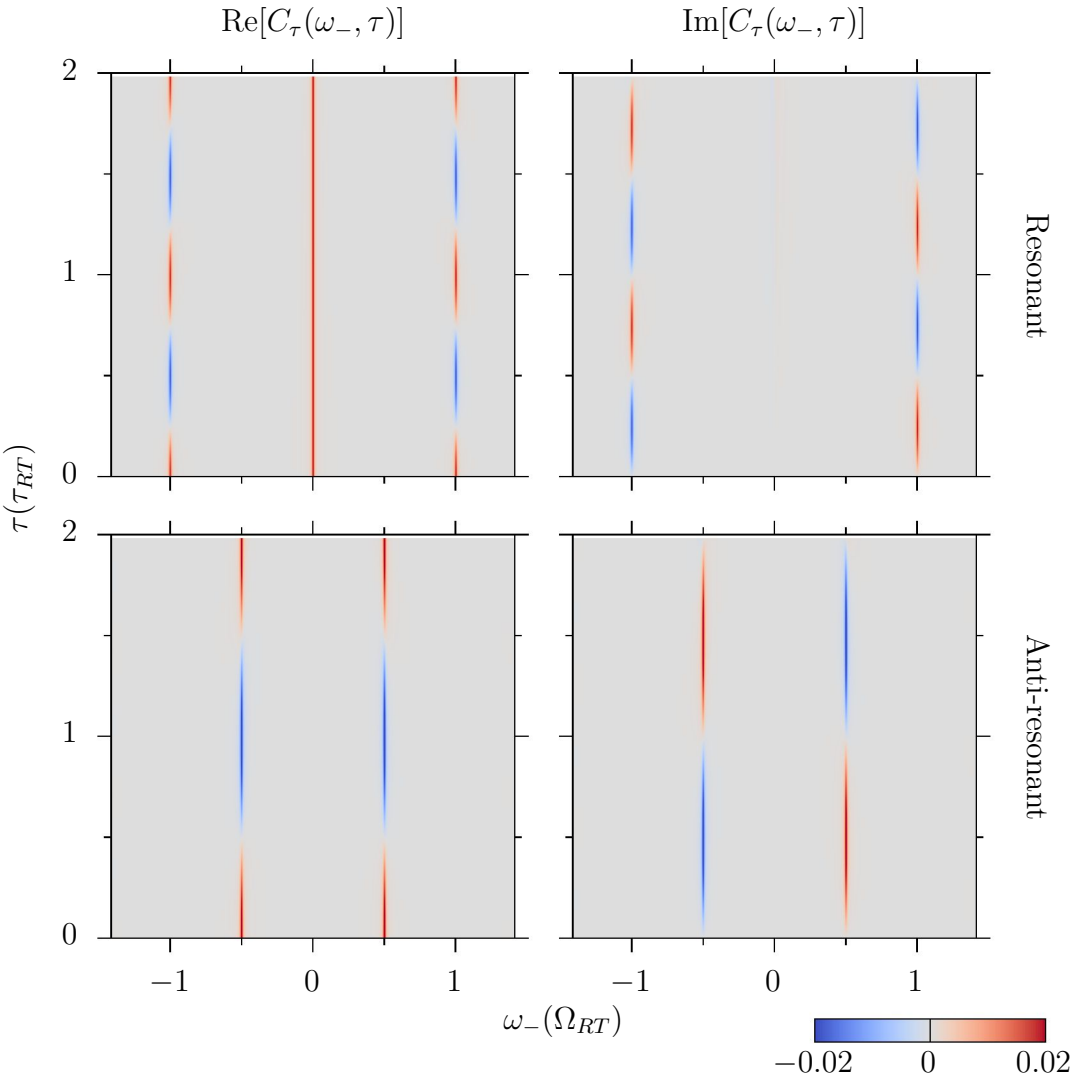

Figure 6.6 – JSA evolution versus time delay. R=0.95

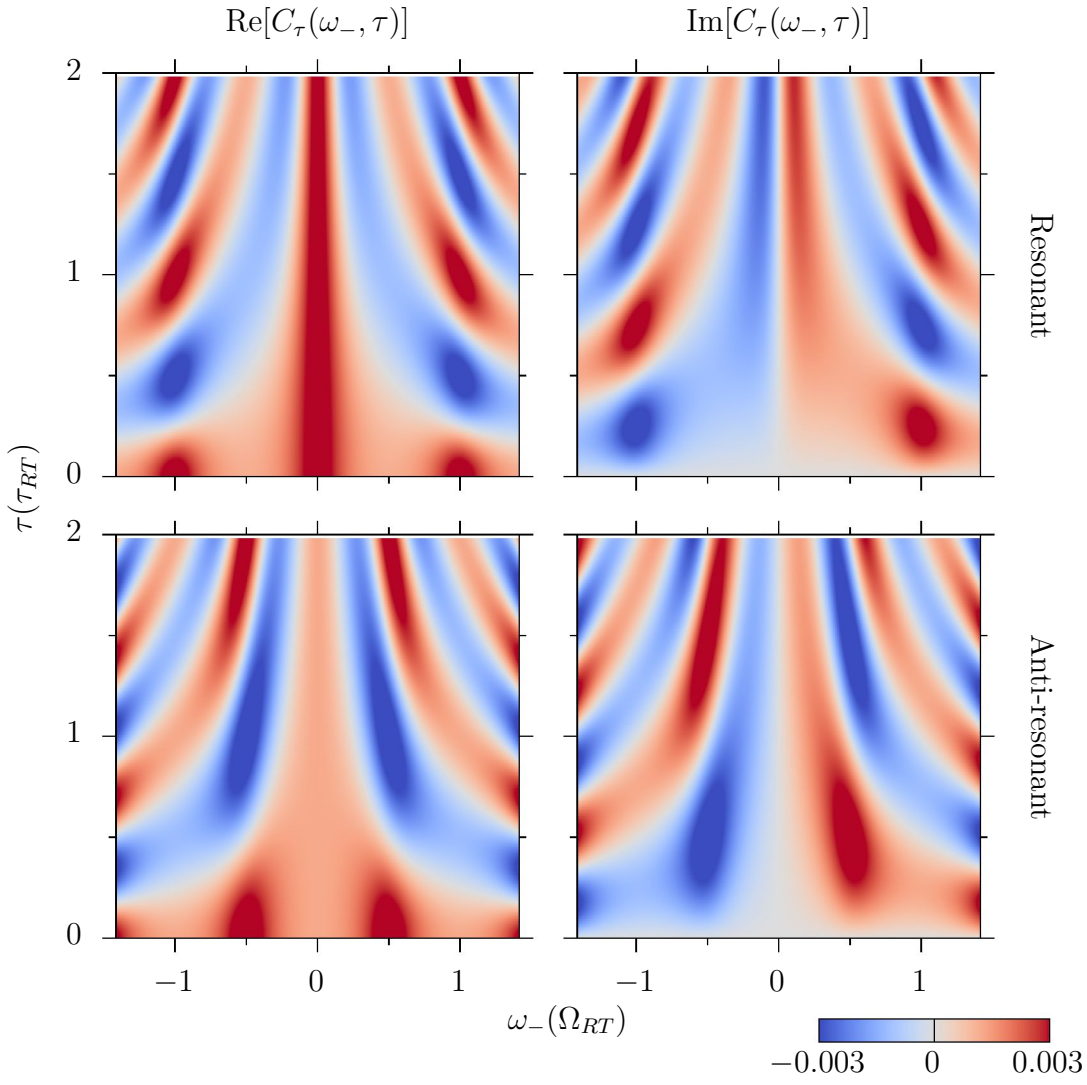

Figure 6.7 – JSA evolution versus time delay. R=0.27

function, we define s by keeping into account both the real and imaginary parts of the JSA:

$$s = \int d\omega_- \mathrm{Re}[C_\tau(\omega_p, \omega_-)]\,\mathrm{Re}[C_\tau(\omega_p, -\omega_-)] + \mathrm{Im}[C_\tau(\omega_p, \omega_-)]\,\mathrm{Im}[C_\tau(\omega_p, -\omega_-)] \tag{6.42}$$

A normalized JSA gives $s = 1$ when it is symmetric and $s = -1$ when it is anti-symmetric. It is trivial to show that two complex numbers $z_1 = a_1 + ib_1, z_2 = a_2 + ib_2$ satisfy the following property:

$$\mathrm{Re}[z_1]\,\mathrm{Re}[z_2] + \mathrm{Im}[z_1]\,\mathrm{Im}[z_2] = a_1 a_2 + b_1 b_2 = \mathrm{Re}[z_1^* z_2] \tag{6.43}$$

By applying this property to the definition of s (6.42) and substituting the delayed JSA (6.38), we find that s gives the HOM correlation probability according to:

$$p_{ab}(\tau) = \frac{1}{2}[1 - s] \tag{6.44}$$

Interestingly, starting from the study of the JSA symmetry, we retrieve the equation that describes the HOM interference pattern. We conclude that, for our biphoton state encoded in both frequency and path (polarization) DOFs, the HOM pattern is a reader of the symmetry of the frequency part of the state, following the trail of previous works [158, 159, 196].

6.4 Time-path description

In this paragraph we complete our study by an analysis based on time and path DOFs.

The expressions (6.18) and (6.19) show that the manipulation of the path symmetry occurs at time delays that are odd multiples of half of the cavity round-trip ($\tau = (2n+1)\tau_{RT}/2$). The occurring of biphoton interference at these values of τ is an unique feature of entangled frequency-comb states, as concluded by Ou's group in their seminal work about biphoton mode-locked states [101]. A nonlinear cavity reflects each photon an unknown number of times before emitting it. The biphoton state emitted from the cavity is given by the superposition of many temporal biphoton quantum paths.

Among these paths, some are identical in the sense that they are indistinguishable from the point of view of the two detectors. Indistinguishable paths interfere with each other and the resulting amplitude determines the outcome of the two entangled photons at the beam splitter output.

Ou's work makes use of Feynman path diagrams to portray the biphoton state in space-time and illustrate which biphoton quantum paths are indistinguishable and interfere.

For example, figure (6.8) shows two indistinguishable paths for the time delay of $\tau = \tau_{RT}/2$.

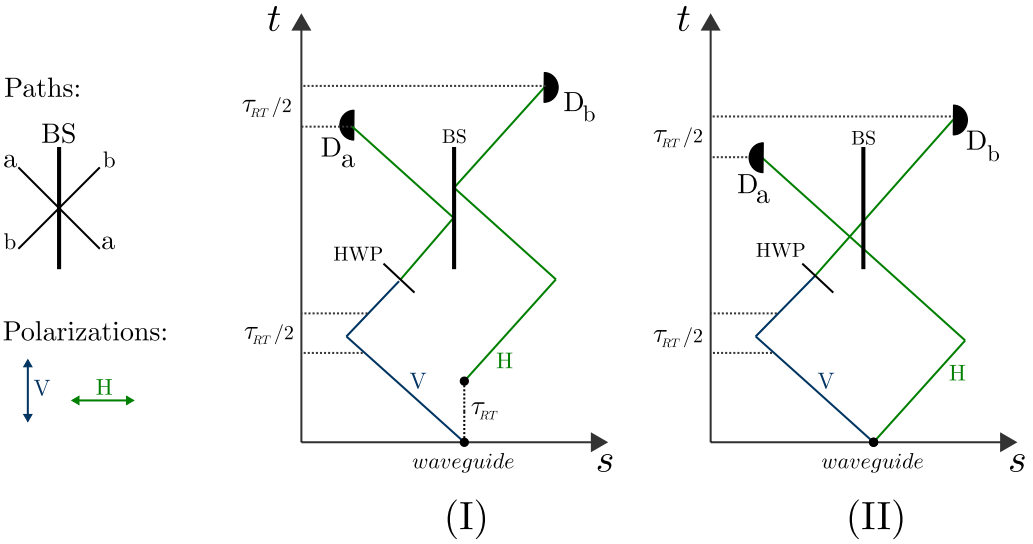

Figure 6.8 – Feynman space-time paths of two indistinguishable biphoton probability amplitudes corresponding to the anti-bunching situation. The waveguide is a nonlinear cavity and emits a SPDC type-II frequency-comb biphoton Bell state. V-polarized photon (blue) and H-polarized photon (green) are separated into paths a and b by a PBS (here not indicated). The V-polarized photon in path b is delayed by $\tau = \tau_{RT}/2$ with respect to the H-polarized photon in path a.
(I) H-polarized photon is emitted after a round-trip from the waveguide output facet. Both photons are reflected at the BS.
(II) H and V-polarized photons are emitted at the same instant. Both photons are transmitted at the BS.
Paths and polarization legends are shown on the left.

In scenario (I), the H-polarized photon is emitted one round trip later than the V-polarized photon. The V-polarized photon is delayed by $\tau = \tau_{RT}/2$ in the interferometer arm b and its polarization is turned by a HWP. At the BS both photons are reflected, so the detector D_a in path a registers a photon count at $\tau = \tau_{RT} - \tau_{RT}/2 = \tau_{RT}/2$ before that the detector D_b detects the other photon in path b.

Scenario (II) presents two differences compared to scenario (I). Firstly, both H and V-polarized photons are emitted at the same time from the waveguide. Secondly, both photons are transmitted at the BS.

Nevertheless, from the detectors point of view, the scenarios (I) and (II) are indistinguishable: in both of them, the detector D_a registers a photon count at an instant $\tau = \tau_{RT}/2$ before that the detector D_b does. Interference raises from the indistinguishability of the two paths [101].

By showing that the two paths are indistinguishable, Ou justifies *why* interference occurs.

We now use Feynman diagrams to predict the *outcome* of HOM interference.

In particular, we predict the probability that the biphoton state undergoes anti-bunching at the beam splitter when the idler photon (V-polarized) is delayed

by half cavity round-trip with respect to the signal photon (H-polarized). We start by calculating the probability amplitudes corresponding to scenarios (I) and (II) of figure (6.8). Therefore, the sum of (I) and (II) probability amplitudes gives the anti-bunching probability amplitude.

In doing so, we approximate the frequency of the two photons to the biphoton wavepacket carrier frequency, which is the central (degeneracy) frequency $\omega_{pump}/2 = \omega_d$. The beam splitter transforms the probability amplitude according to the transformation matrix expressed in equation (1.28).

In scenario (I), the single photons probability amplitudes evolve as:

$$\begin{cases} |a,H\rangle \xrightarrow{\text{Cavity}} e^{i\omega_d\tau_{RT}}\,|a,H\rangle \xrightarrow{\text{R at BS}} i\,e^{i\omega_d\tau_{RT}}\,|b,H\rangle \\ |b,V\rangle \xrightarrow{\text{Delay}} e^{i\omega_d\tau_{RT}/2}\,|b,V\rangle \xrightarrow{\text{HWP}} e^{i\omega_d\tau_{RT}/2}\,|b,H\rangle \xrightarrow{\text{R at BS}} i\,e^{i\omega_d\tau_{RT}/2}\,|a,H\rangle \end{cases} \tag{6.45}$$

The biphoton amplitude (I) is the product of the two photons amplitudes:

$$a_I = (i\,e^{i\omega_d\tau_{RT}}\,|b,H\rangle)(i\,e^{i\omega_d\tau_{RT}/2}\,|a,H\rangle) = -e^{i\omega_d\tau_{RT}3/2}\,|a,b\rangle \tag{6.46}$$

where we omit the polarization label since the two photons are in the same polarization state.

Similarly, we calculate the probability amplitudes of scenario (II):

$$\begin{cases} |a,H\rangle \xrightarrow{\text{T at BS}} |a,H\rangle \\ |b,V\rangle \xrightarrow{\text{Delay}} e^{i\omega_d\tau_{RT}/2}\,|b,V\rangle \xrightarrow{\text{HWP}} e^{i\omega_d\tau_{RT}/2}\,|b,H\rangle \xrightarrow{\text{T at BS}} e^{i\omega_d\tau_{RT}/2}\,|b,H\rangle \end{cases} \tag{6.47}$$

The corresponding biphoton amplitude (II) is:

$$a_{II} = e^{i\omega_d\tau_{RT}/2}\,|a,b\rangle \tag{6.48}$$

The anti-bunching probability amplitude is given by summing up the two biphoton amplitudes (I) (equation (6.46)) and (II) (equation (6.48)):

$$a_{anti-bunching} = a_I + a_{II} = e^{i\omega_d\tau_{RT}/2}(1 - e^{i\omega_d\tau_{RT}})\,|a,b\rangle \tag{6.49}$$

Equation (6.49) indicates that the interference outcome depends on the phase term $\phi = \omega_d\tau_{RT}$. This result agrees with equation (6.25), derived in the study of the evolution of the biphoton state in the frequency-path DOFs.

In this case, we interpret it as follows. When the biphoton wavepacket is resonant with the cavity, which means that its carrier frequency ω_d is a multiple of the cavity round trip, the phase is:

$$\phi_{resonant} = \omega_d\tau_{RT} = \left(n\frac{2\pi}{\tau_{RT}}\right)\tau_{RT} = 2n\pi, \quad n \in N \tag{6.50}$$

The two biphoton amplitudes a_I and a_{II} have opposite sign due to the reflection at the beam splitter and their superposition gives $a_{anti-bunching} = 0$. In other words, a_I (state of both photons reflected) and a_{II} (state of both photons transmitted)

interfere destructively, as it occurs in the well-known HOM experiment for a zero time delay (see section (1.3), equation (1.29)).

Thus, two photons in a resonant state can not leave the beam splitter from opposite output paths. As the beam splitter is lossless there are no other sources of losses in the system, the two photons must exit the beam splitter by taking the same path.

Indeed, if we calculate the bunching probability amplitude (by considering two scenarios (III) and (IV) in which the two photons go out from the same BS port, i.e. one is transmitted and the other is reflected, contrarily to scenarios (I) and (II)), we find:

$$a_{bunching} = -i\, e^{i\omega_d \tau_{RT}/2}(1 + e^{i\omega_d \tau_{RT}})\,|a, b\rangle \tag{6.51}$$

where, in this case, there is a (+) sign in the parenthesis instead of a (−) for at the beam splitter one photon is reflected and the other is transmitted. Equation (6.51) confirms that, when the biphoton wavepacket is resonant with the cavity, bunching occurs. The only difference with respect to the well known HOM interference is that here interference occurs at a non zero time delay: the presence of the cavity makes the interference possible at multiples of $\tau = \tau_{RT}/2$.

Let now consider the case in which the biphoton wavepacket is not resonant with the nonlinear cavity, i.e. the biphoton is anti-resonant.

In the anti-resonant case, the phase ϕ results:

$$\phi_{anti-resonant} = \omega_d \tau_{RT} = \left(n\frac{2\pi}{\tau_{RT}} + \frac{\pi}{\tau_{RT}}\right)\tau_{RT} = (2n+1)\pi, \quad n \in N \tag{6.52}$$

In this case amplitudes a_I and a_{II} interfere constructively and anti-bunching occurs. The presence of a cavity that is anti-resonant with respect to the biphoton wavepacket, for a time delay of $\tau = \tau_{RT}/2$, cancels the effect of the beam splitter, making it transparent for the incoming biphoton state.

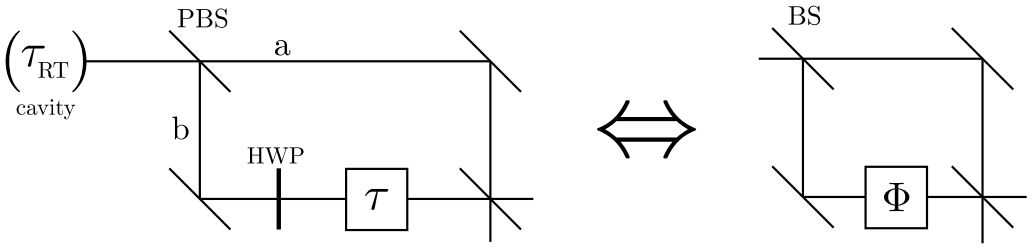

Figure 6.9 – For the anti-resonant (resonant) state, the scheme of cavity and delay line at $\tau = \tau_{RT}/2$ is analog to a Mach-Zender interferometer having $\Phi = 0$ ($\Phi = \pi$).

In other words, as figure (6.9) illustrates, we can think of the system composed by the cavity and the delay line at $\tau = \tau_{RT}/2$ as a beam splitter. The complessive setup is analogous to Mach-Zender interferometers for single photons [197], where for zero phase delays the first beam splitter cancels the second one.

The idea that a cavity behaves like a beam splitter agress with a recent proposal of Ataman [198], which shows that the cavity behaves like a beam splitter for two counter-propagating single photon having different frequencies, given that their frequencies difference has a specific value with respect to the cavity free spectral range.

To conlcude, in this section we have presented an intuitive study of HOM interference in the time domain for biphoton frequency combs. For a comprehensive analytical study, we refer to Olindo's work [187, 199]. There, the cases in which one cavity or two cavities are present along the interferometer paths a and b are discussed and an expression of the correlation coincidences rate is given.

6.5 Hong-Ou-Mandel interference pattern

In this section we study the relationship among the HOM interference pattern and the biphoton JSA, extending the analysis presented in section (1.3).

In CW pumping regime, if the JSA has a perfect mirror symmetry ($C(\omega_-) = C(-\omega_-)$), the HOM correlation probability is given by the Fourier Transform of the JSI ($|C(\omega_-)|^2$):

$$p_{ab}(\tau) = \frac{1}{2}\Big[1-Re\Big[\int d\omega_- |C(\omega_-)|^2 e^{-i\omega_-\tau}\Big]\Big] = \frac{1}{2}\Big[1-Re\Big[\mathcal{F}\Big\{|C(\omega_-)|^2\Big\}\Big]\Big] = \frac{1}{2}[1-V(\tau)] \tag{6.53}$$

where $C(\omega_-) = \phi_{PM}(\omega_p, \omega_-) f_{cav}(\omega_p, \omega_-)$ is the JSA along ω_-, given by the product of phase matching and cavity transmission functions. We introduce $V(\tau) = Re\Big[\mathcal{F}\Big\{|C(\omega_-)|^2\Big\}\Big]$, the real part of the Fourier Transform of the JSI. In the HOM interference pattern, it corresponds to the difference between the interference baseline and the correlation probability at a generic time τ.

To understand how the cavity influences the HOM pattern, let us start by considering the trivial case where the source has no cavity ($R = 0$). This situation has been widely studied in the literature [200, p. 260], [201, p. 101]. In the absence of the biphoton cavity transmission term, $C(\omega_-) = \phi_{PM}$ and $V(\tau)$ is simply the Fourier Transform of the squared phase matching function.

As instance, we may consider a Gaussian phase matching term, centered around the biphoton degeneracy frequency, where $\omega_- = 0$. This type of spectral correlation is usually obtained by the spectral filtering of a biphoton state around the degeneracy frequency. Alternatively, this phase matching function can be achieved without the application of any filtering by using a PPKTP crystal having a custom duty-cycle pattern [202].

We write the phase matching function as:

$$C(\omega_-) = \phi_{PM}(\omega_-) = \frac{1}{\sqrt[4]{2\pi}\sqrt{\sigma_{\omega_-}}} \exp\left[\frac{-1}{4}\left(\frac{\omega_-}{\sigma_{\omega_-}}\right)^2\right] \tag{6.54}$$

to satisfy the normalization of its corresponding JSI in the frequency space:

$$\int d\omega_- |C(\omega_-)|^2 = \int d\omega_- C^*(\omega_-)C(\omega_-) = \int d\omega_- \phi^*_{PM}(\omega_-)\phi_{PM}(\omega_-) = 1 \quad (6.55)$$

The biphoton state bandwidth is the FWHM of its JSI. The biphoton state with the Gaussian phase matching profile of equation (6.54) has a bandwidth of:

$$\Delta\omega_- = 2\sqrt{2\ln 2}\sigma_{\omega_-} \approx 2.36\sigma_{\omega_-} \quad (6.56)$$

The JSI is Gaussian, so we expect $V(\tau)$, the Fourier Transform of its squared value, to be Gaussian as well:

$$V(\tau) = Re\Big[\mathcal{F}\Big\{|C(\omega_-)|^2\Big\}\Big] = \exp\left[-\frac{(\sigma_{\omega_-}\tau)^2}{2}\right] = \exp\left[-\frac{1}{2}\Big(\frac{\tau}{\sigma_\tau}\Big)^2\right] \quad (6.57)$$

σ_τ is proportional to the HOM dip FWHM, given by $\Delta\tau = 2\sqrt{2\ln 2}\sigma_\tau$:.

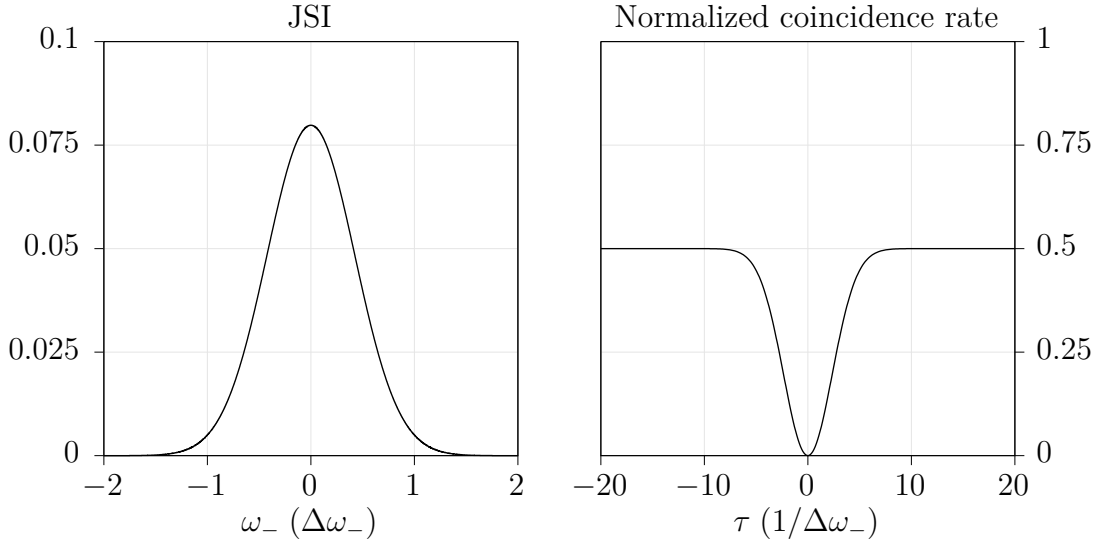

Figure 6.10 – JSI cut along ω_- and corresponding HOM interference pattern for a biphoton state with a Gaussian phase matching JSA (6.54), without the presence of the cavity.

We show in figure (6.10) the JSI of the Gaussian phase matching term (6.54) and the corresponding HOM interference pattern $p_{ab}(\tau) = 1 - V(\tau)$.

Following the property of the Fourier transform $\sigma_{\omega_-}\sigma_\tau = 1$, we can deduce the biphoton state spectral width $\Delta\omega_-$ from the width of the HOM dip $\Delta\tau$:

$$\Delta\omega_- = \frac{8\ln 2}{\Delta\tau} \approx \frac{5.55}{\Delta\tau} \quad (6.58)$$

Not surprisingly, $\Delta\omega_-$ and $\Delta\tau$ are inversely proportional. We remind that, under the hypothesis of no birefringence, $\Delta\omega_-$ is two times the bandwidth of signal

and idler photons. If we consider that they are two wavepackets, their temporal extensions is inversely proportional to their bandwidth. When $\Delta\omega_-/2$ is larger, signal and idler are shorter wavepackets. Therefore, when they are delayed one compared to the other, they interfere over a shorter time length $\Delta\tau$.

Now let study the HOM pattern of a biphoton state with a sinc-shaped JSA. This is the phase matching function of a longitudinal invariant SPDC nonlinear medium, as found in equation (1.23). The normalized JSA reads:

$$C(\omega_-) = \phi_{PM}(\omega_-) = \sqrt{\frac{\Delta n L}{4\pi c}}\,\mathrm{sinc}\left(\frac{L\Delta n}{4c}\omega_-\right) = \sqrt{\frac{g}{\pi\Delta\omega_-}}\,\mathrm{sinc}\left(g\frac{\omega_-}{\Delta\omega_-}\right) \tag{6.59}$$

where $\Delta\omega_-$is the FWHM of the corresponding JSI for $g \approx 0.886\pi$.

The Fourier Transform of the sinc-squared function is the triangular function, defined as:

$$V(\tau) = Re\Big[\mathcal{F}\Big\{|C(\omega_-)|^2\Big\}\Big] = \mathrm{tri}\Big(\frac{\Delta\omega_-}{2g}\tau\Big) = \max\left(0, 1 - \frac{\Delta\omega_-}{2g}|\tau|\right) \tag{6.60}$$

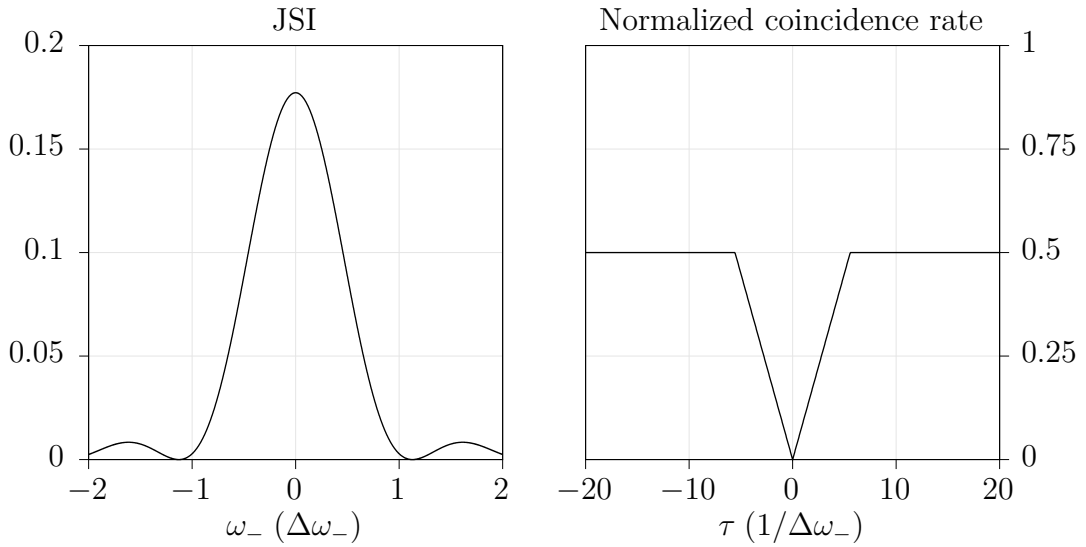

Figure 6.11 – JSI cut along ω_- and corresponding HOM interference pattern for a biphoton state with a sinc phase matching JSA (6.59), without the presence of the cavity.

Figure (6.11) shows on the left the JSI of the sinc shaped phase matching term (6.59) and on the right the corresponding HOM interference pattern. We see that the HOM dip has the shape of an inverted triangle. From equation (6.60), we find that its FWHM is $\Delta\tau = 2g/\Delta\omega_-$. The biphoton bandwidth deduced from the HOM pattern is:

$$\Delta\omega_- = \frac{2g}{\Delta\tau} \approx \frac{5.57}{\Delta\tau} \tag{6.61}$$

6.5.1 One-pass configuration

In this section we illustrate the HOM pattern of the biphoton state emitted by our source in the case of the waveguide one-pass configuration, i.e. we suppose that we apply an anti-reflection coating to the facets and the cavity effect becomes negligible. As a result, the HOM pattern is determined by the phase matching function, shown in figure (2.8). We suppose to pump the source in the CW monochromatic regime at the optimal pump wavelength, corresponding to the maximum of figure (3.1).

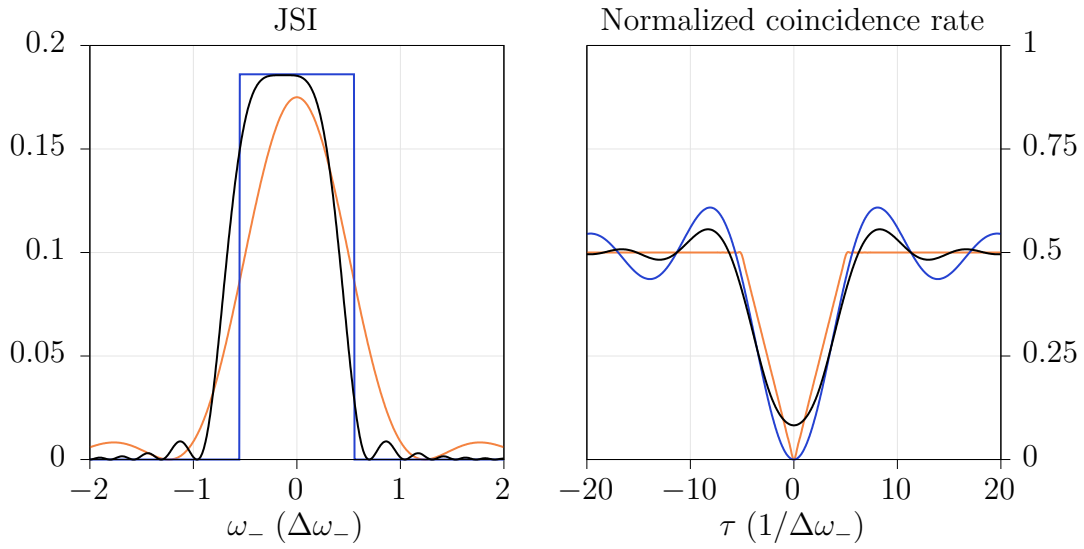

Figure 6.12 – JSI and corresponding HOM interference pattern for a biphoton state generated by sources having three different phase matching terms: a sinc (orange), a rectangle (blue) and our source phase matching (black).

Figure (6.12) compares the JSI cut along ω_- and corresponding HOM pattern of our source (black) with the the case of a rectangular phase matching (blue) and the previously seen case of sinc phase matching (orange). The JSI of a rectangular phase matching is still a rectangular function, so its HOM pattern is a sinc function. As shown in figures (2.8) and (2.10), our source has a JSI with a shape in between a rect and a sinc-squared function. The resulting HOM pattern (black) consists in a dip with a smoothed triangular shape, surrounded by two rapidly decaying oscillations on its sides.

Besides, as also shown in (2.10), the phase matching of our source is not a perfectly mirror-symmetric function due to the presence of birefringence, expressed by the contribution (2.16) to the phase-mismatch (2.14). The resulting HOM pattern has a reduced visibility but does not vary the shape.

We also notice that the biphoton state emitted by our source has a product of bandwidth $\Delta\omega_-$ and temporal extension $\Delta\tau$ which is larger respect to the one of a biphoton state emitted by source with a Gaussian or a sinc shaped phase

matching. We find numerically:

$$\Delta\omega_- \approx \frac{8.38}{\Delta\tau} \tag{6.62}$$

6.5.2 Cavity effect

Starting from the relationship between the HOM pattern and the phase matching function, we study the HOM pattern modifications related to the presence of the cavity. The JSA of the emitted state becomes:

$$C(\omega_p, \omega_-) = \phi_{PM}(\omega_-) f_{cav}(\omega_p, \omega_-) \tag{6.63}$$

This time, the generalized visibility term $V(\tau) = Re\Big[\mathcal{F}\Big\{|C(\omega_-)|^2\Big\}\Big]$ in (6.53), which determines the shape of the HOM pattern, has as an argument the product of two functions: the phase matching and the cavity transmission. According to the convolution theorem of the Fourier Transform, we can express $V(\tau)$ as the convolution of the Fourier Transform of the squared cavity function $f_{cav}(\omega_p, \omega_-)$ with the Fourier Transform of the squared phase matching term $\phi_{PM}(\omega_-)$:

$$\begin{aligned} V(\tau) &= Re\Big[\mathcal{F}\Big\{|C(\omega_-)|^2\Big\}\Big] = Re\Big[\mathcal{F}\Big\{|f_{cav}(\omega_p, \omega_-)|^2 |\phi_{PM}(\omega_-)|^2\Big\}\Big] \\ &= Re\Big[\mathcal{F}\Big\{|f_{cav}(\omega_p, \omega_-)|^2\Big\} * \mathcal{F}\Big\{|\phi_{PM}(\omega_-)|^2\Big\}\Big] \end{aligned} \tag{6.64}$$

where $f_{cav}(\omega_p, \omega_-)$ is the cavity function in the CW pumping regime at the pumping frequency ω_p, defined in (5.34).

In order to obtain an analytical expression of the Fourier Transform of the cavity function, we also neglect dispersion and birefringence ($\tau_V(\omega) = \tau_H(\omega) = \tau_{RT}$). For simplicity, we also suppose that the reflectivity is the same for the two polarization directions ($R_H = R_V = R$). The expression of the cavity function is then given by (5.35). Under the previous assumptions, $f_{cav}(\omega_p, \omega_-)$ is a complex-valued function in ω_- that takes only real values in two cases, corresponding to two specific pump frequencies ω_p:

1. The biphoton state is resonant with the cavity, so its degeneracy (central) frequency is a cavity resonance: $\omega_p \tau_{RT}/2 = n(2\pi)$.

2. The biphoton state is anti-resonant with the cavity, so its degeneracy (central) frequency is in the middle between two consecutive cavity resonances: $\omega_p \tau_{RT}/2 = n(2\pi) + \pi$.

At these pumping conditions, $f_{cav}(\omega_p, \omega_-)$ simplifies into the real-valued function:

$$f_{cav}(\omega_-) = \frac{\pm(1-R)}{1 + R^2 \mp 2R\cos\left(\omega_- \tau_{RT}/2\right)} \tag{6.65}$$

with the upper sign indicates the resonant case and the lower sign the anti-resonant case.

6.5.3 Low-reflectivity approximation

We cannot use the squared form of expression (6.65) to find an explicit analytical expression of the Fourier Transform. However, we can approximate it to a sinusoidal function, whose Fourier Transform is well known. By calculating the average and contrast values of (6.65), we can approximate it to:

$$f_{cav}(\omega_-) = \frac{\pm(1-R)}{1+R^2 \mp 2R\cos(\omega_- \tau_{RT}/2)} \approx \pm A(R) \pm \frac{C(R)}{2}\cos(\omega_- \tau_{RT}/2) = \tilde{f}_{cav}(\omega_-) \tag{6.66}$$

where $A(R)$ and $C(R)$ are the average and contrast factors of f_{cav}. They are functions of R according to:

$$A(R) = \frac{(1+R^2)}{(1+R)^2(1-R)}, \qquad C(R) = \frac{4R}{(1+R)^2(1-R)} \tag{6.67}$$

To quantify the accuracy of this approximation, we introduce the parameter Δ, defined as the variance between the squared functions f_{cav} and $\tilde{f}_{cav}$, normalized to the average value of the squared functions f_{cav}:

$$\Delta = \frac{\left\langle \left| |\tilde{f}_{cav}(\omega_-)|^2 - |f_{cav}(\omega_-)|^2 \right| \right\rangle}{\langle |f_{cav}(\omega_-)|^2 \rangle} \tag{6.68}$$

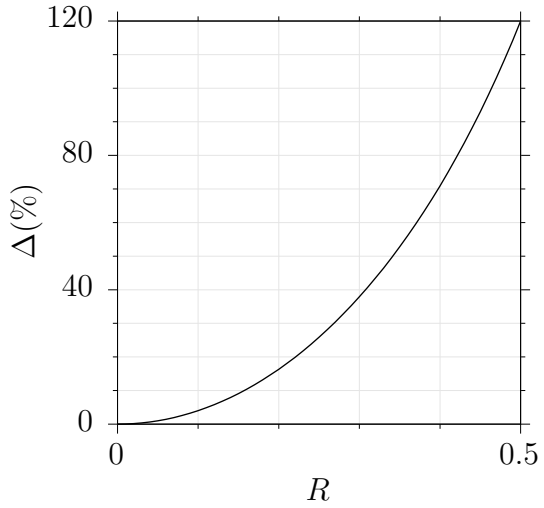

Figure 6.13 – Percentage of accuracy (6.68) of approximation (6.66) respect to the cavity reflectivity R.

The approximation is accurate when $\Delta \to 0$, for which $\tilde{f}_{cav}(\omega_-) \to f_{cav}(\omega_-)$. This occurs at low values of R, as figure (6.13) illustrates. In our source, the average value between H and V-polarized reflectivity is $R = 0.27$ ($R_H = 0.297$, $R_V = 0.243$). At this value of the reflectivity, $\Delta = 30.4\%$, so we consider this

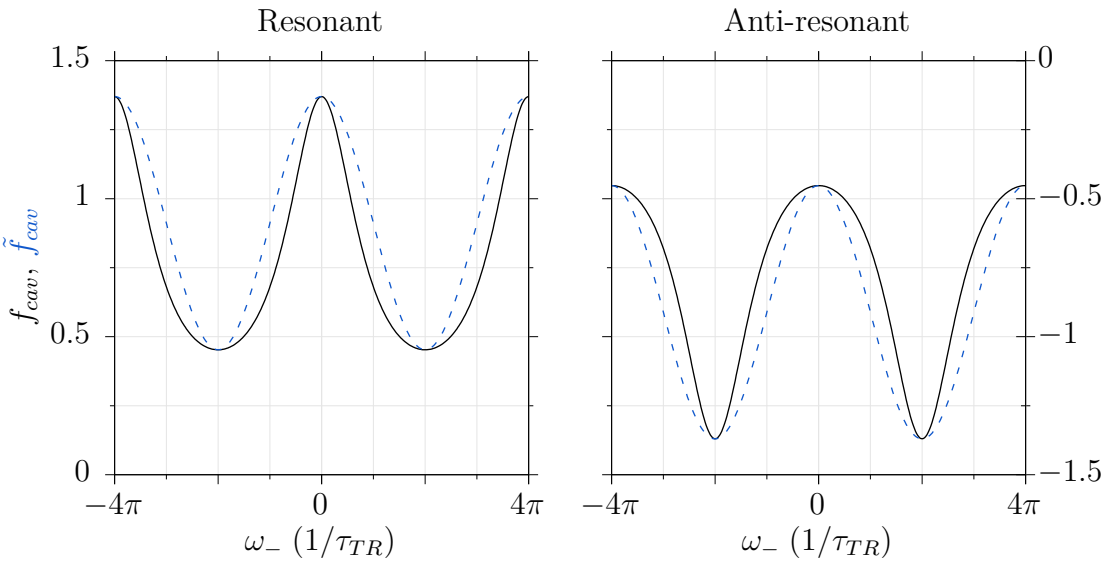

Figure 6.14 – Cavity transmission function in resonant (left) and anti-resonant (right) cases for R=0.27. The exact function $f_{cav}(\omega_-)$ is the black continuous line, while the approximated function $\tilde{f}_{cav}(\omega_-)$ expressed in equation (6.66) is the blue dashed line.

approximation still acceptable for our analysis.

We confirm that the approximation holds in figure (6.14), where we plot $f_{cav}(\omega_-)$ (black continuous line) and $\tilde{f}_{cav}(\omega_-)$ (blue dashed line) for $R = 0.27$. Both the resonant (left) and anti-resonant (right) biphoton state are shown. We also notice that the approximation, following its definition, is more accurate nearby the Fabry-Perot maxima and minima.

In the expression of the approximating cavity transmission function (equation (6.66)), we see that its period along ω_- is the inverse of half the cavity round-trip: $\Omega = 4\pi/(\tau_{RT}) = 2\pi/(\tau_{RT}/2)$. Consequently, we expect to find in the HOM interference pattern replicas of the Fourier transformed squared phase matching function, spaced by half-cavity round-trip $\tau = \tau_{RT}/2$.

By calculating $\mathcal{F}\Big\{|f_{cav}(\omega_p,\omega_-)|^2\Big\} \approx \mathcal{F}\Big\{|\tilde{f}_{cav}(\omega_p,\omega_-)|^2\Big\}$ from equation (6.64), we find:

$$\begin{aligned}\mathcal{F}\Big\{|\tilde{f}_{cav}(\omega_p,\omega_-)|^2\Big\} =& [(1-R)^2(1+R)^4]^{-1}\Big\{ \\ & (1+4R^2+R^4)\delta(\tau) \\ & \pm 2R(1+R^2)[\delta(\tau-\tau_{RT}/2)+\delta(\tau+\tau_{RT}/2)] \\ & + R^2[\delta(\tau-\tau_{RT})+\delta(\tau+\tau_{RT})]\Big\}\end{aligned} \tag{6.69}$$

with " + " in the resonant case and " − " in the anti-resonant one.

As stated in (6.64), the shape of the HOM pattern is determined by the convolution of expression (6.69) with $\mathcal{F}\Big\{|\phi_{PM}(\omega_-)|^2\Big\}$.

According to the sifting property of the Dirac delta function

$$f(t) * \delta(t) = \int_{-\infty}^{\infty} f(t)\delta(t-T)\,dt = f(T) \tag{6.70}$$

equation (6.64) becomes:

$$\begin{aligned} V(\tau) =& Re\Big[\mathcal{F}\Big\{|\tilde{f}_{cav}(\omega_p,\omega_-)|^2\Big\} * \mathcal{F}\Big\{|\phi_{PM}(\omega_-)|^2\Big\}\Big] \\ =& [(1-R)^2(1+R)^4]^{-1} Re\Big[\\ &+ (1+4R^2+R^4)\mathcal{F}\Big\{|\phi_{PM}(\omega_-)|^2\Big\}_{\tau=0} \\ &\pm 2R(1+R^2)\Big[\mathcal{F}\Big\{|\phi_{PM}(\omega_-)|^2\Big\}_{\tau=\tau_{RT}/2} + \mathcal{F}\Big\{|\phi_{PM}(\omega_-)|^2\Big\}_{\tau=-\tau_{RT}/2}\Big] \\ &+ R^2\Big[\mathcal{F}\Big\{|\phi_{PM}(\omega_-)|^2\Big\}_{\tau=\tau_{RT}} + \mathcal{F}\Big\{|\phi_{PM}(\omega_-)|^2\Big\}_{\tau=-\tau_{RT}}\Big]\Big] \end{aligned} \tag{6.71}$$

where the subscript (i.e. $\tau = 0$) indicates the time delay around which the corresponding function $\mathcal{F}\Big\{|\phi_{PM}(\omega_-)|^2\Big\}$ is centered. We note that, as it occurs in the HOM interference of a biphoton state generated without the presence of the cavity, at $\tau = 0$ the HOM pattern is given by $\mathcal{F}\Big\{|\phi_{PM}(\omega_-)|^2\Big\}$. In addition, thanks to the presence of the cavity, there are replicas of $\mathcal{F}\Big\{|\phi_{PM}(\omega_-)|^2\Big\}$ around $\tau = \tau_{RT}/2$ and $\tau = \tau_{RT}$. The replica at half round-trip may be either positive or negative with respect to $V(\tau)$, corresponding to a HOM dip or peak, respectively. This is coherent with what we found previously (equation (6.34)). When the biphoton state is resonant (figure (6.14), left), there is bunching, while when it is anti-resonant (figure (6.14), right) there is anti-bunching.

We also notice that the two replicas do not have the same weight as $\mathcal{F}\Big\{|\phi_{PM}(\omega_-)|^2\Big\}$ centered at the origin, for which $V_0 \propto (1+4R^2+R^4) \approx 1 = R^0$. The first replica at half round-trip is weighted by $V_1 \propto 2R(1+R^2) \approx 2R$, while the second replica at the round-trip by $V_2 \propto R^2$. Since $R << 1$, due to the approximation (6.66), the visibility of the HOM dip/peak quickly decreases with the replica order.

Finally, we observe that by using this approximating model of the cavity we only find two replicas of the HOM pattern, which is in agreement with the assumption of low reflectivity values.

As previously carried out in the absence of the cavity, we calculate $V(\tau)$ in the case of a Gaussian and a sinc-shaped phase matching functions.

For a Gaussian phase matching (6.54), whose squared function Fourier Transform

is expressed in (6.57), we find:

$$\begin{aligned} V(\tau) =& \eta^{-1} Re\left[\mathcal{F}\left\{|\tilde{f}_{cav}(\omega_p,\omega_-)|^2\right\} * \exp\left[-\frac{1}{2}\left(\frac{\tau}{\sigma_\tau}\right)^2\right]\right] \\ =& \eta^{-1}[(1-R)^2(1+R)^4]^{-1} Re\Bigg[\\ &+ (1+4R^2+R^4)\exp\left[-\frac{1}{2}\left(\frac{\tau}{\sigma_\tau}\right)^2\right] \\ &\pm 2R(1+R^2)\left\{\exp\left[-\frac{1}{2}\left(\frac{\tau+\tau_{RT}/2}{\sigma_\tau}\right)^2\right] + \exp\left[-\frac{1}{2}\left(\frac{\tau-\tau_{RT}/2}{\sigma_\tau}\right)^2\right]\right\} \\ &+ R^2\left\{\exp\left[-\frac{1}{2}\left(\frac{\tau+\tau_{RT}}{\sigma_\tau}\right)^2\right] + \exp\left[-\frac{1}{2}\left(\frac{\tau-\tau_{RT}}{\sigma_\tau}\right)^2\right]\right\}\Bigg] \end{aligned} \tag{6.72}$$

where η is the normalization factor, defined as:

$$\eta = \frac{1+R^4+2R^2\left\{2+\exp\left[-\frac{1}{2}\left(\frac{\tau}{\sigma_\tau}\right)^2\right]\right\} \pm 4R(1+R^2)\left\{\exp\left[-\frac{1}{8}\left(\frac{\tau}{\sigma_\tau}\right)^2\right]\right\}}{(1-R)^2(1+R)^4} \tag{6.73}$$

and the upper (lower) sign indicates the resonant (anti-resonant) biphoton state. Starting from $V(\tau)$, we derive the HOM correlation probability according to equation (6.53).

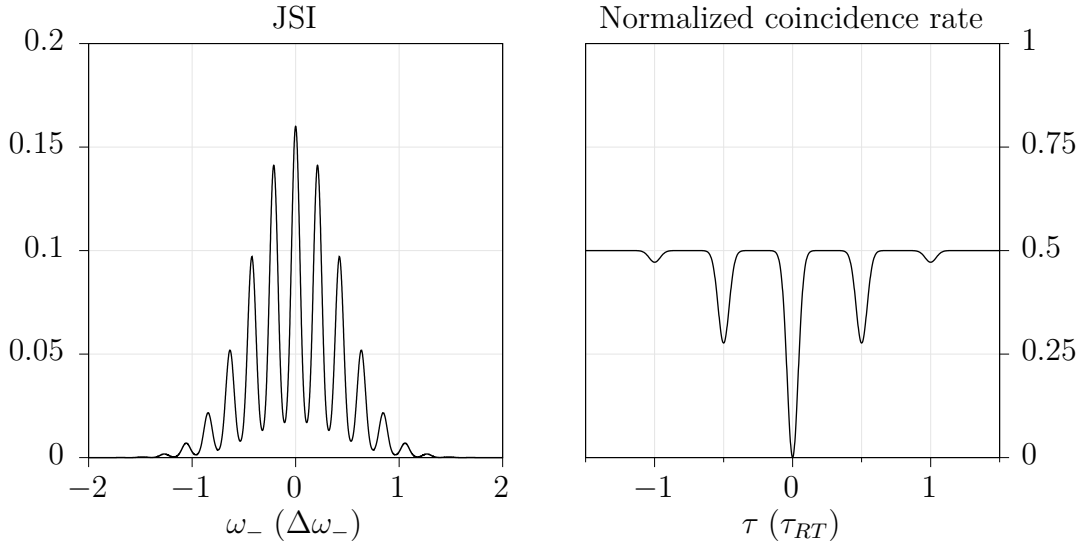

Figure 6.15 – Resonant case: JSI cut along ω_- and corresponding HOM interference pattern for a biphoton state with a Gaussian phase matching (6.54) and resonant with the cavity.

In figure (6.15) we illustrate the cut of the JSI along ω_- and corresponding HOM pattern. We choose $\tau_{RT} = \sigma_\tau = \Delta\tau/(2\sqrt{2\ln 2})$ and $R = 0.27$. On the left,

we recognize the JSI cut characterizing a resonant biphoton state: the central frequency along ω_- belongs to the cavity resonances. In the HOM pattern, all replicas are dips, as we expect in the resonant case described by equation (6.72).

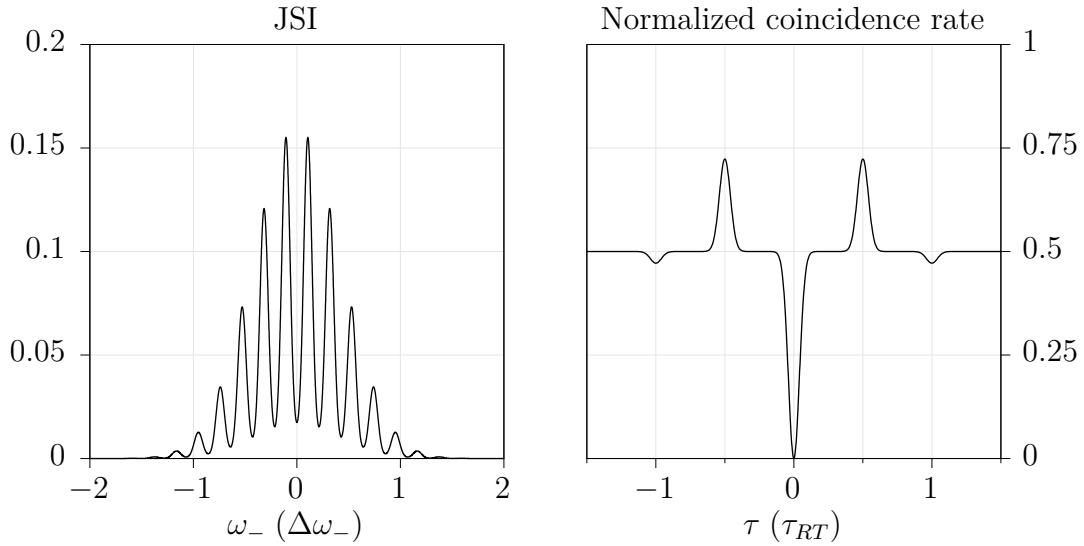

Figure 6.16 – Anti-resonant case: JSI cut along ω_- and corresponding HOM interference pattern for a biphoton state with a Gaussian phase matching (6.54) and anti-resonant with the cavity.

The anti-resonant state is illustrated in figure (6.16). Here the central frequency is anti-resonant with respect to the cavity, so the JSI presents a minima in $\omega_- = 0$. As a consequence, the HOM pattern shows two peaks at $\tau = \pm\tau_{RT}/2$.

We notice that in both resonant and anti-resonant case the central dip is the same as the central HOM dip that occurs without the presence of the cavity (figure (6.10)).

We now study the impact of the cavity on the biphoton state having a sinc-shaped phase matching term, defined in (6.59). The corresponding Fourier Transformed squared function is the triangle defined in (6.60), so that the generalized visibility term reads:

$$\begin{aligned} V(\tau) =& \eta^{-1} Re\left[\mathcal{F}\left\{|\tilde{f}_{cav}(\omega_p,\omega_-)|^2\right\} * \mathrm{tri}\Big(\frac{\Delta\omega_-}{2g}\tau\Big)\right] \\ =& \eta^{-1}[(1-R)^2(1+R)^4]^{-1} Re\Big[\\ &+ (1+4R^2+R^4)\mathrm{tri}\Big(\frac{\Delta\omega_-}{2g}\tau\Big) \\ &\pm 2R(1+R^2)\Big[\mathrm{tri}\Big(\frac{\Delta\omega_-}{2g}(\tau+\tau_{RT}/2)\Big) + \mathrm{tri}\Big(\frac{\Delta\omega_-}{2g}(\tau-\tau_{RT}/2)\Big)\Big] \\ &+ R^2\Big[\mathrm{tri}\Big(\frac{\Delta\omega_-}{2g}(\tau+\tau_{RT})\Big) + \mathrm{tri}\Big(\frac{\Delta\omega_-}{2g}(\tau+\tau_{RT})\Big)\Big]\Big] \end{aligned} \tag{6.74}$$

where, as previously defined, η is the normalization factor and the upper (lower) sign indicates the resonant (anti-resonant) biphoton state interference.

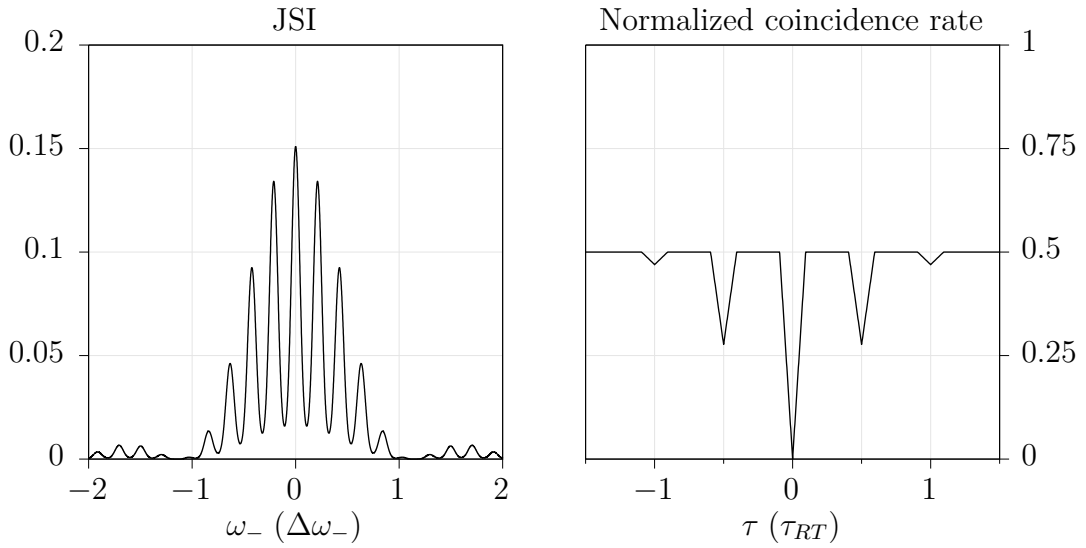

Figure 6.17 – Resonant case: JSI cut along ω_- and corresponding HOM interference pattern for a biphoton state with a sinc phase matching (6.59) and resonant with the cavity.

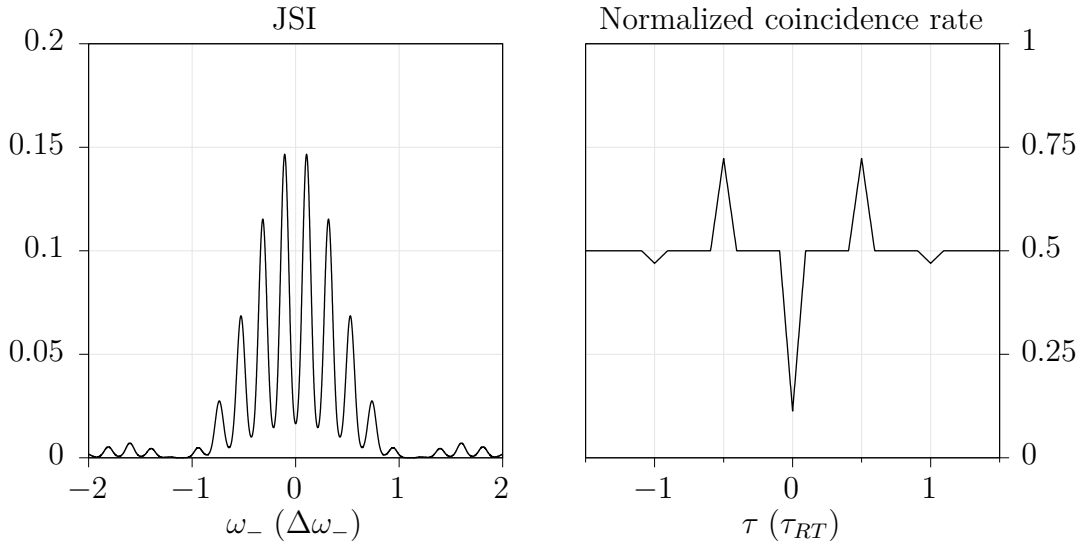

Figure 6.18 – Anti-resonant case: JSI cut along ω_- and corresponding HOM interference pattern for a biphoton state with a sinc phase matching (6.59) and anti-resonant with the cavity.

For comparison, we study the same cavity as before, with $\tau_{RT} = \Delta\tau/(2\sqrt{2\ln 2})$ and $R = 0.27$. Figure (6.17) shows the resonant case, while figure (6.18) the anti-resonant one. The only difference with respect to the Gaussian case is the shape of the HOM dips and peaks, that is now given by the Fourier Transform

of the squared sinc phase matching term. As before, the replicas visibility scales with the value of the cavity reflectivity according to (6.74).

6.5.4 Pumping wavelength effect

In this paragraph we study the intermediate state between resonant and anti-resonant cases. By tuning the pump laser frequency, we can span continuously the JSA pattern and change accordingly the quantum state. As the detuning occurs within a very small frequency bandwidth, of the order of the cavity free spectral range, the phase matching term can be considered constant, while the cavity transmission function varies. The expression of the cavity transmission function is given by equation (5.35) in the case of a cavity with no birefringence and no chromatic dispersion. When the biphoton state is not resonant or anti-resonant with the cavity, the expression (5.35) is a complex-valued function and the resulting JSA contains both symmetric and anti-symmetric components. As consequence, depending on the relative weights of the two constituents of opposite symmetry, the wavefunction behaves differently in a HOM experiment.

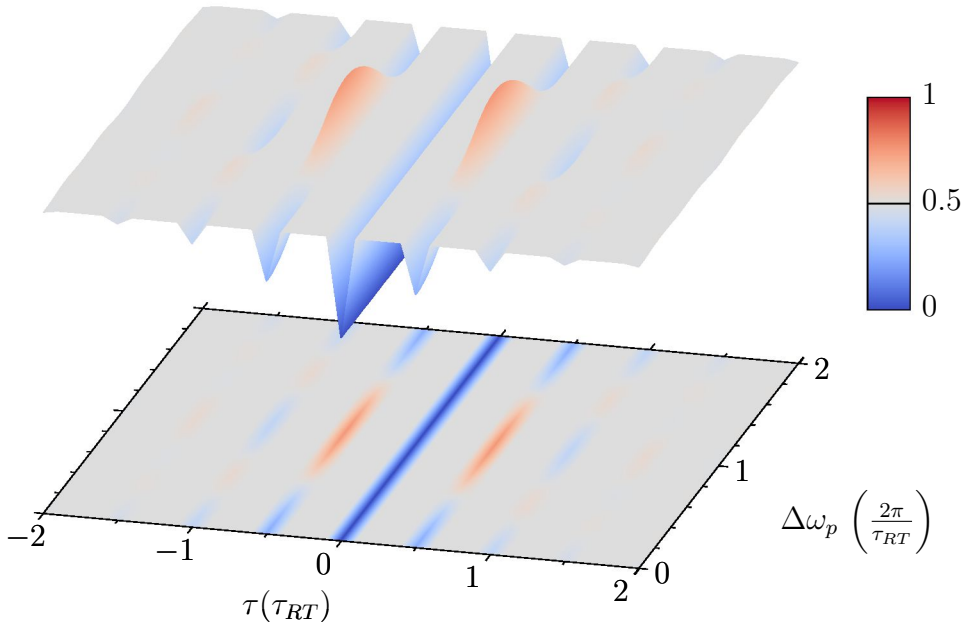

Figure 6.19 – Correlation probability of HOM interference versus pump detuning in the case of a birefringence-less and dispersion-less cavity with low reflectivity $R = 0.27$ and sinc-shaped phase matching function.

Figure (6.19) illustrates the simulated HOM pattern for a cavity having a reflectivity of 0.27 as a function of the pump frequency. $\Delta\omega_p = 0, 2/(2\pi/\tau_{RT})$ correspond to the resonant case, while $\Delta\omega_p = 1/(2\pi/\tau_{RT})$ to the anti-resonant one. We consider a nonlinear medium having a sinc-shaped phase matching function (figure (6.11)), as we can deduce from the triangularly shaped HOM dips and peaks along the delay time direction.

As we are considering a birefringence-less and dispersion-less cavity, the visibility of the dip at zero time delay is maximal, whereas the low value of reflectivity implies that the HOM replicas dip and peak have a low visibility: $V_{\tau_{RT}/2} \approx 0.5$ for the first replica (at the dip $p_{ab}(\tau = \tau_{RT}/2) \approx 0.25$, at the peak $p_{ab}(\tau = \tau_{RT}/2) \approx 0.75$), and $V_{\tau_{RT}} \approx 0.1$ for the second replica, barely visible.

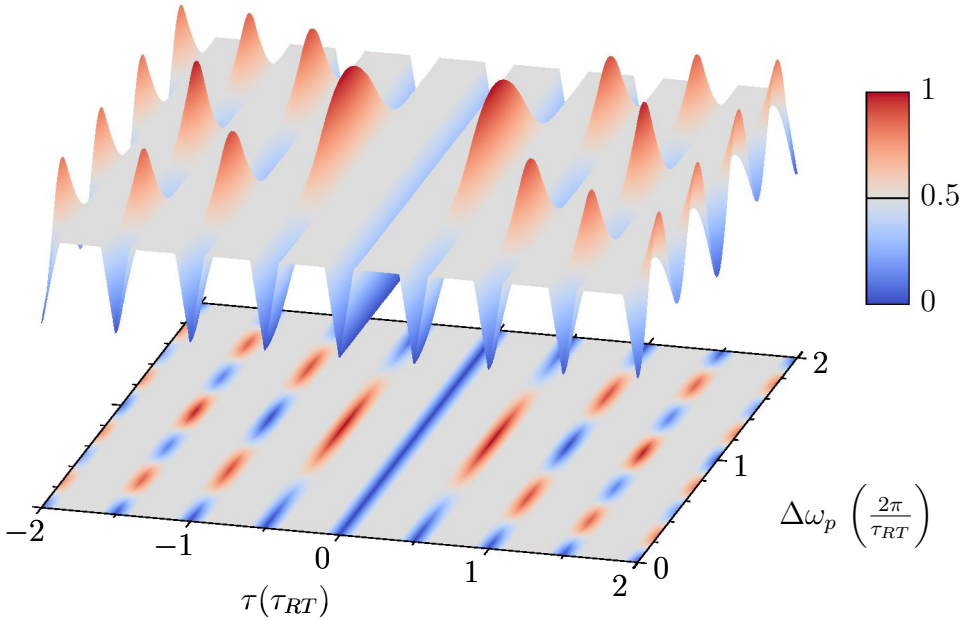

Figure 6.20 – Correlation probability of HOM interference versus pump detuning in the case of a birefringence-less and dispersion-less cavity with high reflectivity $R = 0.9$.

We observe a smooth transition as afunction of the pump frequency from peak to dip. In order to study this dynamic at different time delays, we present a high reflectivity case ($R = 0.9$) in figure (6.20).

Thanks to the high reflectivity, we can distinguish many revivals of the HOM interference, in the form of either dip or peak. Interestingly, we see that, as the time delay increases, the evolution of the biphoton wavefunction from symmetric to anti-symmetric occurs with a finer detuning of the pump frequency. In particular, the frequency of the modulation doubles at every round-trip time.

6.5.5 Reflectivity effect

Previously, within the analytical model approximating the cavity function for low reflectivity values, we have found that the visibility of the first HOM revival (peak or dip) is proportional to the cavity reflectivity, while the visibility of the second order HOM revival is proportional to the squared value of the reflectivity (equation (6.69)).

We now look for the exact solutions of the HOM interference correlation probability for resonant and anti-resonant states as function of the reflectivity. We

do no make any approximation as we proceed numerically by calculating (6.53) by using the cavity Airy transmission function (equation (6.65)). For simplicity, we suppose that the reflectivity is the same for the two orthogonally polarized photons. For the phase matching term, we use the sinc-shaped function shown in figure (6.11), previously used for the calculations shown in figures (6.17) and (6.18). We choose a cavity round-trip of $\tau_{RT} = \Delta\tau/(2\sqrt{2\ln 2})$, where $\Delta\tau$ is the phase matching extension as defined in (6.61).

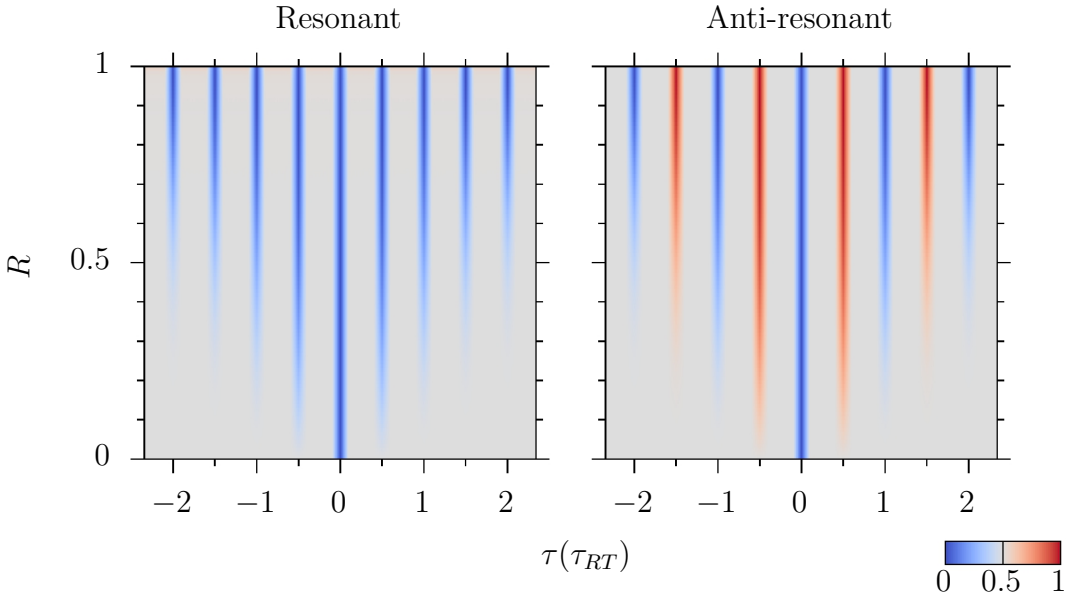

Figure 6.21 – Correlation probability of HOM interference as a function of the cavity reflectivity. Resonant (left) and anti-resonant (right) cases are illustrated.

Figure (6.21) illustrates how the HOM interference pattern varies as a function of the cavity reflectivity R, in the case of resonant and anti-resonant biphoton state. As expected, in the resonant case there is only bunching (blue color), which occurs at delay time that are multiples of half-cavity round-trip. The correlation probability is never higher than the interference baseline value of 0.5 (grey color). Viceversa, in the anti-resonant scenario, anti-bunching (red color) takes place at time delay that are odd multiples of half-cavity round-trip.

In the absence of a cavity ($R = 0$), the HOM pattern shows only a central dip. On the other hand, in the case of a perfect cavity ($R \to 1$), the HOM pattern exhibits many revivals of the central dip. The reason is that in a high-reflecting cavity, the two photons have a high probability of being reflected many times at the input and output cavity mirrors. In this situation, the probability that one photon of the pair undergoes one or more additional reflections respect to the other is important, causing the existence of multiple HOM revivals.

For $0 \leq R \leq 1$, as the cavity reflectivity increases, the visibility of the HOM revival dips and peaks increases. Experimentally, at higher reflectivity values, more dips (peaks) can be detected.

In our AlGaAs ridge waveguide, the average reflectivity for the H and V-polarized photon is $R = 0.27$. For this reflectivity value, we might expect to be

able to detect the first and second order HOM revivals. However, this model does not take into account the cavity birefringence that reduces the HOM visibility, as we study in more details in the next section.

6.6 Hong-Ou-Mandel dip visibility versus cavity birefringence and reflectivity

In this paragraph we consider the more general scenario in which the cavity is birefringent. Following the previous notation (see chapter (2)), we label:

$$\begin{cases} C_{H,V}(\omega_1,\omega_2) = C(\omega_1,\omega_2) \\ C_{V,H}(\omega_1,\omega_2) = C(\omega_2,\omega_1) \end{cases} \tag{6.75}$$

where due to the lack of mirror symmetry:

$$C(\omega_1,\omega_2) \neq C(\omega_2,\omega_1) \tag{6.76}$$

In order to calculate the results of HOM interferometry, we follow the same steps of paragraph (6.2). We retrieve the expression of the wavefunction at the output of the polarising beam splitter (PBS) and half-wave plate (HWP, before interaction with the beam splitter (BS) (see scheme (6.1)).

$$\begin{aligned} |\Psi\rangle = \frac{i}{\sqrt{2}} \iint d\omega_1 d\omega_2 e^{-i\omega_2\tau} \Big(& C(\omega_1,\omega_2)\,|a,\omega_1\rangle\,|b,\omega_2\rangle + \\ & C(\omega_2,\omega_1) e^{-i(\omega_1-\omega_2)\tau}\,|b,\omega_1\rangle\,|a,\omega_2\rangle \Big) \end{aligned} \tag{6.77}$$

By applying the transformation (6.24), we find that after the beam splitter:

$$\begin{aligned} |\Psi\rangle = \frac{i}{2\sqrt{2}} \iint & d\omega_1 d\omega_2 e^{-i\omega_2\tau} \\ & \Big[\Big(C(\omega_1,\omega_2) + e^{-i(\omega_1-\omega_2)\tau} C(\omega_2,\omega_1) \Big)\,|\psi_b\rangle + \\ & \Big(C(\omega_1,\omega_2) - e^{-i(\omega_1-\omega_2)\tau} C(\omega_2,\omega_1 \Big)\,|\psi_f\rangle \Big] \end{aligned} \tag{6.78}$$

with $|\psi_b\rangle = i\,|a,\omega_1\rangle\,|a,\omega_2\rangle + |b,\omega_1\rangle\,|b,\omega_2\rangle$, $|\psi_f\rangle = |a,\omega_1\rangle\,|b,\omega_2\rangle - |b,\omega_1\rangle\,|a,\omega_2\rangle$.

We consider two single-photon detectors placed on path a and on path b. The probability of coincidence detection, in the approximation of frequency independent

detector response, is:

$$\begin{aligned}
p_{ab}(\tau) =& \langle\Psi|\,\hat{M}\,|\Psi\rangle \\
=& \frac{1}{8}\Big[\int d\omega_1' \int d\omega_2' A^*(\omega_1',\omega_2',\tau)\,\langle\psi_f|\Big]\hat{M}\Big[\int d\omega_1 \int d\omega_2 A(\omega_1,\omega_2,\tau)\,|\psi_f\rangle\Big] \\
=& \frac{1}{8}\int d\omega_1 \int d\omega_2 \int d\omega_1' \int d\omega_2' \int d\omega_a \int d\omega_b A^*(\omega_1',\omega_2',\tau)A(\omega_1,\omega_2,\tau) \\
& \Big[\delta(\omega_1'-\omega_a)\delta(\omega_2'-\omega_b)-\delta(\omega_1'-\omega_b)\delta(\omega_2'-\omega_a)\Big] \\
& \Big[\delta(\omega_1-\omega_a)\delta(\omega_2-\omega_b)-\delta(\omega_2-\omega_a)\delta(\omega_1-\omega_b)\Big]
\end{aligned} \tag{6.79}$$

where $A(\omega_1,\omega_2,\tau) = e^{-i\omega_2\tau}\Big(C(\omega_1,\omega_2) - e^{-i(\omega_1-\omega_2)\tau}C(\omega_2,\omega_1)\Big)$ and $\hat{M}$ is the detector operator as defined in (6.27).

By solving the integrals along ω_a, ω_b, ω_1', ω_2' and using the normalization of the JSA, we find the same correlation probability as in (6.29). We rewrite it in the (ω_+,ω_-) basis and in the case of monochromatic CW-pumping regime as:

$$\begin{aligned}
p_{ab}(\tau) &= \frac{1}{2}\Big\{1 - Re\Big[\iint d\omega_1 d\omega_2 C^*(\omega_1,\omega_2)C(\omega_2,\omega_1)e^{-i(\omega_1-\omega_2)\tau}\Big]\Big\} \\
&= \frac{1}{2}\Big\{1 - Re\Big[\iint d\omega_+ d\omega_- C^*(\omega_+,\omega_-)C(\omega_+,-\omega_-)e^{-i\omega_-\tau}\Big]\Big\} \\
&= \frac{1}{2}\Big\{1 - Re\Big[\int d\omega_- C^*(\omega_p,\omega_-)C(\omega_p,-\omega_-)e^{-i\omega_-\tau}\Big]\Big\} \\
&= \frac{1}{2}\Big\{1 - Re\Big[\mathcal{F}\Big\{C^*(\omega_p,\omega_-)C(\omega_p,-\omega_-)\Big\}\Big]\Big\}
\end{aligned} \tag{6.80}$$

The product $C^*(\omega_p,\omega_-)C(\omega_p,-\omega_-)$ in the last line of equation (6.80) confirms that the correlation probability measured in a HOM experiment depends on the symmetry of the JSA. More precisely, it depends on the mirror symmetry of the JSA respect to the degeneracy frequency direction $\omega_1 = \omega_2 = \omega_d$, corresponding to $\omega_- = 0$.

We define V_0 the visibility of the HOM pattern when the time delay accumulated between the two photons is zero ($\tau = 0$).

From equation (6.80), we find that V_0 corresponds to the contrast between the correlation probability at zero time delay and the correlation probability at time delays far from the interference region ($\tau = \tilde{\tau}$):

$$V_0 = \frac{p_{ab}(\tilde{\tau}) - p_{ab}(0)}{p_{ab}(\tilde{\tau})} = Re\Big[\int d\omega_- C^*(\omega_p,\omega_-)C(\omega_p,-\omega_-)\Big] \tag{6.81}$$

Following this definition, V_0 takes values in the range $-1 \leq V_0 \leq 1$, depending on the JSA mirror symmetry. The three limit cases are:

1. $V_0 = 1$, when $C(\omega_p,\omega_-)$ is mirror symmetric
2. $V_0 = 0$, when $C(\omega_p,\omega_-)$ has no mirror symmetry

3. $V_0 = -1$, when $C(\omega_p, \omega_-)$ is mirror anti-symmetric

We now consider the case of a nonlinear medium and an independent cavity, as illustrated in figure (5.3, a), and a CW monochromatic regime. The cut of the JSA along ω_- reads $C(\omega_p, \omega_-) = \phi_{PM}(\omega_-) f_{cav}(\omega_p, \omega_-)$. We also suppose that the phase matching function ϕ_{PM} is symmetric. In the absence of the cavity the HOM interference has perfect coalescence with $V_0 = 1$.

In the following we show that, in the presence of the cavity, the visibility may reduce to values as low as $V_0 = 0$, according to birefringence of the cavity. V_0, as defined in (6.81), cannot take values lower than zero because a delay $\tau \neq 0$ is necessary for the manipulation of the biphoton state statistics.

Non-birefringent cavity

In the case of non birefringent cavity, the resonances of the Fabry-Perot for H and V-polarization photons are equally distant respect to the degeneracy frequency $\omega_{deg} = \omega_1 = \omega_2$. The resulting JSA along ω_- is perfectly mirror symmetric, as shown in figure (5.8). Signal and idler photons probability amplitudes are indistinguishable when they arrive at the beam-splitter and perfect HOM coalescence occurs with $V_0 = 1$.

We can show this analytically by plugging into the definition of visibility the expression of the biphoton JSA under CW pumping previously calculated in (5.30) in the (ω_+, ω_-) basis.

The visibility is:

$$\begin{aligned} V_0 &= Re\Big[\int d\omega_- |\phi_{PM}(\omega_-)|^2 f_{cav}(\omega_p, -\omega_-) f^*_{cav}(\omega_p, \omega_-)\Big] \\ &= (1-R_H)(1-R_V) Re\Bigg[\int d\omega_- \frac{|\phi_{PM}(\omega_-)|^2 e^{i\omega_-(\tau_H - \tau_V)}}{[1 - R_H e^{i\frac{\omega_p+\omega_-}{2}\tau_H}][1 - R_V e^{-i\frac{\omega_p+\omega_-}{2}\tau_V}]} \\ &\qquad \frac{1}{[1 - R_H e^{-i\frac{\omega_p-\omega_-}{2}\tau_H}][1 - R_V e^{i\frac{\omega_p-\omega_-}{2}\tau_V}]}\Bigg] \end{aligned} \tag{6.82}$$

where $\tau_H = \tau_H\Big|_{\frac{\omega_p+\omega_-}{2}}$ and $\tau_V = \tau_V\Big|_{\frac{\omega_p-\omega_-}{2}}$. The term related to the chromatic dispersion cancels out, as far as H and V-polarized photons have the same chromatic dispersion [203, 204, 205]. If the cavity has no birefringence, the two orthogonally polarized photons have the same round-trip time:

$$\tau_H(\omega) = \tau_V(\omega) = \tau_{RT}(\omega) \tag{6.83}$$

To facilitate the calculation, we suppose that the cavity reflectivity is the same for the two orthogonal polarization directions:

$$R_H = R_V = R \tag{6.84}$$

The expression (6.82) simplifies into:

$$V_0 = Re\left[\int d\omega_- \frac{(1-R)^2|\phi_{PM}(\omega_-)|^2}{[1+R^2-2R\cos(\tau_{RT}(\frac{\omega_p+\omega_-}{2})\frac{\omega_p+\omega_-}{2})]} \frac{1}{[1+R^2-2R\cos(\tau_{RT}(\frac{\omega_p-\omega_-}{2})\frac{\omega_p-\omega_-}{2})]}\right] \tag{6.85}$$

This expression corresponds to the normalization of the JSI expressed in (5.33) in the case of no birefringence, so we conclude that $V_0 = 1$: as long as the cavity is not birefringent, it does not deteriorate the visibility of the central HOM dip at zero time delay.

Birefringent cavity

In this paragraph we study the dependence of the HOM central dip visibility upon the cavity birefringence. In first approximation, we neglect the chromatic dispersion, as we assume that it acts equally on H and V-polarized photons. As previously, we also assume $R_H = R_V = R$.

The general expression of the cavity function in a monochromatic CW pump regime (5.34) in the case of a birefringent cavity simplifies into:

$$\begin{aligned} f_{cav}(\omega_p, \omega_-) &= \frac{(1-R)e^{i\omega_p\tilde{\tau}_{RT}/2}e^{i\omega_-\Delta\tau_{RT}/2}}{\left[1-Re^{i\tau_H\frac{\omega_p+\omega_-}{2}}\right]\left[1-Re^{i\tau_V\frac{\omega_p-\omega_-}{2}}\right]} \\ &= \frac{(1-R)e^{i\omega_p\tilde{\tau}_{RT}}e^{i\omega_-\Delta\tau_{RT}/2}}{1+R^2e^{i\omega_p\tilde{\tau}_{RT}/2}e^{i\Delta\tau_{RT}\frac{\omega_-}{2}} - Re^{i\tau_H\frac{\omega_p}{2}}\left[e^{i\tau_H\frac{\omega_-}{2}}+e^{-i\tau_H\frac{\omega_-}{2}}e^{i\Delta\tau\frac{\omega_p-\omega_-}{2}}\right]} \end{aligned} \tag{6.86}$$

where we introduce the average round-trip time $\tilde{\tau}_{RT}$ and the difference of round-trip time $\Delta\tau_{RT}$ between the two polarization directions:

$$\begin{aligned} \tilde{\tau}_{RT} &= (\tau_H + \tau_V)/2 \\ \Delta\tau_{RT} &= \tau_H - \tau_V \end{aligned} \tag{6.87}$$

The integral of the Airy function (6.86) can not be expressed in an explicit analytical form. So, as done in (6.66), we focus on the cases of resonant and anti-resonant states for a low reflecting cavity to have an analytic expression of the visibility. We keep into account the cavity birefringence by introducing δ_{RT}, the phase-delay accumulated among two frequency degenerate H-polarized and V-polarized photons after a cavity round-trip:

$$\delta_{RT}(\omega) = \delta_{H,RT}(\omega) - \delta_{V,RT}(\omega) = \omega(\tau_H - \tau_V) = 2L\frac{\omega}{c}(n_H - n_V) \tag{6.88}$$

The cavity function in the low R approximation reads:

$$\tilde{f}_{cav}(\omega_-) = \pm A(R) \pm \frac{C(R)}{2} \cos\left(\omega_- \tau_{RT}/2 + \delta_{RT}/2\right) \tag{6.89}$$

with the coefficients $A(R)$ and $C(R)$ defined in equation (6.67) and the upper (lower) sign for the resonant (anti-resonant) state.

The visibility in the case of a birefringent cavity (see (6.81)) is:

$$\begin{aligned}\mathrm{Re}\Big[\mathcal{F}\Big\{\tilde{f}^*_{cav}(\omega_-)\tilde{f}_{cav}(-\omega_-)\Big\}\Big] =& [(1-R)^2(1+R)^4]^{-1}\Big\{ \\ & \{1+2R^2[1+\cos(\delta_{RT})]+R^4\}\delta(\tau) \\ & \pm 2R(1+R^2)\cos(\delta_{RT}/2)[\delta(\tau-\tau_{RT}/2)+\delta(\tau+\tau_{RT}/2)] \\ & + R^2[\delta(\tau-\tau_{RT})+\delta(\tau+\tau_{RT})]\Big\}\end{aligned} \tag{6.90}$$

We recognize that the visibility of the HOM central dip ($\tau = 0$) is lowered by the cavity birefringence as $V_0 \propto \{1 + 2R^2[1 + \cos(\delta_{RT})] + R^4\}$. If $\delta_{RT} \neq m2\pi$, m integer, $0 \leq [1 + \cos(\delta_{RT})] < 2$ and the visibility is reduced.

Regarding the first replica at plus or minus half round-trip time ($\tau = \pm\tau_{RT}/2$), we see that δ_{RT} determines if there is bunching or anti-bunching with a periodicity of $m\pi$, since $V_{\tau_{RT}/2} \propto \cos(\delta_{RT}/2)$. On the contrary, the shape and visibility of the second replica at plus or minus one round-trip time ($\tau = \pm\tau_{RT}$) is not changed by the presence of the birefringence.

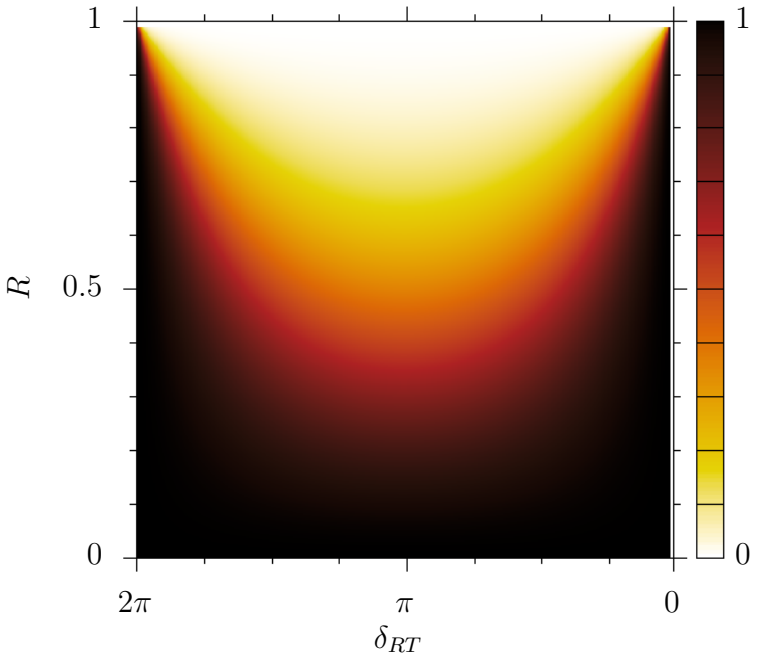

Figure 6.22 – Visibility V_0 versus cavity reflectivity and phase-delay accumulated by H-polarized photons compared to the V-polarized one after one round-trip.

We calculate numerically the impact of the cavity for a general reflectivity value ($0 \leq R \leq 1$), by using the exact form the the cavity function (6.86).

As expected, we see in Figure (6.22) that for a constant value of R, the visibility decreases with the birefringence. While the cavity reflectivity increases, the visibility decreases much more rapidly with the birefringence. As instance, at $R = 0.95$, a round-trip phase-delay of $\delta_{RT} = 0.05$ is enough to have $V_0 \leq 0.1$.

In our source, the average reflectivity for H and V-polarized photons is $R = 0.27$ (5.2). At this reflectivity value, if we suppose that the phase matching function to be perfectly symmetric, we expect the visibility to be in the range $0.75 \leq V_0 \leq 1$, with $V_0 = 0.75$ for $\delta_{RT} = \pi$ (or odd multiples of π), and $V_0 = 1$ for $\delta_{RT} = 0$ (or even multiple of π).

6.7 Experimental demonstration

6.7.1 Hong-Ou-Mandel interference at zero time delay

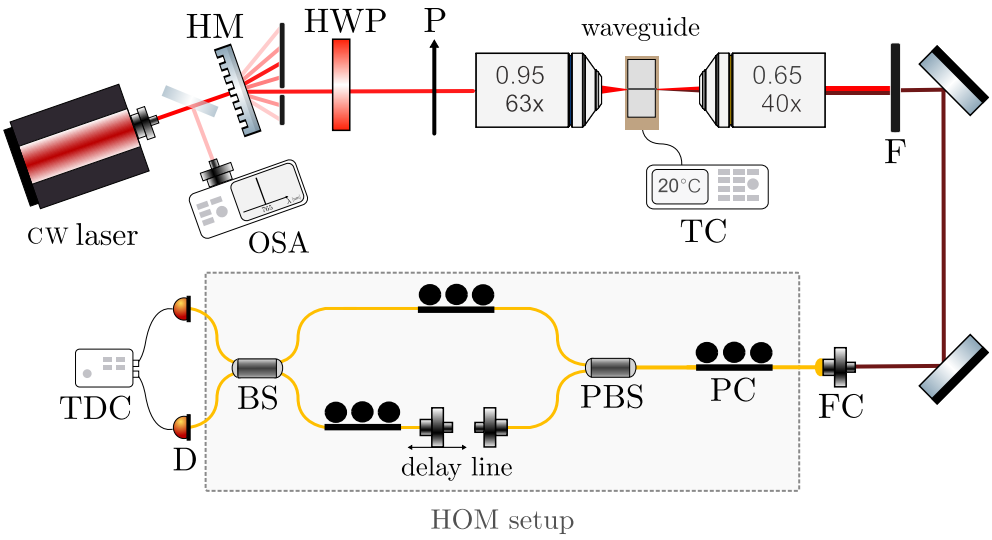

Figure 6.23 – Sketch of the experimental setup for the HOM interference. OSA" optical spectrum analyzer, HM: holographic mask, HWP: half-wave plate, P: polarizer, TC: temperature controller, F: low-pass filter, FC: fiber coupler, PC: polarization controller, PBS: polarising beam splitter, BS: beam splitter, D: single-photon detector, TDC: time-to-digital converter.

In order to perform HOM inteferometry, we have implemented the experimental setup represented in figure (6.23). The first part on the generation and collection in fiber of the SPDC type-II photon pairs is described in section (3.2). Here we focus on the description of the HOM setup, indicated by the dashed line. A fiber polarization controller (PC) compensates the ellipticity acquired by the two polarization states of the two photons during their propagation along the first fiber. The PBS separates the two orthogonally linearly polarized photons, which are

successively recombined at a 50/50 beam splitter (BS). The difference in optical lengths between these two arms is controlled by a free space delay line, which consists in a fixed fiber coupler (FC) and a FC mounted on a motorized stage (ThorLabs^{TM} MTS50/M-Z8). Each BS output is sent to a free-running InGaAs/InP Single-Photon Detector (idQuantique^{TM} ID230). The detectors efficiency is set to 25% and their dead time to 25µs. A time-to-digital converter (TDC, QuTau^{TM} QuTools) measures the signal and idler arrival times, allowing the HOM time-correlation measurement.

Hong-Ou-Mandel at zero time delay

The measurements reported in the following are carried out by using the sample `ABQ71_C1_3`, waveguide in group 11, position 2.

For the measurement of the HOM central dip, we set the waveguide holder temperature to $T = 20°C$ and the CW laser wavelength at $\lambda = 764.315nm$.

We set the integration time at 20s per point, given the average detected coincidence rate of $R = 325$ pair/second for time delays far from the HOM dip. The first step in the calibration of the setup, shown in figure (6.23), is to set the PCs to make the two entangled photons indistinguishable in polarization. Afterwards, we set the center of the delay line scan around the zero position, for which the length of the two interferometers arms is identical. The zero position is first found approximately by using classical interference and then more accurately via a rapid HOM measurement.

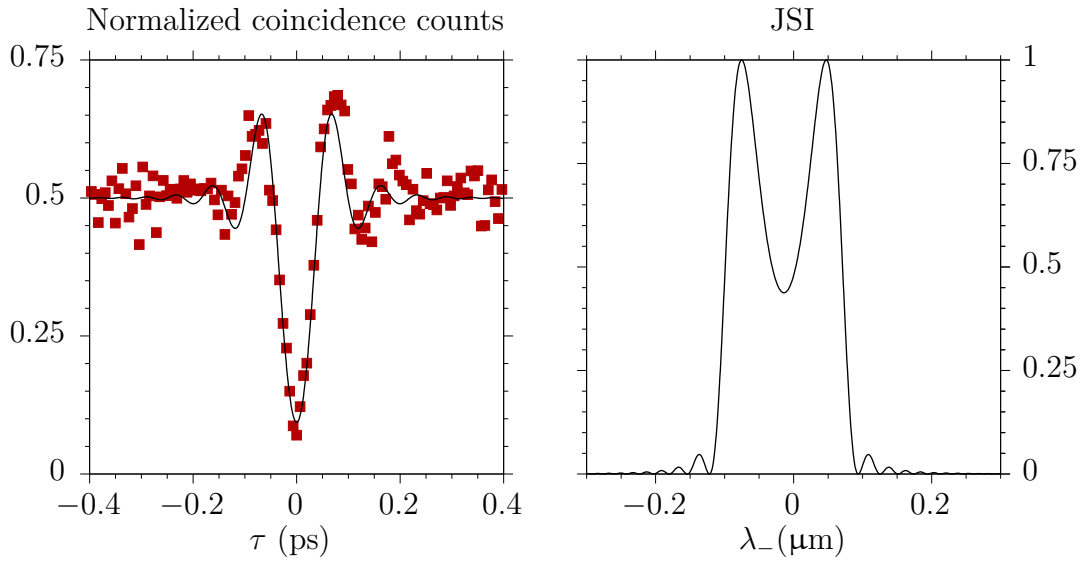

Figure 6.24 – HOM measurement for the sample `ABQ71_C1_3`, waveguide in group 11 and position 3.
Left: HOM measurement (red square) and numerical simulation (continuous black line) at zero time delay.
Right: corresponding JSI numerical simulation.

Figure (6.24) reports the results of the HOM measurement in red dots. For

comparison with the following HOM measurements, we normalize to 0.5 the detected coincidence counts obtained far from the interference region. The optical delay between signal and idler photons is expressed in unit of time. Adjacent points are 6.7fs apart and correspond to a step of 2μm of the free space moving stage.

The HOM dip shows a raw visibility of 0.86, in agreement with the visibility of 0.88 expected from the numerical simulation (see figure (2.10, b)).

We observe that there are two side bumps around the dip in the HOM pattern, which corresponds to an intermediate case among the calculated HOM patterns of figure (2.10 b) and (2.10 d). The measured HOM pattern is a consequence of modal birefringence (2.20) and chromatic dispersion, as explained in more details in section (2.2).

Since we are using a CW monochromatic pump, from the HOM pattern we can retrieve the shape of the biphoton phase matching function [206]. From the simulated phase matching function in (ω_+, ω_-) (2.8), we retrieve the pump frequency $\omega_p = \omega_+$ for which the corresponding simulated HOM pattern is the best fit of the measured data. The simulated HOM pattern is reported in figure (6.24) in a continuous black line. The standard deviation between the measurement data and the fit is $\sigma = 0.0395$. We note that the measured and simulated HOM patterns are obtained at a different pump frequency. The measurement is carried out at $\lambda_{pump} = 764.315$nm, while the calculation at $\lambda_{pump} = 770.466$nm. This difference probably arises from the fact that the calculated phase matching is based on a nominal structure, which may differ from the structure of the measured waveguide due to epitaxial growth uncertainties.

From the HOM fit, we find that the FWHM of the HOM dip is $\Delta\tau = 52.0 \pm 1.7$fs ($\Delta z = 15.9 \pm 0.5$μm). The corresponding JSI fit has a FWHM width of $\Delta\omega_- = 137.1$THz ($\Delta\lambda = 170.1$nm). The product of the biphoton bandwidth and its temporal extension is 7.12, larger than 5.6, the value for a Gaussian (6.58) and sinc phase matching phase matching function (6.61).

6.7.2 Hong-Ou-Mandel interference at half round-trip time delay: preparation

To measure the first HOM replica, two conditions need to be satisfied:

1. Set the pump beam to a specific frequency, for which an either resonant or anti-resonant biphoton state is generated (see section (6.3)).

2. Set the delay line to a specific position, corresponding to half of the cavity round-trip (see section (6.4)).

It is not trivial to fulfill the requirements (1) and (2). On the one hand, we cannot rely on classical interference as no signal is expected at $\tau_{RT}/2$. On the other hand, the expected dip visibility is low ($V < 20\%$), its position is far from the HOM central peak ($z \sim 6$mm) and its width is very small ($\Delta z < 30$μm).

For this reason, we have optimized a specific experimental procedure to find the HOM replica, described in the following.

1. Set the pump frequency to generate a resonant or anti-resonant state

We start with the identification of a pump frequency corresponding to a resonant or anti-resonant state, to measure a dip or a peak, respectively.

In the following, we refer to the set of pump frequencies corresponding to a resonant (anti-resonant) biphoton state as ω_p^R (ω_p^{AR}).

For a constant pump power within the cavity, when $\omega_p = \omega_p^R$ or $\omega_p = \omega_p^{AR}$, the pair production rate is maximal. Therefore, if we set the delay line to a position far from the ones corresponding to HOM interference regions, for $\omega_p = \omega_p^R$ or $\omega_p = \omega_p^{AR}$ we expect a maximum of coincidence rate, while intermediate pump frequencies would result in a lower rate. Conversely, when ω_p is in between two consecutive ω_p^R and ω_p^{AR} values, the pair production rate and the detected rate of coincidences are minimal.

To have a constant pump laser power within the waveguide, we monitor the pump power at the output of the waveguide using a power-meter. According to the measured value, we increase or decrease the pump power injected into the waveguide. In this way, before each measurement of coincidences we check and set the power of the pump laser at the output to 40µW for a fixed wavelength.

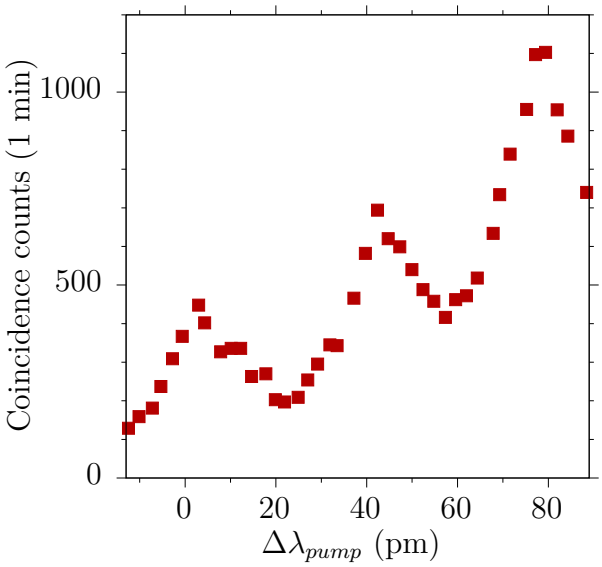

Figure 6.25 – Coincidences out of the HOM interference region respect to the CW pump wavelength. The zero detuning corresponds to $\lambda_{pump} = 764.313$nm.

Figure (6.25) shows the measurement of coincidence versus the pump frequency. The pump detuning $\Delta\lambda_{pump} = 0$ corresponds to $\lambda_{pump} = 764.313$nm.

We observe three local maxima at $\Delta\lambda_{pump} = 2$pm, $\Delta\lambda_{pump} = 42$pm and $\Delta\lambda_{pump} = 79$pm, corresponding to either a set of resonant/anti-resonant/resonant biphoton states or a set of anti-resonant/resonant/anti-resonant two photon states. To distinguish between the two sets, we need to perform a HOM interference experiment. We also see two local minima at 22pm, 57pm, corresponding to pump biphoton state that are neither resonant nor anti-resonant.

The average distance between pump wavelengths generating resonant and anti-resonant states is 38.5pm ($\Delta\nu_{fsr} = 20.52$GHz, $\Delta\omega_{fsr} = 128.97$GHz), which corresponds to the waveguide free spectral range deduced from the transmission measurements ($\Delta\nu_{fsr} = 20.00$GHz, see results presented in (5.3)).

We also notice that in figure (6.25) the maxima and minima are disposed along a monotonically increasing envelope function. The reason is that, as we scan the pump wavelength, we are moving along the positive direction of λ_+ in the phase matching space (negative direction of ω_+ in figure (2.8)). The phase-mismatch decreases while the SPDC efficiency and pair production rate increase, in agreement with figure (3.1).

2. Set the delay time to half-cavity round-trip

After setting the correct pump frequency, we set the delay line to half of the cavity round-trip.

An estimation of the cavity round-trip is obtained from the simulated mode dispersion (2.1) and the physical length of the waveguide, known with some incertitude from the cleaving process ($l = 2 \pm 0.1$mm). To find the exact value of half cavity round-trip, we first launch a HOM interference measurement with a rough scan (step of 10µm) in the range of ±0.6mm. Once we identify the position of the HOM replica, we proceed with a finer scan, with steps of 5µm in the ±0.3mm range and an acquisition time of 30s per each step.

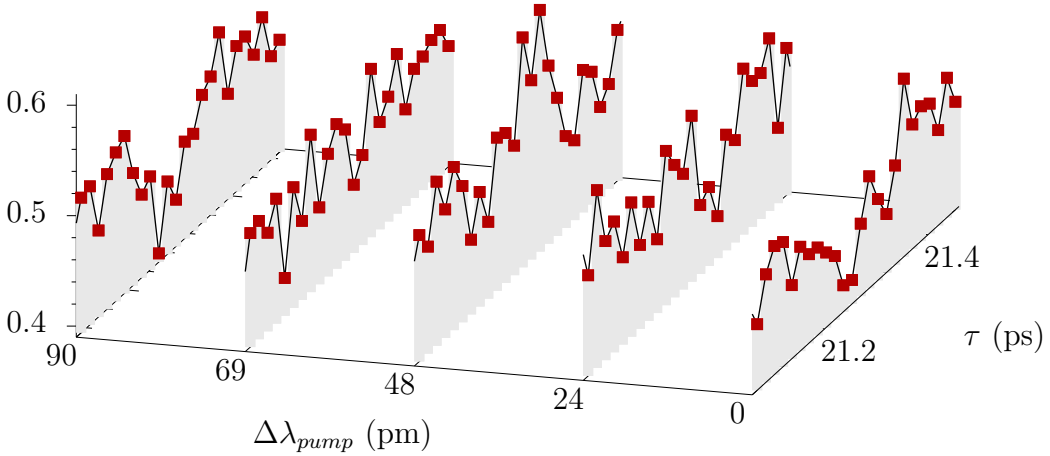

Figure 6.26 – HOM measurement at the time delay of half the cavity round-trip versus the detuning of the CW pumping wavelength respect to $\lambda_{pump} = 764.313$nm.

Figure (6.26) shows the HOM interferograms obtained from these measurements. The experimental data are indicated by red dots, while black lines and grey background are used for visualization purpose. We can distinguish the resonance ($\Delta\lambda_{pump} = 0$pm, 90pm), the anti-resonance ($\Delta\lambda_{pump} = 48$pm) and the non-resonance ($\Delta\lambda_{pump} = 24$pm, 69pm) conditions.

We find the HOM dip and peaks at a signal and idler temporal delayed by $\tau \sim 21.3$ps (spatially delayed by $z \sim 6.38$mm).

6.7.3 Hong-Ou-Mandel interference at half round-trip time delay: measurement

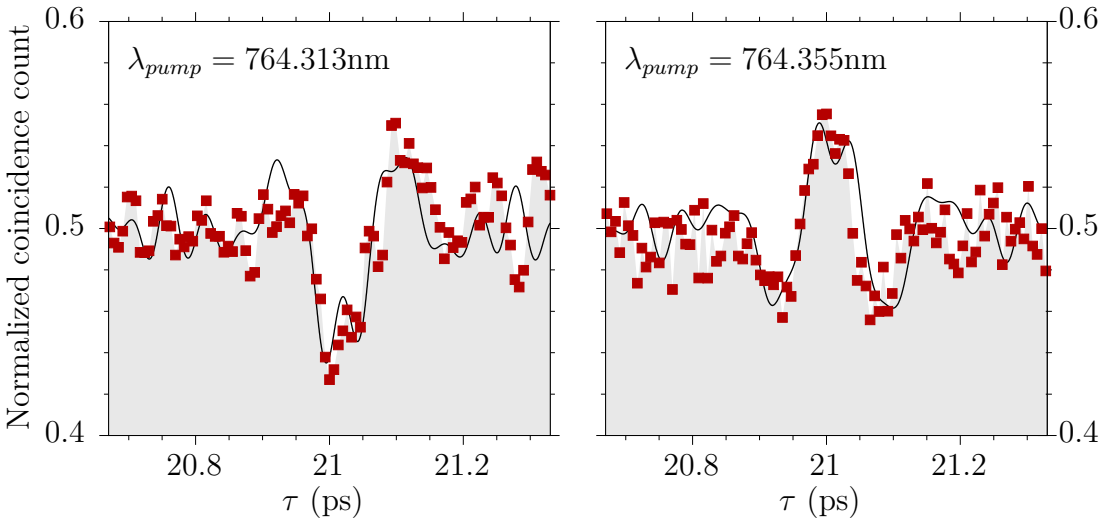

Figure 6.27 – HOM measurement at time delay of half the round trip for a resonant (left) and anti-resonant (right) CW pump wavelength. Red squares: experimental data. Continuous black line: best experimental fit.

Now that we have identified the parameters of the delay line and pump frequency necessary for observing the HOM replica, we can launch HOM measurements having a higher sampling, in order to detect the fine shape of the HOM replica.

In figure (6.27) we illustrate two HOM interferograms, obtained by moving the delay line of steps of 2μm. The experimental data is shown in red dots. Unlike the previous figure, the black continuous line indicates the best theoretical fit. The model is based on the numerically calculated JSA of figure (2.8) , using $\omega_p = 2\pi \cdot 388.91$THz ($\lambda_{pump} = 770.616$nm) in the resonant case, and $\omega_p = 2\pi \cdot 388.99$THz ($\lambda_{pump} = 770.463$nm) in the anti-resonant case, a waveguide length of 2mm and facets reflectivities $R_H = 0.297$, $R_V = 0.243$.

At $\lambda_{pump} = 764.313$nm (figure (6.27), left) we find the HOM dip at $\tau = 20.96$ps ($z = 6.29$mm). In this measurement we integrate for 30s per point. Given the high density of points and limited integration time, we smooth the resulting data by performing a moving average among the three nearest points.

At $\lambda_{pump} = 764.355$nm (figure (6.27), right) we measure the HOM peak centered at 21.02ps (6.30mm) by integrating for 120s per point during an overnight measure. In this case we do not perform any average of the data.

To compare the two measurements, we normalize to 0.5 the coincidence counts of the HOM base line $\bar{R}$. Before the normalization, we check that the number of the base line counts is sufficiently high to assure a low uncertainty. In the bunching

measurement (left), $\bar{R} = 425 \pm 30$ counts, corresponding to an uncertainty of $\sigma_{\bar{R}}/\bar{R} = 7\%$. In the anti-bunching measurement (right), $\bar{R} = 1600 \pm 50$ counts, corresponding to $\sigma_{\bar{R}}/\bar{R} = 3\%$.

We also notice an asymmetry in the HOM dip (left) due to the presence of a narrow peak at higher time delay. In HOM interference, an asynmmetry in the shape of the dip may be due to third-order dispersion effects occurring along the fibers [207]. However, we do not individuate any visible asymmetry in the anti-bunching HOM pattern (right). Thus we are still investigating the origin of this asymmetry.

Part III

AlGaAs devices to generate Orbital Angular Momentum of light

Context and background

In the framework of a collaboration with Ebrahim Karimi (University of Ottawa) and Peter Banzer (Max Planck Institute for the Science of Light, Erlangen), we have started a reflection on the possibility of realizing a novel AlGaAs based integrated device for the generation of a light beam carrying spin angular momentum (SAM) and orbital angular momentum (OAM).

In the following, after a brief introduction about light angular momentum, we report on the realization of the SAM device in chapter (7) on the design of the OAM device in chapter (8).

Angular Momentum of light

In 1619 Kepler observed that a comet tail always points away from the Sun and explained it by introducing for the first time the concept of radiation pressure of light [208]. To justify the existence of the radiation pressure of light, in 1862 Maxwell introduced the idea that light possess a linear momentum, which was experimentally observed by Lebedevin forty years later [209]. Nowadays it is well known that light carriers a linear momentum $\mathbf{p}$ directed along its direction of propagation $\mathbf{k}$ and with an amplitude of $p = h/\lambda$ per photon, as stated by de Broglie's relation. It is also known that, in addition to $\mathbf{p}$, a light beam can carry angular momentum $\mathbf{L}$, directed as well along the direction of propagation of light and defined as:

$$\mathbf{L} = \mathbf{r} \times \mathbf{p} \tag{6.91}$$

According to the definition (6.91), since $\mathbf{r}$ belongs to the transverse plane while $\mathbf{L}$ is aligned along the light propagation direction, an angular momentum can exist only if the light beam has azimuthal momentum in the transverse plane, i.e. $\mathbf{p}_\theta \neq 0$. As a propagating e.m. field is formed by the mutually orthogonal vectors $(\mathbf{k}, \mathbf{E}, \mathbf{H})$, this implies that at least $\mathbf{E}$ or $\mathbf{H}$ have a projection in the direction of propagation as well.

This condition is verified by any optical wave that has a finite extension in the transverse plane [210], which is always the case for light beams observed and measured within an optical system of finite apertures.

Therefore any light beam can, in principle, carry angular momentum. In particular, there are two different kinds of angular momentum:

I Spin angular momentum (SAM, $\mathbf{L} = \mathbf{L_s}$), carried by a circularly polarized beam. Each photon can carry either $\mathbf{L_s} = +\hbar$ or $\mathbf{L_s} = -\hbar$, corresponding to the left and right handedness of the circular polarization.

II Orbital angular momentum (OAM, $\mathbf{L} = \mathbf{L_o}$), carried by a beam with a helicoidal phase structure. Each photon can carry a multiple of the angular momentum quanta, $\mathbf{L_o} = l\hbar$, where $|l|$ is the number of intertwined helices and the sign of l their handedness.

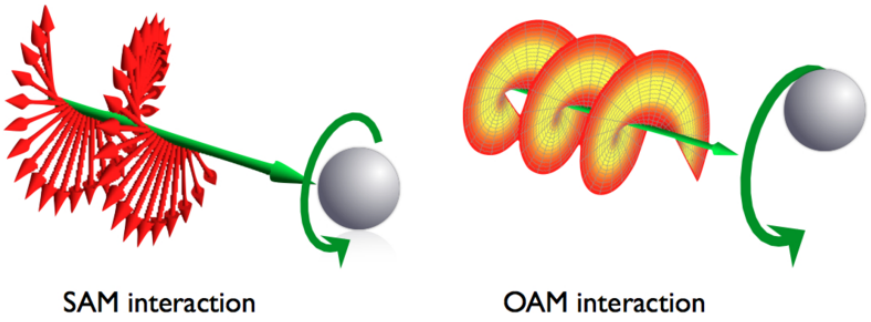

Figure 6.28 – Effect of a beam carrying Spin angular momentum (SAM, left) or first order Orbital angular momentum (OAM, right) on a particle placed on the beam axis. Image from [211].

Figure (6.28) illustrate two light beams carrying SAM (left) and OAM of first order (right) and their action on a particle.

SAM (left) makes the particle spins around the light propagation axis, while OAM (right) forces the particle to rotate in a circular orbit along the beam helicoidal phase structure.

The general definition of angular momentum (6.91) in the case of a light beam can be rewritten using electric and magnetic spatial fields distributions as:

$$\mathbf{J} = \epsilon_0 \int \mathbf{r} \times (\mathbf{E} \times \mathbf{B})\, d^3\mathbf{r} \tag{6.92}$$

The same expression can be derived starting from Noether's theorem [212, 213], which returns light angular momentum expressed in SAM and OAM contributions:

$$\mathbf{J} = \epsilon_0 \int (\mathbf{E} \times \mathbf{A})\, d^3\mathbf{r} + \epsilon_0 \sum_{i=x,y,z} \int \left(E^i\, (\mathbf{r} \times \nabla)\, A^i\right) d^3\mathbf{r} \tag{6.93}$$

The first term refers to the possibility of a light beam to carry SAM, while the second one to twist and to carry OAM.

Orbital Angular Momentum

OAM light beams are natural solutions of the wave equation under paraxial approximation (weak focusing). Two families of solutions are found, depending on the choice of the coordinate system.

In cylindrical coordinates (r, ϕ, z), as discovered by Allen and colleagues [214], Laguerre-Gaussian modes (LG) have a well-defined OAM. They are defined as:

$$\begin{aligned} u(r,\phi,z) =& \frac{C_{lp}^{LG}}{w(z)} \left(\frac{r\sqrt{2}}{w(z)}\right)^{|l|} \exp\left(-\frac{r^2}{w^2(z)}\right) L_p^{|l|}\left(\frac{2r^2}{w^2(z)}\right) \\ & \exp\left(-ik\frac{r^2}{2R(z)}\right) \exp(i\psi(z)) \ \exp(-il\phi) \end{aligned} \tag{6.94}$$

where L_p^l are generalized Laguerre polynomials, C_{lp}^{LG} a normalization constant, $w(z)$ the beam waist at the position z from the focus, $R(z)$ the radius of curvature of the beam and $\psi(z)$ the Gouy phase.

The LG mode phase profile takes the form of $\exp(-il\phi)$, where ϕ is the azimuthal coordinate in the transverse plane and l the OAM order, also known as topological charge. This gives the periodicity and handedness of the helicoidal wavefront. Along the beam axis ($r = 0$), the phase is undefined since it takes all the possible values in $[0, 2\pi)$. Destructive interference generates an optical vortex, with the result that the intensity profile of LG modes has a donut shape centered on the optical axis.

In the following, we refer to LG modes (6.94) having $p = 0$ and indicate them as $\mathrm{LG}_{m,n}$ where m is a right-handedness topological charge and n a left-handedness topological charge. As instance, LG_{10} (LG_{01}) carries OAM of first order and right (left) handedness, LG_{20} (LG_{02}) OAM of second order and right (left) handedness, and so forth.

In Cartesian coordinates (x, y, z), an OAM light beam is described by the superposition of Hermite–Gaussian modes (HG). Therefore every LG mode is given by the superposition of some specific HG modes with a specific phase relation among them. As instance, the first and second order LG modes are given by:

$$\begin{aligned} \mathrm{LG}_{10} &= \mathrm{HG}_{10} + i\mathrm{HG}_{01} \\ \mathrm{LG}_{01} &= \mathrm{HG}_{10} - i\mathrm{HG}_{01} \\ \mathrm{LG}_{20} &= \mathrm{HG}_{20} + \frac{3i}{2}\mathrm{HG}_{11} - \mathrm{HG}_{02} \\ \mathrm{LG}_{02} &= \mathrm{HG}_{20} - \frac{3i}{2}\mathrm{HG}_{11} - \mathrm{HG}_{02} \end{aligned} \tag{6.95}$$

We illustrate in figure (6.29) the superposition of two first order HG modes to give the first order LG modes (first two equations in (6.95)). At top of each row we represent the modes intensity profile, while in the bottom their corresponding phase profile. The HG modes are calculated in Matalb using the library [215] and successively normalized by imposing the integral of their spatial intensity distribution to one. We may notice the opposite handedness of LG_{10} and LG_{01}, since their phase profiles are opposite. Analogously, in figure (6.30) we show how to combine three HG modes to obtain the second order LG modes (last two equations in (6.95)). We observe that the intensity profile of LG_{20} and LG_{02} are donuts

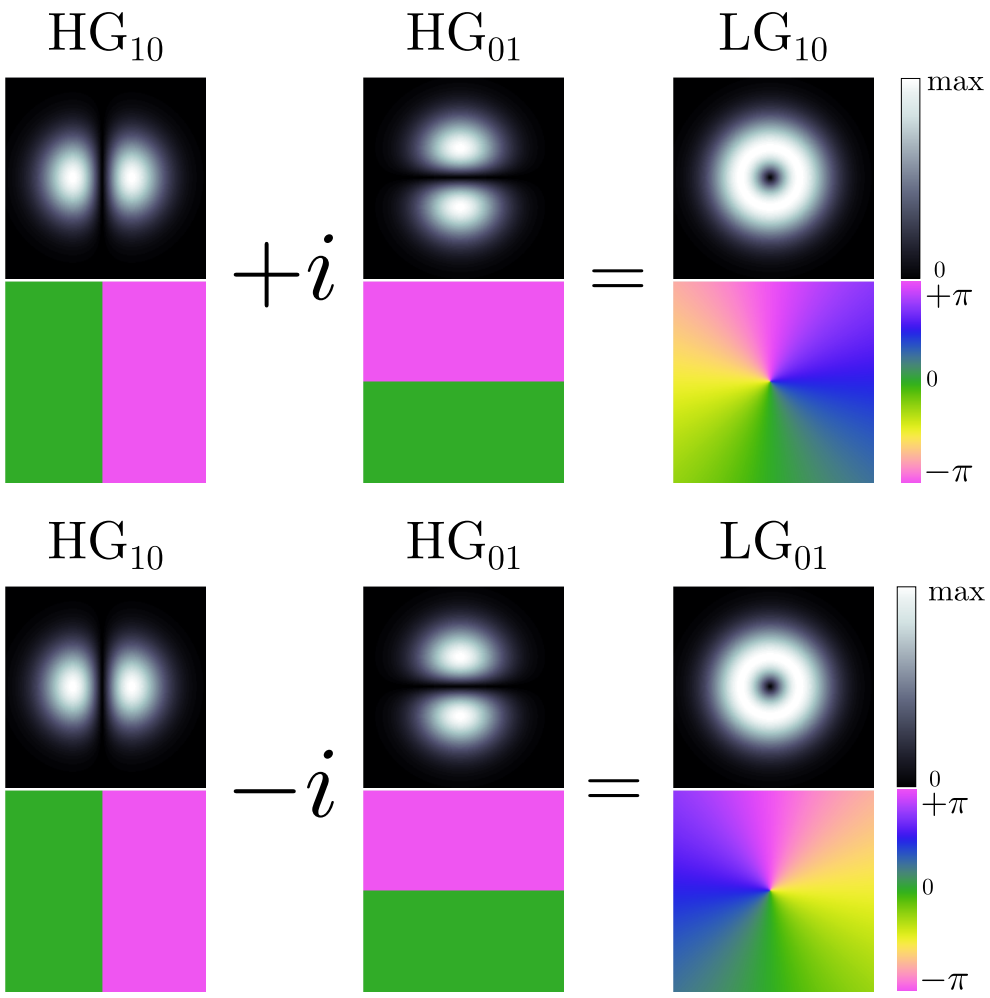

Figure 6.29 – First order LG modes given by the superposition of two HG modes, according to equation (6.95). In each row we show the mode intensity (top) and phase profile (bottom).

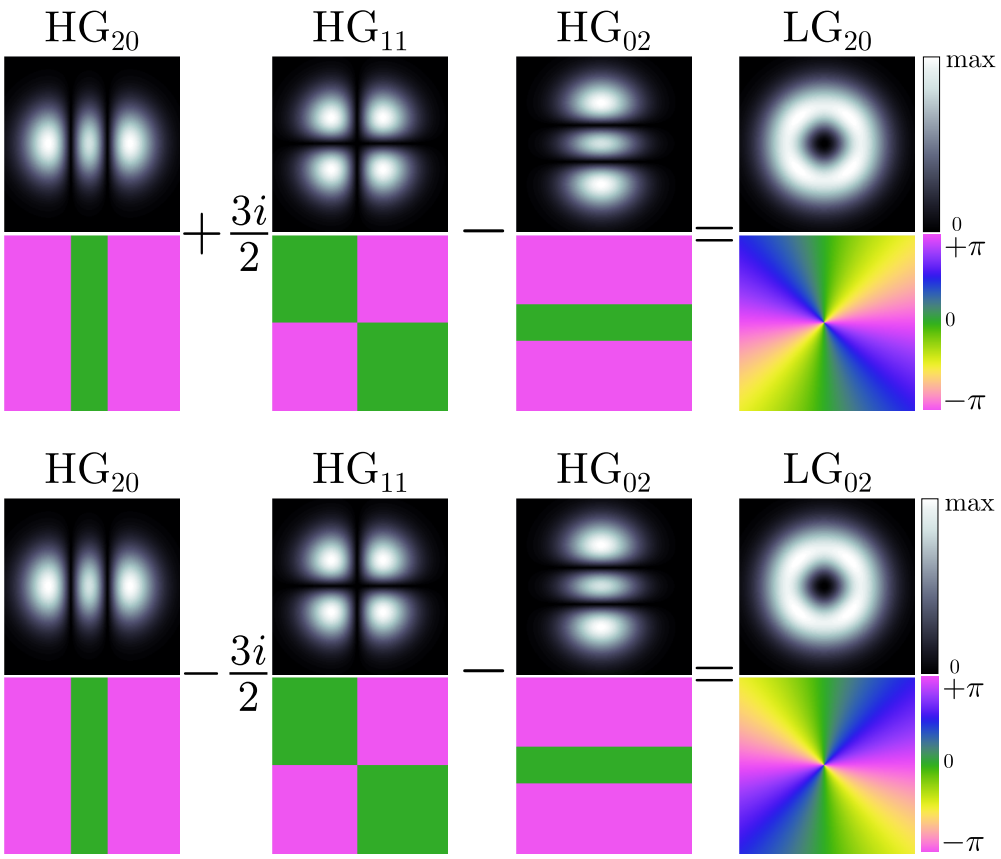

Figure 6.30 – Second order LG modes given by the superposition of three HG modes, according to equation (6.95). In each row we show the mode intensity (top) and phase profile (bottom).

with a larger hole than LG_{10} and LG_{10}, while their phase profiles have a double periodicity, sign that their OAM order is two.

Application and generation of Orbital Angular Momentum

Light Spin and Angular Momentum degrees of freedom have been used in numerous applications [216]. As instance, biosensing, nanoplasmonics and optical tweezing take advantage of SAM and OAM beams amplitude, phase and polarization spatial distribution, while quantum communication and information processing of their Hilbert space, bidimensional for SAM and potentially infinite in the case of OAM.

There are several ways of generating OAM light beam, in both free space and integrated optics [217]. In free space, the most common tools are cylindrical mode converters [214], spiral phase plates [218], computer generated holograms [219, 220], patterned liquid crystals (q-plates) [221, 222] and structured optics [223]. Miniaturized devices include plasmonic antennas metasurfaces [224, 225], sub-wavelength gratings [226] and optical fibers [227].

Integrated optics approaches are based on spiral phase integrated in vertical-cavity surface-emitting laser [228], microlasers [229], micro-ring resonators with angular gratings [230] and microemitters [231]. These integrated devices have the advantages of being broad-band and capable of generating high orders OAM beams. Yet, they work like antennas, with the emission of OAM beams along a direction orthogonal to surface, preventing an easy integration with other photonic circuits. On the contrary, in plane angular momentum emitters would enable an easy and efficient coupling with on-chip components or external optical fibers.

In the following two chapters we present our work on the realization of novel AlGaAs-based devices for the emission of SAM and OAM light beams along the longitudinal direction.

The first device works as an integrated quarter quarter-wave plate, which converts a beam linearly polarized at 45° into a beam that is circularly polarized and carries SAM.

The second device is the analogous of an integrated cylindrical mode converter, since it transforms a first order Hermite-Gaussian beam into a first order Laguerre-Gaussian beam, carrying first order OAM.

Chapter 7

An integrated quarter-wave plate

In this chapter we present the design, fabrication and characterization of an asymmetric AlGaAs waveguide that works as an integrated quarter-wave plate (QWP), capable of introducing a phase-delay of $\pi/2$ between the guided quasi-TE and quasi-TM modes at the telecom wavelength. Thanks to the strong lateral confinement of the sub-wavelength core, these two modes possess a strong longitudinal field component. An input beam linearly polarized along the diagonal direction (LP_{45°) is transformed into a circularly polarized beam that carries SAM on the transverse field component and a first order OAM on the longitudinal field component. We benchmark the device performance by measuring the transmission losses of quasi-TE and quasi-TM modes and the polarization state of a LP_{45° beam coupling out of the device. Due to the cavity effect, the delay between the two emitted quasi-orthogonal modes varies sinusoidally in $\Delta\theta = 95.5^\circ \pm 30^\circ$ at $\lambda \approx 1.55\mu$m, in agreement with a birefringent Fabry-Perot cavity model.

7.1 Design

7.1.1 Working principle

A ridge waveguide confines the electromagnetic field within the transverse (x, y) plane, with the result that a longitudinal electric field component E_z is formed. The spatial distribution of E_z is given by the following expression [232]:

$$E_z(x, y) = -\frac{i\lambda}{2\pi n_{\text{eff}}} \boldsymbol{\nabla}_\perp \cdot \mathbf{E}_\perp \tag{7.1}$$

where $\boldsymbol{\nabla}_\perp \cdot \mathbf{E}_\perp$ is the divergence of the transverse component of the field and n_{eff} its effective refractive index.

The two orthogonally polarized transverse electric (TE) and transverse magnetic (TM) modes acquire a longitudinal component, becoming quasi-orthogonally polarised transverse electric (quasi-TE) and transverse magnetic (quasi-TM) modes. A HG_{00} (fundamental Gaussian) quasi-TE mode acquires a longitudinal field component $E_z(x, y)$ with a spatial distribution that is a HG_{10} mode, while the longitudinal component of a quasi-TM HG_{00} mode is a HG_{01} mode. In a QWP

scheme, the superposition of a quasi-TE and a quasi-TM modes delayed by $\pi/2$ results in a circularly polarized beam, which carries SAM along the fields transverse component. Besides, according to HG to LG transformations (6.95) and the confinement effect (7.1), the field carries OAM of first order in its longitudinal component.

7.1.2 Guidelines

The subwavelength QWP waveguide must satisfy the following requirements:

1. Support HG_{00} quasi-TE and quasi-TM modes and delay them by $\pi/2$.
2. A high confinement of the guided modes in the transverse plane, so that quasi-TE and quasi-TM modes possess a high longitudinal component, according to (7.1).
3. Guide rotational symmetric quasi-TE and quasi-TM modes so that the amplitudes of their longitudinal components are equal as a consequence of (7.1) and satisfy the HG to LG transformation (6.95).

According to these requirements, the device must have the following features:

(a) Monomode: support only fundamental quasi-TE and quasi-TM modes.

(b) Efficient, balanced and tolerant input coupling for quasi-TE and quasi-TM modes.

(c) Low and balanced losses for quasi-TE and quasi-TM modes.

(d) Subwavelength structure, to maximize the ratio of longitudinal to transverse components of the field.

(e) Squared core, to support rotational symmetric quasi-TE and quasi-TM modes.

7.1.3 Device structure

The design process is inspired by the study of Liang and coworkers [233], who propose a hybrid silicon-plasmonic waveguide to realize an integrated QWP. In our case, we choose to realize our device in the AlGaAs platform, given its potential for nonlinear application and electrical injection. Besides, we design a purely dielectric waveguide to avoid the losses induced by the presence of a plasmonic layer.

Our study is carried out by using an approximating analytical model, named effective index method, and Lumerical MODE solver. The details of the design optimization study are reported in my internship thesis [234] that I have done in the same team before starting my thesis. We fulfill all the requirements (a)-(e) by decoupling them.

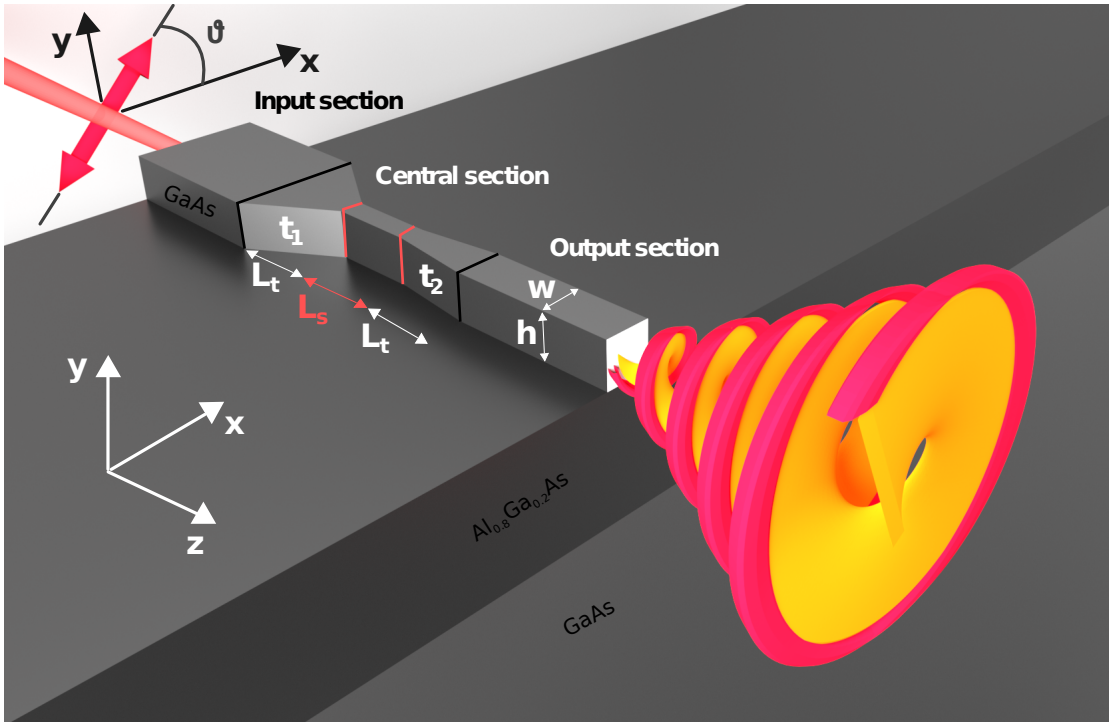

Figure 7.1 – Sketch of the integrated QWP AlGaAs waveguide.For a specific value of L_s, an incoming light beam linearly polarised at $\pi/4$ is transformed into a light beam circularly polarized, carrying SAM in the field transverse component (red) and first order OAM in the field longitudinal component (yellow).

The designed device is a ridge waveguide made of 1.08µm thick GaAs core layer and 1.08µm thick $Al_{0.8}Ga_{0.2}As$ cladding layer, on a GaAs substrate. As illustrated in the sketch of figure (7.1), it is composed by three different parts, each one with a specific function.

The input section is large enough ($w = 3$µm) to allow an easy and tolerant coupling of an incoming laser beam, linearly polarized at $\pi/4$, into the fundamental quasi-TE and quasi-TM modes supported by the waveguide.

The central section consists of two adiabatic tapers and an asymmetric straight section ($w = 0.55$µm). The two adiabatic tapers (300µm long) assure low optical losses, while the asymmetric straight part assures a monomode working condition (only fundamental quasi-TE and quasi-TM modes are supported) and induces birefringence in an isotropic material such as GaAs. Since its width is very close to the cut-off condition for the quasi-TE mode ($w_{cut-off} = 0.50$µm), it delays the quasi-TE modes with respect to the quasi-TM mode, inducing a dephasing of:

$$\Delta\Phi_s = \frac{2\pi}{\lambda}(n_{qTE} - n_{qTM})L_s \tag{7.2}$$

where L_s is the length of the straight part and n_{qTE} and n_{qTM} the effective refractive index of quasi-TE and quasi-TM modes. By setting its length L_s, we can control the accumulated phase-delay $\Delta\Phi$ between quasi-TE and quasi-TM modes. Experimentally, we find that a length of $L_s = 52.8$µm gives an average

accumulated dephase of $\pi/2.01 = 89.5°$.

7.1.4 Supported modes and near-field

The output section has a rotational symmetric square cross-section ($w = h = 1.08\mu m$) to guide a light beam with a HG_{00} profile in the field transverse component and LG_{01} in the longitudinal component.

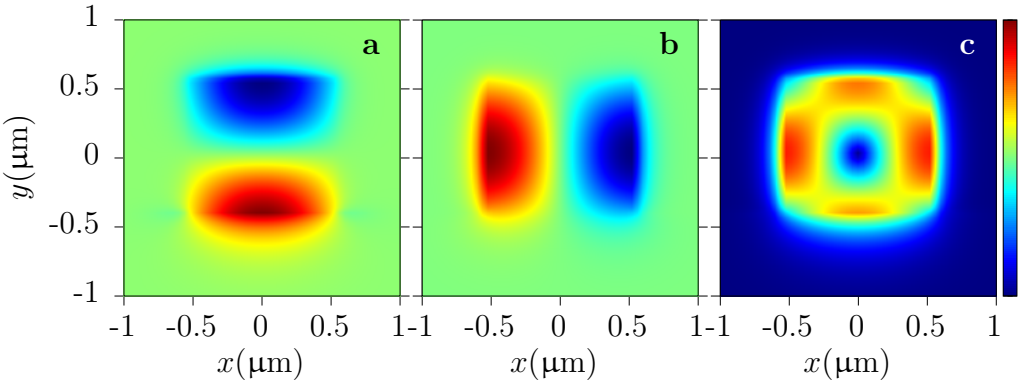

Figure 7.2 – Numerical simulations of the longitudinal component of the real part of quasi-TM (a) and quasi-TE (b) modes in the waveguide output section. When the two modes are delayed by $\pi/2$, a LG_{01} mode is formed, indicated by the donut shaped intensity distribution (c). The fields are calculated at 1550nm.

Figure (7.2) shows a simulation of the real part of the longitudinal component of the supported modes in the device output section. According to (7.1), the waveguide micrometer transverse dimension confines and shapes the longitudinal component of the quasi-TM mode in a HG_{01} mode (a), and the longitudinal component of the quasi-TE mode in a HG_{10} mode (b). The central section introduces a dephasing term of $\pi/2$ between them, so that their superposition is a LG_{01} mode, whose instensity profile is illustrated in (c).

Figure (7.3) shows a FDTD simulation of the longitudinal component of the emitted beam in the near field ($z = \lambda/3 = 517nm$ from the waveguide output facet). The helical phase distribution (a) and the corresponding doughnut intensity profile (b) indicate that the longitudinal field component carries OAM of first order.

However, the phase vortex disappears as the beam propagates in free space, due to the lack of confinement. In figure (7.4) we illustrate the result of a FDTD simulation of the emitted beam. We compare the in plane profile ($y = 0$) of the field transverse (a) and longitudinal (b) components, while the beam propagates from the waveguide output facet ($z = 0$) in free space. We observe that the field longitudinal component vanishes during the propagation of the beam, as the longitudinal intensity values are some dB lower than the transverse intensity values.

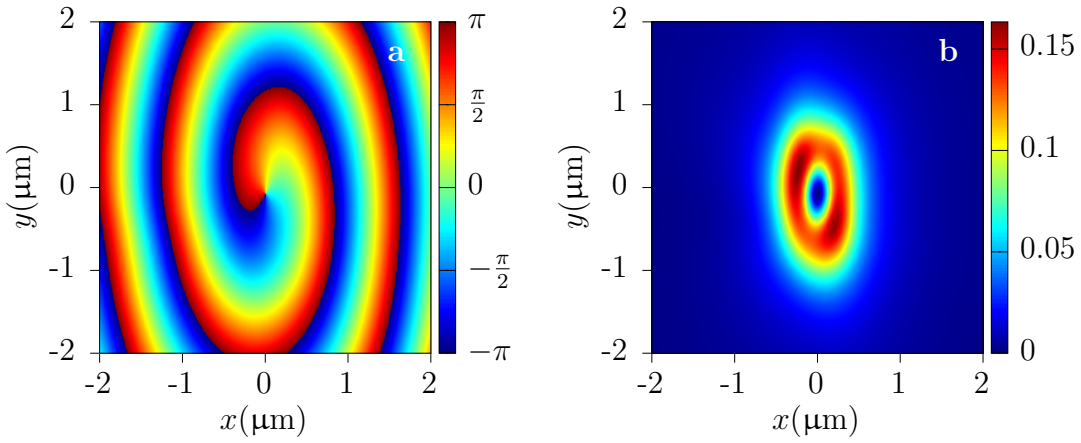

Figure 7.3 – Numerical simulations of the emitted phase (a) and intensity profile (b) of the longitudinal field component in the near-field. The field is calculated at 1550nm.

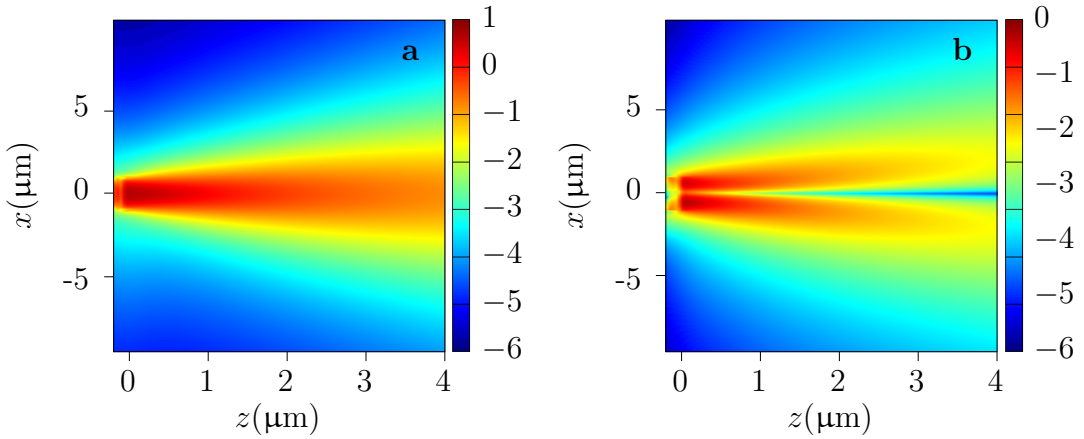

Figure 7.4 – Numerical simulations of the transverse (a) and longitudinal (b) components of the intensity of the electric field as it propagates in free space from the waveguide output facet, from a top view. The intensity scale is logarithmic and expressed in dB. The field is calculated at 1550nm.

7.2 Fabrication

7.2.1 Overview

The AlGAAs wafer was grown by Molecular Beam Epitaxy (MBE) at Laboratoire de Photonique et de Nanostrucutres (Marcoussis, France) and processed by myself in Paris Diderot clean room.

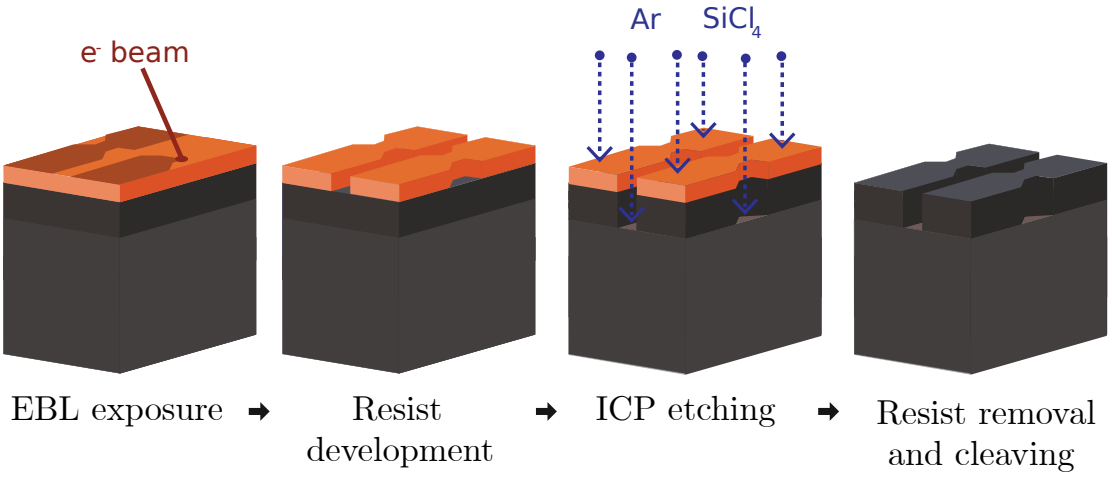

Figure 7.5 – Sketch of the clean room fabrication steps for the fabrication of the device.

Figure (7.5) is a sketch of the main clean room steps to fabricate the device. The process consists of a EBL lithography (ma-N 2403 negative resist) followed by ICP etching, using the optimized spin-coating, exposure and etching parameters presented in (4.3).

In the MPQ clean room, the wafer is cleaved in several samples. We pick one of them and we clean its surface from organic and inorganic impurities using acetone and isopropanol in ultrasound, then water and oxygen plasma etching.

We spin-coat the negative tone resist ma-N 2403 using the parameter reported in table (4.1). The fabrication proceeds in École normale supérieure clean room, where a EBL system (Raith e-Line Plus) exposes the negative resist. This EBL system allows, in addition to standard exposure, a Fixed Beam Moving Stage (FBMS) exposure, in which the electronic beam is fixed while the sample is moved. This procedure enables a rapid exposure of long structures, such as waveguides, and is not prone to writing field boundary issues. For our device, we use it to define input and output sections.

We transfer back the sample to the MPQ clean room, where we develop the resist and perform ICP etching, using a low energy etching based on Ar and $SiCl_4$, as described in (4.3.4). We measure the etched depth by means of a profilometer (Dektak 150) and successively we remove the resist. We end the process by setting the sample length to approximately 2mm via manual cleaving.

Our design [234] is robust with respect to the estimated processing tolerances, summarized in table (7.1).

Fabrication step	Tolerances	Value
MBE growth	$Al_xGa_{1-x}As$ composition	$\Delta x = 5\%$
EBL standard (ma-N 2403)	central section width	$\Delta w_s = \pm 20$nm
EBL moving stage (ma-N 2403)	in, out sections width	$\Delta w_{in,out} = \pm 100$nm
ICP etching	core thickness	$\Delta t_{core} = \pm 50$nm
Cleaving	device length	$\Delta l = \pm 100$µm

Table 7.1 – Uncertainties of each fabrication step.

7.2.2 Electron beam lithography mask

The design of the mask is carried out via the open source software KLayout and Raith eLine proprietary software. The mask drawn in KLayout is exported as a GDS file and imported in eLine. In eLine we add the input and output sections, which, being FBMS paths, cannot be drawn directly in KLayout and are not compatible with a GDS standard file.

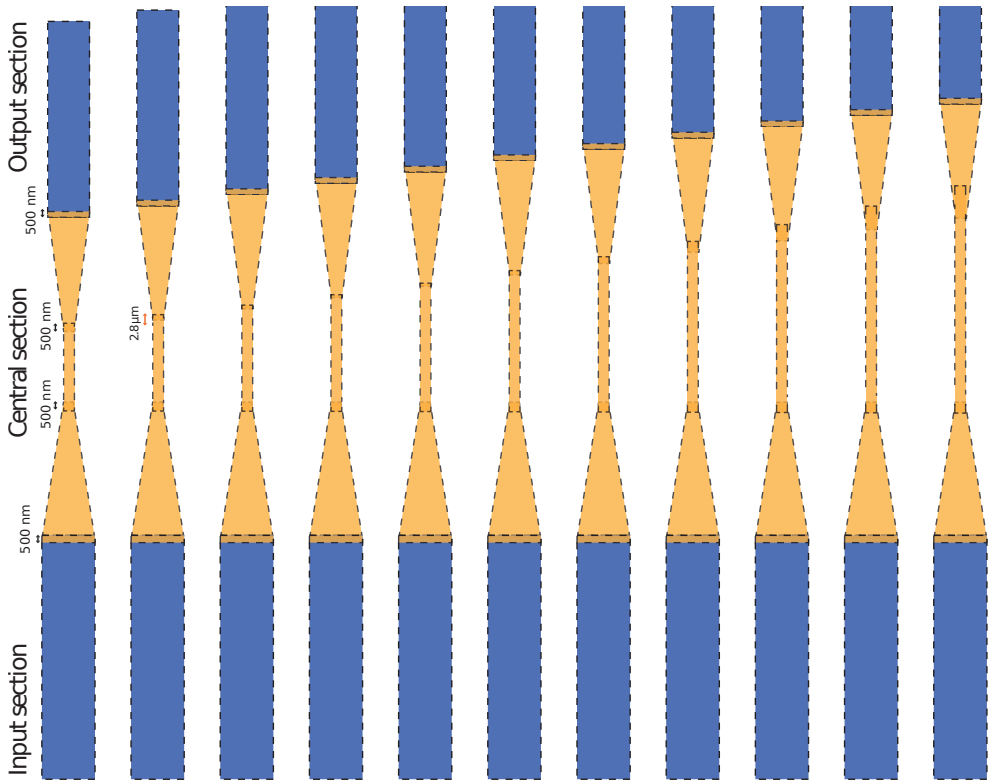

Figure 7.6 – Schematic of the first 11 waveguide as designed in the mask. The central section of the waveguide, in yellow, increases by $\Delta L = 2.8$µm per each waveguide. The input and output sections, in blue, are FBMS path. The overlap between the different sections and at the WF boundary of the thin central section is 0.5µm to avoid the presence of longitudinal gaps after exposure.

A schematic of the first eleven waveguides in the mask is represented in figure (7.6). In total, we draw 31 waveguides, whose central section has a straight part

that increases progressively by $\Delta L = 2.8\mu$m. This range allows to span several induced phase delay according to (7.2), with $\Delta\Phi = 3.3°$. Therefore, even if the effective index of quasi-TE and quasi-TM modes do not correspond to the numerically calculated ones due to the fabrication tolerances (table (7.1)), there is at least one waveguide that induces the desired phase delay of $\Delta\Phi = \pi/2$ with an accuracy of $\Delta\Phi = \pm 3.3°$. The device bandwidth, i.e. the maximum delay that is possible to induce between two orthogonally polarized modes by coupling the light in the waveguide with the longest straight section, is $\Delta\Phi_{BW} = \pm 102.3°$.

The input and output sections, in blue, are 1mm long. They are designed as FBMS paths, instead of polygons. The standard EBL polygons are represented in yellow: two tapers, 300µm long, and the thin central section, having a length varying from 38.8µm to 125.6µm. We may notice that the adjacent sections and the parts forming the central section overlap by 0.5µm. This overlap avoids the presence of a gap at the connection between different polygons and at the writing field (WF) boundaries. More details about how we solve the WF boundary issue and the choice of these parameters can be found in my master thesis [235].

For a dose of $D = 145\mu\text{C/cm}^2$, the time to expose each FBMS path is approximately 3 minutes, while the exposure of the standard EBL central section requires 2 minutes. The exposure of one complete mask of 31 waveguides lasts for more than 4 hours. We set up the lithography to take place over the night and expose two masks.

7.2.3 Electron beam lithography process

In this section we report the procedure used for the EBL, developed with Michael Rosticher, the ENS clean room engineer, to avoid the WF issue and minimize the stitch error between FBMS and EBL expositions.

1. **Preparation of the sample**
   While we make the EBL chamber ventilate, we prepare the sample in the photolithography room, where UV light is filtered out. We take the sample from the gel pack in the alumina case; if its bottom surface is glued to the gel pack, we can easily unstick it by pushing softly its sides. Then we make a small scratch onto one corner of the resist. This generates some particles of dust, necessary in the following gross focusing of the electronic beam on the sample. As we place the sample on the EBL sample holder, we also remove the resist underlying the metallic holder clamp, which adheres better to the GaAs wafer than to the resist surface. We need to avoid any movements of the sample during the exposure, otherwise the pattern would present blurred features. Once we transfer the sample holder in the EBL machine and we close the chamber door, we pump the chamber to vacuum. The chamber pressure needs to reach $p = 2 \times 10^{-5}$mbar and it takes about 20 minutes. In the meantime we can load the mask in the e-Line software and check that layers, doses and geometry are set correctly.

2. **Activation of beam, detector and pre-focusing**

We open the sample holder map and we drive the electronic beam close to the sample by moving the stage. We activate the beam by setting the column acceleration voltage to 20kV and the beam aperture to 10μm. We also check that the angle of scan is set to zero to avoid misalignment between the EBL slow scan and the FBMS fast scan. To see the sample, we select the InLens detector, which measures the reflected primary electrons. If necessary, we adjust the detector sensitivity by playing on its brightness and contrast. We are now ready to focus the beam on the sample. We move the beam on the scratch and look for a small molecule of dust. As it is almost at the same height of the resist, we use it to pre-focus the beam by adjusting its working distance, at a magnification of $M = 150k$.

3. **Set origin and angle correction**
   The sample is identified by the absolute coordinates xy, while electronic beam movements by the EBL internal coordinate uv, so we need to map xy to uv. We move beam to the bottom left corner of the sample. For a fine positioning, we can activate a green cross to indicate the center of the beam. We read the origin position O_{xy} and we set it as the origin for the vectors $\mathbf{u}$ and $\mathbf{v}$. Now we correct the angle misalignment between xy and uv. We move the beam to the sample bottom right corner and we read this position. Thus we set the direction of the vector $\mathbf{u}$ coincident to $\mathbf{x}$ and automatically of the normal vectors $\mathbf{v}$ to $\mathbf{y}$. Now we can check the length of the sample along $\mathbf{u}$ and $\mathbf{v}$, which should be approximately 1×1cm. Once we know the exact sample dimensions, we can choose the starting point (u, v) of the exposure of the mask. The exposed area should be at least 1.5mm far from the sample sides due to resist edge non-uniformity effects.

4. **Beam focusing and writing field alignment**
   We need to fine focus the beam and correct its stigmatism to improve the quality of exposure. We unblank (switch off) the beam and we drive it to a point close to the origin of exposure, where no feature is drawn - e.g. $(1.8\text{mm}, 2\text{mm})$ if origin is $(2\text{mm}, 2\text{mm})$. We magnify at $M = 230K$ and leave the beam switch on for a few seconds on a small area (≈ 100nm) to expose the resist an draw the so-called contamination dot. By looking at the shape of the dot, we adjust the beam focus (dot is blurred), stigmatism (dot is elliptical instead of circular) and alignment (as the beam wobbles, the contamination dot moves in horizontal or vertical direction). Once the parameters are correctly set, we should see a sharp and perfectly circular dot of ≈ 20nm diameter.

5. **Stage and beam alignment**
   To minimize the field stitch errors, we synchronize the beam writing field in uv to the stage interferometric movements in xy. We draw a row of contamination dots and position the beam at the center of the last one with the help of the green cross. By looking at the center of contamination dot, we align the beam within increasingly small writing fields of 10, 5 and 1μm.

We repeat this procedure for both EBL and FBMS scans and we save the new writing field parameters. A good writing field alignment procedure leads to field stitch errors smaller than $10 - 15$nm.

6. **Measure of the beam current**
   Before exposing the resist, we need to measure the beam current (I) to set the area dose (D), the number of electrons per cm^2 which exposes the pattern. The dose is related to the exposure time (t) and exposed area (A) by $D = I \cdot t/A$. To measure the current we drive the blanked beam to the center of a Faraday cup, situated nearby on the sample holder. We measure the current several times to check that it is stable and we pick its average value. Reasonable values of the current are $I = 30 - 38$pA for $V = 20$kV and 10µm aperture.

7. **Set the position list and start exposure**
   The position list includes all the features to expose and the corresponding doses. We load the focus and alignment beam parameters previously set for both the FBMS and standard EBL. Then we drag in the position list the cells of the EBL mask containing the feature to expose. As discussed in the stitch field error paragraph, the mask is made by one waveguide per cell to minimize the stitch field error at the passage between the FBMS and slow EBL scan. Since there are 31 waveguides per mask, we automatize the creation of the position list in the e-Line software through the following procedure:

   (a) Drag in the position list the parameters for standard EBL exposure

   (b) Drag in the position list the first cell. We choose to expose the EBL layer at a position $(u, v)_e$ near the contamination dots. We set its dose to 145µC and thus the polygon dwell time. We simulate the exposure time, which is approximately 2 minutes.

   (c) Drag in the position list the parameters for FBMS exposure

   (d) Drag in the position list the first cell. We choose to expose the FBMS layer at the same position $(u, v)_e$. We set its dose to 145µC and thus the FBMS line speed. We simulate the exposure time, which is approximately 4 minutes.

   (e) We select these first 4 lines in the position list and apply to them *Filter, Matrix Copy*. We set the transformation matrix as $(u, v) = (31, 1)$, $(\Delta u, \Delta v) = (100\mu\text{m}, 0)$ to generate 31 layers 100µm far each other along the horizontal direction, like the adjacent waveguides in our complete mask. We also select the option *adjust automatically the working area* and change the name of the created position list lines to expose all the 31 cells. We can check that the operation has succeeded by both simulating the exposing time of some of them and looking if the waveguides are centered in their working area.

(f) If we need to expose a second mask, we repeat the previous operation with another exposure staring point $(u, v)_e$.

We add at the end of the position list the macro to turn off the beam automatically when the exposure is over and we start the exposure by selecting *Scan, all*.

As we launch the lithography for the night, we come the morning of the following day to extract the exposed sample from the EBL machine. After the lithography process it is important not to expose the sample to light, in order to avoid accidental exposure of the resist ma-N 2403 before the development is performed.

7.2.4 Fabricated device

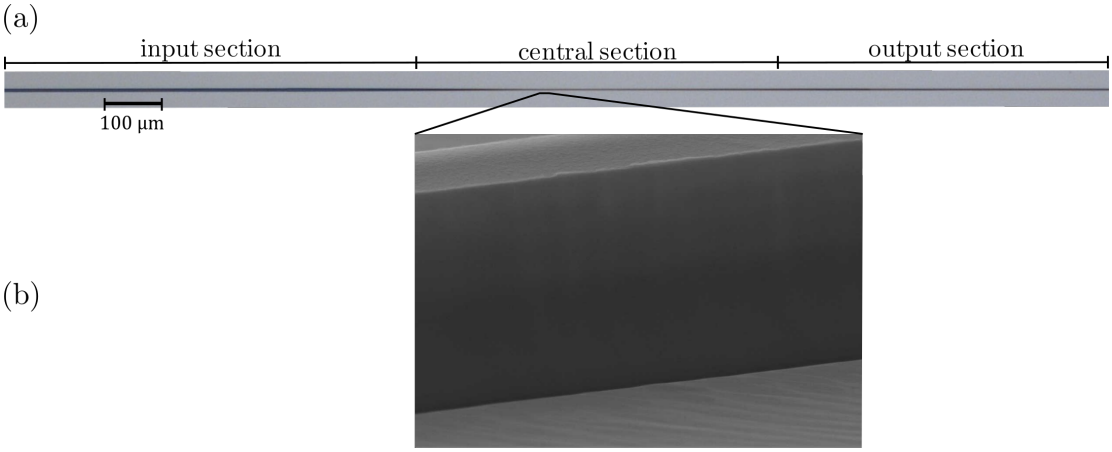

Figure 7.7 – Image of one waveguide in the fabricated chip.
(a) Top-view optical microscope image of input, central and output sections.
(b) A scanning electron microscope image of the sidewall of the central section straight part.

Figure (8.11) shows one among the fabricated waveguides. We can distinguish from a top-view optimal microscope image (a) the three input, central and output sections. In the central section, we distinguish the first taper, followed by the narrow straight part and the second taper. The inset (b) is a side view of the waveguide central section straight part, observed at the SEM. The measured width of the central section is 548 ± 20nm, compatible with the nominal width of 550 ± 20nm. The measured etched height over the sample is $1.09 \pm 0.1\mu$m, compatible with the nominal depth of 1.08μm.

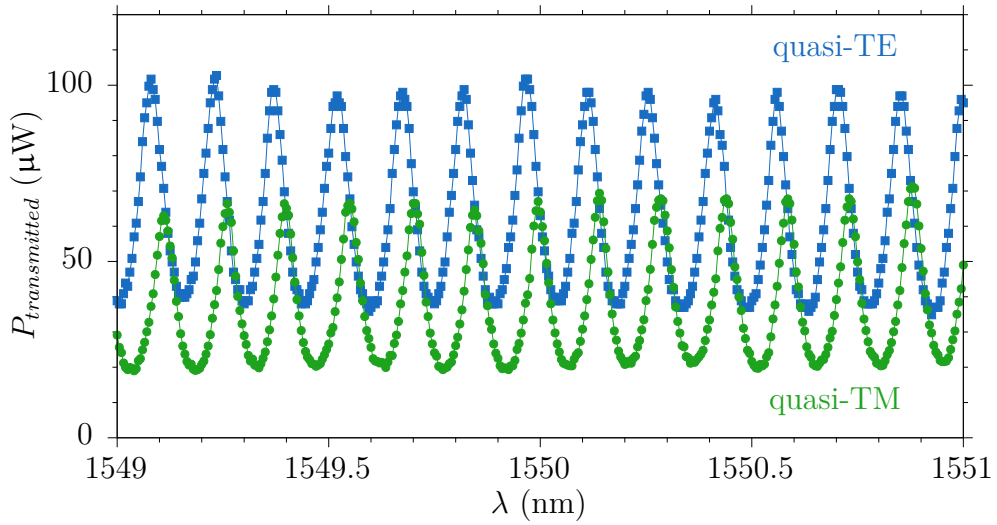

Figure 7.8 – Measured transmitted power of quasi-TE (blue squares) and quasi-TM (green dots) modes across the waveguide as a function of the wavelength. From the contrast of Fabry-Perot fringes and simulated facets reflectivity we find an average one-way transmission losses of $\alpha_{quasi-TE} = 0.8 \pm 0.4\text{cm}^{-1}$, $\alpha_{quasi-TM} = 1.5 \pm 0.4\text{cm}^{-1}$.

7.3 Characterization

7.3.1 Transmission losses

We measure the optical propagation losses, averaged over the wavelength, via the Fabry-Perot transmission power technique [181]. As shown in figure (7.8), we couple in the device a CW laser (Tunics-PR) TE and TM polarized and measure the power of the transmitted quasi-TE and quasi-TM modes as a function of the wavelength. The coupling in and out of the waveguide is done using an input (NA=0.65, M=40X) and an output (NA=0.75, M=60X) microscope objective lens. We calculate the modes transmission losses from the contrast of the Fabry-Perot fringes and their reflectivity [181]. The latter are calculated via a 3D FDTD simulation ($R^{\text{in}}_{quasi-TE} = 0.35$, $R^{\text{out}}_{quasi-TE} = 0.41$, $R^{\text{in}}_{quasi-TM} = 0.27$, $R^{\text{out}}_{quasi-TM} = 0.41$). In the range (1549nm,1551nm), we find that the transmission losses are $\alpha_{quasi-TE} = 0.8 \pm 0.4\text{cm}^{-1}$ and $\alpha_{quasi-TM} = 1.5 \pm 0.4\text{cm}^{-1}$, on average over different waveguides on chip.

7.3.2 Polarization state

To benchmark the device polarization manipulation functionality, we couple in a CW laser (Tunics-PR) linearly-polarized at 45° by a half wave-plate, and acquire the polarization state of the emitted beam via a telecom polarimeter (PAX5720IR3-T), a device composed of a rotating half wave-plate, a polarizer and a power meter. Figure (7.9) shows the polarization measurement performed on the waveguide having a central section straight part long $L_s = 52.8\mu\text{m}$, at

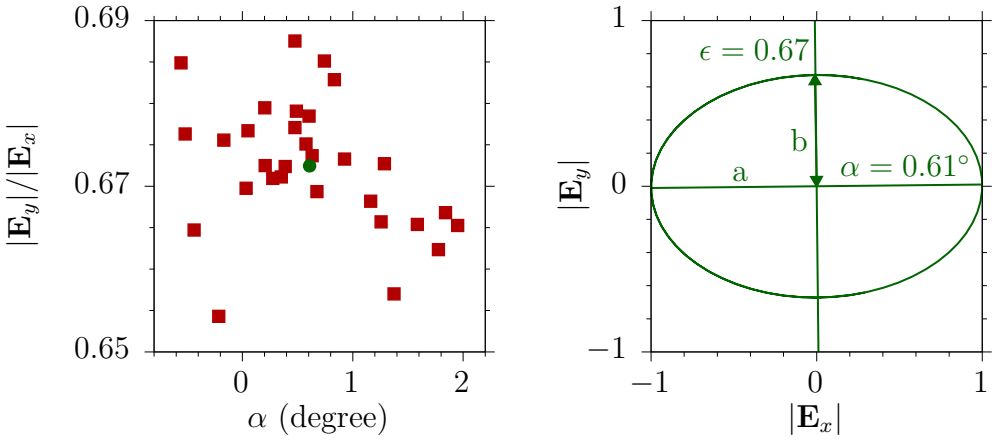

Figure 7.9 – Measured polarisation state at $\lambda = 1550$nm.
Left: ellipticity ($|\mathbf{E}_y|/|\mathbf{E}_x|$) and azimuth ($\alpha$) of the out-coupled beam elliptical polarization state.
Right: representation of the average polarization state (green dot on the left).

$\lambda = 1550$nm. We perform 30 consecutive measurement of the elliptical polarization ellipticity ($|\mathbf{E}_y|/|\mathbf{E}_x|$) and azimuth ($\alpha$), then we calculate their average values. The scattering in the measurements originates from the extinction ratio of the polarizer in the powermeter (10^{-2}). We find an average ellipticity of 0.67 and azimuth of 0.61°, corresponding to a phase delay between quasi-TE and quasi-TM modes of $\Delta\theta = 89.5°$, very close to the desired delay of $\Delta\theta = 90°$ expected from the simulations.

The corresponding polarization state is illustrated in (7.9), on the right. The device does not emit a circularly polarized mode, (unitary ellipticity) because at this wavelength the quasi-TE mode has higher losses than the quasi-TM due to the Fabry-Perot cavity effect. As shown in figure (7.8), at 1550nm the quasi-TM mode is a cavity resonant mode, while the quasi-TE is off-resonance by a phase delay of $\Delta\theta = 89.5°$. To achieve a perfectly circular state at the specific wavelength of 1550nm, we could counter-balance the difference in cavity transmission between the two quasi-orthogonal modes by coupling a beam that has a TM component more important than the TE. From the measured ellipticity, $|\mathbf{E}_x| = |\mathbf{E}_y|/0.67 = 1.5|\mathbf{E}_y|$, corresponding to a linearly-polarized beam at 34°.

7.3.3 Phase delay as a function of the wavelength

Due to the Fabry-Perot cavity effect, the relative delay between quasi-TE and quasi-TM modes is a function of the wavelength, as shown in figure (7.10). The

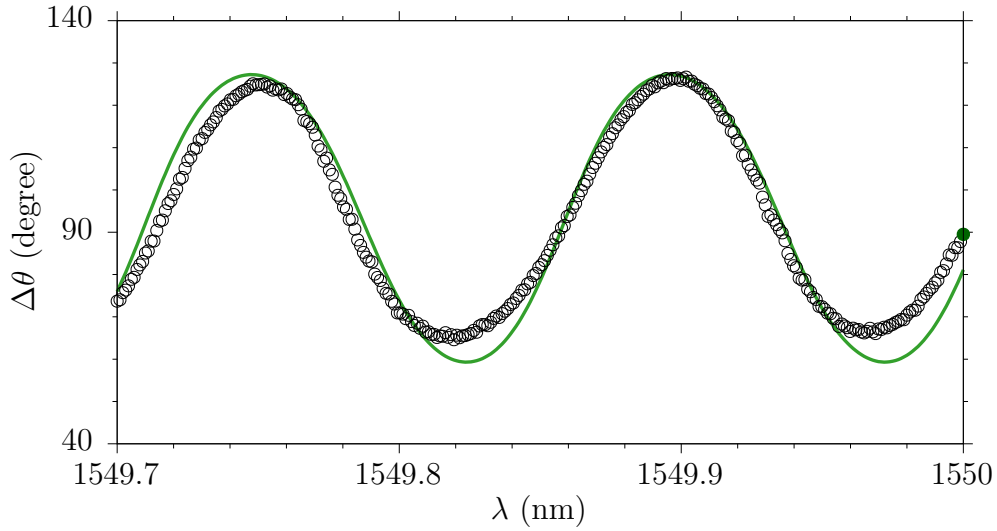

Figure 7.10 – Measured phase delay between the emitted quasi-TE and quasi-TM modes as a function of the wavelength (black open circle) and calculated phase delay according to a birefringent Fabry-Perot cavity (green continuous line).

delay between the emitted quasi-TE and quasi-TM modes is $\Delta\theta = 89.5°$ at 1550nm (green dot), while in the range of (1549.7nm, 1550nm) it varies within $\Delta\theta = 95.5° \pm 30°$ (open circles). This variation is in agreement with a model of a birefringent Fabry-Perot cavity. The transmitted amplitudes of the two orthogonally polarized modes trough a birefringent (and dispersion-less) cavity are given by:

$$\begin{aligned} \mathbf{E_x}^{\text{out}} &= \mathbf{E_x} \frac{(1 - R_{TE}) \exp\left(i\, L\, k_{TE} - \tilde{\alpha}_{TE} L\right)}{1 - R_{TE} \exp\left(i\, 2\, L\, k_{TE} - \tilde{\alpha}_{TE} 2L\right)} \\ \mathbf{E_y}^{\text{out}} &= \mathbf{E_y} \frac{(1 - R_{TM}) \exp\left(i\, L\, k_{TM} - \tilde{\alpha}_{TM} L\right)}{1 - R_{TM} \exp\left(i\, 2\, L\, k_{TM} - \tilde{\alpha}_{TM} 2L\right)} \end{aligned} \tag{7.3}$$

with $\Delta\Phi = L(k_{TE} - k_{TM})$ the one-way phase difference between the two orthogonal modes. In our device $\Delta\Phi$ is determined by the phase-delay accumulated in the central section (7.2).

The phase-difference between the two emitted orthogonally polarized modes depends on the one-way phase difference ($\Delta\Phi$) and the modes Fabry-Perot transmission functions, determined by the cavity physical length L, the modes reflectivities and one-way transmission losses:

$$\Delta\theta = \arg(\mathbf{E_x}^{\text{out}}) - \arg(\mathbf{E_y}^{\text{out}}) = \Delta\theta(\Delta\Phi, L, R_{TE}, R_{TM}, \tilde{\alpha}_{TE}, \tilde{\alpha}_{TM}) \tag{7.4}$$

Figure (7.11) shows the phase delay between the emitted orthogonally polarized modes ($\Delta\theta$, continuous lines) versus their one-way phase delay ($\Delta\Phi$, horizontal dashed lines) as a function of the wavelength.

We consider $\Delta\Phi = \{0°, 30°, 60°, 90°, 120°, 150°\}$. The cavity is $L = 2.69$mm long and the modes have modal reflectivities $R_{TE} = 0.34$, $R_{TM} = 0.38$, one-way

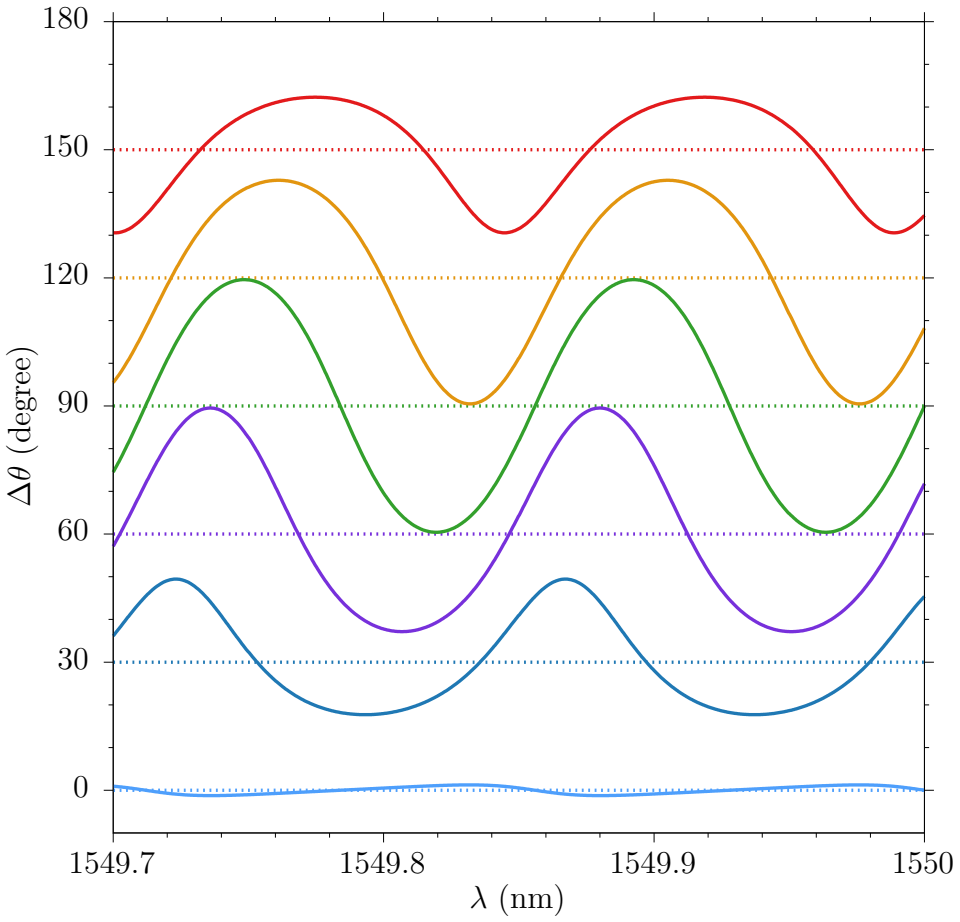

Figure 7.11 – Calculated phase delay between the emitted TE and TM modes ($\Delta\theta$) as a function of the wavelength in a birefringent Fabry-Perot cavity ($R_{TE} = 0.38$, $R_{TM} = 0.34$, $\tilde{\alpha}_{TE} = \alpha_{TE}/2 = 0.75\text{cm}^{-1}$, $\tilde{\alpha}_{TM} = \alpha_{TM}/2 = 0.40\text{cm}^{-1}$, $L = 2.69\text{mm}$, $n_{TE} = 3.1$). The corresponding one-way phase-delay ($\Delta\Phi$) is indicated by a dashed line with the same color.

propagation losses $\tilde{\alpha}_{TE} = \alpha_{TE}/2 = 0.75\text{cm}^{-1}$, $\tilde{\alpha}_{TM} = \alpha_{TM}/2 = 0.40\text{cm}^{-1}$, and effective refractive index $n_{TE} = 3.1$.

We observe that the periodicity of $\Delta\theta$ does not depend on $\Delta\Phi$, but the position of the cavity resonances changes with $\Delta\Phi$. Besides, $\Delta\theta$ oscillates around the corresponding $\Delta\Phi$. The amplitude of the oscillation increases as $\Delta\Phi$ approaches 90° (green) and is minimum when $\Delta\Phi = 0$ (light blue).

Therefore, even when $\Delta\Phi$ is not exactly 90°, $\Delta\theta$ can be 90° for some wavelengths. As instance, for the modal reflectivities and transmission losses of figure (7.11), $\Delta\Phi$ must be within 60° (dashed purple line) and 120° (dashed yellow line) in order to have some wavelengths for which $\Delta\theta$ is 90° (continuous purple and yellow lines).

The experimental data of figure (7.10) agree with this model for $\Delta\Phi = 90°$ (green line), as we show by reporting the green line of figure (7.11) in figure (7.10).

Depending on the application, the Fabry-Perot interference effects can be useful or undesired. If the device has to work as a wavelength-independent QWP, the

Fabry-Perot effect is undesired. In this case, an anti-reflection coating can be applied to the surfaces of input and output facets to minimize it.

Conversely, if the device has to work as a QWP for a specific wavelength which can be arbitrarily tuned, the Fabry-Perot effect can be used to achieve the desired phase-delay for a specific wavelength, within the range indicated in figure (7.11).

7.4 Perspectives

This device demonstrates that a waveguide with an asymmetric core can induce a controlled phase delay between two orthogonally polarised fundamental Guassian modes.

The same concept could also be applied to different spatial modes launched into a device with a similar geometry. In that case, phase vortices would also be imprinted on the transverse field components, hence resulting in a net OAM carried by the beam emitted from the end facet of the waveguide.

For this reason, our next step is to adapt the design of the device by tailoring the dispersion of higher order modes, in order to generate OAM beams.

Chapter 8

An integrated cylindrical mode converter

In this chapter we report the design and the development of the fabrication process of an asymmetric AlGaAs waveguide that works as a cylindrical mode converter. The device working principle comes from a discussion with E. Karimi and P. Banzer. We have worked to its implementation (design and fabrication) on the AlGaAs platform.

Similarly to the integrated quarter-wave plate presented in the previous chapter, this device introduces a phase-delay of $\pi/2$ between HG_{01} and HG_{10} modes, which can be either TE or TM polarized. As a result, an input beam with a HG_{11} spatial mode profile is transformed into a LG_{01} beam, which carries OAM on the electric field transverse component.

8.1 Design

8.1.1 Working principle

The device works as a cylindrical mode converter, a free space optics system of two aligned cylindrical lenses of focal length f sperated by $2\sqrt{f}$. The astigmatism introduced by the cylindrical lenses is responsible for a phase shift of $\pi/2$ between HG_{10} and HG_{01} beams [214, 236], implementing the operation shown in figure (6.29).

As the sketch in figure (8.1) shows, we design an integrated cylindrical mode converter. The devices is similar to the integrated quarter wave-plate presented in the previous chapter (see the sketch of figure (7.1)).

In this case, the waveguide widths and etching depth along input, central and output sections are chosen to support and properly delay the first order HG modes, for both TE and TM polarizations.

Input and output sections are identical and are given by a GaAs squared core with $w_{core} = h_{core} = 3\mu m$.

In the central section the core is narrower, with $w_s = 2.12\mu m$, in order to delay the first order HG horizontal mode (HG_{10}) with respect to the first order HG

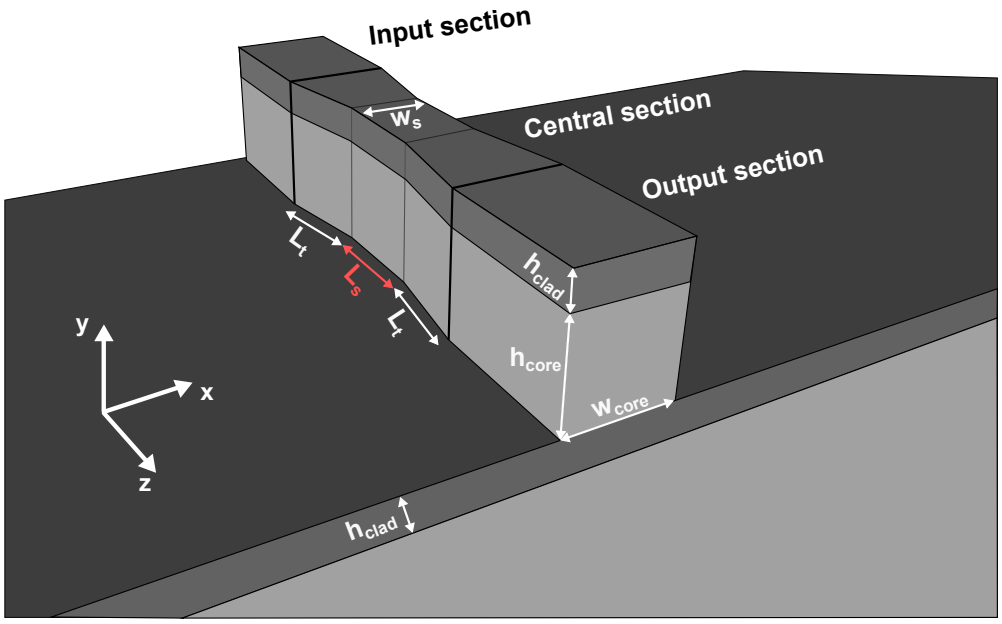

Figure 8.1 – Sketch of the integrated cylindrical mode converter. For a specific value of L_s, an incoming light beam with a HG_{11} spatial distribution (TE or TM polarized) is transformed into a light beam having a LG_{01} spatial distribution (TE or TM polarized), which carries first order OAM in the field transverse component.

vertical mode (HG_{01}), for both TE and TM polarization directions.

An $Al_{0.8}Ga_{0.2}As$ bottom cladding layer with a thickness $h_{clad} = 1\mu m$ assures that the modes are properly guided and do not leak into the substrate.

On the top of the core, a cladding layer identical to the bottom cladding layer is added to preserve the device rotational symmetry: the squared GaAs guiding core is surrounded by air in the lateral direction and $Al_{0.8}Ga_{0.2}As$ in the vertical direction.

8.1.2 Input section

Figure (8.2) and (8.3) report the first order HG modes supported in the input (or output) section at a wavelength of $1.55\mu m$, respectively TE or TM polarized. The modes are calculated via Lumerical Eigenmode solver. The continuous white line indicates the borders of core and top and bottom cladding layers. We can see that the first order modes are well confined within the squared core.

As expected, the HG_{10} (HG_{01}) mode has a phase discontinuity of π along the horizontal (vertical) direction with respect to the core central vertical (horizontal) axis. Given the device rotational symmetry, the coupling of a HG_{11} TE (TM) mode assures the equal excitation of HG_{10} and HG_{01} TE (TM) modes. The shaping of the input beam into a HG_{11} mode can be achieved by means of a SLM or a holographic-mask.

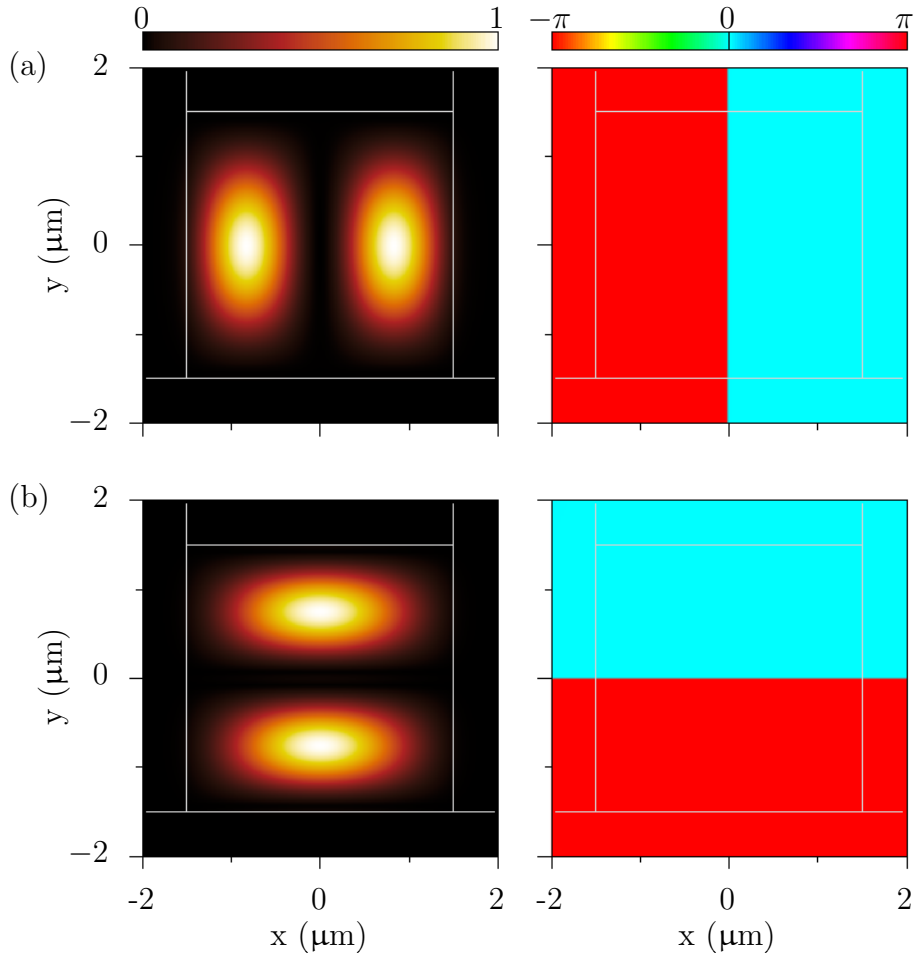

Figure 8.2 – Numerically calculated intensity and phase profile of first order TE modes in the input and output sections.
(a) HG_{10}
(b) HG_{01}

8.1.3 Central section

The central section is made of a straight part and two adiabatic tapers that connect the former to the device input and output sections.

Straight part

The straight part has the function of introducing a controllable delay between the HG_{10} and HG_{01} modes, while assuring at the same time that the modes do not leake into the substrate. Both requirements are fulfilled when the core width is larger than the minimal width corresponding to the modes cut-off.

To find the modes cut-off condition, we calculate via Lumerical eigenmode solver the modes effective refractive index as a function of the core width, for a fixed core height of 3µm. Figure (8.4) shows the result of this numerical simulation, for TE (blue) and TM (green) first order HG modes.

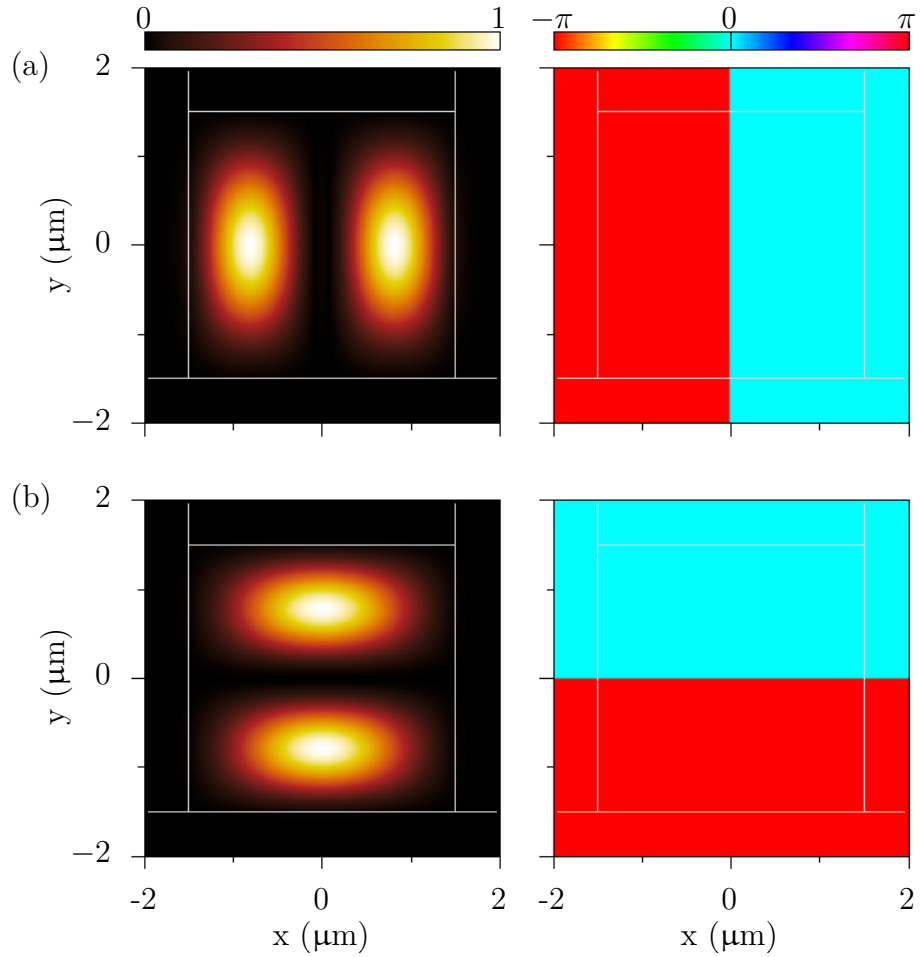

Figure 8.3 – Numerically calculated intensity and phase profile of first order TM modes in the input and output sections.
(a) HG_{10}
(b) HG_{01}

Independently on the core width and polarization direction, the refractive index of HG_{10} modes (continuous lines) are always lower than the refractive index of HG_{01} modes (dashed lines). This difference is due to the fact that the HG_{01} modes have a higher overlap with $Al_{0.8}Ga_{0.2}As$ top and bottom cladding layers, having a refractive index of $n = 2.98$ at 1.55µm, while the HG_{10} modes have a higher overlap with the surrounding air regions, where $n = 1$.

When the core is squared ($\omega_s = h_s = 3\mu m$), the confinement within the core of the HG_{10} and HG_{01} modes is higher, so the difference between their effective refractive index is minimal ($\Delta n_{TE} = 0.052$, $\Delta n_{TE} = 0.002$).

As the core becomes narrower, HG_{10} modes are less confined and leak in the surrounding air with a consequent decreasing of their effective index. The cut-off condition for the TE HG_{10} mode is at $w_2 = 1.76\mu m$, while the cut-off condition for the TM HG_{10} mode is at $w_2 = 1.96\mu m$.

To avoid excessive propagation losses, we set the width of the straight part to

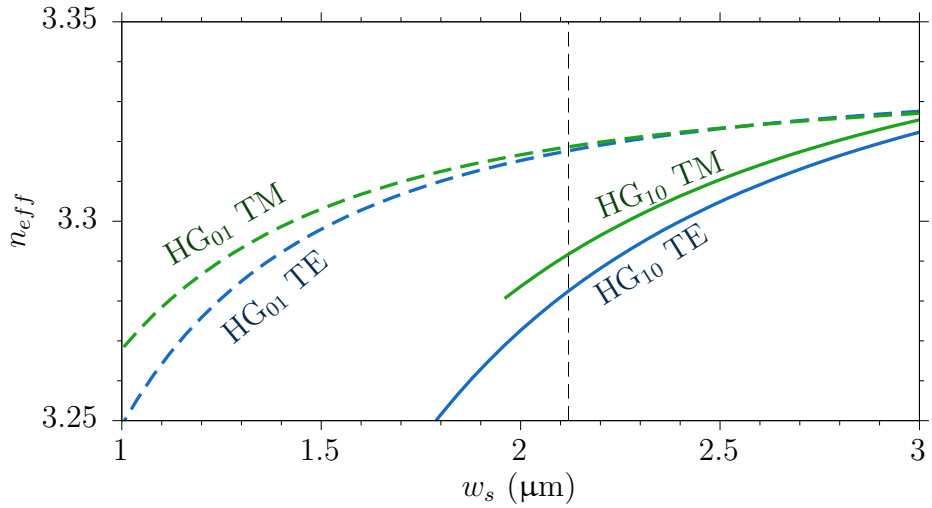

Figure 8.4 – Numerically calculated effective index of HG_{10} TE (blue continuous line) and TM (green continuous line) modes and HG_{01} TE (blue dashed line) and TM (green dashed line) modes as a function of the central section straight part width (w_s), for $h_s = 3\mu m$.

$w_s = 2.12\mu m$, corresponding to the vertical black dashed line in figure (8.4). For this core width, the modal birefringence between HG_{01} and HG_{10} modes, either TE and TM polarized, is:

$$\begin{aligned} \Delta n_{TE} &= n^{TE}_{HG_{01}} - n^{TE}_{HG_{10}} = 0.035 \\ \Delta n_{TM} &= n^{TM}_{HG_{01}} - n^{TM}_{HG_{10}} = 0.027 \end{aligned} \tag{8.1}$$

Adiabatic tapers

We design two compact triangularly-shaped input and output tapers (8.1) to maximize the transmission of the modes from the input section to the straight part of the central section and hence from there to the output section.

In the design of the integrated quarter-wave plate (sketched in figure (7.1)), we relied on very long tapers (300µm) to have an adiabatic transmission of the modes from the input section, 3µm wide, to the straight part of the central section, 0.55µm wide.

In this device, the input section is still 3µm wide, but the straight part is only slightly narrower, as we set its width to 2.12µm. Therefore we expect that an adiabatic transmission can be obtained for shorter tapers.

For the study of the tapers adiabaticity we consider the transmission of the least confined modes, the HG_{10} modes. Figure (8.5) shows the transmission of the HG_{10} TE (blue) and TM (green) modes across a taper as a function of its length. The calculation is carried out by using Lumerical eigenmode expansion solver. We find that a taper length of $L_t = 10\mu m$ assures a transmission higher than 0.99 for both modes, thus we choose this value.

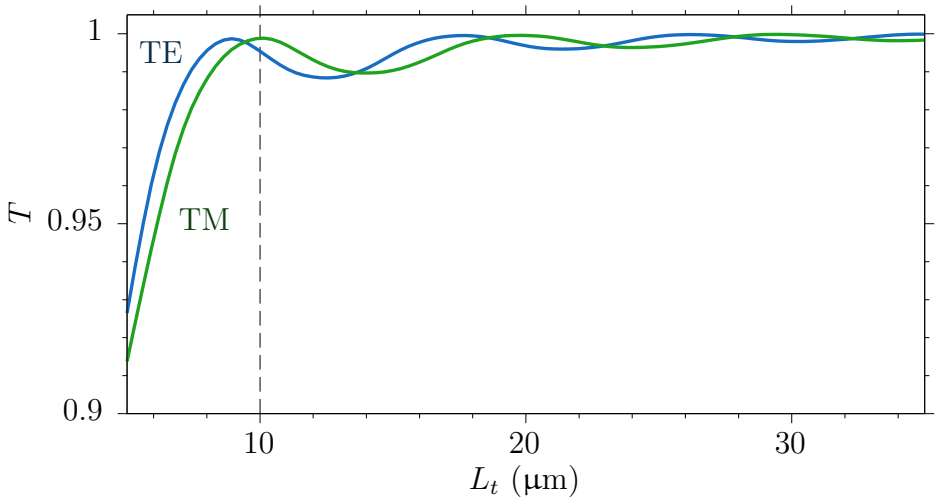

Figure 8.5 – Numerically calculated transmission of one taper (input or output taper) for TE (blue) and TM (green) HG_{10} modes.

Accumulated phase delay

In the central section, the HG_{10} mode acquires a delay with respect to the HG_{01} mode. Since the input and output tapers are identical, the accumulated delay between either TE or TM first order HG modes can be written as:

$$\Delta\Phi_{c,u} = \frac{2\pi}{\lambda}\left[(\Delta n_u L_s + 2\int_0^{L_t} n^u_{HG_{01}}(z) - n^u_{HG_{10}}(z)dz\right] \tag{8.2}$$

where $u = \{\text{TE, TM}\}$ indicates the modes polarization, , Δn_u the birefringence of the straight part given by (8.1) and L_s its length. Since L_t and Δn_u are fixed parameters, we can tune the accumulated phase delay by increasing L_s.

Figure (8.6) illustrates phase-delay accumulated by TE and TM modes in the whole central section, according to equation (8.2), as a function of the straight part length.

We see that first order HG TE modes (blue line) are phase delayed by $\pi/2$ for $L_s = 1\mu\text{m}$, meaning that the most important contribution to the phase delay is given by the input and output tapers. A straight part length of $22\mu\text{m}$ introduces an additional delay of π, as a delay of $3\pi/2$ is reached for $L_s = 23.0\mu\text{m}$. TM modes (green) are phase-delayed by $\pi/2$ for $L_s = 5.3\mu\text{m}$ and by $3\pi/2$ for $L_s = 34.3\mu\text{m}$.

We conclude that a TE LG_{01} (LG_{10}) mode can be obtained by using a waveguide having a straight part of length $L_s = 1\mu\text{m}$ ($L_s = 23.0\mu\text{m}$), while a TM LG_{01} (LG_{10}) mode can be obtained by using a waveguide having a longer straight part, with $L_s = 5.3\mu\text{m}$ ($L_s = 34.3\mu\text{m}$).

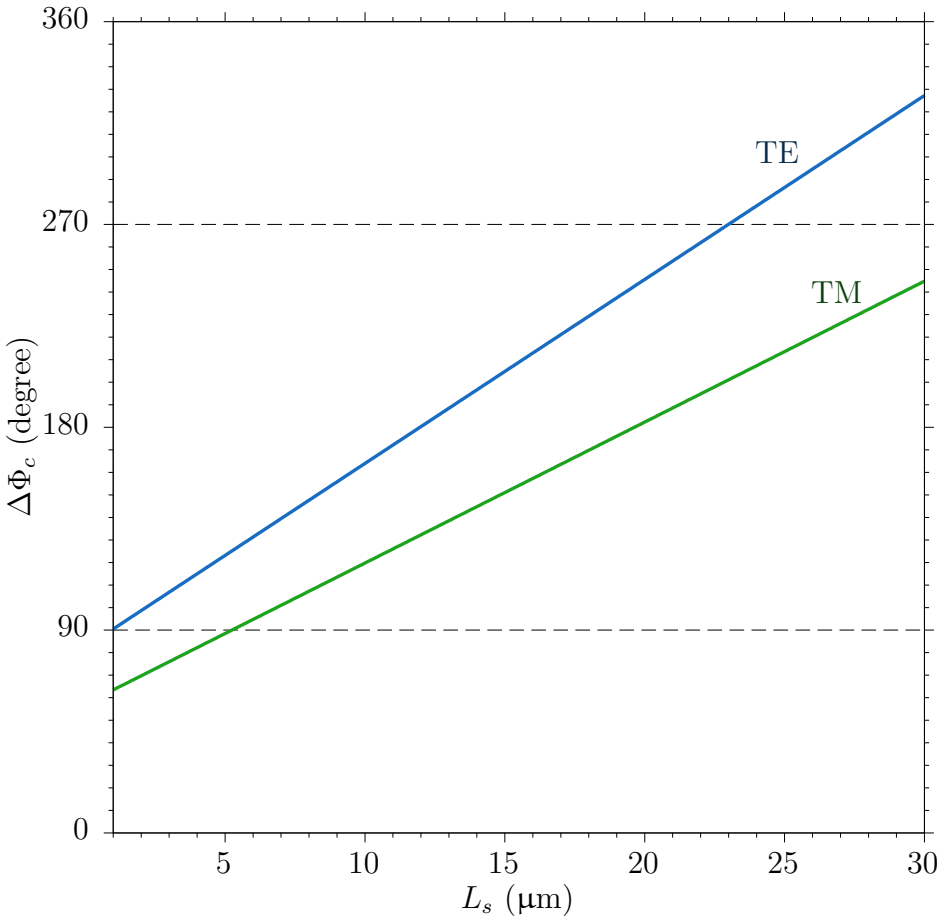

Figure 8.6 – Numerically calculated one pass phase delay accumulated in the central section between TE HG_{01} and HG_{10} modes (blue) and TM HG_{01} and HG_{10} modes (green), as a function of the straight part length (L_s).

8.1.4 Output section

When the phase-delay accumulated between the HG_{01} and HG_{10} modes along the central section is $\pi/2$, a LG_{01} mode propagates in the waveguide output section.

Figure (8.7) shows the intensity and phase spatial distribution of the electric field given by the superposition of TE HG_{10} and HG_{01} modes, for a zero phase-delay (top row) and for a phase-delay of $\pi/2$ (bottom row). If they are not delayed, their superposition gives a HG_{11} mode, characterized by a phase-discontinuity along the anti-diagonal direction. When they are delayed by $\pi/2$, the resulting mode is a LG_{01}, characterized by a phase singularity at the center of the core, responsible for the donut shaped intensity profile. The optical vortex has a negative sign, since the phase grows anticlockwise.

Analogous results are obtained in the case of the superposition of TM HG_{10} and HG_{01} modes, shown in figure (8.8).

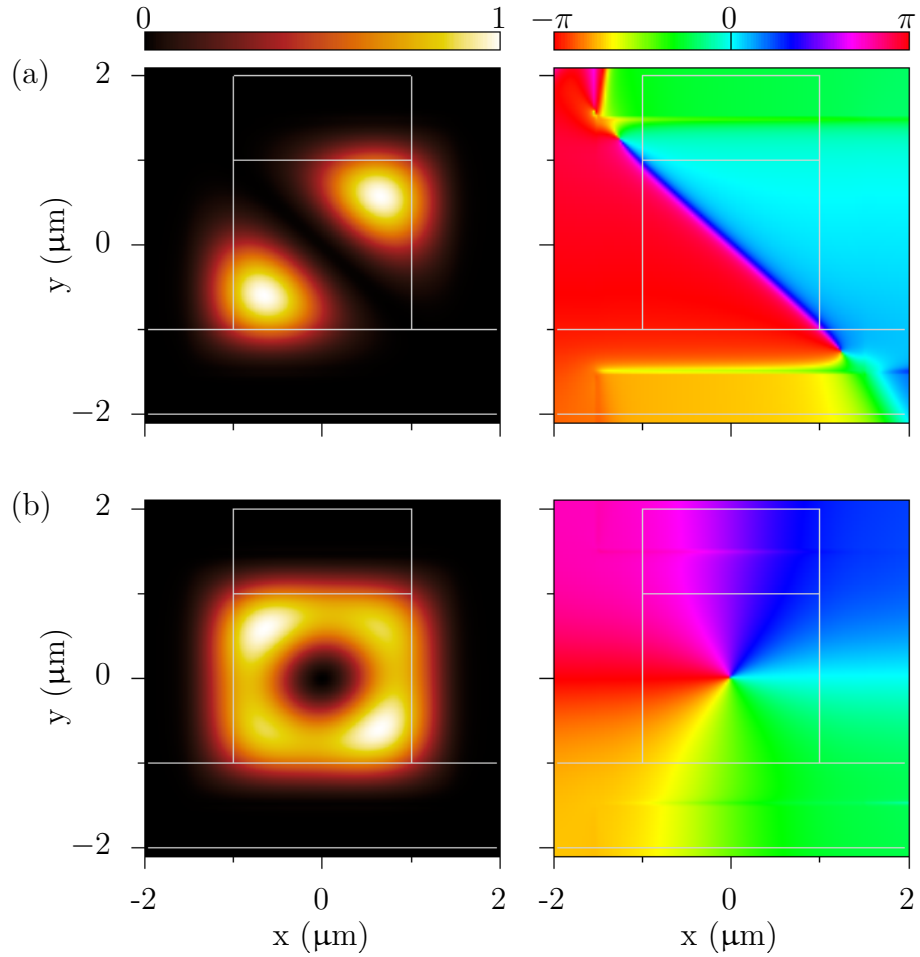

Figure 8.7 – Numerically calculated intensity and phase profile of the injected TE mode HG_{11} in the output section, given by $HG_{10} + HG_{01} \exp(i\Delta\Phi)$, for two values of phase delay:
(a) $\Delta\Phi = 0$
(b) $\Delta\Phi = \pi/2$

8.1.5 Numerical simulation of the emitted far field

Contrary to the quarter-wave plate device presented in the previous chapter, in this device the optical vortex is carried out by the principal component of the electric field (the horizontal polarization direction in TE mode, the vertical polarization direction in TM mode) and so it does not disappear as the modes propagate in the far field.

Figure (8.9) illustrates the far field of the previously calculated LG_{01} modes, for TE (top row) and TM (bottom row) modes. The optical vortex is still present and the intensity profile has a donut-like shape. Due to the fact that the waveguide core is squared and not circular, the intensity profile has a 4-fold symmetry, so the donut shape is slightly more intense along vertical and horizontal axis than along diagonal and anti-diagonal ones.

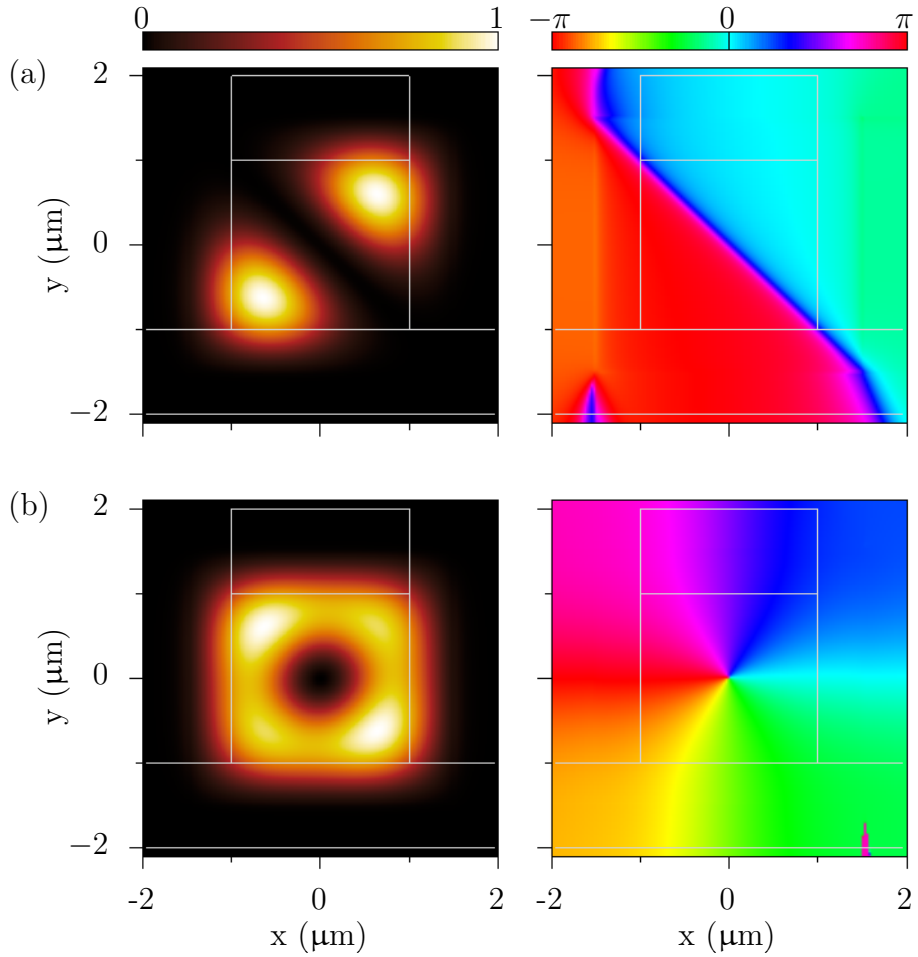

Figure 8.8 – Numerically calculated intensity and phase profile of the injected TM mode HG_{11} in the output section, given by $HG_{10} + HG_{01} \exp(i\Delta\Phi)$, for two values of phase delay:
(a) $\Delta\Phi = 0$
(b) $\Delta\Phi = \pi/2$

8.2 Fabrication

To fabricate the device we rely on the fabrication method used for the quarter-wave plate device (7.2), based on EBL and ICP dry etching.

8.2.1 Electron beam lithography mask

Figure (8.10) is a schematic of the EBL mask. It includes 35 waveguides, with the length of the straight section increasing by step of 1µm among consecutive waveguides.

On the left of the mask, we design a straight waveguide and a waveguide whose central section includes only the input and output tapers ($L_s = 0$). By measuring the phase-delays among two modes in the first three waveguides, we should be able to quantify the delay introduced by each section.

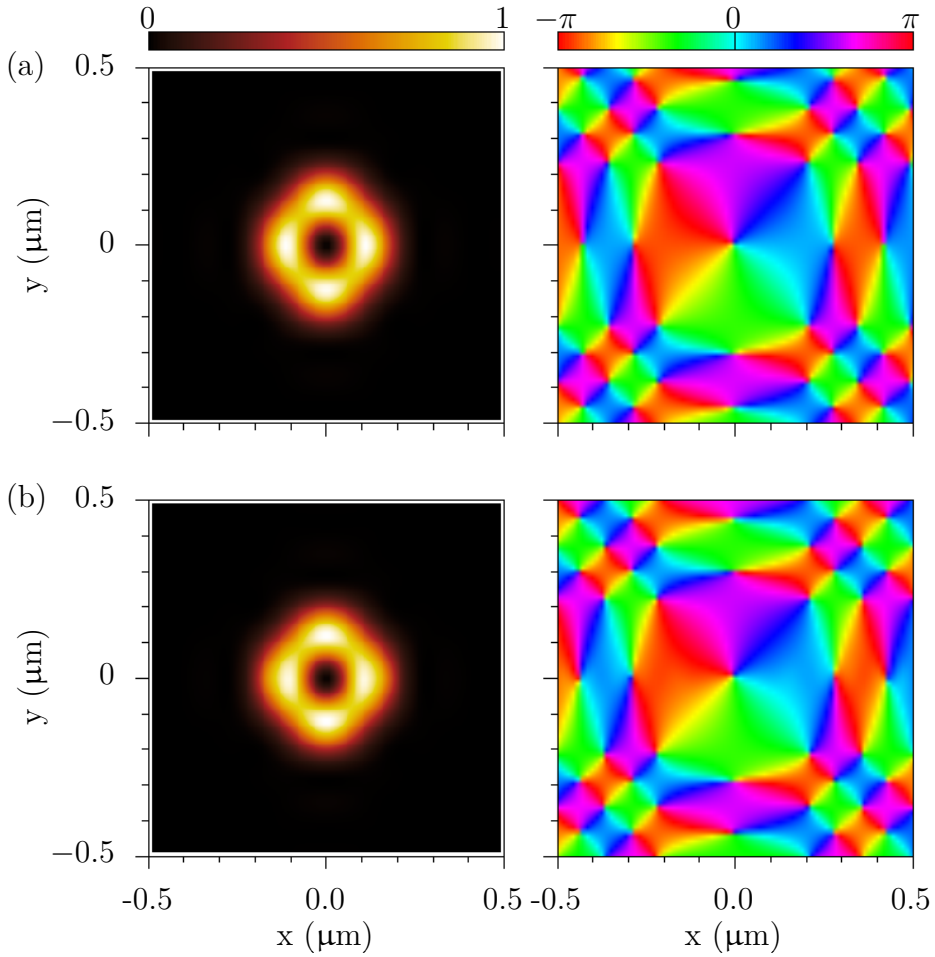

Figure 8.9 – Numerically calculated far field of $LG_{01} = HG_{10} + HG_{01} \exp(i\Delta\Phi)$, $\Delta\Phi = \pi/2$, in the case of:
(a) TE polarized mode.
(b) TM polarized mode.

8.2.2 Processing

To fabricate the device (8.1) we need to etch 1μm of $Al_{0.8}Ga_{0.2}As$ and 3μm GaAs, so we use the resist ma-N 2405 (the reasons of this choice are given in paragraph (4.3.2)).

We choose a dose of $110\mu C/cm^2$ for both standard EBL and FBMS EBL. The lithography of one mask (i.e. the 35 waveguides indicated in figure (8.10)) lasts for 2 hours. We launch a lithography overnight and expose four masks. We develop each sample for 30 seconds and perform ICP etching following the gentle etching (4.3.4). The ICP etching lasts for 6.35 hours, with an average etching rate of 11nm/min.

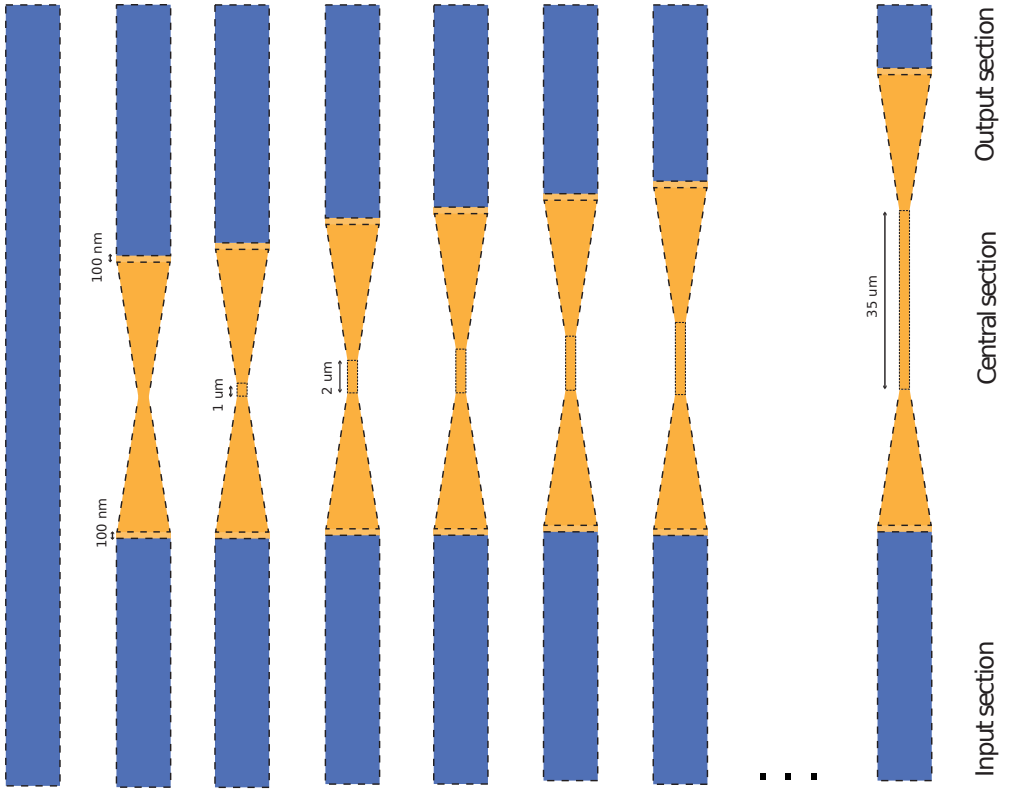

Figure 8.10 – Schematic of the mask used for the sample processing. The length of the central section straight part increases by $\Delta L_s = 1\mu m$ from one waveguide to the next one. The input and output sections, in blue, are FBMS path. The overlap between the different sections is $0.1\mu m$ to avoid the presence of longitudinal gaps after exposure. On the left of the mask there are a straight waveguide and a waveguide having a central section consisting only of the two tapers.

8.2.3 Fabricated device

The fabricated device is shown in figure (8.11). From the SEM image of the waveguide input section (b, left), we deduce that the ma-N 2405 resist (in black) did not cover the waveguide sidewalls until the ending of the etching process. The resist edges are completely etched and so are the edges of the top cladding layer (dark grey) and of the upper part of the core layer (lighter gray). As a result, the waveguide sidewalls are very rough and the guided modes would have too high propagation losses, especially the mode HG_{10}.

This fabrication issue is due to the "roof effect" of the ma-N resist, previously observed for the fabrication of the active laser (see figure (4.5)). In this process, due to the very long time of the ICP etching (6.35h), the premature etching of the resist edges prevents the realization of the structures.

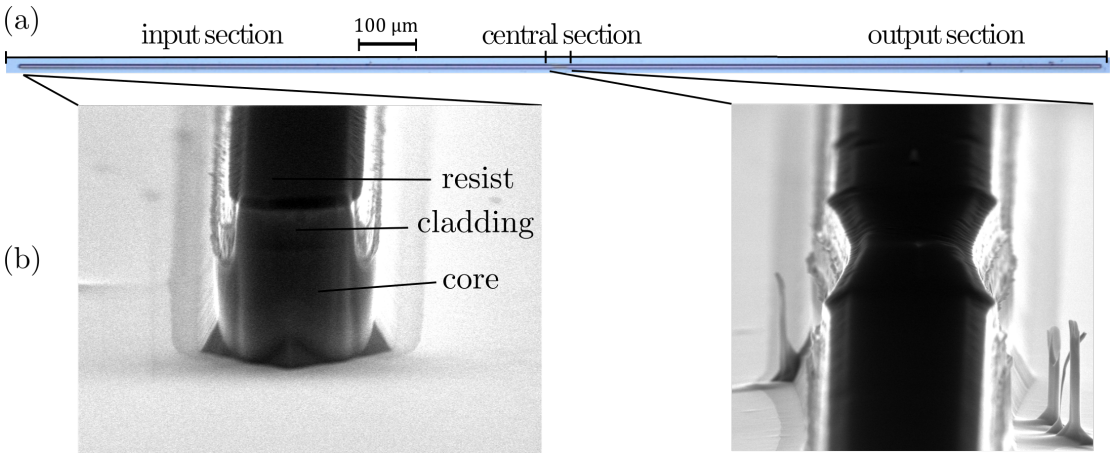

Figure 8.11 – Image of the first waveguide ($L_s = 1\mu$m) of the fabricated chip.
(a) Top-view optical microscope image of input, central and output sections.
(b) A SEM image of the waveguide input facet and central section.

8.3 Perspectives

To overcome the resist etching issue, there are two workable solutions. The first one is to perform the deposition of a hard mask of SiN under the ma-N resist before its spin-coating. The second solution is to use a resist more resistant to etching, such as HSQ. In both cases, the first step consists in performing a dose test to find the new optimal exposure dose.

Here we give the characterization steps that will be necessary to demonstrate the operation of the device once it will be fabricated. Firstly, we need to measure the propagation losses of each propagating mode: TE HG_{01}, TE HG_{10}, TM HG_{01} and TM HG_{10}. To inject these modes in the waveguide, we can use a SLM to shape the coupling beam into the desired spatial distribution and a polarizer to set its polarization. From the measurement of the transmitted power and the contrast of the Fabry-Perot fringes we can deduce the propagation losses of each mode.

Thus, for each polarization direction, we need to couple in the device a HG_{11} mode and measure the spatial distribution of the emitted mode as a function of the length of the straight part of the central section.

This measurement can be done using a CCD camera to directly image the mode. However, this method would not allow to distinguish between LG_{10} and LG_{01} modes, since they both have a donut-shaped intensity distribution profile.

In order to discriminate them, we may perform an interference measurement by removing a part of the laser beam before injection with an unbalanced beam splitter and use it as reference. We can then superpose the light emitted by our device and the reference beam on a screen, taking care that the two beams have the same intensity. The resulting interference pattern will present fringes which are a fingerprint of the mode spatial profile, allowing to distinguish even between LG_{10} and LG_{01} modes [237]. This project will be continued by F. Appas, new PhD student in the QITE team.

Conclusion and Perspectives

This thesis has been devoted to the study of AlGaAs quantum integrated photonics for the development of novel devices and methods capable of generating and manipulating high-dimensional states of light, encoding information in either frequency or angular momentum degrees of freedom. During this investigation, we performed theoretical studies and established numerical routines, optimized clean-room processings and performed experimental characterizations. These complementary tasks have led to the results presented in this manuscript, among which we highlight the generation and manipulation of broadband biphoton frequency-comb states, and to the realization of AlGaAs devices for the emission of beams of light presenting angular momentum.

In the first part of the manuscript we report the study of type-II SPDC process in an AlGaAs waveguide in a monochromatic pump regime and collinear one-pass configuration, with a focus on the joint spectral amplitude of the emitted biphoton state. We show the possibility of generating broadband states of light in the telecom range, a promising resource for quantum communication protocols. Our hypothesis are validated via Hong-Ou-Mandel interferometry, performed without any spectral filtering. The detected interference pattern corresponds to signal and idler photons with a large bandwidth ($\lambda_{s,i}^{FWHM} = 170$nm) and high degree of indistinguishibility ($V = 86\%$). The evaluation of phase matching also indicates that the photons indistinguishibility, a prerequisite for many quantum protocols, can be further increased by reducing the source birefringence. In this perspective, our group is currently developing AlGaAs electro-optics devices in order to control it.

In the second part of the manuscript we take into account the cavity effect due to facets reflectivity. We analyse the generation of two spectrally distinct classes of biphoton frequency-comb states, namely resonant and anti-resonant states, based on the fine tuning of the monochromatic pump frequency. Stimulated Emission Tomography is used to demonstrate our theory by measurements of the joint spectral intensity of resonant and anti-resonant states. Further, we demonstrate how the unique spectral properties of these states can be exploited in a manipulation scheme based only on passive telecom components, namely a polarizing beam splitter and a delay line. When the two photons of the pair are delayed by an odd multiple of half the cavity round-trip, the frequency and path components of the anti-resonant state become anti-symmetric, while the ones of the

resonant state are still symmetric. The experimental demonstration of this scheme is done on AlGaAs sources and the successful state manipulation is demonstrated by Hong-Ou-Mandel interferometry. The generation and manipulation of resonant and anti-resonant frequency-comb states may bring new functionalities to quantum information. In this context, a project in partnership with Nokia Bell Labs and LIP6 laboratories is envisaged for the implementation of novel Quantum Key Distribution communication protocols. Besides, in collaboration with the theoreticians of our team, we are showing that frequency-comb states can be used to implement a frequency-time Gottesman-Kitaev-Preskill (GKP) encoding. The robustness of this encoding, assured by its compatibility with quantum error correction codes, makes it a good fit for the processing of quantum information in noisy machines.

The last part of this work presents the exploration of novel AlGaAs devices for the emission of light beams carrying spin or orbital angular momentum, whose unbounded states have potential applications in communication spatial multiplexing. We demonstrate the realization of an AlGaAs ridge waveguide for the generation of light beams with tailored phase and polarization distributions, carrying spin angular momentum. As a step forward, we design a device with a similar geometry for the generation of a twisted light beam, carrying first order orbital angular momentum. In the next future, the fabrication and characterization of this device will be carried out by our team, in the framework of an international collaboration.

Software Credit

Numerical calculations have been performed using Matlab, Python and Lumerical (FDTD, MODE). VESTA has been used to generate the image of GaAs unit cell.

Plots have been realized in GnuPlot, under the guidance of the built-in documentation and the tutorials from the blog gnuplotting.org by Hagen Wierstorf. Most of the colormaps have been designed by Kenneth Moreland and ColorBrewer.

For the illustrations, I relied on Inkscape. Some of the sketched optical setups include optical components from the ComponentLibrary by Alexander Franzen.

GitHub for students has been used to save the data and the manuscript during the redaction.

List of Publications and Conferences

Publications

[1] G. Maltese, M.I. Amanti, F. Appas, G. Sinnl, A. Lemaitre, P. Millman, F. Baboux and S. Ducci, "Generation and symmetry control of quantum frequency combs", *in submission*, 2019.

[2] N. Fabre, G. Maltese, F. Appas, S. Felicetti, A. Ketterer, A. Keller, T. Coudreau, F. Baboux, M.I. Amanti, S. Ducci and P. Millman, "Encoding robust qubits in integrated biphoton frequency combs", *in submission*, 2019.

[3] G. Maltese, Y. Halioua, A. Lemaitre, C. Gomez-Carbonell, E. Karimi, P. Banzer and S. Ducci, "Towards an integrated AlGaAs waveguide platform for phase and polarisation shaping", *Journal of Optics*, vol. 20, no. 5, 2018.

[4] C. Autebert, G. Maltese, Y. Halioua, F. Boitier, A. Lemaitre, M.I. Amanti, C. Sirtori and S. Ducci, "Electrically injected twin photon emitting lasers at room temperature", *Technologies*, vol. 4, no. 24, 2016.

Communications

[1] G. Maltese, S. Francesconi, F. Appas, A. Raymond, A. Lemaitre, M.I. Amanti, F. Baboux and **S. Ducci**, "Controlling frequency correlations and biphoton statistics in a semiconductor photonic chip", *in SPIE Photonics West*, Invited (Paris, France), February 2019.

[2] G. Maltese, **M.I. Amanti**, F. Appas, G. Sinnl, A. Lemaitre, F. Baboux and S. Ducci, "Generation and manipulation of hyper-entangled frequency combs in an AlGaAs chip", *in International Conference on Integrated Quantum Photonics* (Paris, France), October 2018.

[3] G. Maltese, J. Belhassen, S. Francesconi, A. Lemaitre, M.I. Amanti, F. Baboux, S. Ducci, F. Baboux and **S. Ducci**, "III-V integrated nonlinear

photonic chips for the generation and manipulation of quantum states of light", *in OSA Advanced Photonics* (Zurich, Switzerland), July 2018.

[4] **F. Baboux**, S. Francesconi, J. Belhassen, G. Maltese, A. Lemaitre, M.I. Amanti and S. Ducci, "Engineering of biphoton frequency correlations in semiconductor waveguides", *in International Workshop Institut Henri Poincaré on Quantum Control and Feedback* (Paris, France), June 2018.

[5] **G. Maltese**, A. Minneci, S. Felicetti, A. Lemaitre, F. Baboux, M.I. Amanti, T. Coudreau, P. Milman and S. Ducci, "Frequency-entangled qudits in AlGaAs waveguides", *in Annual meeting GDR Ingénierie Quantique* (Nice, France), November 2017.

[6] J. Belhassen, G. Maltese, S. Francesconi, G. Sinnl, A. Lemaitre, M.I. Amanti, F. Baboux and **S. Ducci**, "AlGaAs photonic devices for quantum information", *in International Conference on Integrated Quantum Photonics,* Invited (Rome, Italy), September 2017.

[7] **G. Maltese**, G. Sinnl, A. Minneci, S. Felicetti, A. Lemaitre, F. Baboux, P. Milman M.I. Amanti and S. Ducci, "Frequency-entangled QuDits in AlGaAs waveguides", *in International Conference on Integrated Quantum Photonics* (Rome, Italy), September 2017.

[8] C. Autebert, A. Minneci, G. Maltese, J. Belhassen, A. Lemaitre, M.I. Amanti, F. Baboux, T. Coudreau, P. Milman and **S. Ducci**, "On-chip generation of frequency-entangled qudits", *in Quantum Information and Measurement - QIM* (Paris, France), April 2017.

[9] C. Autebert, **G. Maltese**, A. Lemaitre, M.I. Amanti, F. Baboux and S. Ducci, "Record Single-To-Noise Ratio in Active and Passive AlGaAs Sources of Entangled Photons", *in Quantum Information and Measurement - QIM* (Paris, France), April 2017.

[10] C. Autebert, G. Boucher, J. Belhassen, G. Maltese, Y. Halioua and **S. Ducci**, "AlGaAs photonic devices: from quantum state generation to quantum communications", *in QCMC* (Singapore), Invited, July 2016.

[11] C. Autebert, G. Boucher, G. Maltese, J. Belhassen, Y. Halioua and **S. Ducci**, "Biphoton engineering and quantum communications with AlGaAs devices", *in Photonics North* (Quebec city, Canada), Invited, May 2016.

Letters
IOP Publishing
Journal of Optics
J. Opt. 20 (2018) 05LT01 (8pp)
https://doi.org/10.1088/2040-8986/aabc1d

Letter

Towards an integrated AlGaAs waveguide platform for phase and polarisation shaping

G Maltese[1], Y Halioua[1], A Lemaître[2], C Gomez-Carbonell[2], E Karimi[3,4], P Banzer[3,5,6] and S Ducci[1]

[1] Laboratoire Matériaux et Phénomènes Quantiques, Université Paris Diderot, Sorbonne Paris Cité, CNRS-UMR 7162, Case courrier 7021, F-75205 Paris Cedex 13, France
[2] CNRS-C2N Centre de Nanosciences et de Nanotechnologies, Université Paris-Sud, Université Paris-Saclay, F-91460 Marcoussis, France
[3] Max Planck—University of Ottawa Centre for Extreme and Quantum Photonics, 25 Templeton Street, Ottawa, ON, K1N 6N5, Canada
[4] Department of Physics, Institute for Advanced Studies in Basic Sciences, 45137-66731 Zanjan, Iran
[5] Max Planck Institute for the Science of Light, Staudtstr. 2, D-91058 Erlangen, Germany
[6] Institute of Optics, Information and Photonics, University Erlangen-Nuremberg, Staudtstr. 7/B2, D-91058 Erlangen, Germany

E-mail: sara.ducci@univ-paris-diderot.fr

Received 1 February 2018, revised 19 March 2018
Accepted for publication 6 April 2018
Published 20 April 2018

Abstract

We propose, design and fabricate an on-chip AlGaAs waveguide capable of generating a controlled phase delay of $\pi/2$ between the guided transverse electric and magnetic modes. These modes possess significantly strong longitudinal field components as a direct consequence of their strong lateral confinement in the waveguide. We demonstrate that the effect of the device on a linearly polarised input beam is the generation of a field, which is circularly polarised in its transverse components and carries a phase vortex in its longitudinal component. We believe that the discussed integrated platform enables the generation of light beams with tailored phase and polarisation distributions.

Keywords: integrated optics, semiconductor waveguides, light angular momentum, AlGaAs

Integrated photonic circuits are one of the most promising platforms for large-scale quantum information systems since they allow for solving critical problems of scalability and reliability, as witnessed by numerous results obtained in the fields of quantum communication, computing, simulations and metrology [1]. In this context, semiconductor materials are particularly attractive to achieve extremely compact and massively parallelised devices; among the different platforms under development, AlGaAs combines the advantages of a direct band-gap, high second-order susceptibility and strong electro-optical Pockels effect [2, 3]. These properties have been exploited to demonstrate a full set of devices for the generation, manipulation and detection of quantum states of light [4–7]. The achievement of more complex photonic circuits requires an accurate tailoring of the properties of the electromagnetic field, e.g. to perform operations on different degrees of freedom of light or to control its interaction with matter qubits associated to single emitters embedded in the circuit [8–11].

Another property of light attracting growing attention, which has not been explored yet in integrated photonic circuits, is its angular momentum that can be subcategorised into spin and orbital angular momentum (OAM) [12]: spin angular momentum (SAM) is associated with beams having either the electric field vector spinning around the propagation axis (longitudinal SAM) or spinning in the propagation or meridional plane (transverse SAM) [13–15]; OAM is associated with the transverse structure of beams, having helical or twisted wavefronts [16]. Both SAM and OAM degrees of freedom of light have paved the way for numerous

applications in biosensing, nanoplasmonics [8, 17, 18], optical tweezing as well as in quantum communications and information processing using high-dimensional spaces [19, 20]. Over the last decades, many different techniques have so far been proposed for generating OAM-carrying optical beams; most of them can be categorised as: cylindrical mode converters [21], spiral phase plates [22], computer-generated holograms (holography) [23, 24], patterned liquid crystals [25, 26], and structured optics [27]. More recently, miniaturised devices [28–30], sub-wavelength optics [31], micro-ring resonators [32], and optical fibres [33–35] capable of supporting or generating OAM have been designed and tested. However, a common feature of such devices is the emission of light carrying OAM in free-space rather than an on-chip coupling or propagation. A first important step towards the on-chip generation of OAM (or SAM) would be the selective phase delay between orthogonal spatial modes (or polarisation states). In this context, a theoretical proposal of a device consisting of a hybrid dielectric-plasmonic waveguide has recently been presented [36]. However, on one hand plasmonic structures usually come with the cost of optical losses; moreover the device presented in [36] suffers from a narrow operation window. More recently, in parallel with our work, a theoretical proposal to implement waveplates using pure dielectric Si waveguides has been presented [37]. In [36, 37], a phase vortex was imprinted on the longitudinal electric field component of the waveguide mode. But so far, no device has been demonstrated experimentally. In this work, we propose, fabricate and experimentally demonstrate a monolithic all-dielectric AlGaAs waveguide that, starting from a linearly polarised (LP) beam, is capable of generating a confined circularly polarised mode (SAM) with a phase-vortex carried by the longitudinal field component. The SAM of the emitted beam is associated with the relative phase between waveguide modes induced by an asymmetric birefringent waveguide, while the appearance of strong longitudinal field components is a consequence of the light confinement within the waveguide. In combination with the aforementioned phase-delay, those longitudinal field components exhibit a helical phase-front (phase vortex). Our device is compatible and adds novel functionalities to the existing set of AlGaAs-based quantum photonic devices; for example, it allows for converting a linear into a circular polarisation opening the way to basis changes for polarisation encoded qubits. Moreover, this work represents a first step towards introducing OAM as degree of freedom to be generated and manipulated directly in integrated photonic circuits.

The device proposed in this work is illustrated in figure 1. It consists of a waveguide with constant core height ($h = 1.08\ \mu$m), insuring single mode excitation, and divided into three sections, as indicated by black lines and corresponding labels. The input section is large enough ($w = 3\ \mu$m) to allow easy coupling of an incoming laser beam, LP at 45°, into the two quasi-orthogonally polarised transverse electric (quasi-TE) and transverse magnetic (quasi-TM) modes of the waveguide. The generation of SAM and of the phase vortex occurs in the central section, which includes two adiabatic tapers and a straight section with a width of $w = 0.55\ \mu$m, being slightly larger than the quasi-TE mode cut-off condition ($w_{\text{cut-off}} = 0.50\ \mu$m). The latter induces mode dispersion, used to control the relative delay between quasi-TE and quasi-TM modes. Indeed, the quasi-TE mode travels faster than the quasi-TM mode, introducing a phase delay of $\pi/2$ for a specific length of the central section. The design of the central section has been chosen such that the phase delay through the length of the straight section can be controlled easily, while maintaining low optical losses thanks to the two adiabatic tapers. The output section has a square cross-section ($h = w = 1.08\ \mu$m) in order to emit a light beam with a Gaussian-like intensity profile.

The profiles of the quasi-TE and quasi-TM modes and the effective mode indices along the waveguide for a free-space wavelength of $\lambda = 1.55\ \mu$m have been investigated using a commercial eigenmode solver [38]. Neither the input nor output sections induce a significant phase delay between the two quasi-orthogonally polarised modes ($\Delta n_{\text{input}} < 0.008$, $\Delta n_{\text{output}} = 0$). On the contrary, the effective refractive indices of the two modes differ significantly in the asymmetric central section of total length L_c. Here two different terms contribute to the phase delay, arising respectively from the birefringence of the two tapers t_1, t_2 of a length L_t, and of the straight section, of a length L_s (figure 1). The induced phase delay between quasi-TE and quasi-TM modes can be expressed as

$$\delta = \frac{2\pi}{\lambda}\int_{-L_c/2}^{L_c/2}\Delta n(z)\mathrm{d}z = \frac{2\pi}{\lambda}\left(\int_{t_1}\Delta n_{t_1}(z)\mathrm{d}z + \Delta n_s L_s + \int_{t_2}\Delta n_{t_2}(z)\mathrm{d}z\right). \quad (1)$$

Along the tapers, the index difference between quasi-TE and quasi-TM modes $\Delta n_{t_{1,2}}(z)$ increases with the waveguide asymmetry. The maximum birefringence is reached at the boundary with the straight section, where $\Delta\ n_s = 0.101$ ($n_{\text{quasi-TE}} = 3.020$, $n_{\text{quasi-TM}} = 3.121$). To assure an adiabatic passage of light, we set the taper length to $L_t = 300\ \mu$m. We control the induced phase delay δ with the length L_s of the straight section. A specific L_s assures the quasi-TM mode to be delayed by $\delta = \pi/2$ compared to the quasi-TE mode after the central section. As the output section shows only negligible birefringence, the device emits a circularly polarised beam.

Note that our design presents two main advantages with respect to that proposed in [37] based on a similar working principle. The size of the input and output sections of our device is much larger thus facilitating in and out-coupling of light. Moreover, adiabatic tapers have been included to join different waveguide sections with various widths, thus low optical propagation losses.

The electromagnetic field confinement within the waveguide results in the formation of longitudinal electric field components E_z, which are an inherent part of the TE and TM modes of the waveguide. Their spatial distribution in the cross-section of the waveguide is given by the following

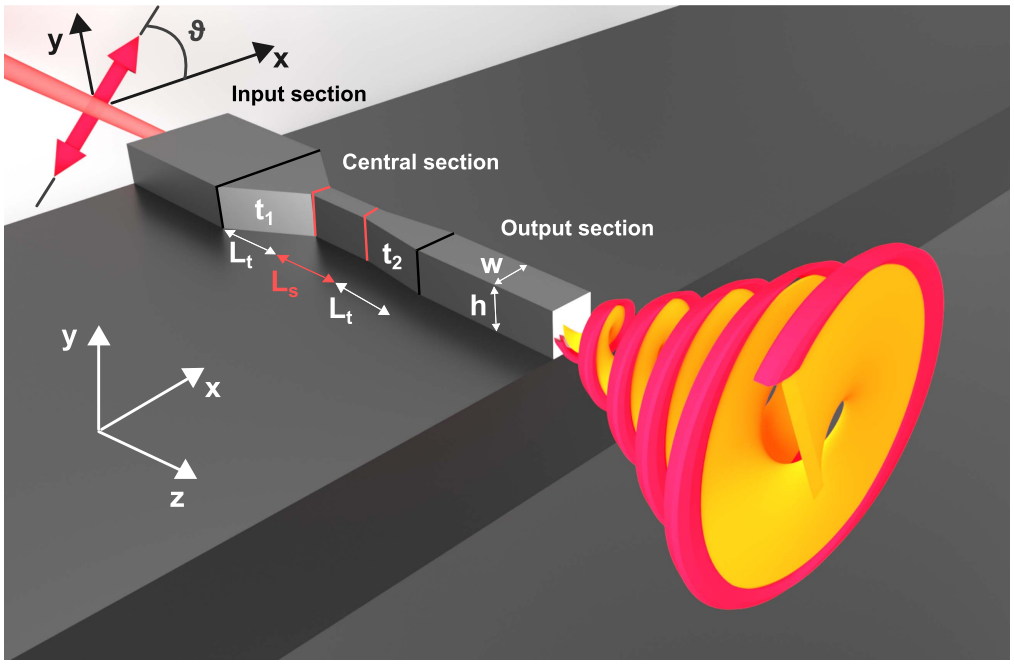

Figure 1. Sketch of the integrated AlGaAs device and its generation of angular momentum. An incoming light beam linearly polarised at 45° is transformed into a light beam carrying spin angular momentum in the field transverse component (red) and a phase vortex in the field longitudinal component (yellow).

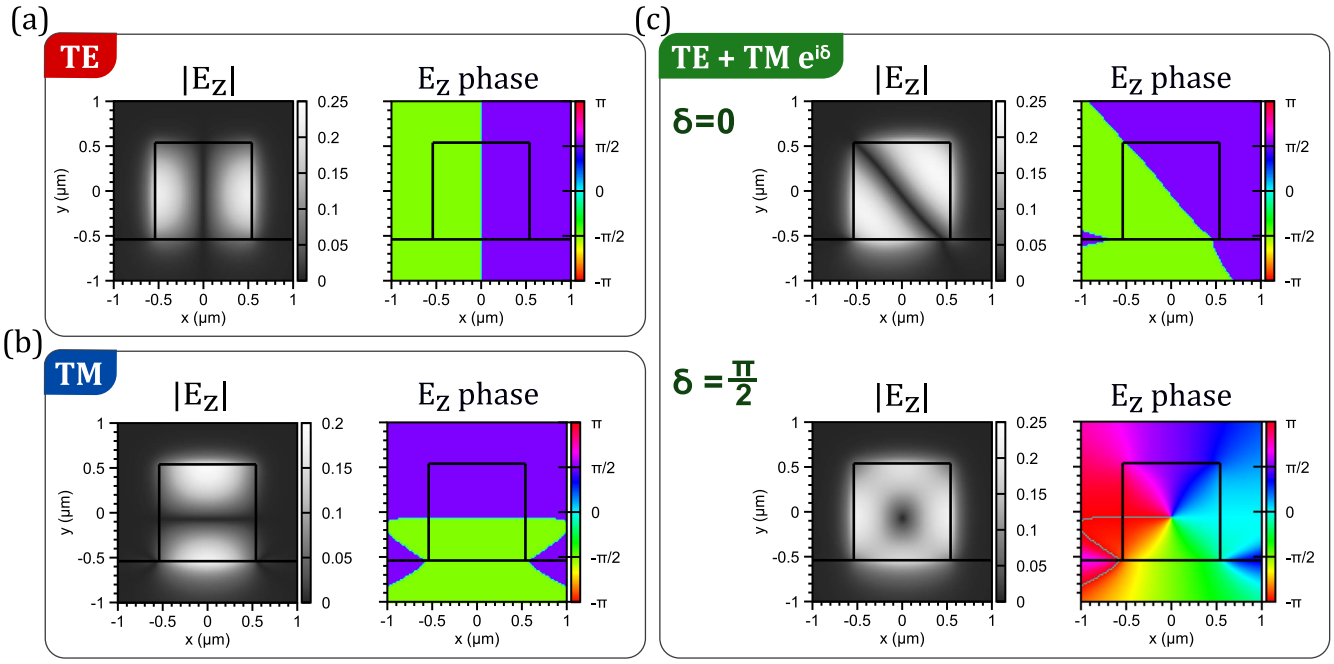

Figure 2. Numerical simulations of the modulus and phase of the longitudinal electric field component of the (a) quasi-TE and (b) quasi-TM modes in the waveguide output section. (c) Resulting longitudinal electric field in the output section for two different phase delays accumulated in the central section.

expression

$$E_z = -\frac{i\lambda}{2\pi n_{\text{eff}}} \nabla_\perp \cdot \mathbf{E}_\perp, \tag{2}$$

where $\nabla_\perp \cdot \mathbf{E}_\perp$ is the transverse divergence of the electric field, and n_{eff} is the effective refractive index [39]. Figures 2(a) and (b) show the amplitude and phase profile of the longitudinal component of the quasi-TE and quasi-TM modes in the waveguide output section, respectively. As equation (2) indicates, $\mathbf{E}_\perp$ and E_z are dephased by $|\pi/2|$. Hence, the longitudinal field components of the TE and TM modes are also delayed by δ. The transverse profiles of E_z for two different phase-delayed superpositions of quasi-TE and quasi-TM modes are illustrated in figure 2(c). The ratio

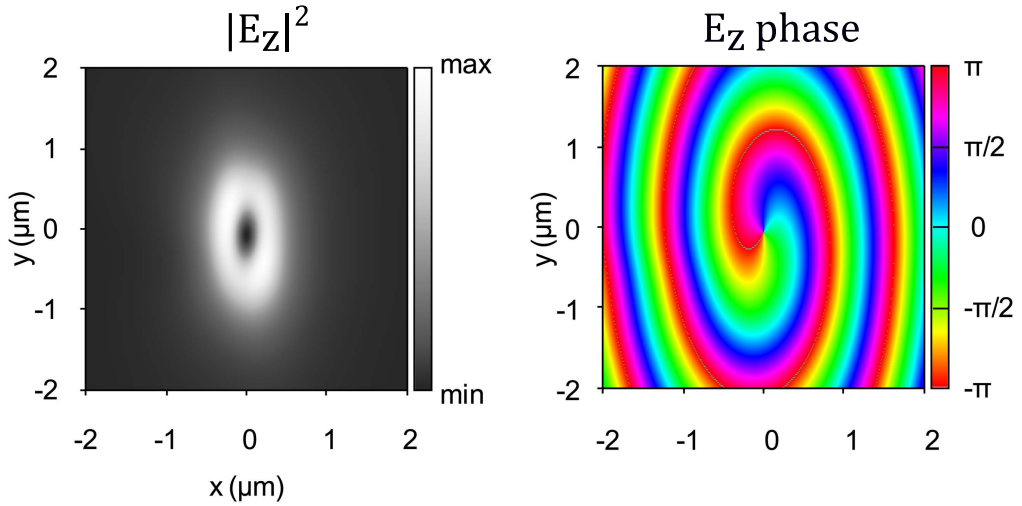

Figure 3. Numerical simulations of the emitted intensity and phase profile of the longitudinal component E_z in the near-field (distance $d = \lambda/3 = 517$ nm from the waveguide output facet).

between the maximum values of E_z and E_x (E_y) in the output section is 0.21 (0.19). As quasi-TE and quasi-TM modes are superposed in the waveguide, an optical vortex can be generated in the output section, depending on the phase δ accumulated in the central section. If the length of this section is chosen such that the relative phase is an integer multiple of π, i.e. $\delta = n\pi$ where $n \geqslant 0$ is a positive integer, E_z exhibits an antisymmetric distribution with respect to the diagonal. If the length of the central section is chosen to have $\delta = (2n + 1)\,\pi/2$, a phase vortex with unit topological charge, $\exp(i\phi)$, is generated. The longitudinal field, thus, possesses a spiral phase distribution and a doughnut-shaped intensity profile. The sign of the phase-vortex can be changed by rotating the input polarisation by $\pm\pi/2$. The longitudinal field components are still relatively strong in close vicinity to the out-coupling facet of the waveguide as light propagates in free-space and where the mode is still spatially confined. Figure 3 shows the simulated near-field electric energy density and phase distributions of E_z. The field has been calculated at a distance of 517 nm away from the waveguide output facet. The helical phase distribution and the corresponding doughnut intensity profile indicate that the field component E_z carries a phase vortex because it is still confined. Due to the very tight confinement of the phase-delayed quasi-TE and quasi-TM modes, also the transverse field component will carry a phase-vortex of charge 2 when projected onto the opposite polarisation handedness (not shown here) [40]. Nonetheless, the conversion efficiency for this OAM generation is very low, and is not to be discussed here.

The fabrication of our device is straight-forward in comparison to hybrid dielectric-plasmonic structures and requires only standard processes. The sample is grown by molecular beam epitaxy on a (100)GaAs substrate. It consists of a 3 μm thick cladding layer of $Al_{0.8}Ga_{0.2}As$ and a 1.08 μm thick core layer of GaAs. As shown in figure 4, waveguides are fabricated using electron-beam lithography (EBL; resist: *maN* − 2403, exposure dose $D = 145\ \mu C\,cm^{-2}$) and inductively coupled plasma etching (ICP). The chip contains several devices having different lengths L_s for the central section; the measurements reported in this work refer to the device having $L_s = 52.8\ \mu$m.

Input and output sections are exposed via the fixed beam and moving stage technique, while the narrower tapers and delay sections are created via standard EBL exposure. The ICP etching makes use of $SiCl_4$ and Ar ions, injected into the chamber by a flow of $\phi = 3\ cm^3\,min^{-1}$ and accelerated by an RF signal of $V = 115$ V at $P = 15$ W. The processing is completed by cleaving the sample into approximately 2 mm long waveguides. The fabricated samples are observed with a scanning electron microscope to inspect the quality. Figure 4 shows the side view of the waveguide delay section, displaying a sidewall roughness of $\Delta w \approx \pm 20$ nm. The measured width of the central section is 548 nm for a nominal width of 550 nm, while the measured height is $1.09 \pm$ μm, to be compared to the nominal one of 1.08 μm.

The optical propagation losses are measured via a standard Fabry–Perot technique [41]. By using a continuous wave tunable laser, we measure the transmitted signal at the device output as a function of the coupled wavelength for both TE and TM modes, as shown in figure 5. From the contrast of the Fabry–Perot fringes and the facets reflectivities, calculated numerically via FDTD ($R^{in}_{quasi-TE} = 0.35$, $R^{out}_{quasi-TE} = 0.41$, $R^{in}_{quasi-TM} = 0.27$, $R^{out}_{quasi-TM} = 0.41$), we find $\alpha_{quasi-TE} = 0.8 \pm 0.4\ cm^{-1}$ and $\alpha_{quasi-TM} = 1.5 \pm 0.4\ cm^{-1}$. These represent typical values if compared to those obtained in other devices of the same chip. We believe that these values depends both on confinement and flanks' roughness; since the design of the taper is adiabatic, we do not expect to have losses coming from its shape. The total coupling losses can be estimated by taking into account the mode overlap and the facets reflectivity. This leads to a total input–output efficiency of 5% for the present device. Note that the use of an anti-reflection coating and of a laser-diode-to-fibre-coupler for the input–output coupling would bring the collection efficiency to 21%.

The experimental setup used for exploring the polarisation state transformation is sketched in figure 6. A

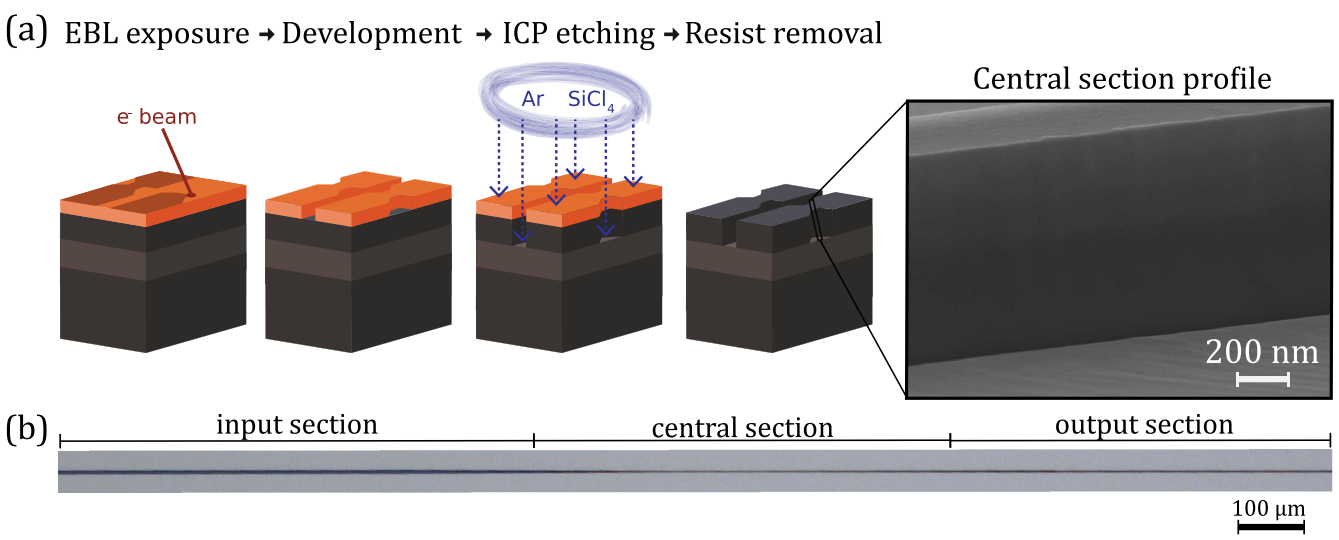

Figure 4. (a) Sketch of the main fabrication and processing steps. Dark grey region corresponds to GaAs; light grey to $Al_{0.8}Ga_{0.2}As$. The waveguides are fabricated with EBL technique and are etched by ICP, using Ar and $SiCl_4$. A scanning electron microscope micrograph of the sidewall of the delay section of the waveguide is shown on the right inset. (b) A top-view optical microscope image of one waveguide, where input, central (including two adiabatic tapers and a straight section) and output sections are indicated.

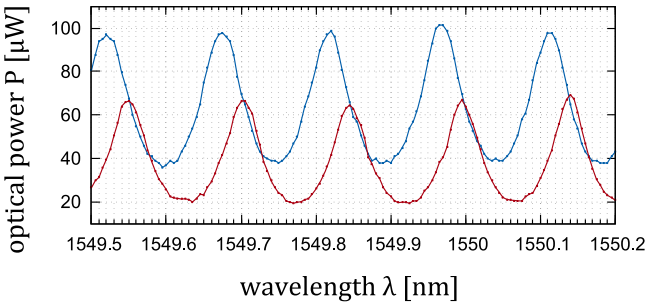

Figure 5. Optical power of the emitted quasi-TE (blue) and quasi-TM (red) modes as a function of the wavelength. From the contrast of the Fabry–Perot fringes and the simulated facets reflectivity, we find $\alpha_{\text{quasi-TE}} = 0.8 \pm 0.4$ cm^{-1}, $\alpha_{\text{quasi-TM}} = 1.5 \pm 0.4$ cm^{-1}.

fundamental Gaussian-shaped laser beam at $\lambda = 1.55$ μm is polarised at 45° by means of a half-wave plate (HWP) and a linear polariser (LP). The beam is coupled into the waveguide by using a microscope objective with a numerical aperture of NA = 0.65 and magnification 40X. The out-coupled beam is collected and collimated with a microscope objective of NA = 0.75, 60X, and its polarisation state is analyzed by means of a commercial polarimeter (PAX5720IR3-T), composed of a rotating HWP, a LP and a power meter.

In our measurements, the out-coupled beam is observed to be elliptically polarised. The polarimeter allows for measuring the ellipse azimuth α (the ellipse major axis angle with respect to the horizontal axis) and ellipticity $\epsilon = b/a$, the ratio of the ellipse's minor b to major a axis. Figure 7(a) shows the results obtained for 30 consecutive measurements at $\lambda = 1.55$ μm. The scattering observed in our results is consistent with the extinction ratio (10^{-2}) of the polariser used for the measurements. The average ellipticity is $\epsilon = 0.67$ and the azimuth equals to $\alpha = 0.61°$. The resulting polarisation state is shown in figure 7(b). A perfectly circular polarisation state ($\epsilon = 1$) is not achieved because of the different optical propagation losses and Fabry–Perot resonance wavelengths of the quasi-TE and quasi-TM modes. The corresponding phase delay between the emitted quasi-TE and quasi-TM modes is $\Delta\phi = 89.5°$ (full green circle in figure 7(c)), while it varies in the range $\Delta\phi = 95.5° \pm 30°$ for $\lambda \in [1.5497, 1.5500]$ μm (blue circles of figure 7(c)). This behaviour is explained by considering the waveguide as a Fabry–Perot birefringent cavity. Quasi-TE and quasi-TM modes travel with different group refractive indices because of the asymmetric boundary conditions, so their Fabry–Perot resonance wavelengths differ and the phase difference between the two shows sinusoidal behaviour. Indeed, our measurements are in good agreement with a Fabry–Perot birefringent cavity model (continuous black line, figure 7(c)), based on the calculated facet reflectivity, the measured optical losses and the cleaved waveguide length.

The performance of the device discussed here can be further improved by many means. If the polarisation of the incident light beam is a possible degree of freedom, the ellipticity of the output state can be controlled for each wavelength through a linear polariser having its transmission axis at an appropriate angle θ (instead of $\theta = 45°$) with respect to the horizontal axis. A perfect circular polarisation state is achievable by compensating the different propagation losses of TE and TM modes in the waveguide at the specific working wavelength. At 1550.0 nm, by coupling in LP at $\theta = 45°$, the output ellipticity is $\epsilon = 0.67$ and the azimuth $\alpha = 0.61°$ (figure 7(b)). Therefore, the LP beam should have $|E_{\text{TE}}| = |E_{\text{TM}}|/\epsilon = 1.5|E_{\text{TM}}|$, corresponding to $\theta = 34°$, to compensate such losses.

Otherwise, an on-chip tuning of the quasi-TE and quasi-TM mode phase delay can be obtained utilizing the strong electro-optical Pockels effect driven by the large second-order nonlinear susceptibility of GaAs. Indeed, the refractive index of the material is linearly proportional to the applied electric field and depends on its orientation with respect to the crystal axis [42]. This effect has already been successfully used to

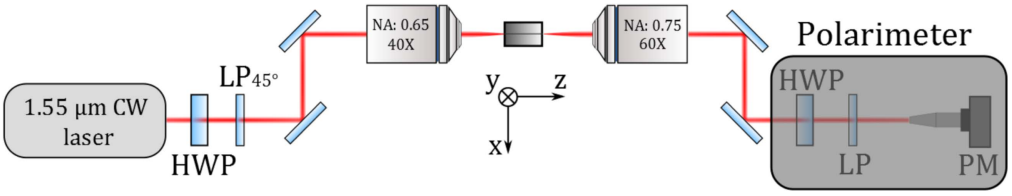

Figure 6. Sketch of the experimental setup used for measuring the polarisation state of the output beam. The incoming laser beam at $\lambda = 1.55$ μm is linearly polarised at 45° by a half-wave plate (HWP) and a linear polariser (LP). Two microscope objectives are used to couple-in (NA = 0.65, 40X) and out-couple (NA = 0.75, 60X) the beam. The polarisation state of the out-coupled beam is reconstructed by a polarimeter.

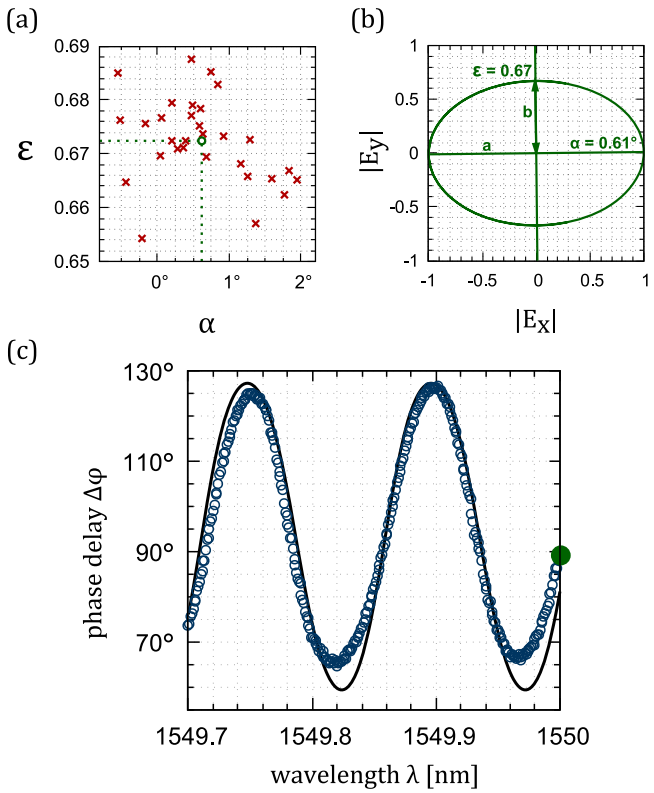

Figure 7. Polarisation state measurements. (a) Measurements (red crosses) and average (green circle) of ellipticity ϵ and azimuth α of the out-coupled beam elliptical polarisation state at $\lambda = 1.55$ μm. (b) Representation of the average polarisation state at $\lambda = 1.55$ μm. (c) Phase delay between the emitted quasi-TE and quasi-TM modes as a function of the wavelength.

develop quantum photonic circuits for the manipulation of single- and two-photon states [43] and could be used in an analogous way to control the phase delay between the two quasi-TE and quasi-TM modes propagating in our device by fabricating an on-chip electro-optical phase shifter. Finally we note that, if required, the Fabry–Perot oscillations could easily be eliminated by adding a standard telecom anti-reflection coating to the waveguide's facets.

The elliptically (ideally circularly) polarised output state measured in the far-field is a direct proof of the birefringence-induced phase-delay in the on-chip waveguide device. Analogously to the effect of spin–orbit coupling induced upon focusing of a circularly polarised mode in free-space [44], the strong confinement of such a circularly polarised electric field in a fundamental mode within the device output section is an indirect evidence of the presence of a phase vortex in its longitudinal field component, as proven also by our simulations. It is worth noting here that a direct measurement of a phase vortex in the longitudinal field component at the nanoscale is a complex task. A simple observation with a CCD camera is not possible since the power ratio between the longitudinal and transverse field components decreases rapidly with the distance from the output facet. A direct evidence of the phase vortex would require, for instance, adapted nanoscale field reconstruction methods [45] or sophisticated near-field scanning optical microscopy techniques [46], which goes beyond the scope of this paper.

With the discussed device, a controlled phase delay can be induced between two orthogonally polarised waveguide modes. Similarly, this concept could also be applied to spatial modes launched into such on-chip devices. This way, phase vortices could also be imprinted on the transverse field components, hence resulting in a net OAM carried by the generated beam emitted from the end facet of the waveguide. For this reason, our next step is to adapt the design of our device and tailor the input states to control the spatial phase distribution of higher order modes and to generate OAM beams.

In summary, we have conceived, fabricated and characterised a waveguide that, starting from a LP beam, is capable of inducing a defined relative phase between quasi-orthogonal waveguide modes. We have proven this concept by generating a confined circularly polarised mode (SAM) with a phase-vortex carried by the longitudinal field component. The device working principle for both transverse and longitudinal fields can be summarised as follows: (i) a quarter-wave plate operation, and (ii) the generation of longitudinal fields due to spatial confinement. Together, however, a longitudinal field possessing a helical phase-front and thus also a phase vortex of charge ± 1 is created. Our proposed device is highly integratable and may constitute an interesting platform for on-chip control and manipulation of quantum states of light, encoded for example in polarisation or OAM. Therefore, it can be used in micron-scale optical manipulation, data multiplexing and quantum information.

Acknowledgments

E K acknowledges the support of the Canada Research Chairs (CRC) Program and Canada Foundation for Innovation (CFI). SD and GM acknowledge the support of Agence Nationale de

la Recherche (ANR-14-CE26-0029-01) and M Rosticher for his help with electron-beam lithography.

ORCID iDs

E Karimi https://orcid.org/0000-0002-8168-7304
S Ducci https://orcid.org/0000-0002-9005-1949

References

[1] O'Brien J L, Furusawa A and Vučković J 2009 Photonic quantum technologies *Nat. Photon.* **3** 687–95
[2] Orieux A, Versteegh M A M, Jöns K D and Ducci S 2017 Semiconductor devices for entangled photon pair generation: a review *Rep. Prog. Phys.* **80** 076001
[3] Dietrich C P, Fiore A, Thompson M G, Kamp M and Höfling S 2016 Gaas integrated quantum photonics: Towards compact and multi-functional quantum photonic integrated circuits *Laser Photonics Rev.* **10** 870–94
[4] Boitier F, Orieux A, Autebert C, Lemaître A, Galopin E, Manquest C, Sirtori C, Favero I, Leo G and Ducci S 2014 Electrically injected photon-pair source at room temperature *Phys. Rev. Lett.* **112** 183901
[5] Orieux A, Eckstein A, Lemaitre A, Filloux P, Favero I, Leo G, Coudreau T, Keller A, Milman P and Ducci S 2013 Direct bell states generation on a iii–v semiconductor chip at room temperature *Phys. Rev. Lett.* **110** 160502
[6] Dai X, Zhang S, Wang Z, Adamo G, Liu H, Huang Y, Couteau C and Soci C 2014 Gaas/algaas nanowire photodetector *Nano Lett.* **14** 2688–93
[7] Sprengers J P *et al* 2011 Waveguide superconducting single-photon detectors for integrated quantum photonic circuits *Appl. Phys. Lett.* **99** 181110
[8] Neugebauer M, Bauer T, Banzer P and Leuchs G 2014 Polarization tailored light driven directional optical nanobeacon *Nano Lett.* **14** 2546–51
[9] Coles R J, Price D M, Dixon J E, Royall B, Clarke E, Kok P, Skolnick M S, Fox A M and Makhonin M N 2016 Chirality of nanophotonic waveguide with embedded quantum emitter for unidirectional spin transfer *Nat. Commun.* **7** 11183
[10] Lodahl P, Mahmoodian S, Stobbe S, Schneeweiss P, Volz J, Rauschenbeutel A, Pichler H and Zoller P 2017 Chiral quantum optics *Nature* **541** 473–80
[11] Mahmoodian S, Prindal-Nielsen K, Söllner I, Stobbe S and Lodahl P 2017 Engineering chiral light–matter interaction in photonic crystal waveguides with slow light *Opt. Mater. Express* **7** 43–51
[12] Allen L, Barnett S M and Padgett M J 2003 *Optical Angular Momentum* (Boca Raton, FL: CRC Press)
[13] Aiello A, Banzer P, Neugebauer M and Leuchs G 2015 From transverse angular momentum to photonic wheels *Nat. Photon.* **9** 789–95
[14] Banzer P, Neugebauer M, Aiello A, Marquardt C, Lindlein N, Bauer T and Leuchs G 2013 The photonic wheel—demonstration of a state of light with purely transverse angular momentum *J. Eur. Opt. Soc. Rap. Publ.* **8** 13032
[15] Neugebauer M, Bauer T, Aiello A and Banzer P 2015 Measuring the transverse spin density of light *Phys. Rev. Lett.* **114** 063901
[16] Allen L, Padgett M J and Babiker M 1999 Iv the orbital angular momentum of light *Prog. Opt.* **39** 291–372
[17] Banzer P, Peschel U, Quabis S and Leuchs G 2010 On the experimental investigation of the electric and magnetic response of a single nano-structure *Opt. Express* **18** 10905–23
[18] Woźniak P, Banzer P and Leuchs G 2015 Selective switching of individual multipole resonances in single dielectric nanoparticles *Laser Photonics Rev.* **9** 231–40
[19] Bouchard F, Fickler R, Boyd R W and Karimi E 2017 High-dimensional quantum cloning and applications to quantum hacking *Sci. Adv.* **3** e1601915
[20] Rubinsztein-Dunlop H *et al* 2016 Roadmap on structured light *J. Opt.* **19** 013001
[21] Allen L, Beijersbergen M W, Spreeuw R J C and Woerdman J P 1992 Orbital angular momentum of light and the transformation of laguerre-gaussian laser modes *Phys. Rev.* A **45** 8185–9
[22] Beijersbergen M W, Coerwinkel R P C, Kristensen M and Woerdman J P 1994 Helical-wavefront laser beams produced with a spiral phaseplate *Opt. Commun.* **112** 321–7
[23] Bazhenov V Y, Vasnetsov M V and Soskin M S 1990 Laser beams with screw dislocations in their wavefronts *Jetp Lett.* **52** 429–31
[24] Heckenberg N R, McDuff R, Smith C P and White A G 1992 Generation of optical phase singularities by computer-generated holograms *Opt. Lett.* **17** 221–3
[25] Marrucci L, Manzo C and Paparo D 2006 Optical spin-to-orbital angular momentum conversion in inhomogeneous anisotropic media *Phys. Rev. Lett.* **96** 163905
[26] Larocque H, Gagnon-Bischoff J, Bouchard F, Fickler R, Upham J, Boyd R W and Karimi E 2016 Arbitrary optical wavefront shaping via spin-to-orbit coupling *J. Opt.* **18** 124002
[27] Bouchard F, Mand H, Mirhosseini M, Karimi E and Boyd R W 2014 Achromatic orbital angular momentum generator *New J. Phys.* **16** 123006
[28] Genevet P, Yu N, Aieta F, Lin J, Kats M A, Blanchard R, Scully M O, Gaburro Z and Capasso F 2012 Ultra-thin plasmonic optical vortex plate based on phase discontinuities *Appl. Phys. Lett.* **100** 013101
[29] Karimi E, Schulz S A, De Leon I, Qassim H, Upham J and Boyd R W 2014 Generating optical orbital angular momentum at visible wavelengths using a plasmonic metasurface *Light: Sci. Appl.* **3** e167
[30] Bouchard F, De Leon I, Schulz S A, Upham J, Karimi E and Boyd R W 2014 Optical spin-to-orbital angular momentum conversion in ultra-thin metasurfaces with arbitrary topological charges *Appl. Phys. Lett.* **105** 101905
[31] Bomzon Z, Biener G, Kleiner V and Hasman E 2002 Space-variant pancharatnam-berry phase optical elements with computer-generated subwavelength gratings *Opt. Lett.* **27** 1141–3
[32] Cai X, Wang J, Strain M J, Johnson-Morris B, Zhu J, Sorel M, O'Brien J L, Thompson M G and Yu S 2012 Integrated compact optical vortex beam emitters *Science* **338** 363–6
[33] Ramachandran S and Kristensen P 2013 Optical vortices in fiber *Nanophotonics* **2** 455–74
[34] Niederriter R D, Siemens M E and Gopinath J T 2016 Continuously tunable orbital angular momentum generation using a polarization-maintaining fiber *Opt. Lett.* **41** 3213–6
[35] Wong G K L, Kang M S, Lee H W, Biancalana F, Conti C, Weiss T and Russell P S J 2012 Excitation of orbital angular momentum resonances in helically twisted photonic crystal fiber *Science* **337** 446–9
[36] Liang Y, Wu H W, Huang B J and Huang X G 2014 Light beams with selective angular momentum generated by hybrid plasmonic waveguides *Nanoscale* **6** 12360–5
[37] Guo J, Liang Y, Huang X G, Guo B and Li J 2016 Pure dielectric waveguides enable compact, ultrabroadband wave plates *IEEE Photonics J.* **8** 1–9

[38] Lumerical Solutions. MODE 2016 https://web.archive.org/web/20170106045226/https://www.lumerical.com/tcad-products/mode/ (Accessed: 11 November 2016)
[39] Driscoll J B, Liu X, Yasseri S, Hsieh I, Dadap J I and Osgood R M 2009 Large longitudinal electric fields (ez) in silicon nanowire waveguides *Opt. Express* **17** 2797–804
[40] Bliokh K Y, Ostrovskaya E A, Alonso M A, Rodríguez-Herrera O G, Lara D and Dainty C 2011 Spin-to-orbital angular momentum conversion in focusing, scattering, and imaging systems *Opt. Express* **19** 26132–49
[41] De Rossi A, Ortiz V, Calligaro M, Lanco L, Ducci S, Berger V and Sagnes I 2005 Measuring propagation loss in a multimode semiconductor waveguide *J. Appl. Phys.* **97** 073105
[42] Acosta-Ortiz S E and Lastras-Martinez A 1989 Electro-optic effects in the optical anisotropies of (001) gaas *Phys. Rev.* B **40** 1426
[43] Wang J *et al* 2014 Gallium arsenide (gaas) quantum photonic waveguide circuits *Opt. Commun.* **327** 49–55
[44] Zhao Y, Edgar J S, Jeffries G D M, McGloin D and Chiu D T 2007 Spin-to-orbital angular momentum conversion in a strongly focused optical beam *Phys. Rev. Lett.* **99** 073901
[45] Bauer T, Orlov S, Peschel U, Banzer P and Leuchs G 2014 Nanointerferometric amplitude and phase reconstruction of tightly focused vector beams *Nat. Photon.* **8** 23–7
[46] Rotenberg N and Kuipers L 2014 Mapping nanoscale light fields *Nat. Photon.* **8** 919–26

technologies

MDPI

Article

Electrically Injected Twin Photon Emitting Lasers at Room Temperature

Claire Autebert [1], Giorgio Maltese [1], Yacine Halioua [1], Fabien Boitier [1,2], Aristide Lemaître [3], Maria Amanti [1], Carlo Sirtori [1] and Sara Ducci [1,*]

1 Laboratoire Matériaux et Phénomènes Quantiques, Université Paris Diderot, Sorbonne Paris Cité, Paris 75205, France; claire.autebert@univ-Paris-diderot.fr (C.A.); giorgio.maltese@univ-Paris-diderot.fr (G.M.); yacine.halioua@univ-Paris-diderot.fr (Y.H.); fabien.boitier@nokia-bell-labs.com (F.B.); maria.amanti@univ-Paris-diderot.fr (M.A.); carlo.sirtori@univ-Paris-diderot.fr (C.S.)

2 Nokia Bell Labs, Route de Villejust, Nozay 91620, France

3 Centre de Nanosciences et de Nanotechnologies, CNRS/Université Paris Sud, Marcoussis 91460, France; aristide.lemaitre@lpn.cnrs.fr

* Correspondence: sara.ducci@univ-Paris-diderot.fr; Tel.: +33-1-5727-6225

Academic Editor: Stephan Reitzenstein
Received: 29 June 2016; Accepted: 8 August 2016; Published: 18 August 2016

Abstract: On-chip generation, manipulation and detection of nonclassical states of light are some of the major issues for quantum information technologies. In this context, the maturity and versatility of semiconductor platforms are important assets towards the realization of ultra-compact devices. In this paper we present our work on the design and study of an electrically injected AlGaAs photon pair source working at room temperature. The device is characterized through its performances as a function of temperature and injected current. Finally we discuss the impact of the device's properties on the generated quantum state. These results are very promising for the demonstration of electrically injected entangled photon sources at room temperature and let us envision the use of III-V semiconductors for a widespread diffusion of quantum communication technologies.

Keywords: entanglement production; semiconductor laser; integrated quantum optics

1. Introduction

Integrated quantum photonics is a very active field of quantum information science. In particular, the maturity of semiconductor technology offers a huge potential to build ultra-compact devices including generation, manipulation and detection of many quantum bits. In these last years, spectacular progress has been done on different material platforms, such as AlGaAs, silicon-on-insulator [1,2], silica-on-silicon [3,4], as well as on their hybrid integration, e.g., with superconducting detectors [5]. In this context, the direct band gap and electro-optics effect characterizing III-V semiconductors are important assets for the achievement of electrically injected, tunable, integrated quantum photonic devices. While quantum dots-based sources working at cryogenic temperatures have allowed us to reach unprecedented levels of brightness and to tune the degree of photon indistinguishability [6], spontaneous parametric down-conversion (SPDC) in AlGaAs has allowed us to produce entanglement on various degrees of freedom with devices working at room temperature and telecom wavelength (see Section 3).

Recently, the utilization of this platform has led to the demonstration of a completely integrated electrically injected device consisting of a quantum-well laser emitting photons at 780 nm that are converted into telecom-wavelength photon pairs by internal spontaneous parametric down-conversion [7].

In this paper we study the behavior of this device as a function of temperature and of the injected current and we discuss the impact of the device's properties on the generated quantum state.

2. Results

2.1. Design and Fabrication

The challenge in designing such a device lies in simultaneously addressing the electrical injection of the laser and the efficient down-conversion of laser photons in photon pairs.

In the nonlinear process, the energy and momentum of the photons are conserved—nothing is exchanged with the crystal. While energy conservation is straightforward, conserving the momentum requires compensating for the phase velocity mismatch of the three interacting photons, which is usually done by using birefringent crystals. However, even if GaAs present a high second-order nonlinearity, which is beneficial for achieving efficient frequency conversion processes ($\chi^{(2)}$ around 110 pm/V at 1550 nm [8]), this material lacks natural birefringence. Among different techniques to achieve phase-matching, the recent development of Bragg reflection waveguides [9,10] represents a breakthrough, since this strategy allows us to reduce the total aluminum content (thus avoiding aging problems of the device) and increases the flexibility of effective index engineering. In our case, two Bragg mirrors provide both a photonic band gap vertical confinement for the laser mode (a transverse electric Bragg mode) and total internal reflection claddings for the photon-pairs modes (one TE_{00} and one TM_{00}). The device's design is dictated by trade-offs that must optimize electrical transport, waveguiding and nonlinear interaction at the same time [11]. Figure 1a,b present, respectively, the simulated intensity profile of the laser Bragg mode and the refractive index and doping profiles of the resulting design.

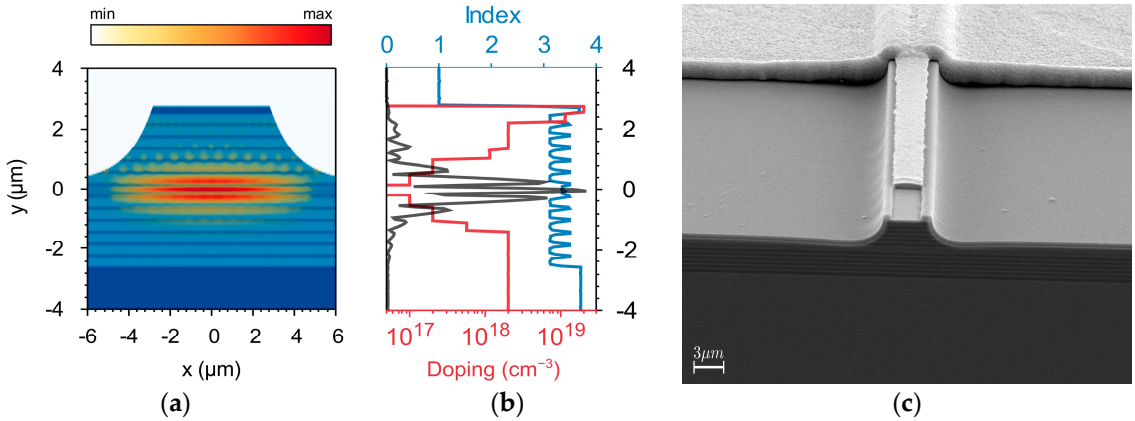

Figure 1. (**a**) Simulated intensity profile for the Bragg mode within the waveguide; (**b**) Refractive index and doping profile of the device; the Bragg mode has a higher overlap with the quantum well than the TE_{00} mode; (**c**) SEM image of the sample showing the facet of the sample and the upper electrode with the thick electrolytic layer.

The sample under study has been grown by molecular beam epitaxy on a (100) GaAs substrate. It consists of two $Al_{0.8}Ga_{0.2}As/Al_{0.25}Ga_{0.75}As$ Bragg reflectors of six periods each surrounding a 365 nm $Al_{0.45}Ga_{0.55}As$ core. A 8.5 nm $Al_{0.11}Ga_{0.89}As$ quantum well is embedded into the core to ensure a gain peaked at 780 nm (see Figure 1a). The top and bottom Bragg reflectors are, respectively, gradually p-doped and n-doped, from 1×10^{17} to 2×10^{18}, in order to ensure efficient electrical injection of the device. An additional highly doped cap layer is added to protect the device and facilitate electrical injection from the upper contact [12]. The device is processed in a standard waveguide geometry, as presented in Figure 1c: 5–6 μm wide and 2 μm deep waveguides are defined by wet etching of the top Bragg reflector. A SiN layer is used for electrical insulation and Ti/Au and Ni/Ge/Au/Ni/Au

layer sequences are used for the top and bottom contact, respectively. A thick electrolytic Au layer is used for the top contact, helping heat management. Samples are cleaved into approximately 2 mm long stripes.

2.2. Optoelectronic Characterization

Figure 2a reports the typical power-current-voltage (PIV) curves as a function of the temperature of one of our samples under electrical pumping; the pulse duration is 60 ns at a repetition rate of 40 kHz. These curves attest for the lasing emission. We observe that at T = 291 K, the I-V curve shows a resistance of R = 3.56 Ω and a turn-on voltage of 1.83 V, which is very close to the quantum well band gap, thus meaning that no current-blocking effects occur at the hetero-interfaces. The P-I curve displays a threshold current of I_{th} = 0.274 A, corresponding to threshold density current J_{th} = 1.5 ± 0.2 kA/cm^2 for a contact surface of S = 1.9 (± 0.2) × 10^{-4} cm^2.

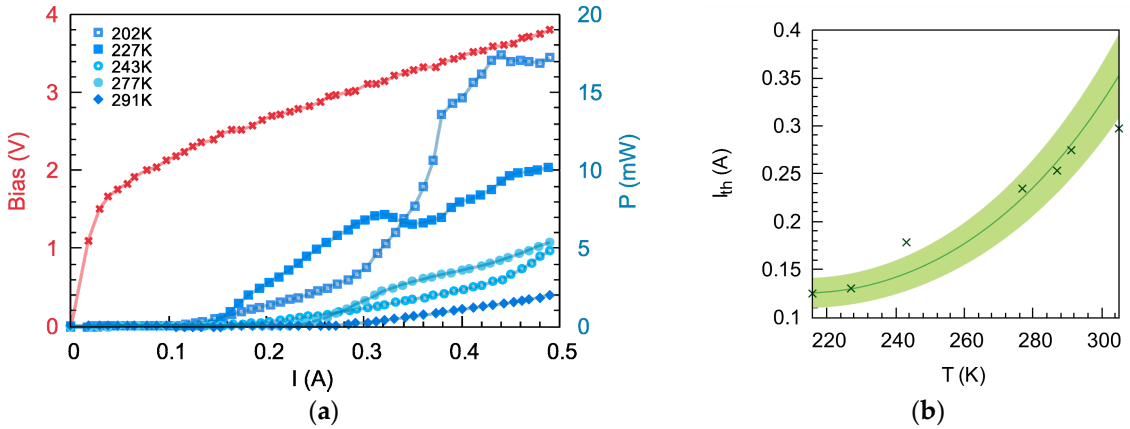

Figure 2. Laser operation. (**a**) Voltage bias (crosses) and emitted power versus injected current. The I-V curve is measured at T_{room} = 291 K, while I-P for T is in the range 202–291 K. At room temperature the laser has a threshold of I_{th} = 0.274 A, a turn on voltage of 1.8 V; (**b**) Measured (crosses) and calculated (continuous line) threshold current as a function of temperature. The error band around the calculated threshold corresponds to the uncertainty of the diode surface after the wet etching and cleaving processes.

As the temperature decreases from T_{room} = 291 K to T = 202 K, the threshold current decreases exponentially as shown in Figure 2b, according to $I_{th} \sim e^{T/T0}$, with T_0 = 87.8 K [13].

These experimental results are compared with the numerical simulations we have developed to design our device; the carrier transport and recombination in the hetero-junction are calculated using a self-consistent solution of the drift-diffusion and Poisson equations. The optical parameters of our modeling are the Bragg mode internal losses, whose value α = 35 cm^{-1} is extracted from the experimental results obtained by a second-harmonic generation measurement [14]; the overlap integral between the Bragg mode and the quantum well Γ = 2.45%, calculated with a commercial eigenmode solver [15]; and the facets modal reflectivity for the Bragg mode R = 0.86, calculated by Finite-Difference Time-Domain (FDTD). The radiative recombination time in the quantum well is set to τ^{rad} = 5 × 10^{-17} m^3·s^{-1}, while the Shockley-Read-Hall non-radiative recombination processes is τ^{SRH} = 5 ns [16]. The waveguide length and width are L = 2 mm and w = 6 μm, respectively, while the doping profile and aluminum contents correspond to the nominal values of the epitaxial structure.

Figure 2b shows the good agreement between the experimental and the calculated threshold current as a function of the temperature in the 216–305 K range, within the uncertainty of the device contact surface S = 1.9 (± 0.2) × 10^{-4} cm^2.

From the calculated internal resistance of the diode ($R_{int} \approx$ 1.5 Ω at room temperature) we evaluate the quality of the fabricated contacts, which introduce an additional resistance lower than R = 2.0 Ω.

The spatial intensity distribution of the emitted laser beam above the threshold is studied by imaging the output facet; the recorded near-field and far-field distributions are reported in Figure 3a, showing a clear evidence of emission on the Bragg mode. For higher values of injected current the Bragg mode can be in competition with the fundamental TE_{00} mode due to index anti-guiding effects coming from a carrier density increase. This might explain the irregular behavior observed in the I-P curve; further studies on this point are in progress.

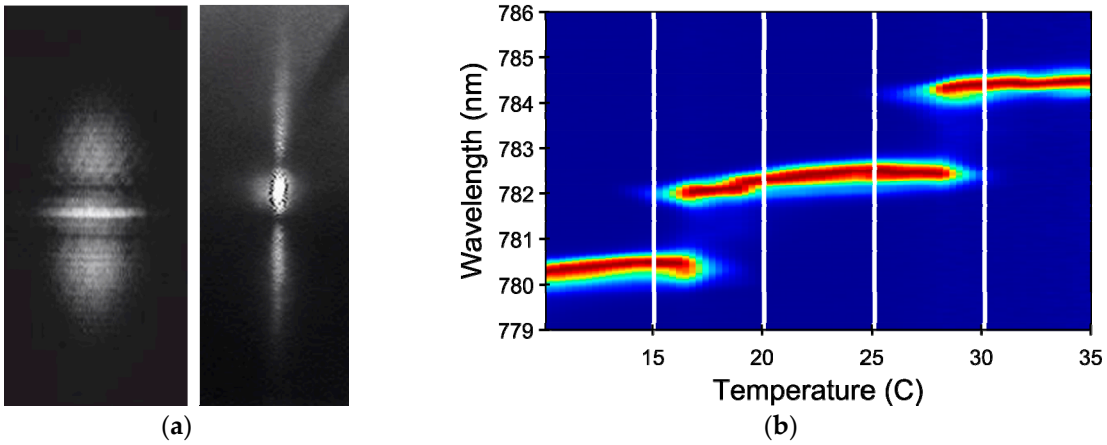

Figure 3. (**a**) Measured near- and far-field emissions of a laser emitting on the Bragg mode; (**b**) Normalized laser emission intensity as a function of wavelength and heat-sink temperature.

Figure 3b displays the laser emission intensity spectra as a function of heat-sink temperature, measured with an Optical Spectrum Analyzer for a laser emitting on the Bragg mode at room temperature. The general trend corresponds to the theoretical temperature dependence of the quantum well band gap (0.23 nm/°C); mode hopping is clearly visible with wavelength jumps of approximately $\Delta\lambda \approx 1.5$–$2$ nm.

We notice that these jumps correspond to more than 35 times the spacing between adjacent longitudinal modes of our device; indeed, taking into account the laser length and the modal dispersion, we find $\Delta\lambda_{FSR} = \lambda^2/2L \times (n - \lambda\, dn/d\lambda)^{-1} \approx 40$ pm [17]. This behavior has already been observed in AlGaAs laser structures [18]; it seems to be explained by the presence of an additional saturable source of losses, resulting from deep-level traps induced in the n-type doped Bragg layers by Si donors. As the traps' absorption is inversely proportional to the photon density, the standing-wave intensity profile of the dominant longitudinal mode $I(z)$ determines the periodicity of the optical loss pattern $\alpha^{traps}(z) = \alpha_0/(1 + I(z)/I_s)$ [19]. By integrating along the whole device length, it is possible to show that the dominant longitudinal mode presents smaller losses than the adjacent modes by a factor $\Delta\alpha \approx 0.05 - 0.1\alpha_0$. In order to verify that our observations are related to this physical process, we have estimated $\Delta\alpha$, calculating the overlaps of the Bragg mode with each n-doped layer. By assuming the reflectivity R = 0.86, we find $\alpha_0 = 5.54\ cm^{-1}$ at room temperature leading to $\Delta\alpha \approx 0.28$–$0.55\ cm^{-1}$, which is compatible with our experimental results (Figure 3b).

The demonstration of the photon pair emission in the telecom range has been done by performing time correlation measurements under electrical injection in a pulsed regime at 601 mA. The emerging TE and TM photon pairs, corresponding to a type-II SPDC, are detected with two InGaAs single-photon avalanche photodiodes (IdQ201) having 20% detection efficiency and a 50 ns gate, synchronized with the current pulses. A time-to-digital converter is used to analyze the time correlations between cross-polarized photons, separated by a polarization beam splitter. Figure 4 shows a histogram of the detection time delays at $T = 25$ °C. The sharp peak emerging from the background is the evidence that photons are produced by pairs. From these data, taking into account the optical losses along the optical path, we estimate an internal generation efficiency of the device of $\sim 10^{-10}$ pairs/injected electron.

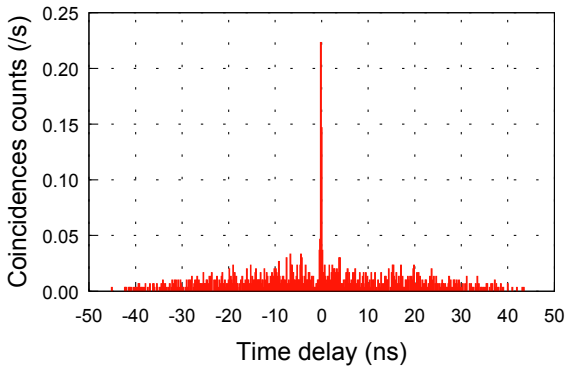

Figure 4. Time-correlation histogram of TE/TM photons around 1.57 µm at T = 15 °C. This sample is electrically injected with current pulses of 601 mA, a duration of 60 ns and a repetition rate of 40 kHz. The data were accumulated during 600 s with a sampling resolution of 162 ps.

3. Discussion and Conclusions

In this section we discuss the impact of the performances of our devices on the quality of the quantum state of the emitted photons and we give some perspectives.

The signal-to-noise ratio (SNR) is evaluated by taking the number of true coincidences within the Full Width Half Maximum (FWHM) of the peak over the background signal on the same time window; Figure 5 reports the SNR value as a function of the injected current for the same sample characterized in Figure 4. For a current value below the laser threshold, no "true coincidence" peak emerges from the noise. For a current value between 450 mA and 600 mA, the SNR increases linearly with the injected current as expected from the typical diode behavior of the device. At high current values the SNR saturates, probably due to thermal effects within the device having an impact on the laser operation and the phase-matching curve.

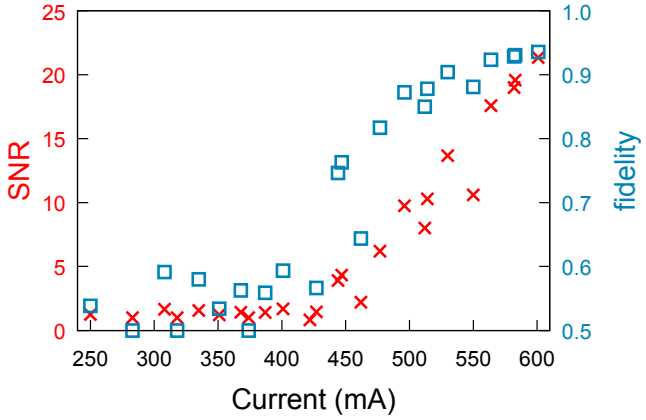

Figure 5. Signal-to-noise ratio and fidelity to a Bell state as a function of the current for one of our devices.

Assuming that the source emits a Werner state, we can estimate the fidelity F to the maximally entangled Bell state $|\psi_+\rangle$: $F = (1 + 3P)/4$ with $P = SNR/(2 + SNR)$. The value of F as a function of the current is also given in Figure 5: we observe that for an injected current of 600 mA, F should reach the value of 93%, which is compliant with an experimental violation of Bell's inequality.

Recently, we have improved the fabrication method of our devices, passing from wet to dry etching to define the waveguides; this has allowed increasing the confinement and overlap of the interacting modes (and consequently the nonlinear process efficiency) while keeping a low level of

optical losses. We have thus reached a SNR value of 1730, which potentially would bring us to the condition of achieving a fidelity value of 99% [20].

In order to check the possibility to drive the device in continuous wave (CW) operation, we have measured the output power as a function of the duty cycle: the observation of a constant peak output power for a duty cycle up to 66% indicates that a CW operation is possible [12].

In parallel, quantum optics experiments on the photon pairs generated by passive samples based on the same phase-matching technique have allowed us to demonstrate high values of indistinguishability [21,22] and entanglement on polarization [23] and energy-time [22]. The quality of the produced quantum state as well as its compatibility with the telecom network have also allowed to use these sources in multi-user quantum key distribution protocols using standard dense wavelength division multiplexers [24]. This approach seems also to be promising for the control of the frequency correlations of the emitted biphoton state; for example, original designs of $Al_xGa_{1-x}N$ devices have been proposed in which quasi-phase-matching of the waveguide core is used to achieve phase-matching at the desired wavelength, while the control of waveguide dispersion is used to control the frequency correlation between the generated photons [25].

In conclusion, Bragg reflection waveguides emerge as an extremely attractive and versatile platform on which to perform scalable photonics-based quantum information tasks. Their ability to be electrically driven at room temperature lets us envision the use of III-V semiconductors for a widespread diffusion of quantum technologies.

Acknowledgments: This work has been funded by the Agence Nationale de la Recherche (ANR-14-CE26-0029-01); the Direction Générale de l'Armement (DGA); the French RENATECH; the Institut Universitaire de France. The authors thank A. Orieux for the design of the sample.

Author Contributions: Claire Autebert, Yacine Halioua, Fabien Boitier did the experiments, Giorgio Maltese, Maria Amanti, Carlo Sirtori contributed to the numerical simulations and interpretation, Aristide Lemaitre did the sample growth; Sara Ducci supervised all the stages of the work and wrote the paper.

Conflicts of Interest: The authors declare no conflict of interest.

References

1. Grassani, D.; Azzini, S.; Liscidini, M.; Galli, M.; Strain, M.J.; Sorel, M.; Sipe, J.E.; Bajoni, D. MicRometer-scale integrated silicon source of time-energy entangled photons. *Optica* **2015**, *2*, 88–94. [CrossRef]
2. Matthews, J.C.F.; Politi, A.; Stefanov, A.; O'Brien, J.L. Manipulation of multiphoton entanglement in waveguide quantum circuits. *Nat. Photonics* **2009**, *3*, 346–350. [CrossRef]
3. Spagnolo, N.; Vitelli, C.; Bentivegna, M.; Brod, D.J.; Crespi, A.; Flamini, F.; Giacomini, S.; Milani, G.; Ramponi, R.; Mataloni, P.; et al. Experimental validation of photonic boson sampling. *Nat. Photonics* **2014**, *8*, 615–620. [CrossRef]
4. Spring, J.B.; Metcalf, B.J.; Humphreys, P.C.; Kolthammer, W.S.; Jin, X.M.; Barbieri, M.; Datta, A.; Thomas-Peter, N.; Langford, N.K.; Kundys, D.; et al. Boson sampling on a photonic chip. *Science* **2013**, *339*, 798–799. [CrossRef] [PubMed]
5. Sprengers, J.P.; Gaggero, A.; Sahin, D.; Jahanmirinejad, S.; Frucci, G.; Mattioli, F.; Leoni, R.; Beetz, J.; Lermer, M.; Kamp, M.; et al. Waveguide superconducting single-photon detectors for integrated quantum photonic circuits. *Appl. Phys. Lett.* **2011**, *99*, 181110. [CrossRef]
6. Somaschi, N.; Giesz, V.; de Santis, L.; Loredo, J.C.; Almeida, M.P.; Hornecker, G.; Portalupi, S.L.; Grange, T.; Antón, C.; Demory, J.; et al. Near-optimal single-photon sources in the solid state. *Nat. Photonics* **2016**, *10*, 340–345. [CrossRef]
7. Boitier, F.; Orieux, A.; Autebert, C.; Lemaitre, A.; Galopin, E.; Manquest, C.; Sirtori, C.; Favero, I.; Leo, G.; Ducci, S. Electrically injected photon-pair source at room temperature. *Phys. Rev. Lett.* **2014**, *112*, 183901. [CrossRef] [PubMed]
8. Shoji, I.; Kondo, T.; Ito, R. Second-order nonlinear susceptibilities of various dielectric and semiconductor materials. *Opt. Quantum Electron.* **2002**, *34*, 797–833. [CrossRef]
9. Yeh, P.; Yariv, A. Bragg reflection waveguides. *Opt. Commun.* **1976**, *19*, 427–430. [CrossRef]

10. Helmy, A.; Bijlani, B.; Abolghasem, P. Phase matching in monolithic Bragg reflection waveguides. *Opt. Lett.* **2007**, *32*, 2399–2401. [CrossRef] [PubMed]
11. Rossi, A.D.; Ortiz, V.; Calligaro, M.; Vinter, B.; Nagle, J.; Ducci, S.; Berger, V. A third-order-mode laser diode for quantum communication. *Semicond. Sci. Technol.* **2004**, *19*, L99–L102. [CrossRef]
12. Autebert, C.; Boucher, G.; Boitier, F.; Eckstein, A.; Favero, I.; Leo, G.; Ducci, S. Photon pair sources in algaas: From electrical injection to quantum state engineering. *J. Mod. Opt.* **2015**, *62*, 1739–1745. [CrossRef]
13. Svelto, O.; Hanna, D.C. *Principles of Lasers*, 5th ed.; Springer: Berlin, Gemany, 2012.
14. Ravaro, M.; Guillotel, E.; Le Dû, M.; Manquest, C.; Marcadet, X.; Ducci, S.; Berger, V.; Leo, G. Nonlinear measurement of mid-infrared absorption in AlOx waveguides. *Appl. Phy. Lett.* **2008**, *92*, 151111. [CrossRef]
15. Lumerical Solutions, I. Available online: http://www.lumerical.com/tcad-products/fdtd (accessed on 25 June 2016).
16. Marvin, D.C.; Moss, S.C.; Halle, L.F. Analysis of transient photoluminescence measurements on GaAs and AlGaAs double heterostructures. *J. Appl. Phys.* **1992**, *72*, 1970–1984. [CrossRef]
17. Lanco, L. Sources Semiconductrices de Photons Jumeaux. Ph.D. Thesis, Université Paris Diderot, Paris, France, 2006.
18. Chinone, N.; Kuroda, T.; Ohtoshi, T.; Takahashi, T.; Kajimura, T. Mode-hopping noise in index-guided semiconductor lasers and its reduction by saturable absorbers. *IEEE J. Quantum Electron.* **1985**, *21*, 1264–1270. [CrossRef]
19. Copeland, J. Single-mode stabilization by traps in semiconductor lasers. *IEEE J. Quantum Electron.* **1980**, *16*, 721–727. [CrossRef]
20. Autebert, C.; Lemaître, A.; Ducci, S. Highly efficient parametric down conversion in a monolithic AlGaAs waveguide. 2016, in preparation.
21. Günthner, T.; Pressl, B.; Laiho, K.; Geßler, J.; Höfling, S.; Kamp, M.; Schneider, C.; Weihs, G. Broadband indistinguishability from bright parametric downconversion in a semiconductor waveguide. *J. Opt.* **2015**, *17*, 125201. [CrossRef]
22. Autebert, C.; Bruno, N.; Martin, A.; Lemaitre, A.; Carbonell, C.G.; Favero, I.; Leo, G.; Zbinden, H.; Ducci, S. Integrated algaas source of highly indistinguishable and energy-time entangled photons. *Optica* **2016**, *3*, 143–146. [CrossRef]
23. Horn, R.T.; Kolenderski, P.; Kang, D.; Abolghasem, P.; Scarcella, C.; Della Frera, A.; Tosi, A.; Helt, L.G.; Zhukovsky, S.V.; Sipe, J.E.; et al. Inherent polarization entanglement generated from a monolithic semiconductor chip. *Sci. Rep.* **2013**, *3*, 2314. [CrossRef] [PubMed]
24. Autebert, C.; Trapateau, J.; Orieux, A.; Lemaitre, A.; Carbonell, C.G.; Diamanti, E.; Zaquine, I.; Ducci, S. Multi-User Quantum Key Distribution with Entangled Photons from an AlGaAs Chip. 2016. Available online: http://arxiv.org/abs/1607.01693 (accessed on 6 July 2016).
25. Svozilyk, J.; Hendrych, M.; Helmy, A.S.; Torres, J.P. Generation of paired photons in a quantum separable state in Bragg reflection waveguides. *Opt. Express* **2011**, *19*, 3115–3123. [CrossRef] [PubMed]

Bibliography

[1] Albert Einstein, Boris Podolsky, and Nathan Rosen. Can quantum-mechanical description of physical reality be considered complete? *Physical review*, 47(10):777, 1935. (cited on page 1).

[2] John S Bell. On the einstein podolsky rosen paradox. *Physics Physique Fizika*, 1(3):195, 1964. (cited on page 1).

[3] Alain Aspect, Philippe Grangier, and Gérard Roger. Experimental realization of einstein-podolsky-rosen-bohm gedankenexperiment: a new violation of bell's inequalities. *Physical review letters*, 49(2):91, 1982. (cited on page 1).

[4] ZY Ou and L Mandel. Violation of bell's inequality and classical probability in a two-photon correlation experiment. *Physical Review Letters*, 61(1):50, 1988. (cited on page 1).

[5] Gregor Weihs, Thomas Jennewein, Christoph Simon, Harald Weinfurter, and Anton Zeilinger. Violation of bell's inequality under strict einstein locality conditions. *Physical Review Letters*, 81(23):5039, 1998. (cited on page 1).

[6] Bas Hensen, Hannes Bernien, Anaïs E Dréau, Andreas Reiserer, Norbert Kalb, Machiel S Blok, Just Ruitenberg, Raymond FL Vermeulen, Raymond N Schouten, Carlos Abellán, et al. Loophole-free bell inequality violation using electron spins separated by 1.3 kilometres. *Nature*, 526(7575):682, 2015. (cited on page 1).

[7] Marissa Giustina, Marijn AM Versteegh, Sören Wengerowsky, Johannes Handsteiner, Armin Hochrainer, Kevin Phelan, Fabian Steinlechner, Johannes Kofler, Jan-Åke Larsson, Carlos Abellán, et al. Significant-loophole-free test of bell's theorem with entangled photons. *Physical review letters*, 115(25):250401, 2015. (cited on page 1).

[8] Lynden K Shalm, Evan Meyer-Scott, Bradley G Christensen, Peter Bierhorst, Michael A Wayne, Martin J Stevens, Thomas Gerrits, Scott Glancy, Deny R Hamel, Michael S Allman, et al. Strong loophole-free test of local realism. *Physical review letters*, 115(25):250402, 2015. (cited on page 1).

[9] Jonathan P Dowling and Gerard J Milburn. Quantum technology: the second quantum revolution. *Philosophical Transactions of the Royal Society*

of London. Series A: Mathematical, Physical and Engineering Sciences, 361(1809):1655–1674, 2003. (cited on page 1).

[10] Sheng-Kai Liao, Wen-Qi Cai, Wei-Yue Liu, Liang Zhang, Yang Li, Ji-Gang Ren, Juan Yin, Qi Shen, Yuan Cao, Zheng-Ping Li, et al. Satellite-to-ground quantum key distribution. *Nature*, 549(7670):43, 2017. (cited on page 1).

[11] Sheng-Kai Liao, Wen-Qi Cai, Johannes Handsteiner, Bo Liu, Juan Yin, Liang Zhang, Dominik Rauch, Matthias Fink, Ji-Gang Ren, Wei-Yue Liu, et al. Satellite-relayed intercontinental quantum network. *Physical review letters*, 120(3):030501, 2018. (cited on page 1).

[12] Hartmut Häffner, Christian F Roos, and Rainer Blatt. Quantum computing with trapped ions. *Physics reports*, 469(4):155–203, 2008. (cited on page 1).

[13] Michel H Devoret and Robert J Schoelkopf. Superconducting circuits for quantum information: an outlook. *Science*, 339(6124):1169–1174, 2013. (cited on page 1).

[14] Immanuel Bloch. Ultracold quantum gases in optical lattices. *Nature physics*, 1(1):23, 2005. (cited on page 1).

[15] Jeremy L O'brien, Akira Furusawa, and Jelena Vučković. Photonic quantum technologies. *Nature Photonics*, 3(12):687, 2009. (cited on page 1).

[16] Christian L Degen, F Reinhard, and P Cappellaro. Quantum sensing. *Reviews of modern physics*, 89(3):035002, 2017. (cited on page 1).

[17] Emanuel Knill, Raymond Laflamme, and Gerald J Milburn. A scheme for efficient quantum computation with linear optics. *Nature*, 409(6816):46, 2001. (cited on page 2).

[18] Seth Lloyd. Universal quantum simulators. *Science*, pages 1073–1078, 1996. (cited on page 2).

[19] Alán Aspuru-Guzik and Philip Walther. Photonic quantum simulators. *Nature physics*, 8(4):285, 2012. (cited on page 2).

[20] Alberto Politi, Jonathan CF Matthews, and Jeremy L O'brien. Shor's quantum factoring algorithm on a photonic chip. *Science*, 325(5945):1221–1221, 2009. (cited on pages 2 and 4).

[21] Linda Sansoni, Fabio Sciarrino, Giuseppe Vallone, Paolo Mataloni, Andrea Crespi, Roberta Ramponi, and Roberto Osellame. Two-particle bosonic-fermionic quantum walk via integrated photonics. *Physical review letters*, 108(1):010502, 2012. (cited on pages 2 and 6).

[22] Chris Sparrow, Enrique Martín-López, Nicola Maraviglia, Alex Neville, Christopher Harrold, Jacques Carolan, Yogesh N Joglekar, Toshikazu Hashimoto, Nobuyuki Matsuda, Jeremy L O'Brien, et al. Simulating

the vibrational quantum dynamics of molecules using photonics. *Nature*, 557(7707):660, 2018. (cited on pages 2 and 7).

[23] Adeline Orieux, Marijn AM Versteegh, Klaus D Jöns, and Sara Ducci. Semiconductor devices for entangled photon pair generation: a review. *Reports on Progress in Physics*, 80(7):076001, 2017. (cited on page 2).

[24] Klaus D Jöns, Lucas Schweickert, Marijn AM Versteegh, Dan Dalacu, Philip J Poole, Angelo Gulinatti, Andrea Giudice, Val Zwiller, and Michael E Reimer. Bright nanoscale source of deterministic entangled photon pairs violating bell's inequality. *Scientific reports*, 7(1):1700, 2017. (cited on page 2).

[25] Daniel Huber, Marcus Reindl, Johannes Aberl, Armando Rastelli, and Rinaldo Trotta. Semiconductor quantum dots as an ideal source of polarization-entangled photon pairs on-demand: a review. *Journal of Optics*, 20(7):073002, 2018. (cited on page 2).

[26] Yasuhiro Shirasaki, Geoffrey J Supran, Moungi G Bawendi, and Vladimir Bulović. Emergence of colloidal quantum-dot light-emitting technologies. *Nature photonics*, 7(1):13, 2013. (cited on page 2).

[27] Shih-Wen Feng, Chun-Yuan Cheng, Chen-Yeh Wei, Jen-Hung Yang, Yen-Ru Chen, Ya-Wen Chuang, Yang-Hsiung Fan, and Chih-Sung Chuu. Purification of single photons from room-temperature quantum dots. *Physical review letters*, 119(14):143601, 2017. (cited on page 2).

[28] Xing Lin, Xingliang Dai, Chaodan Pu, Yunzhou Deng, Yuan Niu, Limin Tong, Wei Fang, Yizheng Jin, and Xiaogang Peng. Electrically-driven single-photon sources based on colloidal quantum dots with near-optimal antibunching at room temperature. *Nature communications*, 8(1):1132, 2017. (cited on page 2).

[29] Shu-Jung Yu, Ming-Wei Kang, Huan-Cheng Chang, Kuan-Ming Chen, and Yueh-Chung Yu. Bright fluorescent nanodiamonds: no photobleaching and low cytotoxicity. *Journal of the American Chemical Society*, 127(50):17604–17605, 2005. (cited on page 2).

[30] Benoit Mahler, Piernicola Spinicelli, Stephanie Buil, Xavier Quelin, Jean-Pierre Hermier, and Benoit Dubertret. Towards non-blinking colloidal quantum dots. *Nature materials*, 7(8):659, 2008. (cited on page 3).

[31] Gediminas Juska, Valeria Dimastrodonato, Lorenzo O Mereni, Agnieszka Gocalinska, and Emanuele Pelucchi. Towards quantum-dot arrays of entangled photon emitters. *Nature Photonics*, 7(7):527, 2013. (cited on page 3).

[32] A Dousse, L Lanco, J Suffczyński, E Semenova, A Miard, A Lemaître, I Sagnes, C Roblin, Jacqueline Bloch, and P Senellart. Controlled light-matter coupling for a single quantum dot embedded in a pillar microcavity

using far-field optical lithography. *Physical review letters*, 101(26):267404, 2008. (cited on page 3).

[33] Andreas V Kuhlmann, Julien Houel, Arne Ludwig, Lukas Greuter, Dirk Reuter, Andreas D Wieck, Martino Poggio, and Richard J Warburton. Charge noise and spin noise in a semiconductor quantum device. *Nature Physics*, 9(9):570, 2013. (cited on page 3).

[34] Adrien Dousse, Jan Suffczyński, Alexios Beveratos, Olivier Krebs, Aristide Lemaître, Isabelle Sagnes, Jacqueline Bloch, Paul Voisin, and Pascale Senellart. Ultrabright source of entangled photon pairs. *Nature*, 466(7303):217, 2010. (cited on page 3).

[35] CL Salter, RM Stevenson, I Farrer, CA Nicoll, DA Ritchie, and AJ Shields. An entangled-light-emitting diode. *Nature*, 465(7298):594, 2010. (cited on page 3).

[36] Marta Arcari, Immo Söllner, Alisa Javadi, S Lindskov Hansen, Sahand Mahmoodian, Jin Liu, Henri Thyrrestrup, Eun Hye Lee, Jin Dong Song, Søren Stobbe, et al. Near-unity coupling efficiency of a quantum emitter to a photonic crystal waveguide. *Physical review letters*, 113(9):093603, 2014. (cited on page 3).

[37] Niccolo Somaschi, Valérian Giesz, Lorenzo De Santis, JC Loredo, Marcelo P Almeida, Gaston Hornecker, Simone Luca Portalupi, Thomas Grange, Carlos Antón, Justin Demory, et al. Near-optimal single-photon sources in the solid state. *Nature Photonics*, 10(5):340, 2016. (cited on pages 3 and 5).

[38] David C Burnham and Donald L Weinberg. Observation of simultaneity in parametric production of optical photon pairs. *Physical Review Letters*, 25(2):84, 1970. (cited on page 3).

[39] David S Hum and Martin M Fejer. Quasi-phasematching. *Comptes Rendus Physique*, 8(2):180–198, 2007. (cited on page 3).

[40] P Xu and SN Zhu. Quasi-phase-matching engineering of entangled photons. *AIP Advances*, 2(4):053807, 2012. (cited on page 3).

[41] S Tanzilli, W Tittel, H De Riedmatten, H Zbinden, P Baldi, M DeMicheli, Da B Ostrowsky, and N Gisin. Ppln waveguide for quantum communication. *The European Physical Journal D-Atomic, Molecular, Optical and Plasma Physics*, 18(2):155–160, 2002. (cited on pages 3 and 5).

[42] Junya Ota, Wataru Narita, Ikuma Ohta, Tomonori Matsushita, and Takashi Kondo. Fabrication of periodically-inverted algaas waveguides for quasi-phase-matched wavelength conversion at 1.55 μm. *Japanese Journal of Applied Physics*, 48(4S):04C110, 2009. (cited on page 3).

[43] Pochi Yeh and Amnon Yariv. Bragg reflection waveguides. *Optics Communications*, 19(3):427–430, 1976. (cited on pages 4 and 24).

[44] AS Helmy. Phase matching using bragg reflection waveguides for monolithic nonlinear optics applications. *Optics express*, 14(3):1243–1252, 2006. (cited on pages 4, 5, and 24).

[45] Hiroki Takesue and Kyo Inoue. Generation of polarization-entangled photon pairs and violation of bell's inequality using spontaneous four-wave mixing in a fiber loop. *Physical Review A*, 70(3):031802, 2004. (cited on page 4).

[46] Hiroki Takesue, Hiroshi Fukuda, Tai Tsuchizawa, Toshifumi Watanabe, Koji Yamada, Yasuhiro Tokura, and Sei-ichi Itabashi. Generation of polarization entangled photon pairs using silicon wire waveguide. *Optics express*, 16(8):5721–5727, 2008. (cited on page 4).

[47] LG Helt, Zhenshan Yang, Marco Liscidini, and JE Sipe. Spontaneous four-wave mixing in microring resonators. *Optics letters*, 35(18):3006–3008, 2010. (cited on page 4).

[48] Joshua W Silverstone, Raffaele Santagati, Damien Bonneau, Michael J Strain, Marc Sorel, Jeremy L O'Brien, and Mark G Thompson. Qubit entanglement between ring-resonator photon-pair sources on a silicon chip. *Nature communications*, 6:7948, 2015. (cited on page 4).

[49] Simeon Bogdanov, MY Shalaginov, Alexandra Boltasseva, and Vladimir M Shalaev. Material platforms for integrated quantum photonics. *Optical Materials Express*, 7(1):111–132, 2017. (cited on page 4).

[50] Alberto Politi, Martin J Cryan, John G Rarity, Siyuan Yu, and Jeremy L O'brien. Silica-on-silicon waveguide quantum circuits. *Science*, 320(5876):646–649, 2008. (cited on page 4).

[51] Wolfram HP Pernice, C Schuck, O Minaeva, M Li, GN Goltsman, AV Sergienko, and HX Tang. High-speed and high-efficiency travelling wave single-photon detectors embedded in nanophotonic circuits. *Nature communications*, 3:1325, 2012. (cited on page 4).

[52] Yoshitomo Okawachi, Kasturi Saha, Jacob S Levy, Y Henry Wen, Michal Lipson, and Alexander L Gaeta. Octave-spanning frequency comb generation in a silicon nitride chip. *Optics letters*, 36(17):3398–3400, 2011. (cited on pages 5 and 8).

[53] Yi Xuan, Yang Liu, Leo T Varghese, Andrew J Metcalf, Xiaoxiao Xue, Pei-Hsun Wang, Kyunghun Han, Jose A Jaramillo-Villegas, Abdullah Al Noman, Cong Wang, et al. High-q silicon nitride microresonators exhibiting low-power frequency comb initiation. *Optica*, 3(11):1171–1180, 2016. (cited on pages 5 and 8).

[54] Gong-Ru Lin, Sheng-Pin Su, Chung-Lun Wu, Yung-Hsiang Lin, Bo-Ji Huang, Huai-Yung Wang, Cheng-Ting Tsai, Chih-I Wu, and Yu-Chieh Chi. Si-rich sin x based kerr switch enables optical data conversion up to 12 gbit/s. *Scientific reports*, 5:9611, 2015. (cited on page 5).

[55] Clemens J Krückel, Attila Fülöp, Thomas Klintberg, Jörgen Bengtsson, Peter A Andrekson, et al. Linear and nonlinear characterization of low-stress high-confinement silicon-rich nitride waveguides. *Optics express*, 23(20):25827–25837, 2015. (cited on page 5).

[56] Pascale Senellart, Glenn Solomon, and Andrew White. High-performance semiconductor quantum-dot single-photon sources. *Nature nanotechnology*, 12(11):1026, 2017. (cited on page 5).

[57] Adeline Orieux, Andreas Eckstein, Aristide Lemaître, Pascal Filloux, Ivan Favero, Giuseppe Leo, Thomas Coudreau, Arne Keller, Pérola Milman, and Sara Ducci. Direct bell states generation on a iii-v semiconductor chip at room temperature. *Physical review letters*, 110(16):160502, 2013. (cited on page 5).

[58] Fabien Boitier, Adeline Orieux, Claire Autebert, Aristide Lemaître, Elisabeth Galopin, Christophe Manquest, Carlo Sirtori, Ivan Favero, Giuseppe Leo, and Sara Ducci. Electrically injected photon-pair source at room temperature. *Physical review letters*, 112(18):183901, 2014. (cited on pages 5, 24, 66, 74, and 77).

[59] Claire Autebert, Giorgio Maltese, Yacine Halioua, Fabien Boitier, Aristide Lemaître, Maria Amanti, Carlo Sirtori, and Sara Ducci. Electrically injected twin photon emitting lasers at room temperature. *Technologies*, 4(3):24, 2016. (cited on pages 5, 74, 75, 77, and 81).

[60] Jianwei Wang, Alberto Santamato, Pisu Jiang, Damien Bonneau, Erman Engin, Joshua W Silverstone, Matthias Lermer, Johannes Beetz, Martin Kamp, Sven Höfling, et al. Gallium arsenide (gaas) quantum photonic waveguide circuits. *Optics Communications*, 327:49–55, 2014. (cited on pages 5 and 56).

[61] JP Sprengers, A Gaggero, D Sahin, S Jahanmirinejad, G Frucci, F Mattioli, R Leoni, Johannes Beetz, M Lermer, M Kamp, et al. Waveguide superconducting single-photon detectors for integrated quantum photonic circuits. *Applied Physics Letters*, 99(18):181110, 2011. (cited on page 5).

[62] Sébastien Tanzilli, Hugues De Riedmatten, Wolfgang Tittel, Hugo Zbinden, Pascal Baldi, Marc De Micheli, Daniel Barry Ostrowsky, and Nicolas Gisin. Highly efficient photon-pair source using periodically poled lithium niobate waveguide. *Electronics Letters*, 37(1):26–28, 2001. (cited on pages 5 and 17).

[63] Florian Kaiser, Bruno Fedrici, Alessandro Zavatta, Virginia D'Auria, and Sébastien Tanzilli. A fully guided-wave squeezing experiment for fiber quantum networks. *Optica*, 3(4):362–365, 2016. (cited on page 5).

[64] Franĉcois Mondain, Tommaso Lunghi, Alessandro Zavatta, Élie Gouzien, Florent Doutre, Marc De Micheli, Sébastien Tanzilli, and Virginia D'Auria. Chip-based squeezing at a telecom wavelength. *arXiv preprint arXiv:1811.02097*, 2018. (cited on page 5).

[65] Cheng Wang, Michael J Burek, Zin Lin, Haig A Atikian, Vivek Venkataraman, I-Chun Huang, Peter Stark, and Marko Lončar. Integrated high quality factor lithium niobate microdisk resonators. *Optics express*, 22(25):30924–30933, 2014. (cited on page 5).

[66] Andrea Guarino, Gorazd Poberaj, Daniele Rezzonico, Riccardo Degl'Innocenti, and Peter Günter. Electro–optically tunable microring resonators in lithium niobate. *Nature photonics*, 1(7):407, 2007. (cited on page 5).

[67] Séverine Diziain, Reinhard Geiss, Matthias Zilk, Frank Schrempel, Ernst-Bernhard Kley, Andreas Tünnermann, and Thomas Pertsch. Second harmonic generation in free-standing lithium niobate photonic crystal l3 cavity. *Applied Physics Letters*, 103(5):051117, 2013. (cited on page 5).

[68] Roberto Osellame, Stefano Taccheo, Marco Marangoni, Roberta Ramponi, Paolo Laporta, Dario Polli, Sandro De Silvestri, and Giulio Cerullo. Femtosecond writing of active optical waveguides with astigmatically shaped beams. *JOSA B*, 20(7):1559–1567, 2003. (cited on page 6).

[69] Stefan Nolte, M Will, J Burghoff, and A Tuennermann. Femtosecond waveguide writing: a new avenue to three-dimensional integrated optics. *Applied Physics A*, 77(1):109–111, 2003. (cited on page 6).

[70] Andrea Crespi, Roberto Osellame, Roberta Ramponi, Daniel J Brod, Ernesto F Galvao, Nicolo Spagnolo, Chiara Vitelli, Enrico Maiorino, Paolo Mataloni, and Fabio Sciarrino. Integrated multimode interferometers with arbitrary designs for photonic boson sampling. *Nature Photonics*, 7(7):545, 2013. (cited on page 6).

[71] Andrea Crespi, Roberto Osellame, Roberta Ramponi, Marco Bentivegna, Fulvio Flamini, Nicolò Spagnolo, Niko Viggianiello, Luca Innocenti, Paolo Mataloni, and Fabio Sciarrino. Suppression law of quantum states in a 3d photonic fast fourier transform chip. *Nature communications*, 7:10469, 2016. (cited on page 6).

[72] Jean-Luc Tambasco, Giacomo Corrielli, Robert J Chapman, Andrea Crespi, Oded Zilberberg, Roberto Osellame, and Alberto Peruzzo. Quantum interference of topological states of light. *Science advances*, 4(9):eaat3187, 2018. (cited on pages 6 and 7).

[73] Giacomo Corrielli, Andrea Crespi, Riccardo Geremia, Roberta Ramponi, Linda Sansoni, Andrea Santinelli, Paolo Mataloni, Fabio Sciarrino, and Roberto Osellame. Rotated waveplates in integrated waveguide optics. *Nature communications*, 5:4249, 2014. (cited on page 6).

[74] David Duchesne, Marcello Ferrera, Luca Razzari, Roberto Morandotti, Brent Little, Sai T Chu, and David J Moss. Hydex glass: a cmos compatible platform for integrated waveguide structures for nonlinear optics. *arXiv preprint arXiv:1505.05953*, 2015. (cited on page 6).

[75] David Duchesne, Marcello Ferrera, Luca Razzari, Roberto Morandotti, Brent E Little, Sai T Chu, and David J Moss. Efficient self-phase modulation in low loss, high index doped silica glass integrated waveguides. *Optics Express*, 17(3):1865–1870, 2009. (cited on page 6).

[76] Christian Reimer, Michael Kues, Piotr Roztocki, Benjamin Wetzel, Fabio Grazioso, Brent E Little, Sai T Chu, Tudor Johnston, Yaron Bromberg, Lucia Caspani, et al. Generation of multiphoton entangled quantum states by means of integrated frequency combs. *Science*, 351(6278):1176–1180, 2016. (cited on pages 6 and 8).

[77] Michael Kues, Christian Reimer, Piotr Roztocki, Luis Romero Cortés, Stefania Sciara, Benjamin Wetzel, Yanbing Zhang, Alfonso Cino, Sai T Chu, Brent E Little, et al. On-chip generation of high-dimensional entangled quantum states and their coherent control. *Nature*, 546(7660):622, 2017. (cited on pages 6, 8, and 103).

[78] Alessia Pasquazi, Marco Peccianti, Yongwoo Park, Brent E Little, Sai T Chu, Roberto Morandotti, José Azaña, and David J Moss. Sub-picosecond phase-sensitive optical pulse characterization on a chip. *Nature Photonics*, 5(10):618, 2011. (cited on page 6).

[79] Patrik Rath, Sandeep Ummethala, Christoph Nebel, and Wolfram HP Pernice. Diamond as a material for monolithically integrated optical and optomechanical devices. *physica status solidi (a)*, 212(11):2385–2399, 2015. (cited on page 6).

[80] P Rath, N Gruhler, S Khasminskaya, C Nebel, C Wild, and WHP Pernice. Waferscale nanophotonic circuits made from diamond-on-insulator substrates. *Optics express*, 21(9):11031–11036, 2013. (cited on page 6).

[81] Kae Nemoto, Michael Trupke, Simon J Devitt, Ashley M Stephens, Burkhard Scharfenberger, Kathrin Buczak, Tobias Nöbauer, Mark S Everitt, Jörg Schmiedmayer, and William J Munro. Photonic architecture for scalable quantum information processing in diamond. *Physical Review X*, 4(3):031022, 2014. (cited on page 6).

[82] Birgit JM Hausmann, Brendan Shields, Qimin Quan, Patrick Maletinsky, Murray McCutcheon, Jennifer T Choy, Tom M Babinec, Alexander Kubanek, Amir Yacoby, Mikhail D Lukin, et al. Integrated diamond networks for quantum nanophotonics. *Nano letters*, 12(3):1578–1582, 2012. (cited on page 6).

[83] KD Jahnke, B Naydenov, T Teraji, S Koizumi, T Umeda, J Isoya, and Fedor Jelezko. Long coherence time of spin qubits in 12c enriched polycrystalline chemical vapor deposition diamond. *Applied physics letters*, 101(1):012405, 2012. (cited on page 6).

[84] Fulvio Flamini, Nicolò Spagnolo, and Fabio Sciarrino. Photonic quantum information processing: a review. *Reports on Progress in Physics*, 82(1):016001, 2018. (cited on page 6).

[85] Andrea Crespi, Roberta Ramponi, Roberto Osellame, Linda Sansoni, Irene Bongioanni, Fabio Sciarrino, Giuseppe Vallone, and Paolo Mataloni. Integrated photonic quantum gates for polarization qubits. *Nature communications*, 2:566, 2011. (cited on page 6).

[86] Philip Walther, Kevin J Resch, Terry Rudolph, Emmanuel Schenck, Harald Weinfurter, Vlatko Vedral, Markus Aspelmeyer, and Anton Zeilinger. Experimental one-way quantum computing. *Nature*, 434(7030):169, 2005. (cited on page 6).

[87] Mario Arnolfo Ciampini, Adeline Orieux, Stefano Paesani, Fabio Sciarrino, Giacomo Corrielli, Andrea Crespi, Roberta Ramponi, Roberto Osellame, and Paolo Mataloni. Path-polarization hyperentangled and cluster states of photons on a chip. *Light: Science & Applications*, 5(4):e16064, 2016. (cited on page 6).

[88] Yoon-Ho Kim, Sergei P Kulik, and Yanhua Shih. Quantum teleportation of a polarization state with a complete bell state measurement. *Physical Review Letters*, 86(7):1370, 2001. (cited on page 6).

[89] Darius Bunandar, Anthony Lentine, Catherine Lee, Hong Cai, Christopher M Long, Nicholas Boynton, Nicholas Martinez, Christopher DeRose, Changchen Chen, Matthew Grein, et al. Metropolitan quantum key distribution with silicon photonics. *Physical Review X*, 8(2):021009, 2018. (cited on page 6).

[90] Charles H Bennett and Gilles Brassard. Quantum cryptography: public key distribution and coin tossing. *Theor. Comput. Sci.*, 560(12):7–11, 2014. (cited on page 6).

[91] Mhlambululi Mafu, Angela Dudley, Sandeep Goyal, Daniel Giovannini, Melanie McLaren, Miles J Padgett, Thomas Konrad, Francesco Petruccione, Norbert Lütkenhaus, and Andrew Forbes. Higher-dimensional orbital-angular-momentum-based quantum key distribution with mutually unbiased bases. *Physical Review A*, 88(3):032305, 2013. (cited on page 7).

[92] Julio T Barreiro, Tzu-Chieh Wei, and Paul G Kwiat. Beating the channel capacity limit for linear photonic superdense coding. *Nature physics*, 4(4):282, 2008. (cited on page 7).

[93] Xi-Lin Wang, Xin-Dong Cai, Zu-En Su, Ming-Cheng Chen, Dian Wu, Li Li, Nai-Le Liu, Chao-Yang Lu, and Jian-Wei Pan. Quantum teleportation of multiple degrees of freedom of a single photon. *Nature*, 518(7540):516, 2015. (cited on page 7).

[94] Dong-Sheng Ding, Zhi-Yuan Zhou, Bao-Sen Shi, and Guang-Can Guo. Single-photon-level quantum image memory based on cold atomic ensembles. *Nature communications*, 4:2527, 2013. (cited on page 7).

[95] Jianwei Wang, Stefano Paesani, Yunhong Ding, Raffaele Santagati, Paul Skrzypczyk, Alexia Salavrakos, Jordi Tura, Remigiusz Augusiak, Laura Mančinska, Davide Bacco, et al. Multidimensional quantum entanglement with large-scale integrated optics. *Science*, 360(6386):285–291, 2018. (cited on page 7).

[96] Alberto Boaron, Gianluca Boso, Davide Rusca, Cédric Vulliez, Claire Autebert, Misael Caloz, Matthieu Perrenoud, Gaëtan Gras, Félix Bussières, Ming-Jun Li, et al. Secure quantum key distribution over 421 km of optical fiber. *Physical review letters*, 121(19):190502, 2018. (cited on page 7).

[97] Mustafa Gündoğan, Patrick M Ledingham, Kutlu Kutluer, Margherita Mazzera, and Hugues De Riedmatten. Solid state spin-wave quantum memory for time-bin qubits. *Physical review letters*, 114(23):230501, 2015. (cited on page 7).

[98] Laurent Olislager, Johann Cussey, Anh Tuan Nguyen, Philippe Emplit, Serge Massar, J-M Merolla, and K Phan Huy. Frequency-bin entangled photons. *Physical Review A*, 82(1):013804, 2010. (cited on pages 7 and 8).

[99] Peter C Humphreys, Benjamin J Metcalf, Justin B Spring, Merritt Moore, Xian-Min Jin, Marco Barbieri, W Steven Kolthammer, and Ian A Walmsley. Linear optical quantum computing in a single spatial mode. *Physical review letters*, 111(15):150501, 2013. (cited on page 8).

[100] Johann Cussey, Frédéric Patois, Nicolas Pelloquin, and Jean-Marc Merolla. High frequency spectral domain qkd architecture with dispersion management for wdm network. In *Optical Fiber Communication Conference*, page OWJ3. Optical Society of America, 2008. (cited on page 8).

[101] YJ Lu, RL Campbell, and ZY Ou. Mode-locked two-photon states. *Physical review letters*, 91(16):163602, 2003. (cited on pages 8, 100, 107, 113, 127, and 128).

[102] Zhenda Xie, Tian Zhong, Sajan Shrestha, XinAn Xu, Junlin Liang, Yan-Xiao Gong, Joshua C Bienfang, Alessandro Restelli, Jeffrey H Shapiro, Franco NC

Wong, et al. Harnessing high-dimensional hyperentanglement through a biphoton frequency comb. *Nature Photonics*, 9(8):536, 2015. (cited on page 8).

[103] Rui-Bo Jin, Ryosuke Shimizu, Mikio Fujiwara, Masahiro Takeoka, Ryota Wakabayashi, Taro Yamashita, Shigehito Miki, Hirotaka Terai, Thomas Gerrits, and Masahide Sasaki. Simple method of generating and distributing frequency-entangled qudits. *Quantum Science and Technology*, 1(1):015004, 2016. (cited on page 8).

[104] Poolad Imany, Jose A Jaramillo-Villegas, Ogaga D Odele, Kyunghun Han, Daniel E Leaird, Joseph M Lukens, Pavel Lougovski, Minghao Qi, and Andrew M Weiner. 50-ghz-spaced comb of high-dimensional frequency-bin entangled photons from an on-chip silicon nitride microresonator. *Optics express*, 26(2):1825–1840, 2018. (cited on page 8).

[105] Roberto Osellame. Optical physics: A larger quantum alphabet. *Nature*, 546(7660):602, 2017. (cited on pages 9 and 105).

[106] Irfan Ali-Khan, Curtis J Broadbent, and John C Howell. Large-alphabet quantum key distribution using energy-time entangled bipartite states. *Physical review letters*, 98(6):060503, 2007. (cited on page 9).

[107] Michael Kues, Christian Reimer, Joseph M Lukens, William J Munro, Andrew M Weiner, David J Moss, and Roberto Morandotti. Quantum optical microcombs. *Nature Photonics*, 13(3):170, 2019. (cited on page 9).

[108] Joseph M Lukens and Pavel Lougovski. Frequency-encoded photonic qubits for scalable quantum information processing. *Optica*, 4(1):8–16, 2017. (cited on page 9).

[109] Hsuan-Hao Lu, Joseph M Lukens, Nicholas A Peters, Ogaga D Odele, Daniel E Leaird, Andrew M Weiner, and Pavel Lougovski. Electro-optic frequency beam splitters and tritters for high-fidelity photonic quantum information processing. *Physical review letters*, 120(3):030502, 2018. (cited on page 9).

[110] Christian Reimer, Stefania Sciara, Piotr Roztocki, Mehedi Islam, Luis Romero Cortés, Yanbing Zhang, Bennet Fischer, Sébastien Loranger, Raman Kashyap, Alfonso Cino, et al. High-dimensional one-way quantum processing implemented on d-level cluster states. *Nature Physics*, page 1, 2018. (cited on page 9).

[111] Daniel Gottesman, Alexei Kitaev, and John Preskill. Encoding a qubit in an oscillator. *Physical Review A*, 64(1):012310, 2001. (cited on page 9).

[112] Pochi Yeh. *Optical waves in layered media*, volume 61. Wiley-Interscience, 2005. (cited on pages 12 and 13).

[113] Arthur L Schawlow and Charles H Townes. Infrared and optical masers. *Physical Review*, 112(6):1940, 1958. (cited on page 13).

[114] Robert W Boyd. *Nonlinear optics*. Elsevier, 2003. (cited on pages 13 and 35).

[115] Christophe Couteau. Spontaneous parametric down-conversion. *Contemporary Physics*, 59(3):291–304, 2018. (cited on page 13).

[116] Lukas G Helt, Marco Liscidini, and John E Sipe. How does it scale? comparing quantum and classical nonlinear optical processes in integrated devices. *JOSA B*, 29(8):2199–2212, 2012. (cited on pages 14 and 30).

[117] Marco Liscidini and JE Sipe. Stimulated emission tomography. *Physical review letters*, 111(19):193602, 2013. (cited on pages 14 and 101).

[118] Frank Träger. *Springer handbook of lasers and optics*. Springer Science & Business Media, 2012. (cited on page 14).

[119] JM Manley and HE Rowe. Some general properties of nonlinear elements-part i. general energy relations. *Proceedings of the IRE*, 44(7):904–913, 1956. (cited on page 16).

[120] S Roux, P Barritault, O Lartigue, Laurent Cerutti, Eric Tournié, B Gérard, and A Grisard. Mid-infrared characterization of refractive indices and propagation losses in gasb/alxga1- xassb waveguides. *Applied Physics Letters*, 107(17):171901, 2015. (cited on page 17).

[121] Junbo Han, Payam Abolghasem, Bhavin J Bijlani, and Amr S Helmy. Continuous-wave sum-frequency generation in algaas bragg reflection waveguides. *Optics letters*, 34(23):3656–3658, 2009. (cited on page 18).

[122] Bhavin J Bijlani and Amr S Helmy. Bragg reflection waveguide diode lasers. *Optics letters*, 34(23):3734–3736, 2009. (cited on page 18).

[123] Jiří Svozilík, Martin Hendrych, Amr S Helmy, and Juan P Torres. Generation of paired photons in a quantum separable state in bragg reflection waveguides. *Optics express*, 19(4):3115–3123, 2011. (cited on page 18).

[124] Cyril Hilsum and Alistair Christopher Rose-Innes. *Semiconducting III–V Compounds: International Series of Monographs on Semiconductors*, volume 1. Elsevier, 2014. (cited on page 18).

[125] GA Wolff and JD Broder. Microcleavage, bonding character and surface structure in materials with tetrahedral coordination. *Acta Crystallographica*, 12(4):313–323, 1959. (cited on page 18).

[126] Amnon Yariv and Pochi Yeh. Photonics, 2007. (cited on page 19).

[127] Ichiro Shoji, Takashi Kondo, Ayako Kitamoto, Masayuki Shirane, and Ryoichi Ito. Absolute scale of second-order nonlinear-optical coefficients. *JOSA B*, 14(9):2268–2294, 1997. (cited on page 19).

[128] Jasprit Singh. *Semiconductor devices: basic principles*. John Wiley & Sons, 2007. (cited on pages 19 and 20).

[129] Martin A Afromowitz. Refractive index of ga1- xalxas. *Solid State Communications*, 15(1):59–63, 1974. (cited on pages 19 and 20).

[130] S Gehrsitz, FK Reinhart, C Gourgon, N Herres, A Vonlanthen, and H Sigg. The refractive index of al x ga 1- x as below the band gap: accurate determination and empirical modeling. *Journal of Applied Physics*, 87(11):7825–7837, 2000. (cited on pages 21 and 27).

[131] NM Ravindra, Preethi Ganapathy, and Jinsoo Choi. Energy gap–refractive index relations in semiconductors–an overview. *Infrared physics & technology*, 50(1):21–29, 2007. (cited on page 21).

[132] Robert C Miller. Optical second harmonic generation in piezoelectric crystals. *Applied Physics Letters*, 5(1):17–19, 1964. (cited on page 21).

[133] M Ohashi, T Kondo, R Ito, S Fukatsu, Y Shiraki, K Kumata, and SS Kano. Determination of quadratic nonlinear optical coefficient of al x ga1- x as system by the method of reflected second harmonics. *Journal of applied physics*, 74(1):596–601, 1993. (cited on pages 21 and 28).

[134] Adeline Orieux, Xavier Caillet, Aristide Lemaître, Pascal Filloux, Ivan Favero, Giuseppe Leo, and Sara Ducci. Efficient parametric generation of counterpropagating two-photon states. *JOSA B*, 28(1):45–51, 2011. (cited on page 21).

[135] Xavier Caillet. *Une microcavité semiconductrice source de photons jumeaux contrapropageants à température ambiante*. PhD thesis, Paris 7, 2009. (cited on page 21).

[136] S Ducci, L Lanco, V Berger, A De Rossi, V Ortiz, and M Calligaro. Continuous-wave second-harmonic generation in modal phase matched semiconductor waveguides. *Applied physics letters*, 84(16):2974–2976, 2004. (cited on page 24).

[137] K Moutzouris, S Venugopal Rao, M Ebrahimzadeh, A De Rossi, M Calligaro, V Ortiz, and V Berger. Second-harmonic generation through optimized modal phase matching in semiconductor waveguides. *Applied physics letters*, 83(4):620–622, 2003. (cited on page 24).

[138] Pochi Yeh, Amnon Yariv, and Chi-Shain Hong. Electromagnetic propagation in periodic stratified media. i. general theory. *JOSA*, 67(4):423–438, 1977. (cited on page 24).

[139] Brian R West and Amr S Helmy. Properties of the quarter-wave bragg reflection waveguide: theory. *JOSA B*, 23(6):1207–1220, 2006. (cited on page 24).

[140] Claire Autebert, Natalia Bruno, Anthony Martin, Aristide Lemaitre, Carmen Gomez Carbonell, Ivan Favero, Giuseppe Leo, Hugo Zbinden, and Sara Ducci. Integrated algaas source of highly indistinguishable and energy-time entangled photons. *Optica*, 3(2):143–146, 2016. (cited on page 24).

[141] CJR Sheppard. Approximate calculation of the reflection coefficient from a stratified medium. *Pure and Applied Optics: Journal of the European Optical Society Part A*, 4(5):665, 1995. (cited on page 25).

[142] Braxton Osting. Bragg structure and the first spectral gap. *Applied Mathematics Letters*, 25(11):1926–1930, 2012. (cited on page 25).

[143] Adeline Orieux. *Sources semiconductrices d'états à deux photons à température ambiante*. PhD thesis, Université Paris-Diderot-Paris VII, 2012. (cited on pages 25, 28, and 61).

[144] Nima Zareian, Payam Abolghasem, and Amr S Helmy. Far field of bragg reflection waveguides: characteristics and closed-form approximation. *Journal of Lightwave Technology*, 29(5):728–735, 2011. (cited on pages 28 and 59).

[145] Yannick Seurin. Etude d'un nouveau dispositif semiconducteur pour les telecommunications quantiques, 2005. (cited on page 28).

[146] Zhenshan Yang, Marco Liscidini, and JE Sipe. Spontaneous parametric down-conversion in waveguides: a backward heisenberg picture approach. *Physical Review A*, 77(3):033808, 2008. (cited on pages 30 and 32).

[147] Yoav Peleg, Reuven Pnini, Elyahu Zaarur, and Loretta Johnson. *Quantum mechanics: based on Schaum's outline of theory and problems of quantum mechanics*. Schaum's Outlines, 2006. (cited on page 30).

[148] JR Ackerhalt and K Rzażewski. Heisenberg-picture operator perturbation theory. *Physical Review A*, 12(6):2549, 1975. (cited on page 31).

[149] R Ghosh, CK Hong, ZY Ou, and L Mandel. Interference of two photons in parametric down conversion. *Physical Review A*, 34(5):3962, 1986. (cited on page 31).

[150] ZY Ou, LJ Wang, and L Mandel. Vacuum effects on interference in two-photon down conversion. *Physical Review A*, 40(3):1428, 1989. (cited on page 31).

[151] Guillaume Boucher. *Biphoton Frequency-Correlations Engineering and Measurement with a Semiconductor Microcavity*. PhD thesis, Sorbonne Paris Cité; Université paris diderot, 2016. (cited on pages 31 and 101).

[152] Gilbert Grynberg, Alain Aspect, and Claude Fabre. *Introduction to quantum optics: from the semi-classical approach to quantized light*. Cambridge university press, 2010. (cited on page 31).

[153] Chong-Ki Hong, Zhe-Yu Ou, and Leonard Mandel. Measurement of subpicosecond time intervals between two photons by interference. *Physical review letters*, 59(18):2044, 1987. (cited on page 35).

[154] Richard Phillips Feynman. Space-time approach to quantum electrodynamics. *Physical Review*, 76(6):769, 1949. (cited on page 35).

[155] Richard P Feynman, Albert R Hibbs, and Daniel F Styer. *Quantum mechanics and path integrals*. Courier Corporation, 2010. (cited on page 35).

[156] CH Holbrow, Enrique Galvez, and ME Parks. Photon quantum mechanics and beam splitters. *American Journal of Physics*, 70(3):260–265, 2002. (cited on page 36).

[157] John Howell. Beam splitter input-output relations, June 2018. `http://www.pas.rochester.edu/~howell/mysite2/Tutorials/Beamsplitter2.pdf`. (cited on pages 36 and 115).

[158] G Weihs and A Zeilinger. Photon statistics at beam splitters: an essential tool in quantum information and teleportation, June 2018. `http://copilot.caltech.edu/documents/278-weihs_zeillinger_photon_statistics_at_beamsplitters_qip.pdf`. (cited on pages 38, 115, 119, and 127).

[159] Kaige Wang. Quantum theory of two-photon wavepacket interference in a beamsplitter. *Journal of Physics B: Atomic, Molecular and Optical Physics*, 39(18):R293, 2006. (cited on pages 38 and 127).

[160] Claire Autebert, Julien Trapateau, Adeline Orieux, Aristide Lemaître, Carmen Gomez-Carbonell, Eleni Diamanti, Isabelle Zaquine, and Sara Ducci. Multi-user quantum key distribution with entangled photons from an algaas chip. *Quantum Science and Technology*, 1(1):01LT02, 2016. (cited on pages 40, 66, and 109).

[161] Hyunseok Jeong and Timothy C Ralph. Schrodinger cat states for quantum information processing. *arXiv preprint quant-ph/0509137*, 2005. (cited on page 40).

[162] ZY Ou and L Mandel. Observation of spatial quantum beating with separated photodetectors. *Physical review letters*, 61(1):54, 1988. (cited on pages 50 and 52).

[163] V Bužek, H Moya-Cessa, PL Knight, and SJD Phoenix. Schrödinger-cat states in the resonant jaynes-cummings model: Collapse and revival of oscillations of the photon-number distribution. *Physical review A*, 45(11):8190, 1992. (cited on page 52).

[164] Gary Taubes. Schizophrenic atom doubles as schrödinger's cat–or kitten. *Science*, 272(5265):1101, 1996. (cited on page 52).

[165] Alexei Ourjoumtsev, Hyunseok Jeong, Rosa Tualle-Brouri, and Philippe Grangier. Generation of optical 'schrödinger cats' from photon number states. *Nature*, 448(7155):784, 2007. (cited on page 52).

[166] Alexei Gilchrist, Kae Nemoto, William J Munro, Timothy C Ralph, Scott Glancy, Samuel L Braunstein, and Gerard J Milburn. Schrödinger cats and their power for quantum information processing. *Journal of Optics B: Quantum and Semiclassical Optics*, 6(8):S828, 2004. (cited on page 52).

[167] H Chen, K Laiho, B Pressl, A Schlager, H Suchomel, M Kamp, S Höfling, C Schneider, and G Weihs. Optimizing the spectro-temporal properties of photon pairs from bragg-reflection waveguides. *arXiv preprint arXiv:1809.03167*, 2018. (cited on page 56).

[168] Peyman Sarrafi, Eric Y Zhu, Ksenia Dolgaleva, Barry M Holmes, David C Hutchings, J Stewart Aitchison, and Li Qian. Continuous-wave quasi-phase-matched waveguide correlated photon pair source on a iii–v chip. *Applied Physics Letters*, 103(25):251115, 2013. (cited on page 63).

[169] Claire Autebert. *AlGaAs photonic devices: from quantum state generation to quantum communications*. PhD thesis, Université Paris 7-Denis Diderot, 2016. (cited on pages 66 and 71).

[170] Prosenjit Rai-Choudhury. *Handbook of microlithography, micromachining, and microfabrication: microlithography*, volume 1. Iet, 1997. (cited on page 68).

[171] David J Grant and Siva Sivoththaman. Electron-beam lithography: From past to present. *University of Waterloo, Canada*, 2003. (cited on page 68).

[172] TR Groves. Electron beam lithography. In *Nanolithography*, pages 80–115. Elsevier, 2014. (cited on page 69).

[173] Micro resist technology. Ma-N 2400 — Negative Tone Photoresist Series. `http://www.microchem.com/`, 2018. Online; accessed 10 Dec 2018. (cited on page 70).

[174] Justin R Bickford. Automatic stripe analysis tool. Technical report, Army Research Laboratory's Sensors and Electron Devices Directorate, 2013. (cited on page 73).

[175] Bickford, Justin R. Analyze Stripes ImageJ plugin. `http://imagejdocu.tudor.lu/doku.php?id=macro:analyze_stripes`, 2013. Online; accessed 03 Dec 2018. (cited on page 73).

[176] Emmanuel Rosencher and Borge Vinter. *Optoelectronics*. Cambridge University Press, 2002. (cited on page 75).

[177] Orazio Svelto and David C Hanna. *Principles of lasers*, volume 4. Springer, 1998. (cited on page 81).

[178] P.K. Tien. Light waves in thin films and integrated optics. *Applied optics*, 10(11):2395–2413, 1971. (cited on page 82).

[179] RJ Deri, E Kapon, and LM Schiavone. Scattering in low-loss gaas/algaas rib waveguides. *Applied physics letters*, 51(11):789–791, 1987. (cited on page 82).

[180] R Regener and W Sohler. Loss in low-finesse ti: Linbo 3 optical waveguide resonators. *Applied Physics B*, 36(3):143–147, 1985. (cited on page 86).

[181] Alfredo De Rossi, Valentin Ortiz, Michel Calligaro, Loïc Lanco, Sara Ducci, Vincent Berger, and Isabelle Sagnes. Measuring propagation loss in a multimode semiconductor waveguide. *Journal of applied physics*, 97(7):073105, 2005. (cited on pages 86 and 176).

[182] Sadao Adachi. Optical dispersion relations for gap, gaas, gasb, inp, inas, insb, al x ga1- x as, and in1- x ga x as y p1- y. *Journal of Applied Physics*, 66(12):6030–6040, 1989. (cited on page 88).

[183] Luis L Sánchez-Soto, Juan J Monzón, and Gerd Leuchs. The many facets of the fabry–perot. *European Journal of Physics*, 37(6):064001, 2016. (cited on page 89).

[184] Yasser Jeronimo-Moreno, Saul Rodriguez-Benavides, and Alfred B U'Ren. Theory of cavity-enhanced spontaneous parametric downconversion. *Laser physics*, 20(5):1221–1233, 2010. (cited on pages 89 and 93).

[185] Nur Ismail, Cristine Calil Kores, Dimitri Geskus, and Markus Pollnau. Fabry-pérot resonator: spectral line shapes, generic and related airy distributions, linewidths, finesses, and performance at low or frequency-dependent reflectivity. *Optics express*, 24(15):16366–16389, 2016. (cited on page 91).

[186] Giorgio Maltese. Two-photon cavity function versus birefringence animated plot. `https://github.com/giomalt/thesis_public_media/blob/master/birefringence_cavity_function.gif?raw=true`, 2019. (cited on page 96).

[187] C Olindo, MA Sagioro, CH Monken, S Pádua, and A Delgado. Hong-ou-mandel interferometer with cavities: theory. *Physical Review A*, 73(4):043806, 2006. (cited on pages 100 and 131).

[188] Andreas Eckstein, Guillaume Boucher, Aristide Lemaître, Pascal Filloux, Ivan Favero, Giuseppe Leo, John E Sipe, Marco Liscidini, and Sara Ducci. High-resolution spectral characterization of two photon states via classical measurements. *Laser & Photonics Reviews*, 8(5):L76–L80, 2014. (cited on page 101).

[189] Lana Sheridan and Valerio Scarani. Security proof for quantum key distribution using qudit systems. *Physical Review A*, 82(3):030301, 2010. (cited on page 105).

[190] HF Chau, Cardythy Wong, Qinan Wang, and Tieqiao Huang. Qudit-based measurement-device-independent quantum key distribution using linear optics. *arXiv preprint arXiv:1608.08329*, 2016. (cited on page 105).

[191] J Nunn, LJ Wright, C Söller, L Zhang, IA Walmsley, and BJ Smith. Large-alphabet time-frequency entangled quantum key distribution by means of time-to-frequency conversion. *Optics express*, 21(13):15959–15973, 2013. (cited on pages 105 and 106).

[192] Fu-Guo Deng, Bao-Cang Ren, and Xi-Han Li. Quantum hyperentanglement and its applications in quantum information processing. *Science bulletin*, 62(1):46–68, 2017. (cited on page 107).

[193] SP Walborn, AN De Oliveira, S Pádua, and CH Monken. Multimode hong-ou-mandel interference. *Physical review letters*, 90(14):143601, 2003. (cited on pages 107 and 115).

[194] Yingwen Zhang, Filippus S Roux, Thomas Konrad, Megan Agnew, Jonathan Leach, and Andrew Forbes. Engineering two-photon high-dimensional states through quantum interference. *Science advances*, 2(2):e1501165, 2016. (cited on page 107).

[195] Marlan O Scully and M Suhail Zubairy. Quantum optics, 1999. (cited on page 117).

[196] Thomas Gerrits, Francesco Marsili, Varun B Verma, Lynden K Shalm, Matthew Shaw, RP Mirin, and Sae Woo Nam. Spectral correlation measurements at the hong-ou-mandel interference dip. *Physical Review A*, 91(1):013830, 2015. (cited on page 127).

[197] Jeremy L O'brien. Optical quantum computing. *Science*, 318(5856):1567–1570, 2007. (cited on page 130).

[198] Stefan Ataman. The quantum optical description of a fabry-perot interferometer and the prediction of an antibunching effect. *The European Physical Journal D*, 69(7):187, 2015. (cited on page 131).

[199] MA Sagioro, C Olindo, CH Monken, and S Pádua. Time control of two-photon interference. *Physical Review A*, 69(5):053817, 2004. (cited on page 131).

[200] Rodney Loudon. *The quantum theory of light*. OUP Oxford, 2000. (cited on page 131).

[201] Zhe-Yu Jeff Ou. *Multi-photon quantum interference*, volume 43. Springer, 2007. (cited on page 131).

[202] P. Ben Dixon, Jeffrey H. Shapiro, and Franco N. C. Wong. Spectral engineering by gaussian phase-matching for quantum photonics. *Opt. Express*, 21(5):5879–5890, Mar 2013. (cited on page 131).

[203] AM Steinberg, PG Kwiat, and RY Chiao. Dispersion cancellation in a measurement of the single-photon propagation velocity in glass. *Physical review letters*, 68(16):2421, 1992. (cited on page 147).

[204] Aephraim M Steinberg, Paul G Kwiat, and Raymond Y Chiao. Measurement of the single-photon tunneling time. *Physical Review Letters*, 71(5):708, 1993. (cited on page 147).

[205] Reinhard Erdmann, David Branning, Warren Grice, and Ian A Walmsley. Restoring dispersion cancellation for entangled photons produced by ultrashort pulses. *Physical Review A*, 62(5):053810, 2000. (cited on page 147).

[206] Marco Barbieri, Emanuele Roccia, Luca Mancino, Marco Sbroscia, Ilaria Gianani, and Fabio Sciarrino. What hong-ou-mandel interference says on two-photon frequency entanglement. *Scientific reports*, 7(1):7247, 2017. (cited on page 152).

[207] Zeudi Mazzotta, Simone Cialdi, Daniele Cipriani, Stefano Olivares, and Matteo GA Paris. High-order dispersion effects in two-photon interference. *Physical Review A*, 94(6):063842, 2016. (cited on page 156).

[208] Johannes Kepler. *De Cometis Libelli Tres*. Avgvstae Vindelicorvm, A. Apergeri, 1619. (cited on page 159).

[209] P. Lebedew. Untersuchungen über die Druckkräfte des Lichtes. *Annalen der Physik*, 311:433–458, 1901. (cited on page 159).

[210] Joseph W Simmons and Mark J Guttmann. States, waves, and photons: A modern introduction to light. *States, waves, and photons: A modern introduction to light., by Simmons, JW; Guttmann, MJ. Reading, MA (USA): Addison-Wesley, 279 p.*, 1970. (cited on page 159).

[211] Wikimedia Commons, E. Karimi. Angular momentum interaction. `https://commons.wikimedia.org/wiki/File:Sam-oam-interaction.png`, 2019. Online; accessed 18 Feb 2018. (cited on page 160).

[212] F. J. Belinfante. On the current and the density of the electric charge, the energy, the linear momentum and the angular momentum of arbitrary fields. *Physica*, 7:449–474, May 1940. (cited on page 160).

[213] Konstantin Y Bliokh, Aleksandr Y Bekshaev, and Franco Nori. Dual electromagnetism: helicity, spin, momentum and angular momentum. *New Journal of Physics*, 15(3):033026, 2013. (cited on page 160).

[214] Les Allen, Marco W Beijersbergen, RJC Spreeuw, and JP Woerdman. Orbital angular momentum of light and the transformation of laguerre-gaussian laser modes. *Physical Review A*, 45(11):8185, 1992. (cited on pages 161, 164, and 181).

[215] Andri M. Gretarsson. Basic paraxial optics toolkit. `https://fr.mathworks.com/matlabcentral/fileexchange/15459-basic-paraxial-optics-toolkit`, 2019. Online; accessed 30 Jan 2019. (cited on page 161).

[216] Halina Rubinsztein-Dunlop, Andrew Forbes, Michael V Berry, Mark R Dennis, David L Andrews, Masud Mansuripur, Cornelia Denz, Christina Alpmann, Peter Banzer, Thomas Bauer, et al. Roadmap on structured light. *Journal of Optics*, 19(1):013001, 2016. (cited on page 164).

[217] Xuewen Wang, Zhongquan Nie, Yao Liang, Jian Wang, Tao Li, and Baohua Jia. Recent advances on optical vortex generation. *Nanophotonics*, 7(9):1533–1556, 2018. (cited on page 164).

[218] MW Beijersbergen, RPC Coerwinkel, M Kristensen, and JP Woerdman. Helical-wavefront laser beams produced with a spiral phaseplate. *Optics Communications*, 112(5-6):321–327, 1994. (cited on page 164).

[219] V Yu Bazhenov, MV Vasnetsov, and MS Soskin. *Laser beams with screw dislocations in their wavefronts*. PhD thesis, 1990. (cited on page 164).

[220] NR Heckenberg, R McDuff, CP Smith, and AG White. Generation of optical phase singularities by computer-generated holograms. *Optics letters*, 17(3):221–223, 1992. (cited on page 164).

[221] Lorenzo Marrucci, C Manzo, and D Paparo. Optical spin-to-orbital angular momentum conversion in inhomogeneous anisotropic media. *Physical review letters*, 96(16):163905, 2006. (cited on page 164).

[222] Hugo Larocque, Jérémie Gagnon-Bischoff, Frédéric Bouchard, Robert Fickler, Jeremy Upham, Robert W Boyd, and Ebrahim Karimi. Arbitrary optical wavefront shaping via spin-to-orbit coupling. *Journal of Optics*, 18(12):124002, 2016. (cited on page 164).

[223] Frédéric Bouchard, Harjaspreet Mand, Mohammad Mirhosseini, Ebrahim Karimi, and Robert W Boyd. Achromatic orbital angular momentum generator. *New Journal of Physics*, 16(12):123006, 2014. (cited on page 164).

[224] Patrice Genevet, Nanfang Yu, Francesco Aieta, Jiao Lin, Mikhail A Kats, Romain Blanchard, Marlan O Scully, Zeno Gaburro, and Federico Capasso. Ultra-thin plasmonic optical vortex plate based on phase discontinuities. *Applied Physics Letters*, 100(1):013101, 2012. (cited on page 164).

[225] Ebrahim Karimi, Sebastian A Schulz, Israel De Leon, Hammam Qassim, Jeremy Upham, and Robert W Boyd. Generating optical orbital angular momentum at visible wavelengths using a plasmonic metasurface. *Light: Science & Applications*, 3(5):e167, 2014. (cited on page 164).

[226] Ze'ev Bomzon, Gabriel Biener, Vladimir Kleiner, and Erez Hasman. Space-variant pancharatnam–berry phase optical elements with computer-generated subwavelength gratings. *Optics letters*, 27(13):1141–1143, 2002. (cited on page 164).

[227] Siddharth Ramachandran and Poul Kristensen. Optical vortices in fiber. *Nanophotonics*, 2(5-6):455–474, 2013. (cited on page 164).

[228] Huanlu Li, David B Phillips, Xuyang Wang, Ying-Lung Daniel Ho, Lifeng Chen, Xiaoqi Zhou, Jiangbo Zhu, Siyuan Yu, and Xinlun Cai. Orbital angular momentum vertical-cavity surface-emitting lasers. *Optica*, 2(6):547–552, 2015. (cited on page 164).

[229] Pei Miao, Zhifeng Zhang, Jingbo Sun, Wiktor Walasik, Stefano Longhi, Natalia M Litchinitser, and Liang Feng. Orbital angular momentum microlaser. *Science*, 353(6298):464–467, 2016. (cited on page 164).

[230] Xinlun Cai, Jianwei Wang, Michael J Strain, Benjamin Johnson-Morris, Jiangbo Zhu, Marc Sorel, Jeremy L O'Brien, Mark G Thompson, and Siyuan Yu. Integrated compact optical vortex beam emitters. *Science*, 338(6105):363–366, 2012. (cited on page 164).

[231] Zhenwei Xie, Ting Lei, Fan Li, Haodong Qiu, Zecen Zhang, Hong Wang, Changjun Min, Luping Du, Zhaohui Li, and Xiaocong Yuan. Ultra-broadband on-chip twisted light emitter for optical communications. *Light: Science & Applications*, 7(4):18001, 2018. (cited on page 164).

[232] Jeffrey B Driscoll, Xiaoping Liu, Saam Yasseri, Iwei Hsieh, Jerry I Dadap, and Richard M Osgood. Large longitudinal electric fields (ez) in silicon nanowire waveguides. *Optics Express*, 17(4):2797–2804, 2009. (cited on page 165).

[233] Yao Liang, Han Wen Wu, Bin Jie Huang, and Xu Guang Huang. Light beams with selective angular momentum generated by hybrid plasmonic waveguides. *Nanoscale*, 6(21):12360–12365, 2014. (cited on page 166).

[234] Giorgio Maltese. Design of an algaas on-chip device to generate a oam/sam light beam. `https://github.com/giomalt/thesis_public_media/blob/master/Maltese_SaclayM2_internshipMPQ.pdf?raw=true`, 2015. (cited on pages 166 and 170).

[235] Giorgio Maltese. Algaas on-chip device emitting a light beam carrying spin and orbital angular momentum. `https://www.politesi.polimi.it/handle/10589/120982`, 2015. (cited on page 172).

[236] MJ Padgett and L Allen. The angular momentum of light: optical spanners and the rotational frequency shift. *Optical and quantum electronics*, 31(1):1–12, 1999. (cited on page 181).

[237] M Harris, CA Hill, PR Tapster, and JM Vaughan. Laser modes with helical wave fronts. *Physical Review A*, 49(4):3119, 1994. (cited on page 192).

Generation and manipulation of high-dimensional photonics states with AlGaAs chips

This thesis is devoted to the development of novel integrated devices and methods for the generation and manipulation of high-dimensional states of light, encoding information in either frequency or angular momentum degrees of freedom.

We report on the study of an AlGaAs waveguide implementing type-II spon-taneous parametric down conversion process in a monochromatic pump regime, with a focus on the joint spectral amplitude of the emitted biphoton state. The generation of broadband biphoton states of light in the telecom range is theoretically proposed and experimentally demonstrated. A Hong-Ou Mandel interferometry, performed without any spectral filtering, indicates that signal and idler photons are emitted over a large bandwidth (170nm) and with a high degree of indistinguishability (V=0.86). By considering the cavity effect due to waveguide facets reflectivity, we propose the generation of biphoton frequency-comb states. More specifically, we show that a fine tuning of the monochromatic pump frequency enables the generation of two classes of frequency-comb states, resonant and anti-resonant states, and reconstruct their joint spectral via Stimulated Emission Tomography. We exploit the unique spectral properties of these states in a manipulation scheme based only on passive telecom components, namely a polarizing beam splitter and a delay line. The experimental demonstration of this scheme is done on AlGaAs sources and the successful state manipulation is demonstrated by Hong-Ou-Mandel interferometry.

In addition, we demonstrate the realization of an AlGaAs ridge waveguide for the generation of light beams with tailored phase and polarization distributions, carrying spin angular momentum, and present the design of a device with a similar geometry for the generation of a twisted light beam, carrying first order orbital angular momentum.

Keywords: quantum optics, photonics, spontaneous parametric down conversion, entanglement, quantum frequency combs, orbital angular momentum, AlGaAs

Génération et manipulation d'états photoniques de haute dimension avec des puces AlGaAs

Cette thèse est consacrée au développement de nouveaux dispositifs semiconducteurs intégrés et de méthodes pour la génération et la manipulation d'états lumineux de haute dimension. Nous présentons l'étude d'un guide d'onde AlGaAs utilisant un processus de conversion paramétrique spontanée de type II en régime de pompage monochromatique, s'intéressant en particulier à l'amplitude spectrale jointe de l'état émis. La source fonctionne à température ambiante, émet des paires de photons dans le domaine des télécommunications et est compatible avec l'injection électrique. La génération d'états biphotoniques à large bande est démontrée expérimentalement par la reconstruction de l'intensité spectrale jointe et par une expérience de Hong-Ou-Mandel indiquant que les photons signal et complémentaire sont émis sur une large bande spectrale (170 nm) et avec un haut degré d'indiscernabilité (V=0,86). De plus, nous montrons que l'effet de cavité dû à la réflectivité des facettes des guides d'onde conduit à la production de peignes de fréquence à deux photons. Cette plateforme est utilisée pour démontrer une méthode originale de génération et de contrôle de la symétrie des états peignes exploitant les effets de cavité et un retard imposé entre les deux photons de chaque paire. Plus spécifiquement, nous montrons qu'un réglage fin de la fréquence de la pompe permet de générer des états peignes résonnants et anti-résonants permettant de manipuler la symétrie de la fonction d'onde. La méthode peut être adaptée et appliquée à une grande variété de systèmes, massifs ou intégrés, augmentant ainsi leur flexibilité et la richesse des états générés en vue de la mise en œuvre de nouveaux protocoles d'information quantique. En outre, nous démontrons la réalisation d'un guide d'onde AlGaAs pour la génération de faisceaux lumineux portant un moment angulaire de spin et présentons la conception d'un dispositif pour la génération d'un faisceau lumineux portant un moment orbital angulaire de premier ordre.

Mots clés: optique quantique, photonique, conversion paramétrique, intrication, état en peigne de fréquences, moment orbital angulaire, AlGaAs